Hybridisation of mixed transition metal oxide with graphene as advanced electrode material for symmetric supercapacitor application

Wei Hau Low

Thesis submitted to the University of Nottingham for the degree of

Doctor of Philosophy

February 2021

Abstract

Nowadays, imminent deficiency of fossil fuels and rising environmental concerns have triggered the immense research enthusiasm for the development of green and renewable energy sources. Lately, supercapacitors are emerging as one of the competent energy storage devices owing to their excellent capacitive properties, long term cycling stability as well as remarkable power density. In this sense, the promising family of mixed transition metal oxides (MTMO) possesses felicitous as active electrode materials for supercapacitor due to their multiple oxidation states and ions, leading to superior specific capacitance. Moreover, many researchers are dedicated in hybridising the MTMO with graphene nanosheets as advanced electrode materials due to the peculiar properties of graphene, which ameliorate the electrical conductivity and enlarge the specific surface area of the nanocomposite for Faradaic redox reaction. The current thesis emphasis on the latest evolution of MTMO and the integration of MTMO with graphene nanosheets as active electrode materials, with a comprehensive study of their synthetic approaches. In addition, the energy storage mechanism of distinct types of supercapacitor and the critical factors affecting the electrochemical activities of transition metal oxide-based materials are also delineated.

Based on the literature review, solvothermal technique was acknowledged as one of the effective synthetic routes for MTMO/graphene nanocomposites, which impress by its versatility in controlling the morphology and growth mechanism (nucleation and diffusion process) of the reactants. Additionally, solvothermal method is also a simple and cost effective process with high scalability potential. In chapter 4, graphene/nickel vanadate ($Ni_3V_2O_8$) nanocomposites were successfully

synthesised through the solvothermal method. The nanocomposites integrate separately the advantages of graphene sheet and pseudocapacitive nature of $Ni_3V_2O_8$, leading to outstanding electrochemical performance than the pristine $Ni_3V_2O_8$. Optimisation on the weight ratios between the graphene and $Ni_3V_2O_8$ were conducted to determine the perfect synergistic effect between the highly conductive graphene sheet and the pseudocapacitive $Ni_3V_2O_8$. Among the graphene/$Ni_3V_2O_8$ nanocomposites, G-4NVO as promising electrode material performed an eminent specific capacitance of 368 Fg^{-1} at a current density of 0.5 Ag^{-1} and energy density of 51 Wh/kg at a power density of 920 W/kg. An excellent cycling stability with 92 % capacitance retention and coulombic efficiency of nearly 100 % were achieved after 3000 charge-discharge cycles at $1Ag^{-1}$.

A series of graphene/cobalt vanadate ($Co_3V_2O_8$) nanomaterials with multiple weight ratios were prepared and their respective physical and electrochemical performances were evaluated in chapter 5. The nanocomposite with weight ratio of 1:4 (G-4CVO) exhibited the highest specific capacitance of 275.2 Fg^{-1} at 0.8 Ag^{-1}. A specific capacitance of 216 Fg^{-1} was obtained at high current density of 1.2 Ag^{-1}. The electrode material maintained 81 % of its charge storage capability after 3000 cycles, signifying its outstanding cycling stability. Additionally, G-4CVO delivered remarkable energy and power densities, signifying its potential as advanced electrode material for supercapacitor application.

In chapter 6, the energy storage capability of the electrode material can be improved by combining graphene with zinc vanadate ($Zn_3V_2O_8$) to form the “sheet on sheet” architecture. For comparison, different weight ratios were applied to prepare the nanocomposites by using the solvothermal method. The synergistic effect between graphene and $Zn_3V_2O_8$ resulted in enhanced capacitive performance. Among the nanocomposites, G-3ZVO delineated a specific capacitance of 313.6 Fg^{-1} at 0.8 Ag^{-1}. Besides, 80 % of the initial capacitance was retained as the current density increased to 1.2 Ag^{-1}, suggesting its good rate capability. G-3ZVO achieved a specific capacitance of 246.8 Fg^{-1} (86 % retention) after experiencing 3000 repeated galvanostatic charge-discharge cycles, confirming its exceptional cycling stability. Furthermore, this symmetrical supercapacitor exhibited a maximum energy density of 43.55 Wh/kg.

A distinctive, nanobelts like manganese vanadate (MnV_2O_6) decorated on graphene nanaosheets was developed via the solvothermal method as electrode material for symmetric supercapacitor (Chapter 7). The effect of weight ratio (graphene:MnV_2O_6) on the structural and electrochemical performances was also determined to study the detail synergistic effect between graphene and MnV_2O_6. G-8MVO revealed the maximum specific capacitance of 348 Fg^{-1} at the current density of 0.5 Ag^{-1}. A capacitance retention of 88 % was achieved after 3000 cycles, suggesting its excellent cycling stability. In addition, G-8MVO obtained a maximum energy density of 48.33 Wh/kg at a power density of 880.6 W/kg, highlighting the potential of this material to bridge the gap between the battery and supercapacitor.

In chapter 8, graphene/aluminium vanadate (AlV_3O_9) nanocomposites were developed through the deposition of 3D lion’s mane like AlV_3O_9 microspheres on graphene sheets. Different physical and electrochemical properties were obtained by varying the weight ratios between graphene and AlV_3O_9. Notably,

nanocomposite with the weight ratio 1:5 (G-5AlV) showed a specific capacitance of 268.8 Fg^{-1} at 0.8 Ag^{-1}. A specific capacitance of 192 Fg^{-1} was obtained as the current density increased to 1.2 Ag^{-1}, suggesting its remarkable rate capability. Besides, a capacitance retention of 82 % was achieved together with a coulombic efficiency of nearly 100 % after 3000 repeated charge-discharge cycles, confirming its excellent cycling stability and good reversibility. The remarkable energy and power densities of G-5AlV suggest that it has a great potential in hybrid supercapacitor application.

In short, five desired graphene/MTMO nanocomposites were successfully synthesised in this work and their physical, chemical and electrochemical properties were analysed comprehensively. Besides, the effect of weight ratio between graphene and MTMO was well determined to study the best synergistic effect between both nanomaterials for advanced supercapacitor performance. Thus, it proves that all the research objectives in this PhD study have been achieved accordingly.

Acknowledgement

First of all, I would like to express my deepest gratitude to my supervisors, Prof Poi Sim Khiew and Dr Siew Shee Lim for their consistent guidance, supervision and support throughout the whole period of my PhD study in University of Nottingham Malaysia Campus. Prof Khiew is a kind person, who spent a lot of time discussing the experimental planning, data analysis, paper writing with me and he gave me valuable suggestion to overcome all the difficulties during my PhD study. I would also like to convey my appreciation to the collaborators, Prof Chin Hua Chia and Dr Wee Siong Chiu for their valuable analytical supports on the sample.

I would like to acknowledge the financial support from Ministry of Higher Education Malaysia (FRGS grant code: FRGS/1/2019/STG02/UNIM/01/1 and FRGS/1/2016/STG02/UNIM/02/1) and Faculty Research Grant (GPF043B-2018). The technical support by The University of Nottingham Malaysia Campus is greatly appreciated.

I would like to express my warmest gratitude to my parents and sister for their endless support and encouragement. Without their eternal love, I would not be able to overcome all the difficulties in my daily life and complete my PhD research program within the timeframe.

Last but not least, I would like to thank the Foundation in Engineering and Department of Chemical Engineering for giving me enough support during my PhD research.

Publication List

1. **W.H. Low**, P.S. Khiew, S.S. Lim, C.W. Siong, E.R. Ezeigwe, Facile solvothermal designing of graphene/$Ni_3V_2O_8$ nanocomposite as electrode for high performance symmetric supercapacitor, Journal of Alloys and Compounds, 768 (2018) 995-1005.
2. **W.H. Low**, P.S. Khiew, S.S. Lim, C.W. Siong, E.R. Ezeigwe, Recent development of mixed transition metal oxide and graphene/mixed transition metal oxide based hybrid nanostructures for advanced supercapacitors, Journal of Alloys and Compounds, 775 (2019) 1324-1356.
3. **W.H. Low**, P.S. Khiew, S.S. Lim, C.W. Siong, C.H. Chia, E.R. Ezeigwe, Facile synthesis of graphene-$Zn_3V_2O_8$ nanocomposite as a high performance electrode material for symmetric supercapacitor, Journal of Alloys and Compounds, 784 (2019) 847-858.
4. **W.H. Low**, C.W. Siong, C.H. Chia, S.S. Lim, P.S. Khiew, A facile synthesis of graphene/$Co_3V_2O_8$ nanocomposites and their enhanced charge storage performance in electrochemical capacitors, Journal of Science: Advanced Materials and Devices, 4 (2019) 515-523.
5. **W.H. Low**, S.S. Lim, C.H. Chia, C.W. Siong, P.S. Khiew, Three-dimensional lion's mane like AlV_3O_9 deposited on graphene surface for supercapacitors with a promising electrochemical performance, Journal of Science: Advanced Materials and Devices, 5 (2020) 164-172.

6. **W.H. Low**, S.S. Lim, C.H. Chia, C.W. Siong, P.S. Khiew, One dimensional MnV_2O_6 nanobelts on graphene as outstanding electrode material for high energy density symmetric supercapacitor (Sumitted to Journal).

List of Figures

List of Tables

Nomenclature

A list of symbols is provided with a short description and unit.

Symbol	**Description and Unit**
C_s	Specific capacitance (Fg^{-1})
η	Coulombic Efficiency (%)
I	Discharge current (A)
Δt	Discharge time (s)
ΔV	potential window (V)
m	Mass of the electrode material (g)
t_C	Charge time (s)
t_D	Discharge time (s)
E	Energy density ($Whkg^{-1}$)
P	Power density ($kWkg^{-1}$)

Abbreviation	**Description**
AACVD	Aerosol assisted chemical vapour deposition
AC	Activated carbon
1D	One dimensional
2D	Two dimensional
3D	Three dimensional
CF	Carbon fabric
CNT	Carbon nanotubes
CV	Cyclic voltammetry
D.I	Deionised water
EDL	Electrical double layer

EDLC	Electrical double layer capacitor
EDX	Energy dispersive x-ray spectroscopy
EELS	Electron energy loss spectroscopy
EG	Ethylene glycol
EIS	Electrochemical impedance spectroscopy
ESR	Equivalent series resistance
ESS	Energy storage system
FESEM	Field emission scanning electron microscopy
GCD	Galvanostatic charge discharge
G-AlV	Graphene-aluminium vanadate nanocomposites
G-CVO	Graphene-cobalt vanadate nanocomposites
G-MTMO	Graphene-mixed transition metal oxide
G-MVO	Graphene-manganese vanadate nanocomposites
G-NVO	Graphene-nickel vanadate nanocomposites
G-ZVO	Graphene-zinc vanadate nanocomposites
HOPG	Highly pyrolytic graphite flakes
HRTEM	High resolution transmission electron microscopy
IR	Internal resistance
LIB	Lithium ion battery
LIBs	Lithium ion batteries
LRTEM	Low resolution transmission electron microscopy
MOF	Metal organic framework
MOF-C	Metal organic framework combustion techniques
MTMO	Mixed transition metal oxide
MTMOs	Mixed transition metal oxides
NCO-rGO	$NiCo_2O_4$-reduced graphene oxide
NVO	Pure nickel vanadate
OER	Oxygen evolution reaction
OMEP	Ordered macro-porous electrode plate

R_{ct}	Charge transfer resistance
R_{esr}	Equivalent series resistance
R_s	Solution resistance
rGO	Reduced graphene oxide
rNHGO	Reduced nanohole graphene oxide
SEM	Scanning electron microscopy
SWCNT	Single wall carbon nanotubes
TEM	Transmission electron microscopy
TMO	Transition metal oxide
W	Warburg Impedance
XPS	X-ray photoelectron spectroscopy
XRD	X-ray diffraction

Contents

Chapter 1: Introduction

1.1 Background

With the rapid development of modern economies, the demands on non-renewable energy resources such as crude oil, coal, diesel and etcetera increase tremendously, leading to energy crisis and the occurrence of greenhouse effect[1, 2]. Thus, development of robust, environmental benign, cost effective and renewable energy has drawn considerable research enthusiasm as next generation energy resources to tackle these urgent environmental issues[2, 3]. Myriad of energy storage appliances such as solar and wind energies, biofuel, conventional capacitors, lithium ion batteries and supercapacitors were developed and widely employed in high technology industries[3, 4]. Among these energy storage devices, supercapacitors, also known as ultracapacitors or electrochemical capacitors, are the most sought-after candidate for energy storage owing to its unique electrochemical performances such as high power density, excellent coulombic efficiency and fast charge-discharge rate as compared to lithium ion batteries, dielectric capacitor, fuel cells and others[5]. Besides, the superior cycling stability or long cycle life exhibited by a supercapacitor also embellished the efficiency of energy utilisation[3]. Nevertheless, the unsatisfactory energy density has restricted its practical applications[6]. Typically, energy density is substantially dependent on the specific capacitance value and the working potential range of the devices[7]. Therefore, determination of the most effective approach to improve the energy density of a supercapacitor while preserving its exceptional power density has become a major concern for the researchers in order to realise its practical application.

The energy and power densities of various energy storage system (ESS) such as commercial capacitors, supercapacitors, batteries and fuel cells are demonstrated in Figure 1.1[8].

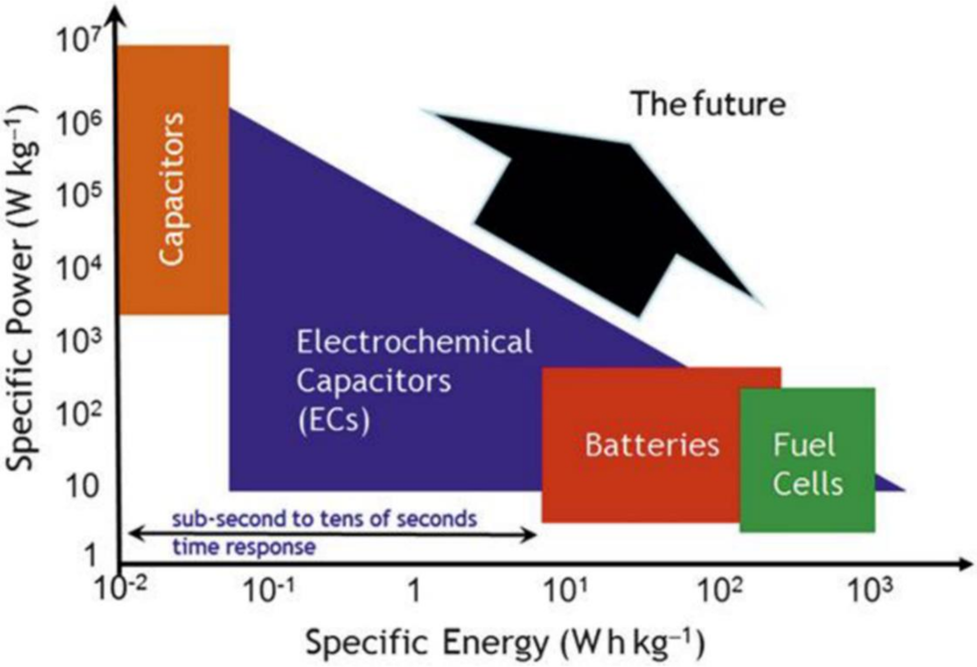

Figure 1.1: Ragone plot for various energy storage system. Reprinted with permission from ref.[8]. Copyright 2011, Materials Research Society.

Based on Figure 1.1, it is worth noting that none of the single energy source has fulfilled both power and energy density regions at the same time. The specific power of conventional capacitor is the highest as compared to other ESS but at the same time with the lowest specific energy. Furthermore, it can be observed that supercapacitors and batteries bridge the gap between the conventional capacitor and the fuel cells, revealing their ideal energy storage capabilities. The comparison between the supercapacitor and battery in terms of energy storage mechanism, charge storage determinants, energy density (Wh/kg), power density (W/kg), charge time, discharge time, cycle life, construction configuration, existence of internal potential (IR) and coulombic efficiency (%) is depicted in Table 1.1.

Table 1.1: Comparison between Supercapacitor and Battery[9].

Features	Supercapacitor,a	Battery,b
Energy Storage Mechanism	Physical	Chemical
Charge Storage Determinants	Microstructure and electrolyte	Active mas and thermodynamics
Energy Density	1 to 10 Wh/kg	20-100 Wh/kg
Power Density	500 to 10,000 W/kg	<1000 W/kg
Power Limitation	Electrolyte conductivity	Depending on reaction kinetic and mass transport
Charge Time	Seconds to minutes	1-5 hours
Discharge Time	Seconds to minutes	1 to 3 hours
Cycle Life	More than 500,000, (Ease in charge input and output)	Less than 2000, (irreversible redox reaction and phase change)
Cycle Life Limitation	Due to the occurrence of side reactions	Physically stable Chemically reversible
Configuration	Bipolar	Bipolar
Internal Potential (IR)	Due to high area platform and electrolyte	Due to the active material and the electrolyte.

Note: The data mentioned in the column of a and b were referred to the electrical double layer capacitors (EDLC) and lithium ion batteries (LIB) respectively.

From Figure 1.1 and Table 1.1, it is remarkable that supercapacitor possesses a higher energy density than the conventional capacitor, as well as higher power density than the lithium ion battery (LIB). Typically, a supercapacitor comprises of two electrodes on each side of the cell, which are separated by a separator as delineated in Figure 1.2.

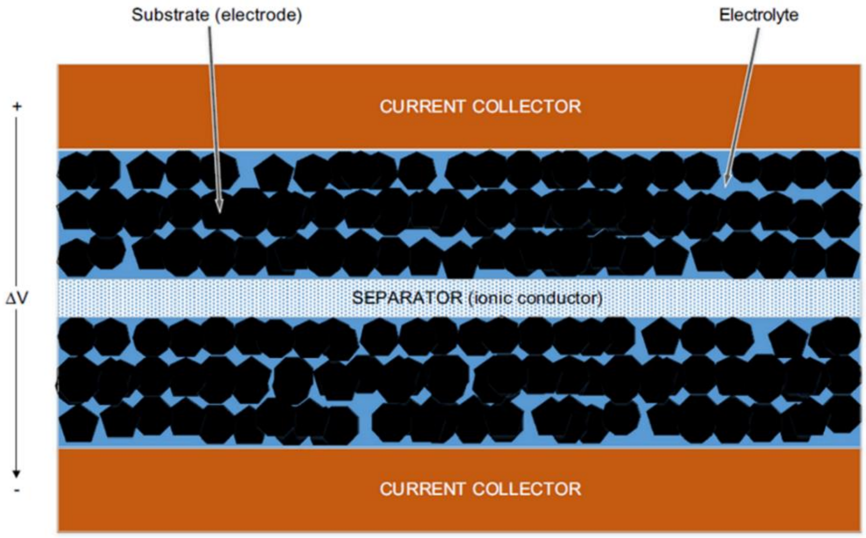

Figure 1.2: A schematic diagram of symmetric supercapacitor. Reprinted with permission from ref.[9]. Copyright 2016, Elsevier.

Both electrodes are similar for symmetric supercapacitor but different for the asymmetric supercapacitor. Besides, paper or polymer is employed as the separator for supercapacitor due to their inherent properties such as good ionic conductivity, high electrical resistivity, excellent ion permeability and fine thickness to ease the ionic charge transportation and hence augmenting the electrochemical performance[10]. Generally, the charge storage systems of supercapacitor are classified into two categories, namely electrical double layer capacitor (EDLC) and pseudocapacitor. As for the EDLC, the carbonaceous materials like activated carbon, single wall carbon nanotube (SWCNT), graphene, reduced graphene oxide (rGO) and etcetera are employed as the electrode where the electrical energy is stored by nanoscopic ion adsorption at the electrode/electrolyte interface. Contrarily, the pseudocapacitive materials like transition metal oxides and conducting polymer are utilised as the electrode for pseudocapacitor where the charge storage mechanism involves the fast Faradaic redox reaction[11]. The nature of the electrode material is crucial for the capacitive performance of the supercapacitor. Typically, pseudocapacitor possesses larger specific capacitance and higher energy density than EDLC due to the multiple oxidation states of transition metal oxides which allow rapid redox reaction for the enhancement of capacitance[12-15]. Among the pseudocapacitive materials, transition metal oxides (TMO) are sought-after as electrode material for pseudocapacitor. This is mainly attributed to the unique properties of TMO, including changeable valence which offers ideal pseudocapacitance, allows the intercalation of ions and electrons into the lattice of the metallic compounds and their inherent high stability[16-20]. Among the TMO, ruthenium oxide (RuO_2) has been extensively researched as it exhibits high specific capacitance (up to 1580 Fg^{-1}) and good electrical conductivity, and hence serves as one of the most promising candidates for supercapacitor applications[21]. Nevertheless, the acute toxicity, high cost and rareness of ruthenium elements have impeded its wide range applications[3-5]. Apart from RuO_2, other metal oxides like NiO, Co_3O_4, MnO_2 and V_2O_5 were widely investigated and proved to be naturally abundant, lucrative and also environmentally benign[22]. However, their practical applications were hampered by their relatively low specific capacitances. Thus, recent advances have acclaimed mixed transition metal oxides (MTMOs) as the most promising and low-cost candidates for supercapacitor applications as MTMO can advocate diverse redox reactions owing to the coexistence of two distinct metal species in a single crystal structure. Besides, the synergistic effect between the sole metal oxide in MTMO can enlarge the working potential window and develop more electroactive sites which lead to prominent specific capacitance as compared to single component metal oxide[4, 23, 24]. However, MTMO generally suffer from poor conductivity, inferior cycling stability and occurrence of aggregation during the continuous charge-discharge process[18].

Nanoscale hybridisation or effective combination of EDLC with pseudocapacitors was found to be the most appealing approach to ameliorate the electrochemical performance of MTMO, which is well-acknowledged as hybrid capacitors. Hybrid capacitors combine the intrinsic properties of both EDLC and pseudocapacitance. The hybridisation of MTMO with carbonaceous material, especially graphene develops synergistic effect, leading to improved electrical conductivity and enhanced ions and electron diffusion kinetics at the electrode/electrolyte interface as well as the interior of the electrodes. Furthermore, the introduction of graphene provides more electroactive sites for sufficient Faradaic redox reaction and accommodates the volume expansion during the continuous charge-discharge process[25, 26]. Other than that, the capacitive performances of supercapacitors highly rely on the properties of the electrode material such as morphology[27-30], porosity[31-33], specific surface area[14, 18, 34-37] and process parameters like calcination temperature[38, 39] and mass loading[40-42].

To date, numerous synthetic approaches have been developed to synthesise MTMO nanomaterial, such as hydrothermal/solvothermal, microwave assisted method, electrodeposition method, co-precipitation method, sono-chemical method and others[4, 43]. Recently, hydrothermal/solvothermal synthesis route has been extensively studied and regarded as the one of the most direct, facile and green approaches to fabricate the mixed transition metal oxides. Among various MTMO, the fascinating nature of vanadium based metal oxides in improving the capacitive performance has made it a competent electroactive material for supercapacitor in recent years. Vanadium is the element located in the VB position on the periodic table and associated with the 3d sub family with the valence electron configuration of $3d^3 4s^2$. This indicates that the outermost layer of vanadium consists of five valence electrons which involve in bonding. Besides, it also reveals the multivalent behaviours of vanadium based metal oxides like +5, +4, +3 and +2, resulted in eminent electrochemical activity[44, 45].

There have been many studies on the employment of MTMO as the electrode material for supercapacitor. In addition, the availability of graphene/MTMO has attracted enormous research enthusiasm from the researchers recently. However, the study of the integration of MTMO with graphene is rather scarce. Besides, reduced graphene oxide sheets have been synthesised mostly from the Modified Hummers method followed by chemical reduction process, which entail the adoption of harsh acids, highly reactive oxidizing agents and reducing agents. These additives doesn't merely impose detrimental effect to the environment, but also deteriorate the quality of the graphene. For this reason, the liquid phase exfoliation of highly pyrolytic graphite flakes using ethanol as the eco-green solvent is employed to synthesise graphene required for this research.

1.2 Problem statement

Nowadays, the integration of the advantages of both EDLC and pseudocapacitor has attracted enormous research attention in supercapacitor. Despite the EDLC electrode materials, especially graphene offers large specific surface area and increase the electrical conductivity, its poor specific capacitance and energy density has limited its practical application. Contrarily, mixed transition metal oxide based electrode materials are applied in the pseudocapacitor, which resulted in high specific capacitance and energy density. However, the poor power density, electrical conductivity and cycling stability have hindered its commercialisation. The inferior cycling stability of pseudocapacitive materials is attributed to the poor adaptation of volume expansion and extraction during the continuous charge discharge process, resulting in the rapid degradation of the pseudocapacitive electrode.

In order to overcome these obstacles, hybridisation of EDLC materials (graphene) with pseudocapacitive materials (mixed transition metal oxide) in the hybrid supercapacitor is an effective way since it offers large specific surface area, good electrical conductivity, excellent cycling stability, high specific capacitance and etcetera.

1.3 Aim and Objectives

Motivated by the aforementioned benefits of the nanoarchitecture and graphene composite, this research will emphasise on the facile and eco-green synthesis of novel graphene/MTMO nanocomposites as innovative electrode materials for high performance symmetric supercapacitors. The particular research activities in this project aim to:

- To synthesise a series of novel graphene/MTMO nanocomposites (graphene/$Ni_3V_2O_8$, graphene/$Co_3V_2O_8$, graphene/$Zn_3V_2O_8$, graphene/MnV_2O_6 and graphene/AlV_3O_9) with controllable morphology.
- To determine the inherent physical, chemical and electrochemical properties of the as-synthesised graphene/MTMO nanocomposites.
- To investigate the effect of graphene and the optimum weight ratio between the graphene and MTMO for the best synergistic effect between the both nanomaterials with excellent supercapacitive performance.
- To compare the energy density and power density of the as-synthesised electrode materials with some other research findings.

Chapter 2: Literature Review

Chapter 2 covers the morphological and electrochemical properties of novel MTMO like cobaltites, molybdate, vanadate, tungstate and etcetera. The current design, synthesis and applications of MTMO as well as the hybridisation of MTMO with graphene as the electrode material for supercapacitor were systematically reviewed. Besides, the impact of morphology, electrical conductivity and process parameters on the capacitive performance were also discussed.

2.1 Type of Supercapacitor

2.1.1 Electrical double layer capacitor (EDLC)

As similar to conventional capacitor, the charge storage mechanism of electrical double layer capacitor (EDLC) is non-faradic or based on the theory of electrical double layer, where the charge can be accumulated by reversible adsorption of electrolyte ions at the electrode/electrolyte interface electrostatically[46-48]. Three models have been developed to further demonstrate the working mechanism of electrical double layer (EDL) which are Helmholtz model, the Gouy-Chapman model and the Stern model as unveiled in Figure 2.1[49].

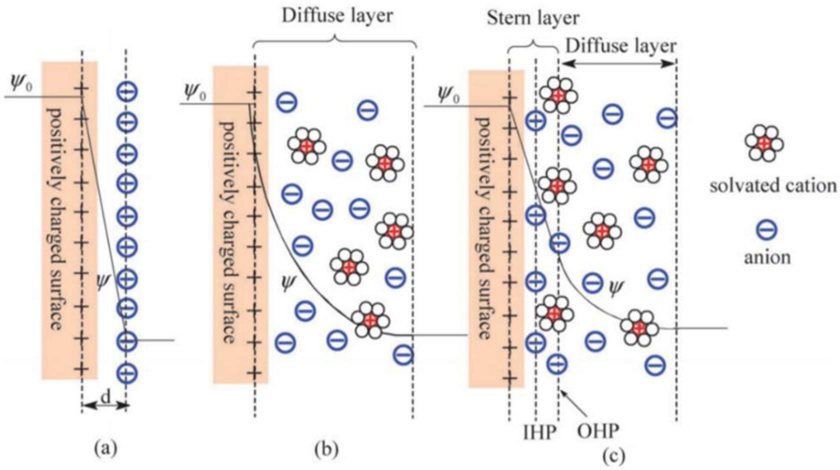

Figure 2.1: Models of electrical double layer, (a) Helmholtz model, (b) Gouy-Chapman model and (c) Stern model. Adapted with permission from ref.[49]. Copyright 2009, The Royal Society of Chemistry.

In the Helmholtz model, two layers of opposite charges are formed at the electrode/electrolyte interface where the positive charge at the solid electronic conductor is balanced by the opposite anion through the double layer distance, d. This is the simplest model to demonstrate the behaviour of EDL and it was further modified by Gouy-Chapman. In the Gouy-Chapman model, diffusion layer was taken into consideration, which comprised of the continuous dispersion of both cations and anions in the electrolyte solution forced by thermal motion. The ions in the electrolyte solution have the tendency to diffuse into the liquid phase region and the thickness of the diffusion layer was governed by the kinetic energy of the electrolyte ions[9, 49-51]. Nevertheless, the overestimation of electrical double layer capacitance is the shortcoming of this model[49]. Lastly, Stern combined both the Helmholtz model and Gouy-Chapman model to particularly acknowledge the development of two areas of ion distribution, namely internal Stern layer and external diffusion layer, which correspond to the Helmholtz layer and Gouy-Chapman layer respectively. In addition, ions are strongly adsorbed by the electrode in the Stern layer. Albeit these models illustrated ample description of the EDL on a flat surface, the elaboration on the real charge transfer mechanism in the supercapacitor is scarce. Figure 2.2 reveals the schematic diagram of EDLC[5].

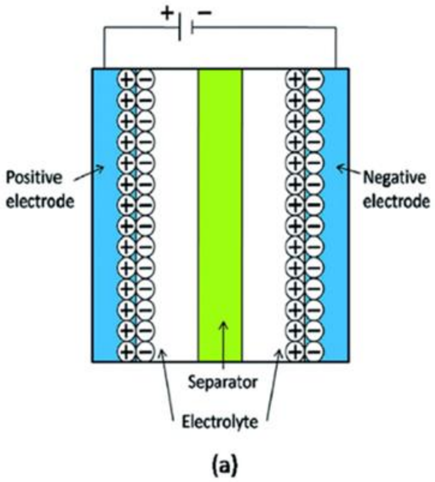

Figure 2.2: Schematic diagram of EDLC. Adapted with permission from ref.[5]. Copyright 2018, Elsevier.

When the voltage is applied, electrons will move from the positive electrode to the negative electrode through an external circuit, resulting in the accumulation of charge on the electrode surfaces. Cations are accumulated on the surface of negative electrode and vice versa for anions. Upon discharge, the electrons transported from negative to positive electrode. As EDLC is non-Faradaic, no occurrence of charge transfers across the boundary between electrode and electrolyte.

Apart from the working mechanism, active material with superior electrical conductivity and high specific surface area is the fundamental point to attain high specific capacitance in EDLC since the quantity of charge being stored is highly dependent on the specific surface area of the electrode materials[52]. Among all the carbonaceous material, graphene as a nanosheet of sp2 bonded carbon atoms with one atom thick in a honeycomb crystal structure has drawn much attention from the research society recently[26]. This is mainly due to its intriguing physical and chemical properties such as high theoretical surface area, superior electrical conductivity, good electrochemical stability, high flexibility and outstanding mechanical tenacity[18, 25]. Figure 2.3 delineates the honeycomb lattice of graphene sheet[53].

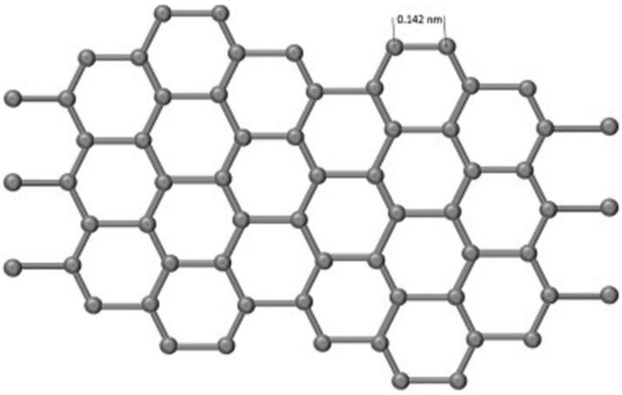

Figure 2.3: Schematic diagram of the honeycomb lattice of graphene. Adapted with permission from ref.[53]. Copyright 2017, Elsevier.

In particular, the presence of graphene will increase the electrical conductivity, encourage the diffusion of electrolyte ions, and hence improve the charge storage effect[42].

2.1.2 Pseudocapacitor

With regard to pseudocapacitors, it is originated from the fast and reversible redox reactions at or near the electrode surface as well as the penetration of adsorbed electrolyte ions through the double layer[5, 9]. The occurrence of Faradaic redox reactions leads to the increment on specific capacitance and the energy density of the supercapacitor as compared to EDLC[54]. Besides, for pseudocapacitance, the electrode potential coupled with the adsorbed active species is a constant logarithmic function of the extent of sorption. Thus, the charge storage in a pseudocapacitor is directly proportional to the charging potential window and the charge storage is initiated by the electrons and ions transportation instead of the accumulation of ions in electrochemical double layer capacitor (EDLC)[55, 56]. Nevertheless, the specific power that pseudocapacitor exhibited is generally lower than that of EDLC, which can be elucidated by the sluggish Faradaic processes[57]. Figure 2.4 demonstrates the schematic illustration of a pseudocapacitor[5].

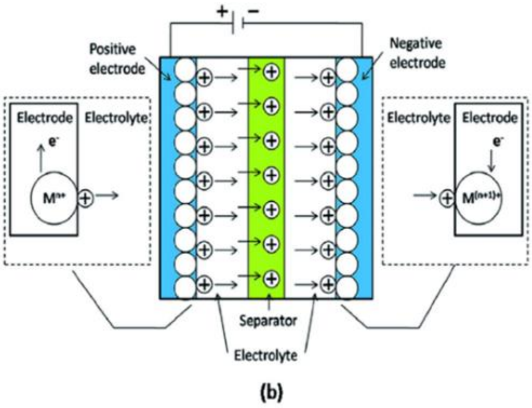

Figure 2.4: Schematic illustration of a pseudocapacitor. Adapted with permission from ref.[5]. Copyright 2018, Elsevier.

When voltage is applied, the anions in the electrolyte will involve in the Faradaic reversible redox reactions and move towards the opposite direction to the cations. Nickel cobaltite ($NiCo_2O_4$) is a simple example of mixed transition metal oxide that possess pseudocapacitive nature from the Faradaic redox reactions and the pertinent charge storage mechanism is revealed in Figure 2.5[58].

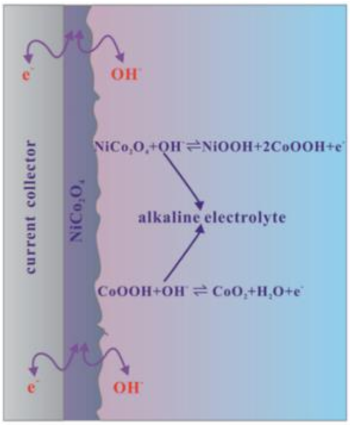

Figure 2.5: A schematic diagram of charge storage mechanism of $NiCo_2O_4$. Adapted with permission from ref.[58]. Copyright 2014, The Royal Society of Chemistry.

Based on Figure 2.5, the charge storage mechanism of $NiCo_2O_4$ comprised the insertion and desertion of charges on the surface and in the bulk of solid electrode in an alkaline solution, which correspond to the following reactions[58]:

$$NiCO_2O_4 + OH^- + H_2O \leftrightarrow NiOOH + 2CoOOH + e^- \qquad (2.1)$$

$$CoOOH + OH^- \leftrightarrow CoO_2 + H_2O + e^- \qquad (2.2)$$

Upon the charge-discharge process, the fast and reversible redox reaction happened, resulting in the valence states change of Co^{3+} to Co^{4+} as well as the Ni^{2+} to Ni^{3+} on the surface of electrode material.

Apart from that, different charge storage mechanisms can be noted from the pseudocapacitive electrode such as under-potential deposition, reversible electrochemical doping-dedoping in conducting polymer and intercalation pseudocapacitance[59]. Herein, the intercalation pseudocapacitance is discussed and its schematic diagram is depicted in Figure 2.6.

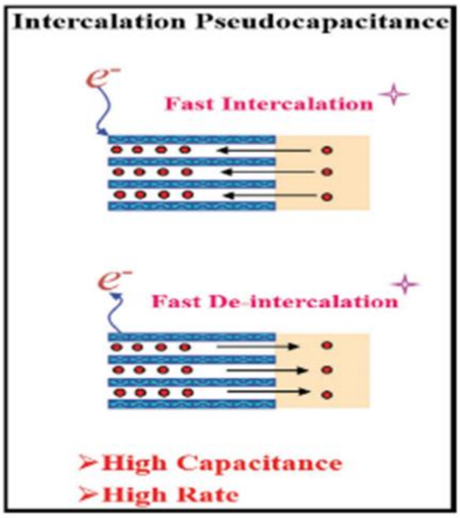

Figure 2.6: Schematic diagram of charge storage mechanism of intercalation pseudocapacitance. Reproduced with permission from ref.[59]. Copyright 2016, The Royal Society of Chemistry.

Intercalation pseudocapacitance is a new type of charge storage mechanism, which rely on the intercalation and de-intercalation of cations such as Na^+, K^+, Li^+ and H^+ in the bulk of active materials. However, it is not restricted by the distribution of cations in the crystalline active materials.

2.1.3 Hybrid supercapacitor

In order to exploit the full advantage of EDLC and pseudocapacitor, hybrid supercapacitor was developed which combined both the charge storage mechanisms. Typically, a hybrid capacitor comprises of two types of electrodes, one of them is capacitor type (non-Faradaic-as power origin) and another electrode is battery type (Faradaic-as an energy source) [60, 61]. The integration of these types of electrodes allows the hybrid supercapacitor to store charge electrostatically and Faradaically, leading to the achievement of high energy and power densities without scarifying its cycling stability. Generally, carbonaceous materials and mixed transition metal oxides (MTMO) are employed as the electrode material for hybrid supercapacitor.

Among the carbonaceous materials, hybridisation of graphene with MTMO as electrode material has been widely investigated, where graphene serves as a supporting matrix and material mediator (encapsulate) with respect to the electrode architecture viewpoint as illustrated in Figure 2.7[62-64].

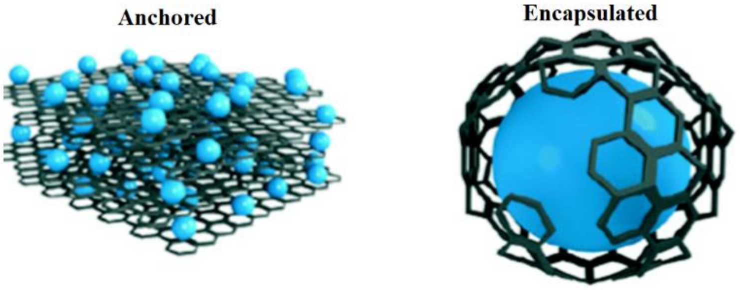

Figure 2.7: Different structural models of graphene nanocomposite. Reprinted with permission from ref.[64] Copyright 2015, Nature Publishing Group.

As the supported matrix in nanocomposite, the incorporated graphene sheets not only behave like a scaffold with enlarged specific surface area for nanoscale active material deposition, but also act as an electronic conductive network to promote the intercalation/de-intercalation processes. Besides, the intimate contact of graphene sheets with the MTMO active material allowed the rapid electron transfer, leading to the occurrence of fast reversible redox reactions and hence enhanced the capacitive performance of a supercapacitor[65-70]. On the other hand, graphene as a media mediator plays a pivotal role in encapsulating the nanoscale active materials, which enhance the specific capacitance, rate capability, mechanical stability and electrochemical stability. These remarkable electrochemical performances can be ascribed to the nano-architectural design of the nanocomposite and the synergistic effect between the graphene sheets and MTMO nanomaterial. Firstly, the integration of graphene sheets in the nanobyhrid enlarged the specific surface area of the nanocomposite, which shorten the ion diffusion pathway and create more electroactive sites for the occurrence of redox reaction as compared to that without graphene. Meanwhile, the formation of the interspaces between the graphene sheets (shell) and the MTMO (core) can serve as the electrolyte ions reservoir, which allow rapid ion diffusion and hence ameliorating the rate capability of the electrode material. In addition, graphene sheets as the shell for the nanohybrid will improve the electrical conductivity, accelerate the rate of charge transfer and contribute to the extra electrical double layer capacitance[62].

Despite the unique intrinsic properties of graphene, the contribution of MTMO in the formation of hybrid supercapacitor is also significant. This is because sole graphene suffers from low specific capacitance when employed in supercapacitor and tends to agglomerate or even restacking irreversibly, leading to the formation of graphite through the van der Waals force upon drying[18]. Thus, the even distribution of MTMO on the graphene sheets effectively impedes the graphene from restacking as depicted in Figure 2.8 and hence provide synergistic advantages to be utilised as the active electrode material for hybrid supercapacitor applications[18].

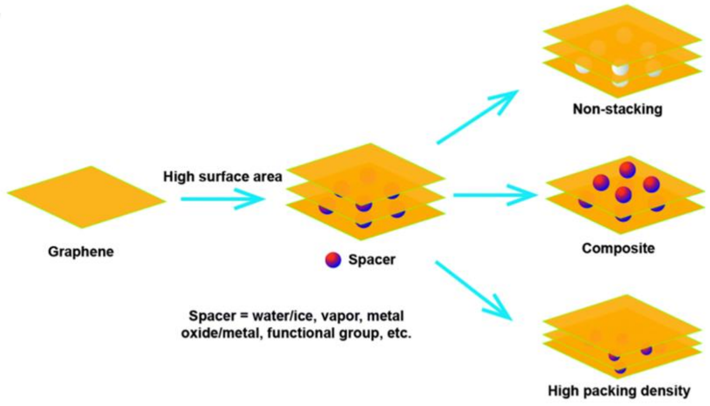

Figure 2.8: Graphene/MTMO nanocomposite with high specific surface area and non-restacking. Adapted with permission from ref.[63]. Copyright 2015, The Royal Society of Chemistry Publishing Group.

2.2 Synthetic strategies for MTMO

2.2.1 Hydrothermal/Solvothermal synthesis

Hydrothermal or solvothermal synthetic route is recognised as a facile one pot synthesis and solution-based approach to prepare MTMO[71, 72]. In addition, this technique enables easy manipulation and involves only simple experimental equipment like a hot air oven and autoclave [73]. In fact, the synthetic strategies of hydrothermal and solvothermal are analogous, where aqueous solution and organic solution are adopted in the process, respectively [4]. This method offers good crystallinity and shape selectivity for the metal oxide based materials[74]. Furthermore, hydrothermal/solvothermal process involves heterogeneous chemical reaction in a closed system (autoclaves), where the precursors of metal oxides are configured as the mixture of reaction substances in a sealed Teflon-lined stainless steel autoclave. Meanwhile, solvent is adopted to dissolve and recrystallise the materials above ambient temperature (>100 ^{o}C) to achieve the saturation pressure condition where internal pressure will build up autogenously[75, 76]. In addition to reaction temperature, the morphology and property of the final product are also significantly influenced by other process parameters, including the amount of dissolved salts, reaction time and the occupied spaces of the closed system[77]. Other than that, a wide range of TMO and MTMO with exceptional oxidation states and low temperature phases can be synthesised by solvothermal approach[78]. Solvothermal approach also offers some advantages such as exclusion of toxic or hazardous catalyst, mild reaction conditions, high product purity, and the formation of highly monodispersed particles with controllable size and morphology[5]. By tuning the reaction temperature, pH and concentration of the solution, MTMO with different dimensional morphologies like 1D, 2D and 3D together with large specific surface area and porous structure can be acquired[15, 25, 32, 33, 36, 77, 79, 80]. For instance, Kumar et al.[32] fabricated 3D porous urchin-shaped $Ni_3V_2O_8$ hollow nanospheres electrode via a template free hydrothermal method with $NH_4(OH)$ as the alkaline medium. The as-synthesised electrode possessed promising specific capacity of 402.8 Cg^{-1} at a current density of 1 Ag^{-1} with enhanced rate capability and cycling stability (88 % retention) after 1000 cycles. Nevertheless, the morphology of $Ni_3V_2O_8$ altered from hollow nanospheres to nanoparticles when NaOH was employed in lieu of $NH_4(OH)$, revealing the significant impact of solution pH on the morphology of the final product. The detailed growth mechanism of $Ni_3V_2O_8$ nanospheres and nanoparticles synthesised by the hydrothermal approach under different alkaline media is demonstrated in Figure 2.9.

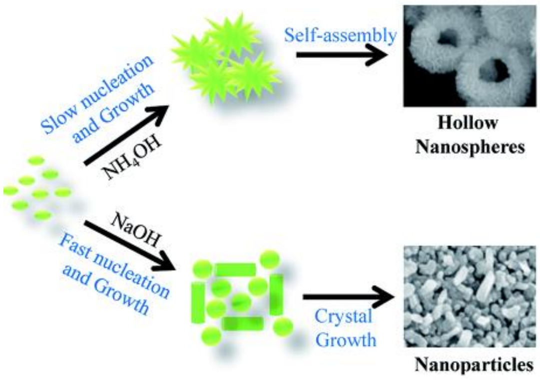

Figure 2.9: Synthesis and growing mechanism of $Ni_3V_2O_8$ nanospheres and nanoparticles by hydrothermal method under different alkaline media. Reprinted with permission from ref.[32]. Copyright 2016, The Royal Society of Chemistry Publishing Group.

It was reported that the specific capacity of $Ni_3V_2O_8$ diminished from 402.8 Cg^{-1} to 326.8 Cg^{-1} at 1 Ag^{-1} when the morphology of $Ni_3V_2O_8$ evolved from nanospheres to nanoparticles. Besides, the $Ni_3V_2O_8$ nanoparticles manifested inferior cycling stability with capacity retention of merely 32 % after 1000 cycles. These results evidently revealed that the morphology, capacitive performance and cycling stability of the final product were susceptible to pH change. Furthermore, hydrothermal synthesis of one dimensional $NiMoO_4$ nanowires radially on carbon cloth was presented by Wang et al.[81] as demonstrated in Figure 2.10.

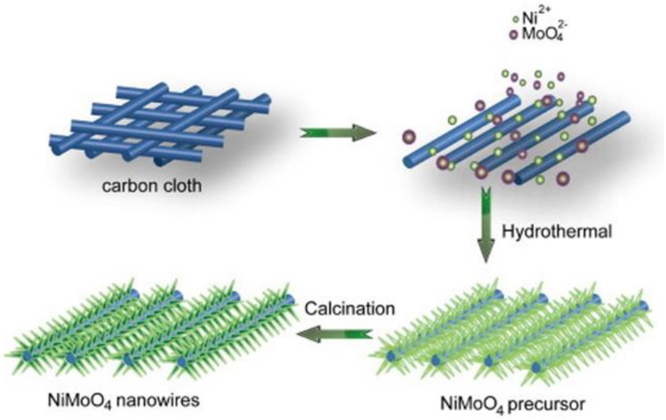

Figure 2.10: Schematic diagram of the synthetic route of $NiMoO_4$ nanowire supported on carbon cloth by a hydrothermal method. Adapted with permission from ref.[81]. Copyright 2014, Nano Energy Publishing Group.

This electrode material exhibited high specific capacitance of 1587 Fg^{-1} at a current density of 5 $mAcm^{-2}$ and capacity retention of 76.9 % after 4000 cycles.

Contrarily, the solvothermal technique involves the use of organic solvent like ethanol and ethylene glycol [58]. Figure 2.11 depicted the anchoring of 2D $NiCo_2O_4$ nanosheets on reduced graphene oxide (rGO) by solvothermal method with the use of ethylene glycol (EG) as solvent, followed by calcination process [33].

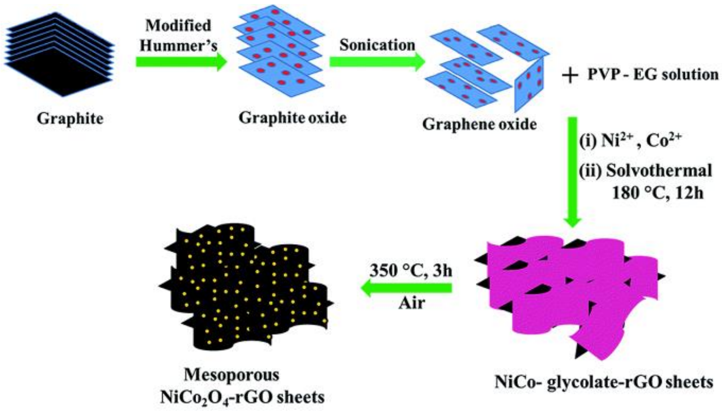

Figure 2.11: Synthesis mechanism of ultrathin mesoporous $NiCo_2O_4$-rGO nanocomposite. Reprinted with permission from ref.[33]. Copyright 2015, The Royal Society of Chemistry Publishing Group.

As electrode material for supercapacitor, $NiCo_2O_4$-rGO nanocomposite delivered an excellent specific capacitance of 870 Fg^{-1} at 2 Ag^{-1} and 600 Fg^{-1} at a current density of 20 Ag^{-1}. Besides, 90% of the initial capacitance was retained after 5000 continuous charge-discharge cycles, revealing its outstanding cycling stability. This remarkable electrochemical performance can be elucidated by the present of rGO, which not only improved the electrical conductivity of the nanocomposite but also served as a buffer matrix to accommodate the large volume expansion during the continuous charge-discharge process[25, 82].

2.2.2 Microwave assisted technique

The microwave assisted approach is a simple and fast synthetic method for the fabrication of micro and nano-sized composite materials. This can be assigned to the exceptional versatility exhibited by microwave, where the reaction time can be shortened substantially from days and hours to minutes or seconds as compared to the conventional heating methods[4, 5]. Particularly, microwave assisted technique has the functionality of controlled heating, benefiting the growth of nanomaterial since the synthesis process is immensely depending on the reaction temperature[77]. Besides, this technique can suppress side reaction and accelerate the kinetics of crystallisation process, resulting in the development of high purity nano-architecture material and large production yield[83]. Recently, microwave-assisted technique has been widely utilised in the industry and academia for the one-pot synthesis of myriad metal oxide and bimetallic oxide nanostructured materials[84-89]. For instance, reduced graphene oxide (rGO)/Fe_2O_3 nanocomposite was developed by Saraf, Natarajan and Mobin[89] as the electrode material for supercapacitor applications via microwave assisted technique. The corresponding synthetic route is demonstrated in Figure 2.12.

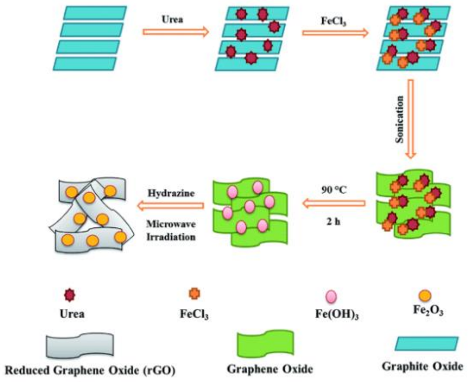

Figure 2.12: Synthetic route of rGO/Fe_2O_3 nanocomposite by microwave-assisted approach. Adapted with permission from ref.[89]. Copyright 2017, The Royal Society of Chemistry Publishing Group.

It manifested a specific capacitance of 577.5 Fg^{-1} at a current density of 2 Ag^{-1} and 437.5 Fg^{-1} at 10 Ag^{-1}, revealing its high specific capacitance and eminent rate capability. The authors ascribed its superior electrochemical performance to the positive synergistic effects between rGO platelets and Fe_2O_3 nanoparticles, in which Fe_2O_3 nanoparticles were encapsulated by the rGO. The intimate contact between rGO platelets and Fe_2O_3 nanoparticles effectively inhibited the agglomeration of nanoparticles, leading to enhanced electrochemical performance and improved structural integrity of the electrode material[90]. Besides, the crinkles on the corrugated rGO nanosheets impeded the restacking of nanosheets and reduced the ions and electrons diffusion pathway, further enhanced the electrochemical output [91, 92]. In addition, the interconnecting 3D network structure between rGO and Fe_2O_3 nanoparticles also strengthened the thermal stability of the nanocomposite [89].

Nevertheless, it is challenging to control the phases and the morphology of the MTMO in microwave assisted approach[4]. One of the strategies to enhance its morphological control is by integrating with solvothermal/hydrothermal process, where a shorter reaction time and better morphological control can be achieved [4, 5, 77]. Besides, nanoparticles with narrow size range and high purity can be synthesised through this microwave-hydrothermal coupled technique.

2.2.3 Sol-gel technique

Generally, sol-gel technique is a tedious process comprising of chemical and physical processes, which correlated with hydrolysis, polymerisation, gelation, condensation, drying and densification methods[5]. The term of sol-gel is derived from the fact that agglomeration of micro particles/molecules takes place in a solution to form sol under the well-controlled environment and the as-synthesised sol eventually channels with each other to form a comprehensive chain (gel)[73]. The sol-gel technique can be concisely summarised to be the transformation of a precursor solution into an inorganic solid through the chemical synthetic route[4]. Besides, the synthetic route of MTMO in the sol-gel process can be classified into two types, namely colloidal and polymeric methods. The variations between them stem from the adoption of precursors, where water and alcohol apply to the colloidal and polymeric routes, respectively[73]. The sol-gel process has attracted considerable interests in the synthesis of MTMO due to its easy manipulation and low cost. In addition, a product with high homogeneity and purity can be obtained via this technique[77]. Sol-gel technique can be divided into four stages[58], which include (i) preparation of precursor solutions, (ii) development of intermediates as sol, (iii) transformation from sol to gel and followed by (iv) thermal annealing treatment. Here, the morphological and electrochemical performances of the as-synthesised MTMO are significantly influenced by these parameters such as types of surfactant and solvent employed, reaction temperature and time[4].

To date, there have been a number of reports about the synthesis of MTMO through sol-gel technique for supercapacitor application[93-98]. For instance, in 2012, Liu and co-workers[97] reported the mesoporous $NiO/NiCo_2O_4/Co_3O_4$ composite fabricated by sol-gel process (Figure 2.13), demonstrating a superior specific capacitance of 1717 Fg^{-1}, excellent rate capability and cycling stability with the specific capacitance retention of 94.9 % after 1000 charge-discharge cycles.

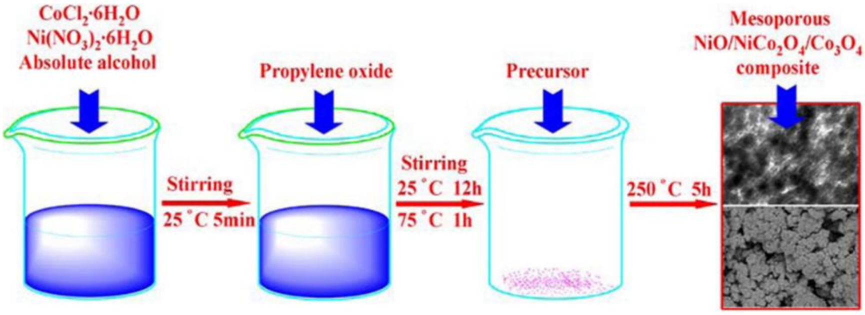

Figure 2.13: Sol-gel synthetic route of mesoporous $NiO/NiCo_2O_4/Co_3O_4$ composite. Reprinted with permission from ref.Liu, Kong, Lu, Li, Luo and Kang [97]. Copyright 2012, American Chemical Society.

Interestingly, the specific capacitance of the composite was higher as compared to the individual NiO, $NiCo_2O_4$ and Co_3O_4, suggesting the synergistic effect among the metal oxides on enhancing the electrochemical performance. Firstly, the formation of composite ameliorated the electrical conductivity and hence increased charge transfer rate. Secondly, the mesoporous structure within the $NiO/NiCo_2O_4/Co_3O_4$ composite offered larger specific surface area with more electroactive sites available for the occurrence of redox reaction, and hence improving the pseudocapacitance of the electrode material[99, 100]. Nonetheless, the practical application of sol-gel process in the large scale production of MTMO is still very challenging, which is mainly due to the extensive adoption of organic solvents and reagents in the process[4].

2.2.4 Electrodeposition technique

Electrodeposition is a one-step facile approach employed in the synthesis of MTMO as electrode material for supercapacitor application, in which the working principle of electrodeposition relies on the electrochemical redox reactions and the deposition of metal on the electrode when the electric current flows through the metal salt solution[4, 77]. This process has been extensively applied in the formation of

MTMO[101-105]. The selection of anion, pH of metal solution and deposition potential are crucial factors which should be deliberated during the deposition process of MTMO on electrode. The mechanism of electrodeposition process comprised of three stages[101, 106]: (i) formation of precursor solution, (ii) co-electrodeposition of nanoparticles, and lastly (iii) thermal decomposition.

Here, the synthesis of $NiCo_2O_4$ via electrodeposition has been widely acknowledged as the electroreduction of nickel nitrate ($NiNO_3$) and cobalt nitrate ($CoNO_3$) mixed solution. During the process, co-electrodeposition of nickel and cobalt hydroxides occurred and followed by a thermal treatment to convert the subcarbonate into MTMO. As an example, Du et al.[101] electrodeposited the $NiCo_2O_4$ nanosheet arrays (10 nm) on the flexible carbon fabric (CF) as the promising electrode material for supercapacitors. As demonstrated in Figure 2.14, the presence of air spaces or interparticle pores between the nanosheet arrays increased the electroactive sites for redox reaction and facilitated the electrolyte ions diffusion by shortening the diffusion pathway. Thus, an eminent specific capacitance of 2658 Fg^{-1} at current density of 2 Ag^{-1}, excellent cycling stability and rate capability were acquired.

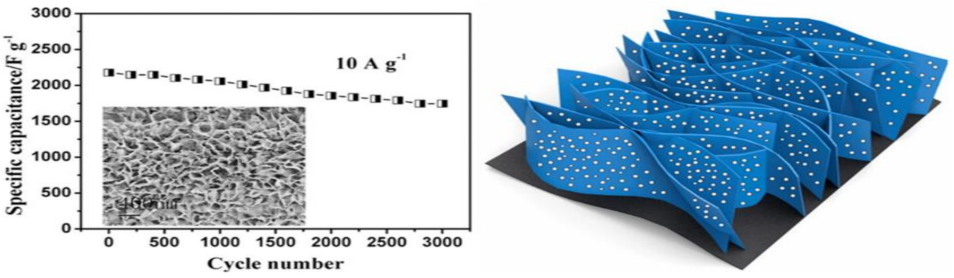

Figure 2.14: The schematic diagram of as-synthesised $NiCo_2O_4$ nanosheet arrays embedded on flexible CF. Reprinted with permission from ref.[101]. Copyright 2013, American Chemical Society.

Besides, mesoporous $NiCo_2O_4$ coated on ultrafine nickel wire was fabricated by Wang et al.[103] via the facile electrodeposition of Ni-Co-Zn alloy, de-alloying and oxidation processes (Figure 2.15).

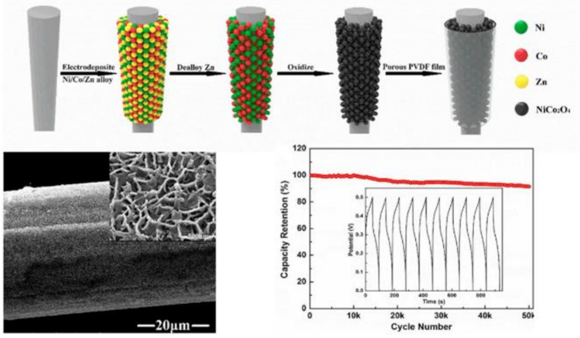

Figure 2.15: Synthetic process of porous $NiCo_2O_4$ anchoring on the ultrafine nickel wire by electrodeposition and de-alloying processes, the morphology and cycling stability of the as-synthesised mesoporous $NiCo_2O_4$ on ultrathin nickel wire. Reprinted with permission from ref.[103].Copyright 2018, Elsevier.

The as-prepared composite possessed a remarkable specific capacitance of 315.4 Cg^{-1} at 1 Ag^{-1} and 65.3 % of capacitance was retained as the current density increased from 1 to 20 Ag^{-1}, revealing its excellent rate capability. In addition, 94.8 % of the initial specific capacitance was well preserved even after 20,000 continuous charge-discharge cycle, manifesting its outstanding cycling stability. The author ascribed the enhanced electrochemical performance to the mesoporous structure and high specific surface area of the composite, which enabled effective occurrence of Faradaic redox reactions. Besides, the improved electrical conductivity also led to the rapid electron transfer[107-109]. The enhanced cycling stability could be assigned to its binder free and exceptional architecture of nickel wire, where the active material ($NiCo_2O_4$) with spinel structure was directly anchored on the surface of nickel wire substrate, which minimised the resistance and increased the cycle life of the particular electrode[103].

Albeit electrodeposition is advantageous for the synthesis of MTMO with uniform morphology, the scalability of electrodeposition process is still a dominant factor that hinders its practical application[4, 5, 77].

2.2.5 Chemical precipitation method

Chemical precipitation is another simple and common strategy in the large-scale synthesis of micro/nanoscale material like MTMO for catalysis process and energy storage system. Chemical precipitation takes place only when the concentration of single solid exceeds the equilibrium solubility of the host solid, leading to the formation of a new phase namely supersaturation[5]. This can be attributed to the rapid quenching or ions implantation. Besides, high process temperature in the system promotes the diffusion of particle which leads to the aggregation into precipitates[73]. In addition, introduction of insoluble element into the solution during the chemical reaction increases the density of the solution, which may also result in the development of precipitates. Contrarily, the precipitation process is accelerated with the adoption of soluble element, where the solution becomes supersaturated. Or else, no nucleation would occur[5]. As similar to hydrothermal/solvothermal technique, chemical precipitation also involves precursors and precipitates, while the rate of reaction occurs rapidly in the process (typically within several minutes). For chemical precipitation, metal cations such as $Ni(NO_3)_2$, $Zn(NO_3)_2$ and etc. are generally considered as the soluble salts and the precipitates are formed after drying. Once dried, the precipitates will undergo calcination treatment to decompose into final products and the calcination temperature used is usually lower than that of the ceramic method[5]. Up to date, a great deal of work was done on fabricating the MTMO for supercapacitor applications using this approach [110-114]. For instance, a mesoporous $Ni_{0.3}Co_{2.7}O_4$ electrode with hierarchical structure was developed by Wu et al[112] at different calcination temperatures (400-500°C) as illustrated in Figure 2.16.

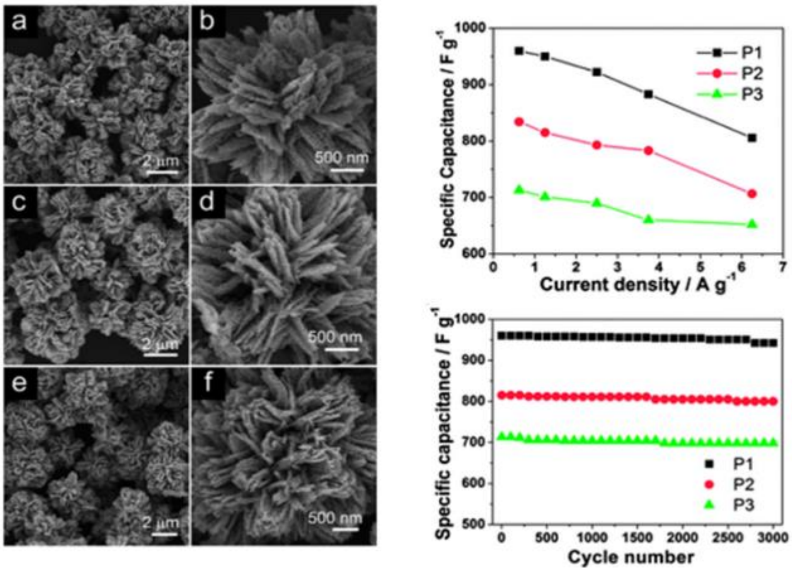

Figure 2.16: SEM images of $Ni_{0.2}Co_{2.7}O_4$ at different calcination temperatures: a-b) 400 °C, c-d) 450 °C and d-e) 550 °C and electrochemical performance of $Ni_{0.3}Co_{2.7}O_4$. Reprinted with permission from ref.[112]. Copyright 2013, The Royal Society of Chemistry.

The as-synthesised $Ni_{0.2}Co_{2.7}O_4$ offered high specific capacitance of 960, 834 and 713 Fg^{-1} (current density of 0.625 Ag^{-1}) at calcination temperature of 400, 450 and 550 °C respectively. Among these samples, the sample calcined at low temperature (400 °C) exhibited the highest specific capacitance, which can be attributed to the formation of abundant meso-pores and micro-pores in the range of 5-100 nm. The mesoporous structure of the $Ni_{0.2}Co_{2.7}O_4$ enhanced the electrochemical performance by providing more electroactive surface for the occurrence of redox reaction as well as benefiting the penetration of electrolyte ions.

Besides, Barmi and Sundaram[113] reported the synthesis of cobalt molybdate nanospheres via chemical precipitation with the employment of surfactant (Pluronic F127), as revealed in Figure 2.17.

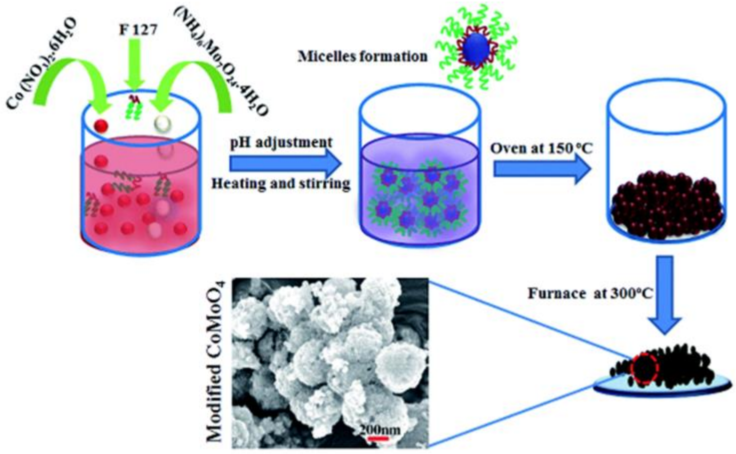

Figure 2.17: Synthetic route of $CoMoO_4$ with the presence of F127 as surfactant. Adapted with permission from ref.[113]. Copyright 2016, The Royal Society of Chemistry Publishing Group.

The as-prepared nanospheres exhibited a high specific capacitance of 69 Fg^{-1} at current density of 1 Ag^{-1} when utilized as the positive electrode for asymmetric supercapacitor with activated carbon as negative electrode. Furthermore, an outstanding cycling stability could be observed, where 80 % of the initial capacitance was retained after 2000 charge-discharge cycles. The capacitance fading can be ascribed to the reduced electron conductive carbon coating on the surface, resulting in the increased ion diffusion resistance during the cycling test.

Despite this method possesses many merits in the synthesis of MTMO, the difficulties in controlling the morphology of the as-synthesised MTMO is still an obstacle that hinders its practical application.

2.2.6 Metal organic framework (MOF)

Recently, metal organic framework (MOF) has aroused tremendous interest as templates or precursors for the synthesis of MTMO with porous structures for supercapacitor applications[115, 116]. According to the research conducted by Yaghi and Li in 1990s, the working mechanism in the metal organic framework is through anchoring the inorganic metallic ions onto the organic linkers through the strong covalent bonds[117]. The metallic cations serve as the electroactive sites for redox reaction whereas the open crystal framework promotes the reversible insertion and de-insertion of the electrolyte ions[118]. Besides, nanocomposite with one (1D), two (2D) and three dimensions (3D) can be developed with MOF, depending on the organic and inorganic units. Furthermore, the pore sizes of the MOF nanocomposites can be tailored to ameliorate the electrochemical performance as supercapacitor electrode. By direct annealing treatment, the MOF nanomaterials will decompose into their corresponding metal oxides as revealed in Figure 2.18[115]. Meanwhile, appropriate manipulation of calcination temperature and time leads to the formation of MOF derived pure metal oxide with desired composition, pore size distribution and surface area[119, 120].

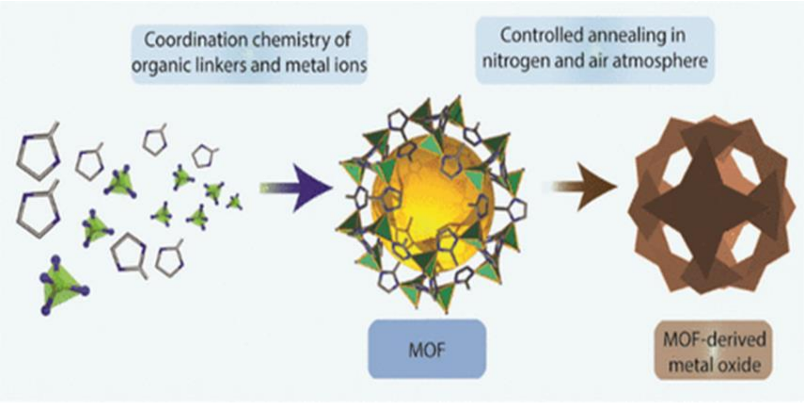

Figure 2.18: Schematic diagram on the synthesis of porous metal oxide nanoarchitechture with enormous surface area from MOF. Adapted with permission from ref.[115]. Copyright 2017, American Chemical Society.

On the other hand, porous transition metal oxide nanocomposite can be produced by direct thermal annealing of binary MOF composite in air under high temperature condition or via the two-step annealing process, where nitrogen and air are introduced in the first and second stages of the process, respectively (Figure 2.19).

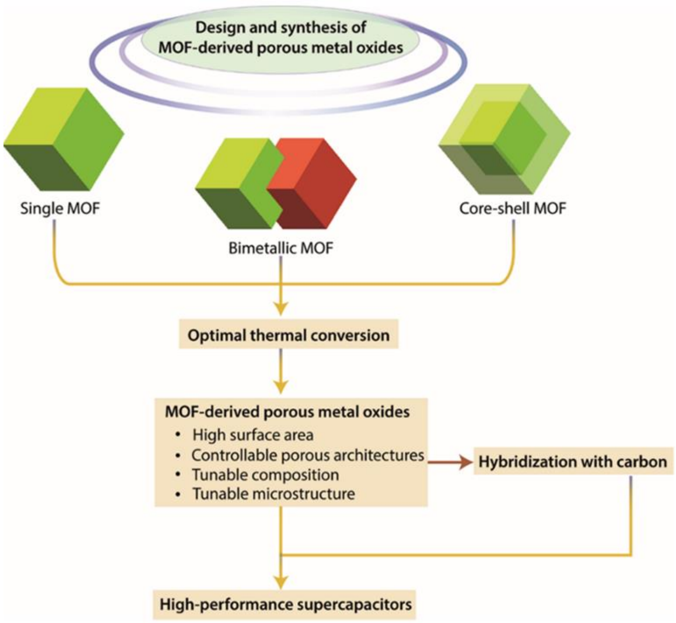

Figure 2.19: Algorithm for the fabrication of porous metal oxide nanohybrid for supercapacitor application. Reprinted with permission from ref.[115]. Copyright 2017, American Chemical Society.

To date, a variety of transition metal oxides and MTMO have been synthesised by the MOF precursors such as NiO, ZnO, TiO_2, Mn_2O_3, $CuCo_2O_4$, $NiCo_2O_4$, $ZnCo_2O_4$ and others[115, 121-126]. Cao and his co-researchers[126] reported the rational design of MOF derived hollow $NiCo_2O_4$ arrays on flexible carbon cloth ($NiCo_2O_4$-CC) as electrode for supercapacitor application, as demonstrated in Figure 2.20.

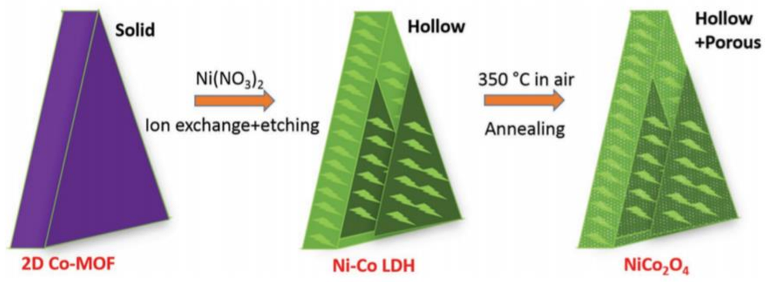

Figure 2.20: Schematic illustrations of the MOF derived hollow $NiCo_2O_4$ arrays on carbon cloth ($NiCo_2O_4$-CC). Ni-Co LDH represented the Ni-Co layered double hydroxide. Reprinted with permission from ref.[126]. Copyright 2017, Wiley-VCH Verlag GmbH & Co.

The as-obtained $NiCo_2O_4$-CC possessed enormous specific surface area (11.6 m^2g^{-1}) as compared to the Co_3O_4-CC (8.4 m^2g^{-1}), suggesting the significant impacts of porous structures on promoting the specific surface area. Besides, $NiCo_2O_4$-CC exhibited a specific capacitance of 1055.3 Fg^{-1} at small current density of 2.5 $mAcm^{-2}$ and retained as 483.3 Fg^{-1} when the current density was increased from 2.5 to 60 $mAcm^{-2}$, manifesting its excellent energy storage ability and superior rate capability. The eminent specific capacitance and rate capability could be attributed to the inherent porous and hollow nanostructures of $NiCo_2O_4$-CC, which provided more electroactive sites and facilitated the diffusion of electrolyte ions into the electrode material by shortening the ion diffusion pathway.

Albeit the MOF-derived MTMO possessed remarkable specific capacitance, poor electrical conductivity and inferior cycling stability have hampered its practical applications as supercapacitor electrodes.

2.2.7 Summary of the synthetic approach

The summary of the working mechanism and the technical practices in the fabrication of MTMO-based electrodes is manifested in this section. Here, six classes of synthesis methods namely hydrothermal/solvothermal, microwave assisted, sol-gel method, electrodeposition, chemical precipitation and metal organic framework(MOF) were reviewed and summarised comprehensively.

The hydrothermal/solvothermal approach can alter the morphology of the nanocomposite by tuning the reaction temperature, pH and the concentration of the auxiliaries. Contrarily, myriad conductive matrix such as nickel foam and carbon textiles can be incorporated with the MTMO in electrodeposition approach, which provides intriguing synergistic effect by adjusting the process parameters like pH and concentration of the solution. As for sol-gel process, chemical and physical processes correlated with the hydrolysis, polymerisation, gelation, condensation, drying and densification methods are involved. Besides, the working mechanism of electrodeposition in the synthesis of MTMO relies substantially on the electrochemical redox reactions and deposition of metal on the electrode when the electric current flows through the metal salt solution. Furthermore, chemical precipitation allows the fabrication of MTMO with mild reaction conditions. Lastly, nanocomposite in one (1D), two (2D) and three dimensions (3D) with large specific surface area and porous structure can be prepared from MOF, depending on the organic and inorganic units within the crystal framework. A comparison on these synthetic methods is developed and delineated in Table 2.1.

Table 2.1: Comparison of advantages and disadvantages of different synthetic approaches of MTMO.

Synthetic Technique	Pros	Cons
Hydro/Solvothermal	- High purity materials can be produced. - Possible for large-scale synthesis. - Facile method (Free of toxic chemical).	-Involved relatively high temperature and pressure.

	- Monodispersed nanoparticles with manageable morphology can be acquired.	
Microwave assisted	-Possible for large-scale synthesis -Speeding up the rate of reaction and hence reduce the reaction duration.	-Challenging in morphological and structural control.
Sol-gel	-Low reaction temperature -High purity materials can be produced. -Possible for large-scale synthesis	-Not feasible in fabricating film with porous structure.
Electrodeposition	-Producing composite with consistent morphology	-Challenging for large-scale synthesis
Chemical precipitation	-Possible for large-scale synthesis. -Simple route with mild reaction temperature.	-Difficult in controlling the morphological and structural behaviours of the nanoparticles.
Metal Organic Framework (MOF)	-Nanocomposite with 1D, 2D and 3D can be synthesised. -High porosity and large specific surface area of the nanocomposite.	- Challenging to produce electrode with enhanced electrochemical performance.

2.3 Critical factors that affecting the electrochemical performance of transition metal oxide-based materials

Generally, the supercapacitive performances of transition metal oxide-based electrode materials are governed by some factors such as morphological structure, loading mass of active material, electrical conductivity and thermal annealing effect[2, 127]. In this section, the influences of the aforementioned parameters on the electrochemical activities were discussed in details.

2.3.1 Morphological structure

According to the findings of Feng et al.[2], the specific capacitance of an electrode material is substantially affected by its morphology, size, specific surface area and pore size distribution. It is sufficiently evident that morphology has high impact on the specific surface area of the electrode material. As an example, the porosity and specific surface area of the electrode materials are interrelated. This can be elucidated by the pore sizes and pore volume generated as well as the pore size distribution for a given overall specific surface area of the active material. However, the specific surface area is not in a linear relationship with measured specific capacitance as only a small portion of electrode material is involved in the Faradaic redox reaction or electrochemically penetrated by the electrolyte ions. Therefore, it can be concluded that the availability of the electroactive sites and accessibility to electrolyte ions are the crucial parameters determining the capacitive performance of an electrode material.

2.3.2 Mass loading of the metal oxide

In general, an electrode material with remarkable capacitive performance and high mass loading are necessary for practical supercapacitor applications as it exhibits high energy and power densities. However, it has been reported by some researchers that overloading of metal oxide leads to the agglomeration and aggregation which in turn deteriorates the capacitive performance of the electrode [24, 25, 28, 36, 40-42, 128-130]. In particular, overloading of metal oxide results in poor electrical conductivity and offers limited electroactive sites for Faradaic redox reaction, hence leading to inferior electrochemical outputs[2]. For instance, Ezeigwe and co-workers[28] developed the $NiMoO_4$ nanorods decorated on graphene sheet via facile solvothermal technique. In the extension of this work, different weight ratios of graphene to $NiMoO_4$ (1:1, 1:4, 1:8 and 1:16) were prepared to further evaluate the synergistic effect between the nanocomposites. The $NiMoO_4$ nanorods were uniformly anchored on the surface of graphene sheet as the weight ratio of graphene to $NiMoO_4$ was 1:8. Contrarily, agglomeration of nanorods could be observed when the weight ratio of graphene to $NiMoO_4$ increased from 1:8 to 1:16, suggesting that weight ratio of 1:8 was the critical point for these nanocomposites.

2.3.3 Electrical conductivity

Apart from mass loading, electrical conductivity is another concern for TMO based material to be virtually utilised in supercapacitor. Typically, the resistance associated with the electron conduction is dominant for a material with poor conductivity especially in the condition of high charge-discharge rate. Specifically, the charge-discharge process is confined in the finite volume near the current collector and the specific capacitance will diminish tremendously[131]. This will hinder the practical applications of the TMO based material as functional electrode.

2.3.4 Thermal annealing effect

Calcination is an essential process employed to improve the crystallinity of the nanomaterial as well as to induce the formation of mixed transition metal oxide nanocomposite. Nevertheless, calcination of MTMO based materials at high temperature may lead to the agglomeration of the active composite which adversely affects its structural and electrochemical properties, and similar findings were also reported by other researchers[38, 87, 112, 132, 133]. As an example, Xu and co-authors[38] designed an ultrathin $NiCo_2O_4$ nanobelt deposited on graphene sheet via hydrothermal method. Here, the optimal calcination temperature was determined by evaluating the pseudocapacitive properties of bare spinel $NiCo_2O_4$ at different calcination temperatures (250, 300, 250, 400 ^{o}C for 2 hrs). The authors claimed that calcination temperature of 250 ^{o}C was the optimal temperature for the heat treatment of $NiCo_2O_4$ nanobelt. Under this temperature, mesoporous and interconnected $NiCo_2O_4$ nanobelts were formed which contributed to larger specific surface area for redox reaction. In contrast, bare spinel $NiCo_2O_4$ prepared at 300^{o}C and onwards suffered from structural agglomeration and hence exhibited unsatisfactory electrochemical outputs.

2.4 Supercapacitor electrode materials

2.4.1 Mixed Transition Metal Oxide (MTMO) based supercapacitor

Evolution during the past decade, tremendous increment in energy demands compels the researchers to work on the environmentally benign and renewable energy storage system like supercapacitor. Currently, researchers are engrossed in mixed transition metal oxides as electrode materials owing to their intriguing electrochemical properties as compared to single transition metal oxides. As for MTMO, the synergistic effect between the multiple metal compositions and low activation energy for electron transportation lead to higher specific capacitance and electrical conductivity as compared to that of single TMO[134]. In this section, the synthesis and contribution of multifarious MTMOs as supercapacitor electrode were extensively reviewed and classified according to their principal metallic groups in chemical compositions.

2.4.1.1 Metal Cobaltites

Spinel metal cobaltites ($M_xCo_{3-x}O_4$; where M = Ni, Zn, Cu, Mn, Fe, etc.) with iso-architectural nature to that of Co_3O_4 are considered as one of the most competitive electrode materials for practical supercapacitor application owing to its superior capacitive performance, cycling stability and rate capability[4]. Among these reported spinel metal cobaltites, nickel cobaltite ($NiCo_2O_4$) with the structural formula of $Co^{2+}_{1-x}Co^{3+}_{x}[Co^{3+}Ni^{2+}_{x}Ni^{3+}_{1-x}]O_4$; where 0<x<1 has gained enormous research interests by virtue of its unique advantages which include low cost, natural abundance, non-toxic and offers exceptional electrochemical activities. In particular, the cations foregoing the brackets ($Co^{2+}_{1-x}Co^{3+}_{x}$) are considered to be allocated in the tetrahedral lattice sites whereas the cations remaining in the brackets ($Co^{3+}Ni^{2+}_{x}Ni^{3+}_{1-x}$) are allocated in the octahedral lattice sites[106, 135]. Concisely, the lattice configuration of $NiCo_2O_4$ with the spinel mineral generic formula of AB_2O_4 is depicted in Figure 2.21[136], where O atoms are allocated in the cubic close-packed architecture, Co and Ni cations occupied the tetrahedral and octahedral lattice sites.

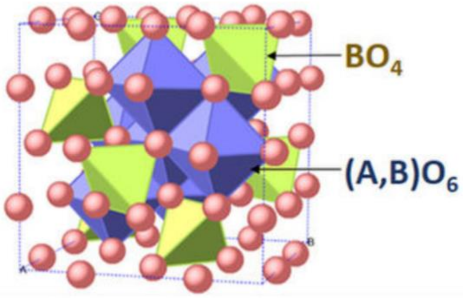

Figure 2.21: Spinel lattice structure of $NiCo_2O_4$. Reprinted with permission from ref.[136]. Copyright 2015, Scientific Reports.

Generally, the $NiCo_2O_4$ electrode is operated under a voltage window of 0 to 0.55 V in an alkaline electrolyte and the Faradaic redox reactions involved are expressed as follows [58]:

$$NiCO_2O_4 + OH^- + H_2O \leftrightarrow NiOOH + 2CoOOH + e^- \quad (2.3)$$

$$CoOOH + OH^- \leftrightarrow CoO_2 + H_2O + e^- \quad (2.4)$$

Most researchers discovered that $NiCo_2O_4$ possesses several morphological architectures, such as nanoplatelets, nanoparticles, nanorods, nanosheets, microspheres and etcetera [137-146]. Each morphology exhibits different supercapacitive performances. For instance, Yan et al.[137] synthesised the $NiCo_2O_4$ nanosheets and nanowires through electrodeposition and hydrothermal methods, respectively. Once the nanostructures were successfully formed, the authors modified the oxygen vacancies of these nanostructures by reducing them with different concentrations of $NaBH_4$. The detailed synthesis routes of these nanostructures and their corresponding oxygen vacancies are delineated in Figure 2.22. Additionally, the morphological structures of $NiCo_2O_4$ nanosheets and nanowires before and after chemical reduction are also discussed.

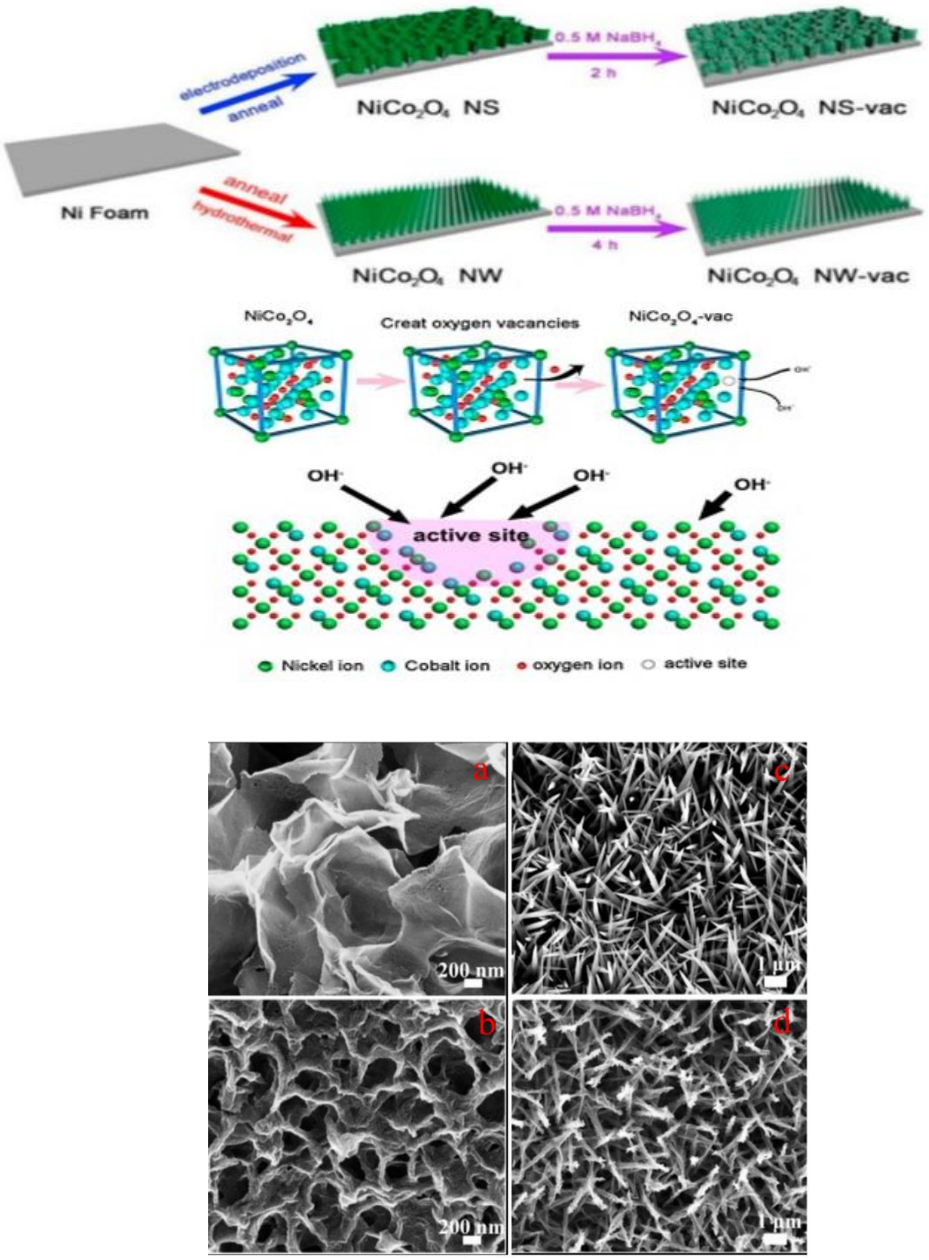

Figure 2.22: Top) Synthetic routes illustration of $NiCo_2O_4$ nanosheets and nanowires as well as their corresponding oxygen vacancies. Bottom) SEM images of (a and b) $NiCo_2O_4$ nanosheets before and after chemical reduction, (c and d) $NiCo_2O_4$ nanowires before and after chemical reduction. Adapted with permission from ref.[137]. Copyright 2018, Elsevier.

Both the reduced $NiCo_2O_4$ nanosheets and nanowires exhibited higher specific capacitance (1590 and 1280 Fg^{-1}) at current density of 1 Ag^{-1} as compared to sole $NiCo_2O_4$ nanosheets and nanowires (898 and 600 Fg^{-1}), indicating that oxygen vacancies on the surface of active material promoted the OH^- ions adsorption capability and also advocated the rapid reversible redox reactions. Besides, the capacitance retention of the as-reduced $NiCo_2O_4$ nanosheets and nanowires were 79.12 and 85.56 % after 10000 and 5000 cycles, respectively, implying its superior cycling stability. This result suggested that the presence of oxygen vacancies provided more electroactive sites and eased the ions and electron transfer.

Furthermore, $NiCo_2O_4$ nanoparticles with a diamond-shaped hexahedral porous sheet structures was successfully developed by Li and co-authors[138] via facile hydrothermal method (varying the contents of urea and ammonium fluoride) followed by calcination process as shown in Figure 2.23.

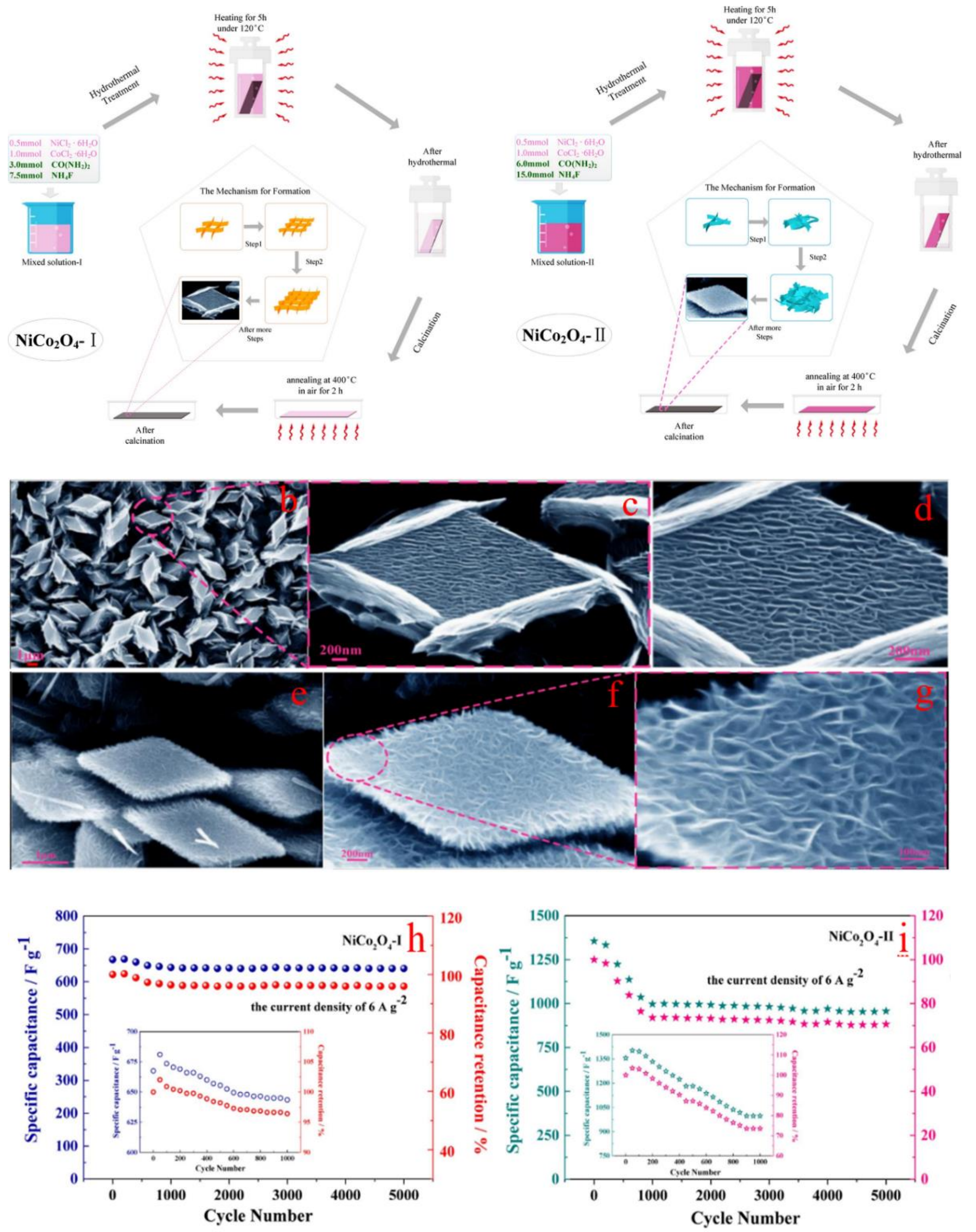

Figure 2.23: (a) Schematic illustrations of $NiCo_2O_4$-I and II nanoparticles synthesis. (b,c,d) SEM images of $NiCo_2O_4$-I nanoparticles. (e,f,g) SEM images of $NiCo_2O_4$-II nanoparticles. (h and i) Cycling test of both $NiCo_2O_4$-I and II nanoparticles. Reproduced with permission from ref.[138].Copyright 2018, Elsevier.

The SEM images showed the $NiCo_2O_4$-I and II nanoparticles which were spun by nanosheets with size ranges of 3 to 4.5 μm and 2 to 3.5 μm, respectively. Moreover, the specific capacitance of $NiCo_2O_4$-I and II nanoparticles electrode materials were

690.75 and 1710.9 Fg^{-1} at current density of 1 $mAcm^{-2}$ in 6M KOH aqueous electrolyte, unveiling the eminent charge storage capability of $NiCo_2O_4$-II nanoparticles. This could be elucidated by the wider contact area between $NiCo_2O_4$-II nanoparticles with the electrolyte as compared to $NiCo_2O_4$-I, which assured effective redox reactions and hence improved the specific capacitance. Nevertheless, it could be realised that 96.4 and 73.56 % of initial capacitance were retained after 5000 cycles for $NiCo_2O_4$-I and $NiCo_2O_4$-II, suggesting the excellent cycling stability of $NiCo_2O_4$-I. This could be due to the greater dissolution of $NiCo_2O_4$-II nanoparticles into the electrolyte upon the cycling test.

Other than $NiCo_2O_4$, zinc cobaltites[147-154] ($ZnCo_2O_4$) and copper cobaltites[155-163] ($CuCo_2O_4$) have been perceived as the potential electrode materials for supercapacitor application as well. The pertinent electrochemical characteristics of these materials are depicted in Table 2.2.

Table 2.2: $ZnCo_2O_4$ and $CuCo_2O_4$ with different synthetic routes and their electrochemical properties.

Morphology	**Synthetic approach**	**Specific capacitance (Fg^{-1})**	**Current density (Ag^{-1})**	**Cycling stability**	**Ref**
Mn-doped $ZnCo_2O_4$ nanoparticles	Hydrothermal	707.4	0.5	-	[147]
Urchin-like $ZnCo_2O_4$ microspheres on nickel foam	Hydrothermal	1143	1.25	77 % (6000 cycles)	[148]
2D porous $ZnCo_2O_4$ thin sheets	Hydrothermal	3.07 Fcm^{-2}	1.04 $mAcm^{-2}$	97.6 % (5000 cycles)	[149]
$ZnCo_2O_4$ microflowers and microsheets on Ni foam	Hydrothermal	2256 Fg^{-1} (microflowers)	2 $mAcm^{-2}$	90 % (2000 cycles)	[150]

3D porous ZnCo$_2$O$_4$ sheet array coated with Ni(OH)$_2$	Electrodeposition	4.6 Fcm^{-2}	2 mAcm^{-2}	70 % (2200 cycles)	[151]
3D hierarchical peony-like ZnCo$_2$O$_4$	Hydrothermal	440	1	155.6 % (after 3000 cycles)	[152]
Mesoporous ZnCo$_2$O$_4$ nanosheets	Hydrothermal	835.26	1	73.28 % (1000 cycles)	[153]
Porous ZnCo$_2$O$_4$ microspheres	Self-template solvothermal	542.5	1	95.5 % (2000 cycles)	[154]
Mesoporous CuCo$_2$O$_4$ nanowires	Nanocasting from silica template	1210	2	93.5 % (4250 cycles)	[155]
CuCo$_2$O$_4$ nanoparticles	Solution combustion	338	1	96 % (5000 cycles)	[156]
3D flower-like CuCo$_2$O$_4$/NF	Hydrothermal	771	100 mVs^{-1}	130 % (3000 cycles)	[157]
CuCo$_2$O$_4$ nanobelts	Hydrothermal	809	0.667	127 % (1800 cycles)	[158]
CuCo$_2$O$_4$ nanograsses	Hydrothermal	796	2	94.7 % (5000 cycles)	[159]
Nanotrees with CuCo$_2$O$_4$ trunks and NiO branches	Hydrothermal	2219	1	95.3 % (10000 cycles)	[160]
Hierarchical CuCo$_2$O$_4$@CuCo$_2$O$_4$ nanowires arrays	Hydrothermal	888.9	2 mAcm^{-2}	101.77 % (2000 cycles)	[161]
Cubic CuCo$_2$O$_4$ nanoparticles	Hydrothermal	765 mAhg^{-1}	2	95 % (2000 cycles)	[162]
CuCo$_2$O$_4$ hollow spheres	Bimetal-organic framework	1700	2	93.7 % (5000 cycles)	[163]

Taking ZnCo$_2$O$_4$ as an illustration, Shang et al.[152] designed a novel self-assembled 3D hierarchical peony-like ZnCo$_2$O$_4$ electroactive materials by facile hydrothermal technique. The hierarchical peony-like ZnCo$_2$O$_4$ nanoarchitecture is composed of interlinking nanosheets with thickness of ~30 nm, which reinforced the structural tenacity and generated crevices for rapid ions transportation within the redox phases. The relevant redox reactions are formulated as follows:

$$Co_2O_4^{2-} + OH^- + 2H_2O \leftrightarrow 2\ CoOOH + e^- \qquad (2.5)$$

$$CoOOH + OH^- \leftrightarrow CoO_2 + H_2O + e^- \qquad (2.6)$$

Furthermore, this novel nanostructure exhibited a remarkable specific capacitance (440 Fg^{-1} at 1 Ag^{-1}), reasonable rate capability (67.7 % when the current density altered from 1 to 20 Ag^{-1}) and excellent capacitance retention (155.6 %) after 3000 cycles, suggesting its potential to be used as electrode material for practical supercapacitor application. The superior electrochemical activities of peony-like $ZnCo_2O_4$ could be ascribed to several rationales: i) the appearance of pores and crevices provided rapid ions diffusion pathway and offered multiple electroactive sites for Faradaic reaction. ii) Peony-like $ZnCo_2O_4$ possessed enormous nanosheets, which provided high specific surface area and strengthened the mechanical stability of the nanomaterial by accommodating the architectural strain during the cycling test.

2.4.1.2 Metal Molybdates

Lately, metal molybdates ($MMoO_4$; where M=Ni, Co, Zn, etc.) have attracted diverse research interests as one of the potential candidates for supercapacitor application[164]. This is because of its low cost, abundance and prominent electrochemical performances. Among the various metal molybdates such as $NiMoO_4$, $CoMoO_4$, $ZnMoO_4$, $FeMoO_4$, $MnMoO_4$, $SnMoO_4$ and etc, nickel molybdate ($NiMoO_4$) plays a vital role in supercapacitor application. Typically, $NiMoO_4$ comprises two stable phases namely α-$NiMoO_4$ and β-$NiMoO_4$, which can be distinguished by their crystal lattice configurations. For α-$NiMoO_4$, the molybdate ions are allocated in the octahedral lattice sites under ambient temperature whereas for β-$NiMoO_4$, the molybdate ions are organised in the tetrahedral lattice sites at high temperature. Meanwhile, the monoclinic architecture of α-$NiMoO_4$ composed of NiO_6 and MoO_6 octahedral operating groups which form via the cross linking networks[165]. $NiMoO_4$ can offer various oxidation states which contribute to effective redox reactivity. Similarly, $NiMoO_4$ can be fabricated into multifarious architectures like nanoparticles, nanocrystals, shell-like structures, nanorods, nanoplatelets, urchin-like flowers and nanospheres[164-173]. Regrettably, the evolution of $NiMoO_4$ based nanomaterials was hindered by short cycle life and insufficient capacity, which resulted from tremendous volume variation and dense structure [166]. Hence, formation of porous structural $NiMoO_4$ seems to be a promising solution to rectify this conundrum. As an illustration, a porous worm-like $NiMoO_4$ anchored on the electrospun carbon nanofibers ($NiMoO_4$/ECNF) was successfully fabricated by Tian et al.[166]. The morphology and electrochemical activities of this nanocomposite are revealed in Figure 2.24.

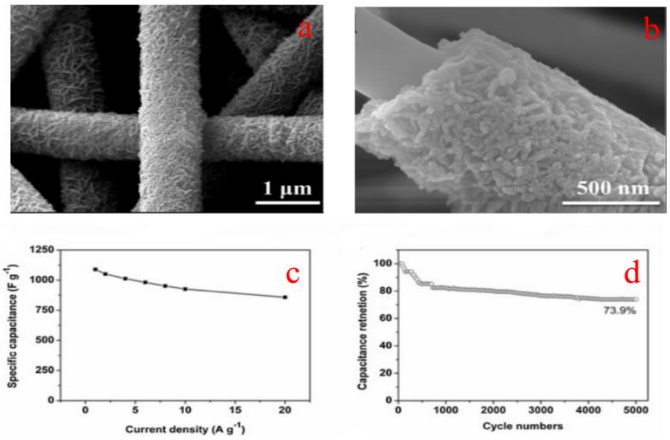

Figure 2.24: (a-b) SEM images of crystalline worm-like $NiMoO_4$-ECNF nanocomposite. (c) Specific capacitance of $NiMoO_4$/ECNF nanocomposite at different current densities. (d) Cycling test of $NiMoO_4$/ECNF nanocomposite. Reproduced with permission from ref.[166]. Copyright 2018, Elsevier.

By virtue of its unique architecture, the as-synthesised electrode exhibited a high specific capacitance of 1088.5 Fg^{-1} at 1 Ag^{-1}, outstanding rate capability of 860.3 Fg^{-1} at 20 Ag^{-1} and reasonable cycling stability (73.9 % retained after 5000 cycles). These advanced capacitive performances could be elucidated by the larger specific surface area endowed by porous worm-like morphology, which diminished the ions diffusion pathway. Besides, the reinforced cycling stability was ascribed to the robust integrated electrode, which rendered adequate air spaces between the worm-like $NiMoO_4$ and hence resisted the volume expansion during the continuous charge discharge process. A 3D porous $NiMoO_4$ nanoflakes arrays directly deposited on Ni foam was reported by Adhikary et al.[167], which possessed an ultrahigh specific capacitance of 2004 Fg^{-1} at 2 Ag^{-1}. Additionally, the low equivalent series resistance of 0.62 Ω and good capacitance retention of 80% after 1000 cycles were acquired. The enhanced electrochemical properties could be explicated as follows: i) homogenous distribution of the $NiMoO_4$ nanoflakes on Ni foam. ii) synergistic effect between the Ni and Mo elements. iii) porous architecture of the nanocomposite.

Besides, the evolution of molybdenum with cobalt[174-180] and zinc[181, 182] based oxides materials have aroused tremendous research interest lately due to their low cost, environmentally friendly and good capacitive performance[4]. Generally, $CoMoO_4$ with high cell parameters of (a=10.21 Å, b=9.268 Å, c=7.022 Å) and stable electrochemical properties is highly preferable. As an example, Li et al.[174] synthesised a core-shell $CoMoO_4@Co_3O_4$ nanocomposite decorated on a 3D ordered macro-porous electrode plate (OMEP) as the active electrode through the multi-steps hydrothermal approach as demonstrated in Figure 2.25.

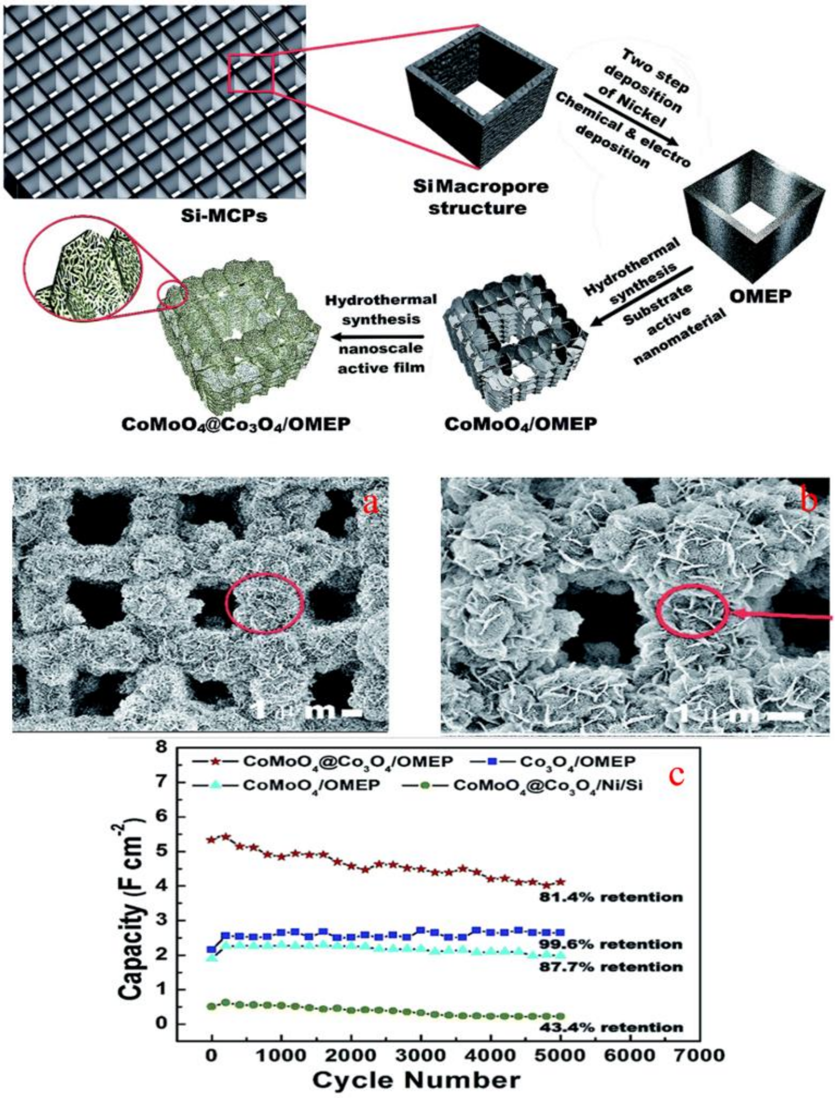

Figure 2.25: Top) Formation mechanism of the $CoMoO_4@Co_3O_4$/OMEP nanocomposite synthesised. Bottom) (a-b) SEM images of $CoMoO_4@Co_3O_4$/OMEP nanocomposites and (c) its corresponding cycling stability test. Reproduced with permission from ref.[174]. Copyright 2017, The Royal Society of Chemistry.

The formation mechanism of this $CoMoO_4@Co_3O_4$/OMEP nanocomposite was as follows: i) $CoMoO_4$ was anchored onto the radically OMEP via hydrothermal self –assembly to generate the 3D hierarchical $CoMoO_4$/OMEP nanoarchitecture. ii) the as-synthesised $CoMoO_4$/OMEP nanoarchitecture co-operated with nanocomposite layer of Co_3O_4 to form $CoMoO_4@Co_3O_4$/OMEP multi-dimensional nanocomposite. This peculiar core-shell nanoarchitecture offered enormous electroactive sites for effective redox reactions[175]. As for electrochemical analyses, the redox reactions of $CoMoO_4$ involved in KOH electrolyte are expressed as follows:

$$3[Co(OH)_3] \leftrightarrow Co_3O_4 + 4H_2O + OH^- + 2e^- \quad (2.7)$$

$$Co_3O_4 + H_2O + OH^- \leftrightarrow 3CoOOHH_2O \quad (2.8)$$

$$CoOOH + OH^- \leftrightarrow CoO_2 + H_2O + e^- \quad (2.9)$$

It is noteworthy that the $CoMoO_4$@Co_3O_4 nanoarchitectures were uniformly distributed on the sidewall of macro-porous OMEP, resulting in more ions diffusion channels for effective space utilisation of the electrode material. The authors claimed that this nanocomposite possessed a high specific capacitance of 1168 Fg^{-1} at current density of 4 $mAcm^{-2}$ and excellent cycling stability (81.4% capacitance retention) after 5000 cycles. The capacitance fading could be ascribed to the deformation and reconstruction of the active material, which was originated from the redox reactions of $CoMoO_4$ and Co_3O_4. The advancements in specific capacitance and cycling stability were due to the unique 3D ordered porous structure, which enlarged the solid liquid interfacial area, accelerated the ions diffusion, prohibited the agglomeration or aggregation of the nanomaterials and allowed effective utilisation of the active electrode materials.

2.4.1.3 Metal Vanadates

As an appealing mixed transition metal oxide, metal vanadate stands out from the other MTMO owing to its promising electrochemical results and intriguing properties such as broad operating potential window resulted from multiple oxidation states of vanadium elements, naturally abundant and lucrative[3]. The electrochemical behaviours of these metal vanadates are exclusively dependent on the synthetic methods and the morphologies developed. Up to date, considerable findings have been performed on evaluating the potential of metal vanadate as energy storage devices (supercapacitor and lithium-ion battery) such as $Ni_3V_2O_8$[6, 30, 32, 79, 183, 184], $Zn_3V_2O_8$[185-188], $Co_3V_2O_8$[6, 189-192], AlV_3O_9[193-195], MoV_2O_8[39, 128] and etc. For instance, Vishnukumar et al.[79] reported the synthesis of NiO / $Ni_3V_2O_8$ nanocomposite via facile solvothermal process for high performance supercapacitor applications and its morphological and electrochemical properties are delineated in Figure 2.26.

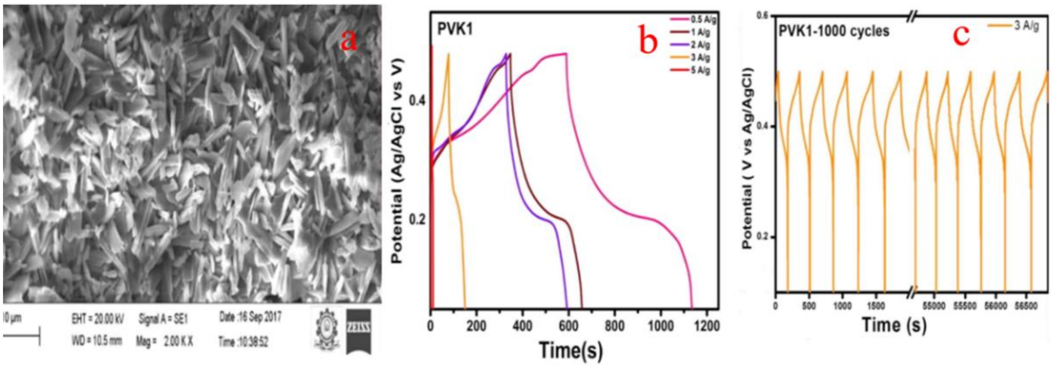

Figure 2.26: a) SEM image, b) galvanostatic charge discharge at 1Ag^{-1}, c) cycling test of NiO/$Ni_3V_2O_8$ nanorods. Reprinted with permission from ref.[79]. Copyright 2018, Elsevier.

The authors studied the effect of reaction time (10, 14 and 18 hrs) on the electrochemical performances and noted that the nanocomposite synthesised within 10 hrs exhibited remarkable pseudocapacitive value of 653 Fg^{-1} at current density of 1 Ag^{-1} and 96 % of initial capacitance was well preserved after 1000 cycles. Besides, the symmetrical charge-discharge curves upon cycling test was observed from Figure 26c, suggested its superior coulombic efficiency. The prominent capacitive activities of NiO/$Ni_3V_2O_8$ with the reaction time of 10 hrs was due to the nanorods structural organisation with homogenous distribution, whereas for other products (14 and 18 hrs), non-homogenous distribution and agglomeration occurred and hence attenuated their capacitive storage.

Other than that, a 3D porous $Co_3V_2O_8$ nanoroses was fabricated by Zhang and his co-workers[190] via solvothermal method. Figure 2.27 delineates the possible formation mechanism of 3D porous $Co_3V_2O_8$ nanoroses and its corresponding structural and electrochemical outputs.

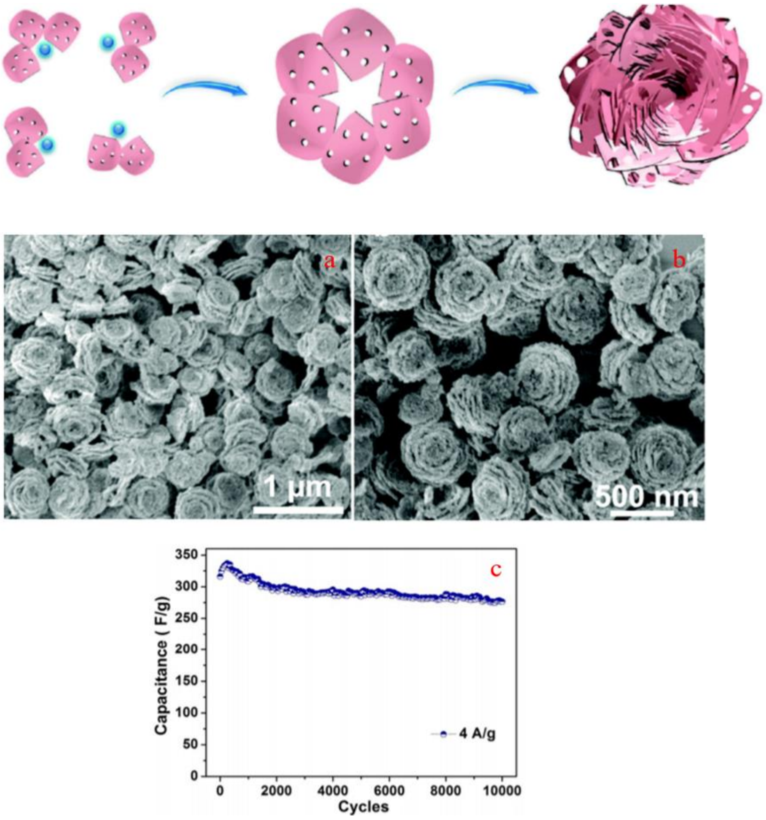

Figure 2.27: Top) Schematic diagram of $Co_3V_2O_8$ nanoroses. Bottom) (a-b) SEM images, (c) cycling stability test of 3D porous $Co_3V_2O_8$ nanoroses. Adapted with permission from ref.[190]. Copyright 2017, The Royal Society of Chemistry.

The detailed formation mechanism could be expressed as follows: i) nucleation of Co^{2+} and VO_3^- ions surrounded the methanol bubbles. ii) aggregation and further growth into diverse nanoflakes. iii) further aggregation of nanoflakes into nanoplates. iv) assembly of nanoplates into 3D nanoroses as the reaction time prolonged.

From Figure 2.27, the 3D porous nanoroses was successfully designed with the size ranging from 383 to 589 nm and the average size was approximately 474 nm. Besides, the 3D porous $Co_3V_2O_8$ nanoroses possessed a high specific capacitance of 371.3 Fg^{-1} at 0.5 Ag^{-1} and 85.4% of the specific capacitance was retained when the current density increased from 1 to 10 Ag^{-1}, revealing its good charge storage capability and superior rate capability. Moreover, the 3D porous nanoroses electrode displayed impressive cycling performance with a capacitance retention of 89.6 % after 10000 continuous charge discharge cycles. Reasonable energy and power densities were manifested by the 3D porous nanoroses electrode. These fascinating electrochemical performances could be assigned to the porous nanoroses structures of $Co_3V_2O_8$, which facilitated the migration of electrolyte ions to the bulk of electrode material. Moreover, the occurrence of reversible redox reactions of Co^{2+} and Co^{3+} dominated the pseudocapacitance. Lastly, the large specific surface area of 3D mesoporous nanoroses (112.97 m^2g^{-1}) and well-defined pore structure allowed intimate contact between the electroactive sites and electrolyte, which is beneficial for pronounced redox reactions. Microwave-assisted synthesis of novel $Zn_3(OH)_2V_2O_7.2H_2O$ and $Zn_2V_2O_7$ nanoarchitectures was conducted by Li and his group[185]. The relevant synthetic process is illustrated in Figure 2.28.

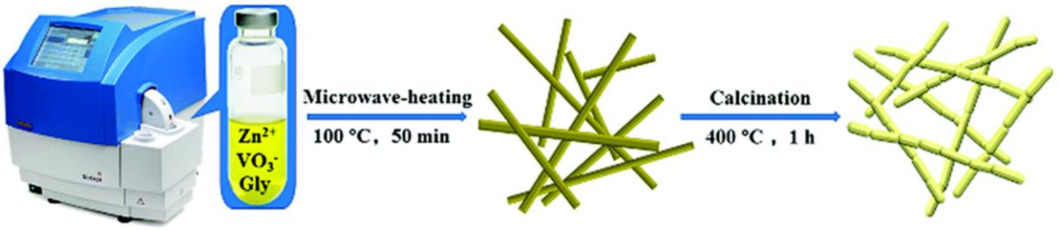

Figure 2.28: Synthetic process of $Zn_3(OH)_2V_2O_7.2H_2O$ and $Zn_2V_2O_7$ active materials. Reprinted with permission from ref.[185]. Copyright 2017, The Royal Society of Chemistry.

Here, glycine served as the surfactant and $Zn_2V_2O_7$ was obtained after the calcination process. The related redox reaction mechanisms are expressed as follows:

$$Zn_3(OH)_2V_2O_7.2H_2O + xK^+ + xe^- \leftrightarrow K_xZn_3(OH)_2V_2O_7 + 2H_2O \tag{2.10}$$

$$Zn_2V_2O_7 + xK^+ + xe^- \leftrightarrow K_xZn_2V_2O_7 \tag{2.11}$$

The as-fabricated electrode material ($Zn_2V_2O_7$) delivered an excellent capacitance of 427.7 Fg^{-1} at 1 $mAcm^{-2}$ as compared to $Zn_3(OH)_2V_2O_7.2H_2O$ (207.8 Fg^{-1} at 1 $mAcm^{-2}$). Besides, 83.71 % of its initial capacitance was retained after 1000 cycles, suggesting its appealing cycling performance. This result could be explicated by the formation of nanowire-shaped $Zn_2V_2O_7$ assembled by interconnected elliptical nanoparticles, which enhanced the diffusion of electrolyte to the active sites upon cycling.

2.4.1.4 Metal Tungstate

In present, many researchers are devoted to evaluate and determine the feasibility of metal tungstate as electrode materials for supercapacitors as it is cost effective, less toxic, abundant in nature and possesses low operating potential together with high capacitive performance[196]. Particularly, the high electrical conductivity of tungsten material makes it a promising candidate for supercapacitor applications. As reported in some literatures, nickel tungstate ($NiWO_4$) has electrical conductivity in the order of 10^{-7} to 10^{-2} Scm^{-1}, which is higher than that of the pristine Ni, NiO as well as metal molybdate[197]. Moreover, metal tungstates as an independent entity like $NiWO_4$, $CoWO_4$, $ZnWO_4$, $MnWO_4$ and $FeWO_4$ perform outstanding electrochemical activities, which can be ascribed to the synergistic effect between the distinct metallic substances[196]. However, metal tungstate also encompasses several limitations like severe volume expansion during the continuous charge-discharge process which leads to inferior rate capability and cycling stability. The aforementioned problem can be rectified by customising the metal tungstate into nanostructural form such as nanoparticles, nanoflakes, nanowires and etcetera[196-207]. For instance, He et al.[197] synthesised the $NiWO_4$ nanoparticles and $CoWO_4$ nanoshuttles on nickel foam by facile one-pot hydrothermal route as depicted in Figure 2.29.

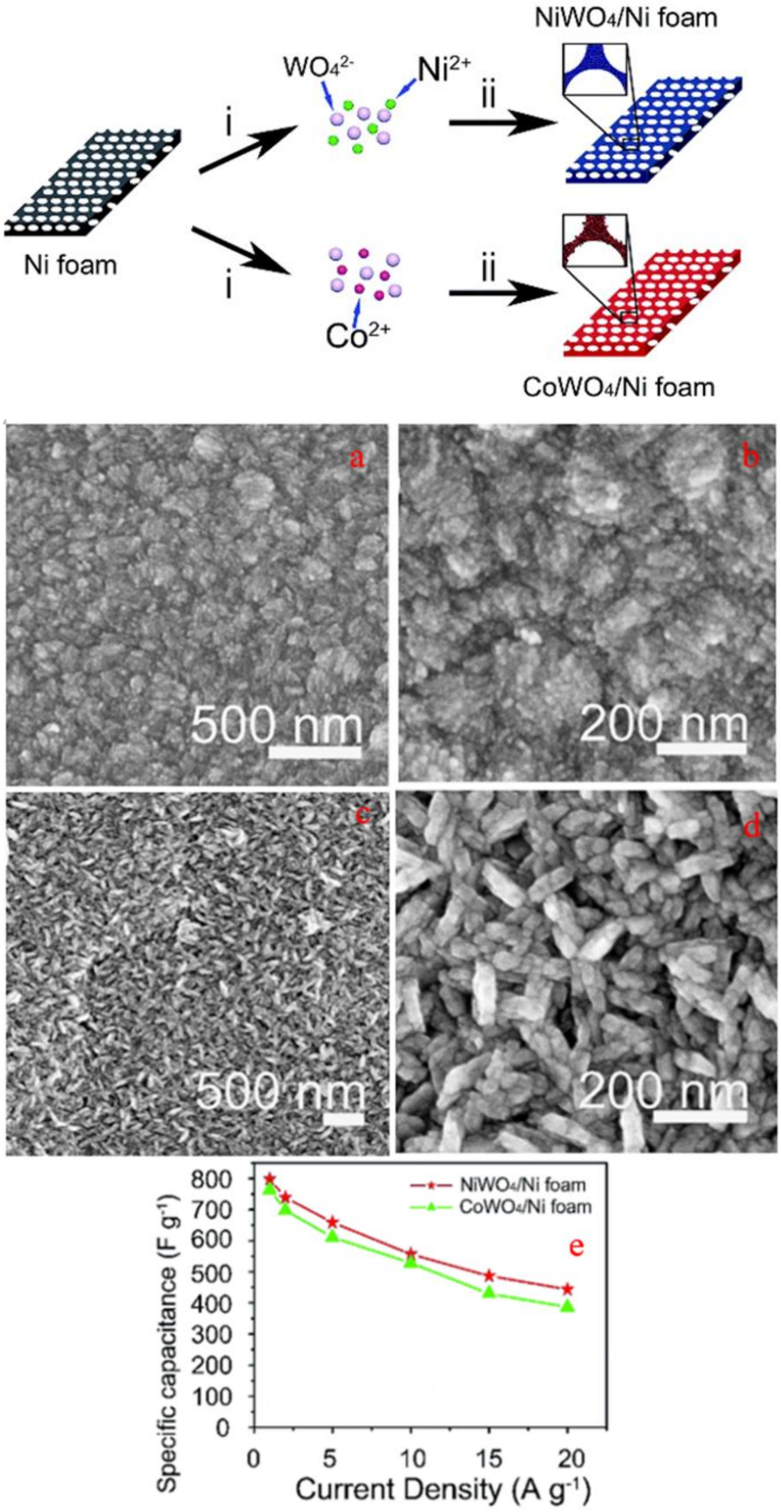

Figure 2.29: Top) Schematic illustrating the formation of $NiWO_4$ and $CoWO_4$ on Ni foam. Bottom) (a-b) SEM images of $NiWO_4$@Ni foam, (c-d) SEM images of $CoWO_4$@Ni foam. (e) A comparison of specific capacitance for $NiWO_4$@Ni foam and $CoWO_4$@Ni foam as a function of current density. Reprinted with permission from ref.[197]. Copyright 2015, The Royal Society of Chemistry.

Here, nickel foam was employed as the current collector due to its macro-porous structures that offered large specific surface area, shortened the ions diffusion pathway and provided exceptional electrical conductivity[197]. The as-synthesised $NiWO_4$ nanoparticles and $CoWO_4$ nanoshuttles on nickel foams revealed a specific capacitance of 797.8 and 764.4 Fg^{-1} respectively at current density of 1 Ag^{-1}. Besides, only 55.6 % and 50.6 % of the initial capacitances were preserved as the current density increased from 1 to 20 Ag^{-1} for $NiWO_4$@Ni foam nanoparticles and $CoWO_4$@Ni foam nanoshuttles respectively. The capacitance fading could be assigned to the severe potential drop and ineffective contribution of active materials in the redox reaction as the current density increased. Furthermore, the cycling test was performed via the CV analysis in between 0 to 0.6 V for 6000 cycles. Interestingly, the specific capacitances acquired were 2.06 and 2.81 times higher than their initial capacitance after 6000 cycles for $NiWO_4$@Ni foam nanoparticles and $CoWO_4$@Ni foam nanoshuttles, respectively revealing the superior cycling stability of both materials. Moreover, a small decrement on the specific capacitance was observed between 3000 and 4500 cycles, which could be elucidated by: i) increase in surface wettability of electrode material by the electrolyte upon cycling and ii) dissolution of some nanoparticles into the electrolyte solution which caused the activation of interior nanoparticles.

An electrospun 3D porous $ZnWO_4$ nanoparticles was fabricated by Yang and co-workers[208] and its corresponding nanostructures and capacitive activities are unveiled in Figure 2.30.

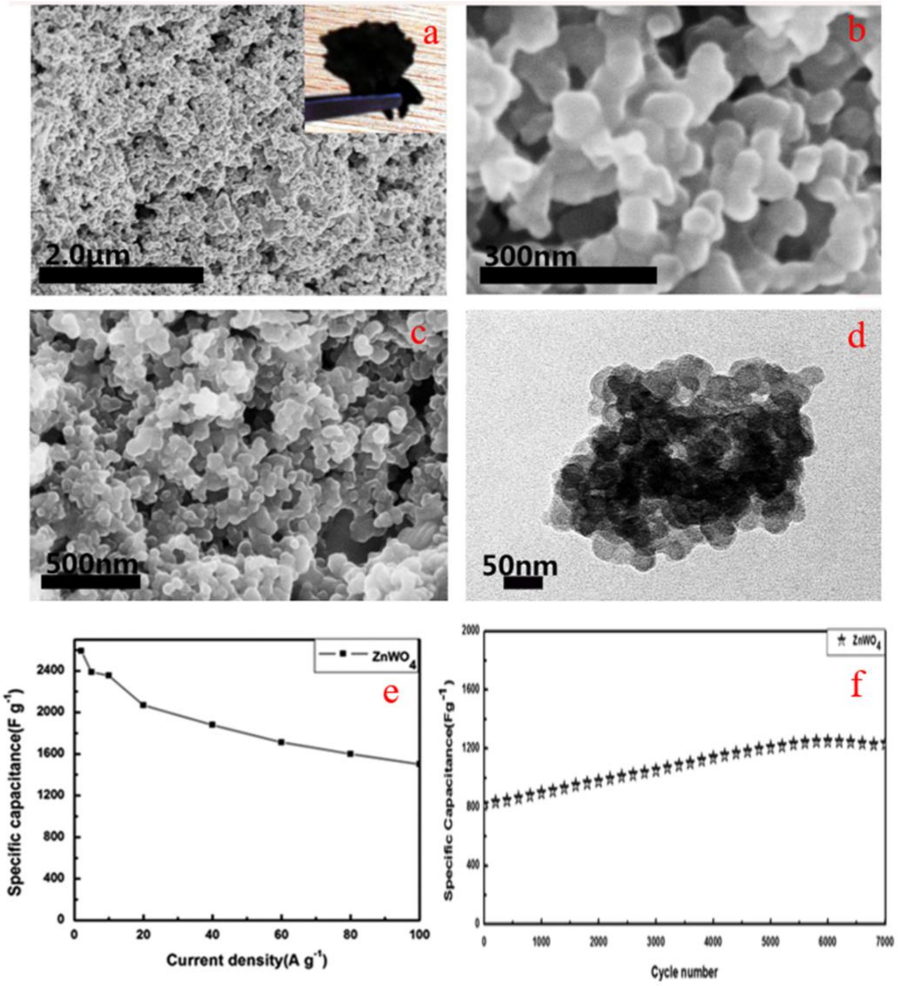

Figure 2.30: (a-d) Representative SEM images of 3D porous $ZnWO_4$ nanoparticles in different magnifications. (e) specific capacitance of 3D $ZnWO_4$ electrode at various current densities. (f) Cycling test of 3D $ZnWO_4$. Reproduced with permission from ref.[208]. Copyright 2016, Elsevier.

Interestingly, the electrode material demonstrated eminent specific capacitance of 2590 Fg^{-1} at the current density of 2 Ag^{-1} under the working potential range of 0.3 to 0.55 V, whereas the specific capacitance was 1089.8 Fg^{-1} when the potential window was varied from 0 to 0.55 V. Besides, it is noteworthy that 74.8 % of specific capacitance was retained as the current density altered from 2 to 100 Ag^{-1}, suggesting its extraordinary rate capability. In addition, an increase in specific capacitance was observed after 10000 cycles (from 818.2 to 1252.2 Fg^{-1} at 10 Ag^{-1}), as a result of improved reaction activities upon cycling.

2.4.1.5 Others MTMOs

In addition to the aforementioned MTMO, metal ferrite (MFe_2O_4) [209-215] and metal manganites (MMn_2O_4) have also been investigated as the electrode material for supercapacitor. Spinel ferrites are potential electrode materials as they are naturally abundant, lucrative, highly stable and eco-friendly [215]. For instance, Sagu et al.[215] reported the synthesis of nanstructured cobalt ferrite ($CoFe_2O_4$) thin films through aerosol-assisted chemical vapour deposition approach (AACVD) for applications in supercapacitors. The as-synthesised electrode material showed excellent capacitive performance and rate capability with areal capacitance of 540 μFcm^{-2} and 500 μFcm^{-2} at current densities of 40 and 120 μAcm^{-2}, respectively. Besides, it is interesting to note that the coulombic efficiency increased with the current density, where the coulombic efficiencies were 69 % and 79 % as the current density was raised from 40 to 120 μAcm^{-2}. This phenomenon could be explicated by the sluggish kinetics of oxygen evolution reaction (OER). Hence, it is profitable to construct a supercapacitor with excellent rate capability in order to avoid the OER side reactions. Furthermore, good cycling performance was observed for $CoFe_2O_4$ electrode with a capacitance fading of only 20 % after 7000 continuous charge-discharge cycles. The capacitance fading was most likely due to the electrolyte decomposition by OER upon cycling.

Metal manganites (MMn_2O_4) are regarded as one of the potential candidates for supercapacitor electrode fabrication as they possess multiple oxidation states which offer sufficient accessible spots for rapid redox reaction. In view of all the metal manganites, $NiMn_2O_4$ with spinel structure is perceived as the practicable and prospective electrode material by virtue of its remarkable electrochemical properties such as high specific capacitance and excellent energy and power density[216-221]. For example, Bhagwan and his groups[221] studied the electrochemical features of spinel $NiMn_2O_4$ nanofibers with align, mesoporous and high aspect ratio. They reported that reasonable specific capacitance of 410 Fg^{-1} was obtained at 1 Ag^{-1} but decreased to 275 Fg^{-1} as the current density was raised from 1 to 5 Ag^{-1}, indicating its acceptable capacitive performance and good rate capability. Moreover, 95 % of its initial capacitance was preserved after 5000 cycles at 5 Ag^{-1}, revealing the excellent cycling stability of the spinel $NiMn_2O_4$ nanofibers. The diffusion coefficient of the active material was calculated to be approximately 4.84×10^{-11} cm^2s^1. Higher diffusion coefficient of the electrode material leads to rapid migration of electrolyte ions to the surface of the bulk electrode and hence ameliorating the electrochemical activities.

Albeit mixed transition metal oxides offer impressive theoretical capacitance associated with the redox reaction, they still suffer from low electrical conductivity, poor rate performance and inferior cycling stability as well as non-effective utilisation of the active material during the electrochemical reaction as compared to the hybrid electrode materials (combination of MTMO with carbonaceous material). Therefore, the following section reviewed comprehensively the morphological and electrochemical properties of the hybrid materials as supercapacitor electrodes, which synergistically exploited the EDLC and Faradaic characteristics of the active material for advanced charge storage performance.

2.4.2 Graphene-Mixed Transition Metal Oxides (G-MTMO) based supercapacitor

The capability to harness the energy is imperative for human civilisation especially in the field of portable electronic appliances since their demands are increasing tremendously [62]. Thus, hybridisation of carbonaceous materials with diverse mixed transition metal oxides (G-MTMO) is revealed as a functional and effective strategy to ameliorate the electrochemical performances of supercapacitors. Despite activated carbon (AC) exhibits large specific area, its poor electrical conductivity has limited its practical application for supercapacitor. For carbon nanotubes (CNT), it possesses larger specific surface area and better electrical conductivity than that of activated carbon. Nevertheless, its high contact resistance with the current collector and cost-ineffectiveness has hindered its practical employment[222]. As compared to other carbonaceous materials like AC and CNT, graphene has received massive attentions from the researchers recently[26].

Graphene is recognised as one of the wonderful elements in the field of science and technology. Graphene as the hexagonal crystalline monolayer of graphite is one of the essential crystalline allotropes of carbon atoms with a C-C bonds distance of 0.142 nm[223]. It can be applied in a wide range of applications such as thin film transistors, supercapacitors, high sensitivity chemical sensors, anti-corrosion coating and others. Among the allotropes of carbon atoms, graphene is the only allotrope where each carbon atom is tightly bounded to its neighbouring atoms by an inimitable electrostatic force. As delineated in Figure 2.31, each carbon atom in graphene is sp^2 hybridised and it has 3 bonds bonded with different neighbouring C atoms. The sp^2 hybridisation consists of s, p_x and p_y orbitals. In the hexagonal lattice of graphene, three different carbon atoms covalently bonded to each carbon atom and results in one free electron. The free electron is held by the p_z orbital[224].

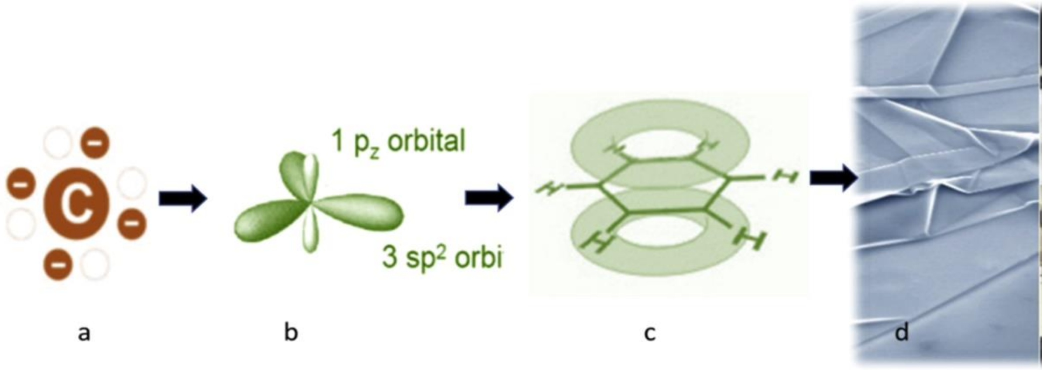

Figure 2.31: a to c) Schematic diagram of the fundamental bonding of graphene and d) SEM image of pure graphene sheet. Reproduced with permission from ref.[224]. Copyright 2020, Elsevier.

The properties of graphene significantly rely on the number of layers and the defects of the graphene layers. Graphene consists of some intriguing physical and chemical properties such as large theoretical surface area (~2630 m^2/g), excellent thermal (~5×10^3 $Wm^{-1}K^{-1}$) and electrical conductivity (~10^4 $\Omega^{-1}cm^{-1}$), good electrochemical stability, high flexibility and good structural tenacity[18, 25]. The hybridisation of graphene sheet with nanoscale MTMO enlarges the accessible specific surface of the active materials. Meanwhile, the synergistic effect and intimate contact between the two phases promote the electrons and ions diffusion process. Secondly, various synthetic approaches integrated with 2D graphene sheets lead to facile and controllable formation of nanocomposite with distinct nanostructures towards targeted functionalisation like supercapacitors. Thirdly, the free-standing 2D graphene nanosheets consist of 2D edge plane sites which accelerate the ions adsorption process and thereby enhancing the specific energy and specific power of graphene-MTMO nanocomposite[62, 225]. In this section, the synthesis and contribution of various graphene-MTMO (G-MTMO) nanocomposites as supercapacitor electrode were extensively studied and organised according to their predominant metallic groups in chemical composition. In particularly, distinctive results and elucidations were given for certain advanced G-MTMO nanocomposites.

2.4.2.1 Graphene-Metal Cobaltites

Recently, the integration of graphene with metal cobaltite as nanocomposites has drawn tremendous research enthusiasm owing to its improved physical and electrochemical properties as compared to sole metal cobaltites. Table 2.3 summarises state-of-the-art in graphene-metal cobaltite nanocomposites [25, 26, 130, 226-237] as working electrode for supercapacitor system.

Table 2.3: Summary of graphene-metal cobaltites nanocomposites.

Morphology	**Synthetic approach**	**Specific capacitance (Fg^{-1})**	**Current density (Ag^{-1})**	**Cycling stability**	**Ref**
Fe-Co oxides nanoparticles/Crumpled graphene	Aerosol spray pyrolysis	325	0.1	80 % (2000 cycles)	[130]
3D Free-standing $NiCo_2O_4$@graphene foam	Freeze casting method	563	2	95 % (5000 cycles)	[226]
$NiCo_2O_4$/3D graphene	Hydrothermal	2300	1	94.3 % (5000 cycles)	[227]
Graphene wrapped $CuCo_2O_4$ hollow spheres	Hydrothermal	1813	2	95.2 % (6000 cycles)	[228]
rGO wrapped porous $NiCo_2O_4$ composite	Hydrothermal	1185	2	98 % (10000 cycles)	[25]
NiCo2O4 nanobundles-rGO	Hydrothermal	1278	1	95 % (1000 cycles)	[229]
$NiCo_2O_4$ hexagonal nanoplates/rGO	Hydrothermal	947.4	0.5	97.9 % (3000 cycles)	[26]

$NiCo_2O_4$ nanosheets/rGO	Solution based method	1186.3	0.5	97 % (100 cycles)	[230]
$ZnCo_2O_4$-rGO	Hydrothermal	3222	1	94 % (5000 cycles)	[231]
Mesoporous $ZnCo_2O_4$-rGO	NF template	2009	10 $mAcm^{-2}$	100 % (2000 cycles)	[232]
Mesoporous $ZnCo_2O_4$ nanowires on rGO sponges	Hydrothermal	1116.6	$2mVs^{-1}$	93.4 % (5000 cycles)	[233]
3D $ZnCo_2O_4$ nanoflakes@rGO	Hydrothermal	1613	1	97.3 % (5000 cycles)	[234]
Honeycomb-like $NiCo_2O_4$@$Ni(OH)_2$ on 3D N-doped graphene-CNT sponge	Pyrolysis	1810	1	87 % (5000 cycles)	[235]
1D $NiCo_2O_4$ nanorods on graphene	Hydrothermal	1292	0.5	145 % (2000 cycles)	[236]
Spinel $NiCo_2O_4$ nanowires on rGO	Hydrothermal	1248	2 $mAcm^{-2}$	90 % (2000 cycles)	[237]

Rajagopalan and his group[25] fabricated a reduced graphene oxide (rGO) wrapped porous $NiCo_2O_4$ nanocomposite (NCO-rGO) through hydrothermal process with ammonium hydroxide as pH regulator. The formation mechanism and its corresponding morphologies and electrochemical outputs are unveiled in Figure 2.32. Additionally, the effect of rGO content on the electrochemical performances was also evaluated comprehensively.

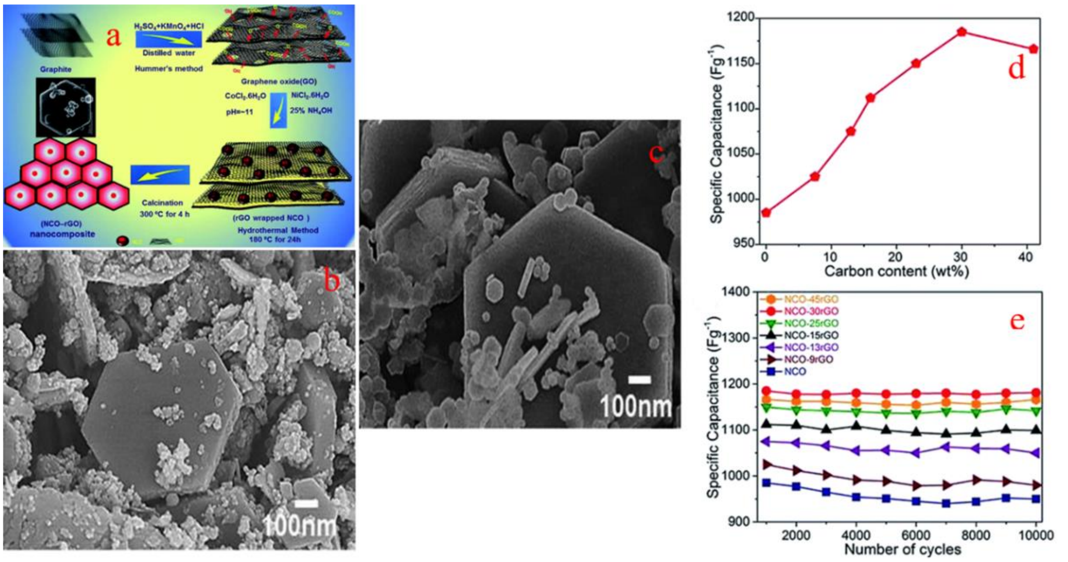

Figure 2.32: a) Schematic diagram of the synthesis procedure for the NCO-rGO hexagonal nanocomposite. (b and c) SEM images of pristine NCO and NCO-rGO nanocomposite respectively. d) Specific capacitance versus weight of rGO. e) Cycling performance of different NCO-rGO nanocomposite at 2 Ag^{-1}. Reproduced with permission from ref.[25]. Copyright 2017, The Royal Society of Chemistry.

Figure 2.32a illustrates the mechanism on the coordination of metal cation with the functional groups of graphene oxide as well as the transformation of these metallic cations to cluster-like metal hydroxides via altering the pH of solution. Specific capacitances of 980 and 1185 Fg^{-1} were reported for sole NCO and NCO-rGO nanocomposite, respectively. The discrepancy could be assigned to the development of well-interconnected networks of rGO, which allowed intimate contact between the surface of active material with electrolyte ions during the inter/de-intercalation process. Besides, the presence of rGO minimised the ions migration pathway and eased the diffusion process of electrolyte ions to the redox centres. In addition, the agglomeration of nickel cobaltite particles was hindered by rGO which assured effective reversible redox reactions at the electrode/electrolyte interface. As for cycling stability test, around 98% of initial capacitance was retained for NCO-30rGO nanocomposite, which is higher than that of pristine NCO

(90 %) over 10000 cycles. The improved cycling stability could be ascribed to the peculiar nanoarchiteture of NCO-30rGO, where the rGO not only improved the electrical conductivity but also served as a buffer matrix to adapt the volume expansion or variation during the continuous charge-discharge process. Furthermore, distinct electrochemical properties could be acquired by altering the rGO content in the NCO-rGO nanocomposites. It was observed that specific capacitance of NCO-rGO nanocomposites increased as rGO content was raised up to 30 %. Above the 30% critical point, capacitance fading occurred as a result of reduction on the active material composition (NCO). This led to the reduction of density of the active NCO which is prominent for energy storage.

Apart from $NiCo_2O_4$, zinc cobaltite incorporated with rGO ($ZnCo_2O_4$-rGO) with intertwined sheets grown onto nickel foam was conducted by Gao et al.[231] through a facile hydrothermal deposition process followed by calcination treatment as shown in Figure 2.33.

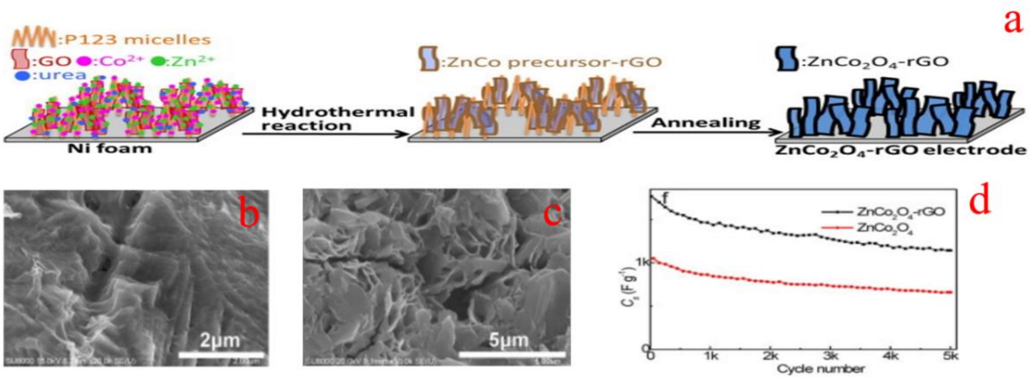

Figure 2.33: a) Schematic illustration on the preparation of $ZnCo_2O_4$-rGO nanocomposite. (b-c) SEM images of pristine $ZnCo_2O_4$ and $ZnCo_2O_4$-rGO nanocomposite respectively. d) Cycling test of sole $ZnCo_2O_4$ and $ZnCo_2O_4$-rGO. Reprinted with permission from ref.[231]. Copyright 2018, Elsevier.

The corresponding Faradaic redox reactions of $ZnCo_2O_4$-rGO nanocomposite could be expressed as follow:

$$Co_2O_4^{2-} + H_2O \leftrightarrow 2CoOOH + 2OH^- \qquad (2.12)$$

$$CoOOH + H_2O + e^- \leftrightarrow Co(OH)_2 + OH^- \qquad (2.13)$$

Impressively, a specific capacitance of 3222 Fg^{-1} was achieved by $ZnCo_2O_4$-rGO electrode material at current density of 1 Ag^{-1}. As the current density increased from 1 to 20 Ag^{-1}, a specific capacitance of 860 Fg^{-1} was retained, suggesting its superior rate capability. In contrast, pristine $ZnCo_2O_4$ electrode material manifested a specific capacitance of 1208 Fg^{-1} at 1 Ag^{-1}, revealing its inferior capacitive performance. The high specific capacitance of $ZnCo_2O_4$-rGO nanocomposite could be elucidated by the integration of high specific surface area graphene nanosheet with the hierarchical macroporous architecture of $ZnCo_2O_4$, which allowed more electroactive sites available for rapid redox reactions and hence improving the charge storage capability. Furthermore, 35 % capacitance deterioration over 5000 successive charge-discharge cycles was recorded for $ZnCo_2O_4$-rGO electrode material as compared to sole $ZnCo_2O_4$ (62% capacitance retention), implying the satisfactory cyclic stability of $ZnCo_2O_4$-rGO nanocomposite. In the same study, an asymmetric supercapacitor with $ZnCo_2O_4$-rGO nanocomposite as positive electrode and activated carbon as negative electrode was fabricated using 2M KOH as the electrolyte. The as-synthesised asymmetric supercapacitor delivered an energy density of 49.1 $Whkg^{-1}$ at power density of 400 Wkg^{-1}.

2.4.2.2 Graphene-Metal Molybdates

In addition to graphene/metal cobaltite, graphene/metal molybdate has also attracted considerable attention for supercapacitor application recently. Among various graphene/metal molybdate based electrode materials such as G-$NiMoO_4$[238-247], G-$CoMoO_4$[80, 248-253], G-$ZnMoO_4$[254-256] and etc[257-259]., graphene/cobalt molybdate (G-$CoMoO_4$) was identified as a potential candidate for charge storage system owing to its advanced electrochemical properties, good mechanical stability and electronic conductivity. As an example, flower like nanoflake $CoMoO_4$-rGO nanocomposites grown on Ni foam was reported by Jinlong and co-workers[248]. The nanoflakes like $CoMoO_4$-rGO nanohybrid exhibited an outstanding specific capacitance of 856.2 Fg^{-1} at current density of 1 Ag^{-1}. In addition, only 5.5 % of the total capacitance decayed after 2000 continuous intercalation/de-intercalation process as compared to that of single $CoMoO_4$ (10.8 %). The authors reported that the nanocomposite had larger specific surface area and average pore diameter than that of the pristine $CoMoO_4$ nanoparticles, suggesting the enhancement of surface area through integration with graphene sheets. The eminent electrochemical properties could be attributed to the following rationales: i) The flower-like nanoarchitecture encouraged the ions (OH^-) and electrons transportation which accelerated the rate of reaction. ii) The graphene networks offered adequate electroactive spaces, which enabled effective utilisation of the graphene/$CoMoO_4$ nanocomposite electrode material. iii) graphene served as a cushion to absorb or reduce the structural stress or volume variation during the continuous charge-discharge process and thus prevented the structural deformation.

Other than $CoMoO_4$, the combination of $NiMoO_4$ with graphene for application in hybrid capacitor was performed by Jinlong et al.[239], where the $NiMoO_4$ nanoparticles and quantum dots were homogeneously distributed on the surface of the reduced nanohole graphene oxide (rNHGO). As for comparison, the $NiMoO_4$@reduced graphene oxide (rGO) was also synthesised and its corresponding electrochemical performances was determined. Figure 2.34 delineates the morphological structures and the electrochemical activities of $NiMoO_4$@rGO and $NiMoO_4$@rNHGO.

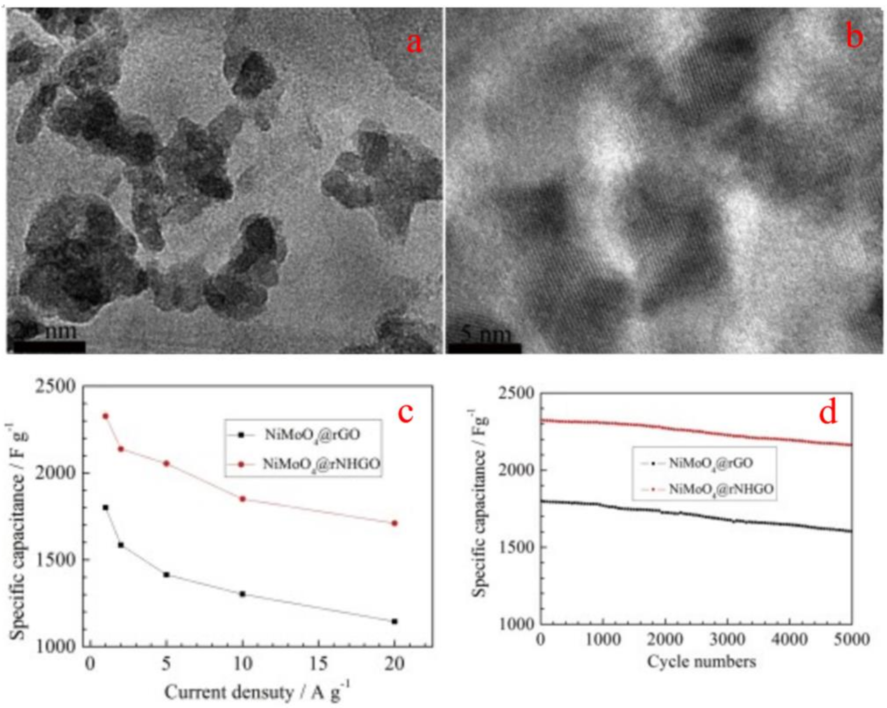

Figure 2.34: (a-b) TEM images of $NiMoO_4$@rGO and $NiMoO_4$@rNHGO respectively. c) The specific capacitance of two electrodes at various current densities. d) Cycling test of the two electrodes. Reprinted with permission from ref.[239]. Copyright 2017, Elsevier.

The specific surface area of $NiMoO_4$@rNHGO nanocomposite (166.9 m^2g^{-1}) was higher than that of $NiMoO_4$@rGO (117.6 m^2g^{-1}). In fact, electrode material in nanoscale dimension offers larger specific surface area with abundant electroactive sites for Faradaic redox reaction. Furthermore, $NiMoO_4$@rNHGO nanocomposite exhibited exceptional specific capacitance (2327.3 Fg^{-1} at 1 Ag^{-1}) and excellent cycling stability (93 % retention after 5000 cycles) when compared to $NiMoO_4$@rGO (1801.2 Fg^{-1} and 89.1 % capacitance retention after 5000 cycles). The remarkable electrochemical outputs of $NiMoO_4$@rNHGO could be attributed to several factors: Firstly, the direct growth of $NiMoO_4$ nanoparticles and quantum dots on the rNHGO allowed intimate contact between the active material and the current collector, resulting in effective ions diffusion. Moreover, the larger specific surface area of $NiMoO_4$@rNHGO could offer more electroactive spaces for the reversible redox reaction which prolonged the cycle life and reinforced the structural tenacity. Lastly, the synergistic effect between the quantum dots, $NiMoO_4$ nanoparticles and rNHGO reduced the electrolyte ions diffusion route to the bulk of electrode during the charge-discharge process.

2.4.2.3 Graphene-Metal Vanadates

In comparison to the traditional Faradaic bimetallic vanadates, the incorporation of bimetallic vanadates with graphene demonstrates better electrochemical activities by virtue of the synergistic effect between the graphene nanosheet (EDLC) and metal vanadates (pseudocapacitance). Hence, many researchers are devoted to evaluate and determine the feasibility of graphene-metal vanadate nanocomposites as the electrode material for supercapacitors, where the studied materials include graphene-cobalt vanadate (G-$Co_3V_2O_8$), graphene-nickel vanadate (G-$Ni_3V_2O_8$), graphene-bismuth vanadate (G-$BiVO_4$) and etcetera[29, 42, 260-265]. However, the number of literature reported on these nanocomposites as electrode for supercapacitor applications is rather scarce as compared to other nanocomposites.

For example, Kumar and coworkers[29] decorated $Ni_3V_2O_8$ nanosheets arrays on aminated rGO through tandem hydrothermal and freeze drying process. The peculiar sheet-like nanoarchitecture of nickel vanadate/reduced graphene oxide nanocomposite (NiV@rGO) and the synergistic effect between rGO and $Ni_3V_2O_8$ nanosheets rendered the electrode with higher specific capacitance (170 Cg^{-1}) when compared to the bare rGO (63 Cg^{-1}) at current density of 0.5 Ag^{-1}. In particular, the high specific capacitance of $Ni_3V_2O_8$/rGO nanocomposite was assigned to the presence of rGO sheets that impeded the agglomeration of $Ni_3V_2O_8$ nanosheets and hence provided more active sites for better ionic diffusion. The nanocomposite showed remarkable cycling performance with a capacitance retention of 97.2 % after 1400 cycles at 0.5 Ag^{-1}. Besides, lower charge transfer resistance was observed for NiV@rGO as the integration of rGO increased the electrical conductivity of the nanocomposite and thus leading to lower charge diffusion resistivity. The pertinent morphological and electrochemical characterisations of NiV@rGO active electrode material are depicted in Figure 2.35.

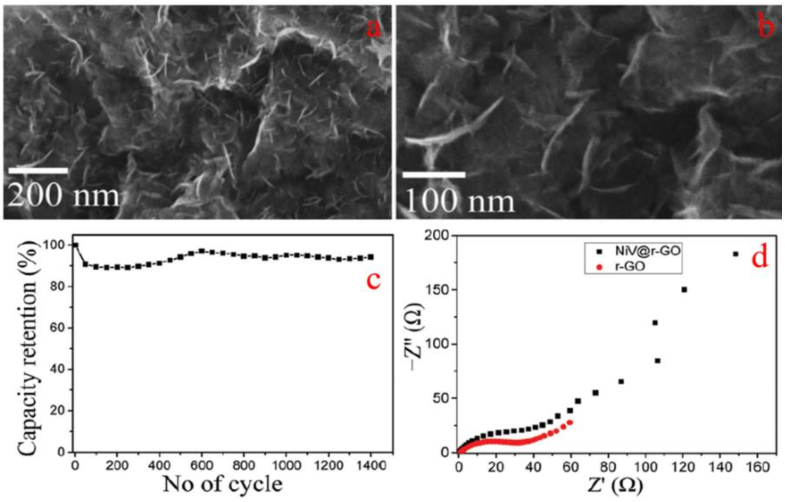

Figure 2.35: (a-b) The SEM images of NiV@rGO nanocomposite. (c) The cycling test at 0.5 Ag-1. (d) EIS plot of NiV@rGO and bare rGO. Reprinted with permission from ref.[29]. Copyright 2017, The Royal Society of Chemistry.

The integration of bismuth vanadate with reduced graphene oxide ($BiVO_4$/rGO) was conducted by Dutta et al.[260] through facile hydrothermal technique at 200°C for 90 minutes (B-90). In an extension of this work, the reaction time was varied (30 min, 60 min, 90 min and 120 min) in the synthesis of $BiVO_4$/rGO nanocomposite to evaluate the impact of reaction time on the capacitive performance. The morphologies of the optimised $BiVO_4$/rGO along with its corresponding supercapacitive activities are demonstrated in Figure 2.36.

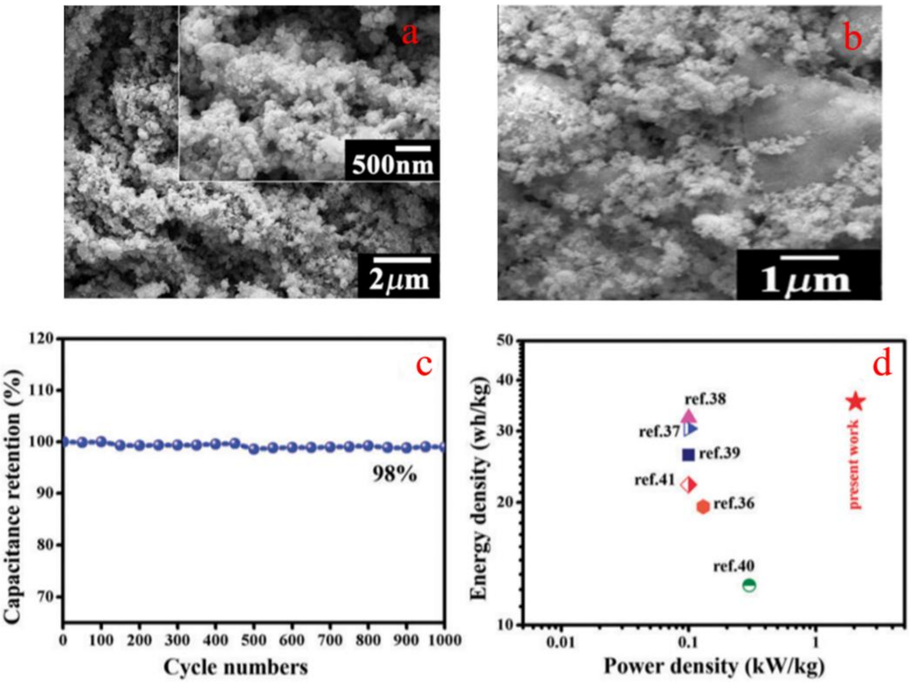

Figure 2.36: (a-b) SEM images of pristine $BiVO_4$ and $BiVO_4$/rGO nanocomposite respectively. (c) Cycling stabiility graph of $BiVO_4$/rGO nanocomposite. (d) Ragone plot for $BiVO_4$/rGO nanohybrid as compared to other reported metal oxides. Reprinted with permission from ref.[260]. Copyright 2018, The Royal Society of Chemistry.

The SEM analysis indicated that the thin rGO nanosheets were well decorated by the $BiVO_4$ nanoparticles at 200 °C for 90 minutes. As the reaction time increased to 120 minutes, the aggregation of $BiVO_4$ nanoparticles into larger particles with irregular sizes was observed. The reversible redox reaction of $BiVO_4$/rGO electrode material was assigned to the redox pairs of V(4)/V(5) and the reaction mechanism is expressed as follows:

$$BiVO_p + qM^+ + qe^- \leftrightarrow V_{2p-q}O_pM_q^{q+} \tag{2.14}$$

where M is the electrolyte ions. The authors claimed that excellent specific capacitance of 400 Fg^{-1} was achieved by $BiVO_4$/rGO nanocomposite when compared to sole $BiVO_4$ (149 Fg^{-1}) at the scan rate of 5 mVs^{-1}. Moreover, only 2 % of capacitance attenuated after 1000 cycles for $BiVO_4$/rGO nanocomposite, revealing its good cycling stability. Furthermore, a maximum specific energy of 35.37 $Whkg^{-1}$ was observed for the $BiVO_4$/rGO nanocomposite electrode. In this case, the unique electrochemical properties of $BiVO_4$/rGO nanocomposite could be elucidated by: i) incorporation of rGO increased the electrical conductivity and thus accelerated the ionic transportation. ii) optimum reaction time (90 min) for the synthesis of $BiVO_4$/rGO nanocomposite which effectively prohibited the agglomeration of nanomaterials.

2.4.3.4 Graphene-Metal Tungstates

Besides, the integration of metal tungstate with graphene as electrode material is also a research hotspot recently owing to its appealing supercapacitive performances. The incorporation of graphene with nickel tungstate (G-$NiWO_4$) and cobalt tungstate (G-$CoWO_4$) along with their pertinent capacitive outputs were reported by the researchers[14, 41, 266]. For instance, Xu and co-workers[41] proposed a controllable synthetic strategy which decorates nickel tungstate nanoparticles uniformly on reduced graphene oxide nanosheets to form firmly coupled nanohybrid. The $NiWO_4$ nanoparticles on the surface of rGO sheet behaved like spacers which prohibited the graphene sheet from restacking. Moreover, overlapping of each rGO sheet could lead to the formation of 3D network which facilitated the diffusion of electrolyte ions and hence accelerated the Faradaic reversible reaction. The nanohybrid delivered a high capacitance of 1031.3 Fg^{-1} at 0.5 Ag^{-1}, excellent capacitive stability (99.24 % after 5000 cycles) and reasonable rate capability (72.1 % retained at 8 Ag^{-1}). The outstanding capacitive performances could be explicated as follows: i) graphene as a highly conductive matrix hindered the agglomeration of $NiWO_4$ nanoparticles and ameliorated the electrical conductivity of the nanocomposite. ii) multiple oxidation states and synergistic effect between the $NiWO_4$ nanoparticles and rGO sheets accelerated the diffusion of electrolyte ions to the bulk of electrode. iii) graphene adapted to the swelling or expansion of the active material efficiently upon cycling. In the extension of this work, the authors also reported that the specific capacitance increased as the graphene content was raised from 10 to 20 mL while diminished with further increment afterwards. This could be due to the severe aggregation between rGO and $NiWO_4$ which attenuated the specific capacitance.

In another similar work, Naderi et al.[266] constructed a nanocomposite of cobalt tungstate anchored on the surface of nitrogen doped reduced graphene oxide ($CoWO_4$@NRGO) via in-situ sonochemical process for high performance supercapacitors. The $CoWO_4$@NRGO nanohybrid exhibited a high specific capacitance of 597 Fg^{-1} at scan rate of 5 mVs^{-1}, excellent cycling stability with 97.1 % initial capacitance retention after 4000 cycles and high energy density of 67.9 $Whkg^{-1}$ at power density of 500 Wkg^{-1}, demonstrating its impressive capacitive performance. The attractive electrochemical properties could be ascribed to the synergistic effect between the pseudocapacitance of $CoWO_4$ and EDLC of NRGO sheets as well as the uniform distribution of $CoWO_4$ nanoparticles on the NRGO, which resulted in more accessible sites for Faradaic redox reaction.

2.4.3.5 Others Graphene/MTMO

In addition to the MTMO discussed above, the incorporation of metal ferrites [267-272] and metal manganites[273-276] with graphene sheets have also been widely studied for supercapacitor applications. For instance, Liu and co-authors[267] prepared the $CoFe_2O_4$/graphene via facile hydrothermal process by employing the steel rolling sludge as the iron precursors. Here, the steel rolling sludge was considered as a recycled, environmentally benign and lucrative precursor. The authors suggested that the integration of graphene into $CoFe_2O_4$ nanoparticles hampered the agglomeration of $CoFe_2O_4$ nanoparticles. The $CoFe_2O_4$/rGO nanocomposite showed excellent Faradaic redox reactions with high specific capacity of 166.5 Cg^{-1} and 127.0 Cg^{-1} at current density of 0.5 and 10 Ag^{-1}, respectively. In this work, the concept of “specific capacity” was practiced instead of “specific capacitance”, owing to the battery type electrode material species of $CoFe_2O_4$. The capacity deterioration as the current density increased from 0.5 to 10 Ag^{-1} could be assigned to the non-effective utilisation of the active electrode material at high current density as a result of rapid ionic diffusion process. Furthermore, the electrode material delivered a reasonable cycling stability with capacity retention of 79.3% after 5000 continuous charge-discharge cycles. The loss of specific capacity was due to the dissolution of some active materials into the electrolyte solution upon cycling. As for metal manganites, $NiMnO_3$ nanoparticles decorated on the reduced graphene oxide was developed by Kakvand et al.[273] via facile electrostatic co-precipitation method. The as-prepared nanocomposite demonstrated a high specific capacitance of 285 Fg^{-1} at 1 Ag^{-1}, excellent cycle life with 93.5 % and 87 % capacitance retention after 1000 and 4000 cycles, respectively. The nanocomposite demonstrated an acceptable energy density of 27.3 $Whkg^{-1}$ in symmetric supercapacitor. The remarkable capacitive activities could be ascribed to the following factors: i) rGO increased the specific surface area of the nanocomposite and maximised the contact between $NiMnO_3$ nanoparticles and rGO sheets. ii) the substantial contribution of the EDLC mechanism which was originated from the rGO of the nanocomposite. iii) homogeneous distribution of $NiMnO_3$ nanoparticles on the rGO surface which reinforced the mechanical strength of material and hindered the agglomeration and volume expansion during cycling.

In short, the state-of-the-art examples clearly revealed the synergistic effect between MTMO and graphene materials. Hence, incorporation of graphene with MTMO is an appealing approach to promote the capacitive performance and overcome the limitation (low electrical conductivity) of single MTMO for high performance supercapacitor application.

Chapter 3: Experimental Materials and Characterisation methods

3.1 Materials

Pristine high pyrolytic grahite flakes (with 99 % carbon purity) were purchased from Bay Carbon, USA. Nickel(II) nitrate hexahydrate (($Ni(NO_3)_2.6H_2O$) was purchased from Merck. Zinc chloride ($ZnCl_2$), Cobalt chloride hexahydrate ($CoCl_2.6H_2O$), Aluminium chloride hexahydrate ($AlCl_3.6H_2O$), Manganese nitrate trihydrate ($Mn(NO_3)_2.3H_2O$) and Lithium hydroxide (LiOH) were purchased from R&M chemicals. Sodium orthovanadate (Na_3VO_4) and Ammonium metavanadate (NH_4VO_3) were purchased from Acros Organics. Carbon black and ethanol were purchased from Alfa Aesar and QReC with the purity of 99 and 96 %, respectively. Hydrochloric acid was procured from Fisher Scientific, USA. Besides, potassium hydroxide (KOH), N-methyl-2-pyrrolidinone (NMP) and polyvinylidene fluoride (PVDF) were purchased from Sigma-Aldrich. Deionised water (D.I) from Millipore system was used throughout the whole experiment. All other chemicals were at least of analytical grade and used without further purification.

3.2 Synthesis of graphene

Graphene was synthesised through the previous reported liquid phase exfoliation technique[277]. In general, 50 mg of high pyrolytic graphite flakes was dispersed in 100 mL solution of deionized water and ethanol with the volume ratio of 3:2 under ultrasonication (frequency-30 kHz) for 4 hours at the room temperature to obtain a darkish black colour solution. Lastly, the solution was centrifuged and dried overnight at 70 ^{o}C.

3.3 Material characterisation

The crystallite structures of the as-synthesised nanocomposites were analysed by X-ray diffraction (XRD) using a Philip PANanalytical X'pert X-ray diffractometer with Cu K_α radiation (λ= 1.54060 Å) that operated at 33mA and 45kV in the range of 10 to 80° together with the step size of 0.02°. Raman spectra were examined on a Renishaw inVia Raman spectrometer with the wavelength of the incident diode laser of 514nm. The morphology, microstructure and elemental composition of the samples were characterised by the field emission scanning electron microscopy (FESEM-FEI Quanta-400) equipped with an EDX analyser and further confirmed via the transmission electron microscopy (TEM) and high resolution transmission electron microscopy (HRTEM) using JEOL-JEM-2100F analyser. X-ray photoelectron spectroscopy (XPS) measurements were conducted on a Thermo Scientific Analyser using Al K_α X-ray radiation as the constant analyser.

3.3.1 X-ray diffraction spectroscopy (XRD)

X-ray diffraction spectroscopy (XRD) is a simple and effective analytical instruments which adopt to analyse the crystallographic structural information of the sample in a wide range and deliver the detail about the unit cell dimensions. The working mechanism of XRD is simplify as follows: i) Emission of x-ray beams with particular wavelength toward the inspected specimen. ii) Once the x-ray beams impinge on the sample, the x-ray beams will be scattered in all direction and interact with the atoms of the sample before being reflected. iii) The diffracted x-rays beam with distinct intensities will be assembled by a detector and being further processed to develop the specific spectrum[278].

3.3.2 Field emission scanning electron microscopy (FESEM)

Field emission scanning electron microscopy (FESEM) is a 3D high-resolution morphological imaging instrument employed to determine the morphology of the inspected specimen in micro or nano range. The operating mechanism of FESEM comprised of directing a tiny electron beam scanning over the surface of the specimen, where the emitted electron beam was generated by the electrons gun with two wires connected to higher voltage sources of 15 to 30 KVA. Meanwhile, the emitted beam is emphasised on the inspected sample via the electro-magnetic lenses. Once the electron beam bombards the specimen surface, backscattered or secondary electrons detected will be captured by the detector allocated above the specimen and the assembled signals will be processed to synchronize images of particular sample.

3.3.3 Transmission electron microscopy (TEM)

Transmission electron microscopy (TEM) is another impressive imaging instruments, which capable of providing the in-depth physical properties of the as-determined sample in 2D nano and atomic ranges. The TEM imaging approaches include low resolution TEM (LRTEM), high resolution TEM (HRTEM), elemental distribution mapping and electron energy loss spectroscopy (EELS) and etc. The working mechanism of TEM can be elucidated as follow: i) Directing the electrons generated by the field emission beam into the sample. ii) Transmission of these electrons beam through the specimen and assembled on the detector. iii) The assembled electrons will be transformed to electrical signal and further processed to display high resolution images of morphological structure as well as lattice spacing at the atomic level.

3.3.4 Raman spectroscopy

Raman spectroscopy is a spectroscopic technique employed to study the chemical composition of the inspected specimen according to the vibrational modes. In this system, the analysis is relied on the emission of monochromatic light onto the sample at a desired frequency and evaluate the magnitude of the scattered light. In particular, the laser light contacts with phonons or other elements appeared in the system, leading to the shifting of the energy of laser photons and hence provides the details about the phonon conditions in the system.

3.3.5 Energy dispersive X-ray spectroscopy

Energy dispersive x-ray spectroscopy (EDS) is a qualitative instruments utilised to determine the elementary composition of the sample comprehensively. Typically, it coupled with the FESEM or TEM and the elementary investigation can be conducted together with the imaging. The chemical composition of the sample is determined based on the binding energy of the emitted x-rays.

3.3.6 X-ray photoelectron spectroscopy (XPS)

X-ray photoelectron spectroscopy (XPS) is a powerful surface-sensitive instrument used to analyse the chemical composition and the oxidation states of the sample. XPS study is conducted by introducing the Al-kα x-rays to the sample surface, causing the photoelectrons to be emitted from the sample surface. Typically, the analysis can be divided into two parts, namely wide scan full survey study and narrow scan elemental survey study. All the valuable information of chemical composition and valence states are determined based on the binding energies provided.

3.4 Electrochemical measurements

The electrochemical behaviour of the as-prepared nanocomposites was characterised by the cyclic voltammetry (CV), galvanostatic charge discharge (GCD) and the electrochemical impedance spectroscopy (EIS) on the Metrohm Autolab electrochemical workstation (PGSTAT302F). All the electrochemical characterisations were performed in a symmetrical two electrodes system with the employment of 2M KOH as the electrolyte. The working electrodes were prepared by incorporating the active materials (nanocomposite) with the carbon black as the conducting agent and polyvinylidene fluoride (PVDF) as the binder with a weight percentage of 70, 20 and 10 % respectively in the presence of N-methyl-2-pyrrolidinone (NMP). The obtained slurry was then coated on the aluminium foil and dried in the oven.

3.4.1 Cyclic voltammetry (CV)

Cyclic voltammetry (CV) is a powerful and impressive potentiodynamic electrochemical approach which is based on sweeping the voltage of the working electrode between the upper and lower limits at a constant scan rate to determine the reduction and oxidation reactions of the molecular species. In particular, the potential of the working electrode will increase at a fixed scan rate until it reaches the set upper potential and begin to reduce at the same scan rate until it reaches the targeted lower potential. The resulting voltage change between the working and counter electrodes during the process of potential sweep will compel the electrons to migrate to and fro between the electrodes, leading to the generation of electrical current in the external circuit. These resulting current, potential and duration are interpreted to provide pertinent details about the electrode material such as redox peaks, reversibility, specific capacitance, mechanical strength and etc.

3.4.2 Galvanostatic charge-discharge (GCD)

Galvanostatic charge-discharge is another electrochemical evaluation technique utilised to determine the capacitive performance of an electrode material. The working mechanism of GCD is based on the intercalation and de-intercalation of the working electrode at a particular current density. Here, the quantity of charges transferred are remain constant. Distinct current density applied in the GCD test will result in different potential and duration which being collected and analysed to offer beneficial information about the capacitive performance of the particular material. The specific capacitance of an electrode material can be calculated as followed:

$$C_s = 4\left[I \times \frac{\Delta t}{(\Delta V \times m)}\right] \qquad (3.1)$$

Where C_s denotes the specific capacitance(Fg^{-1}), I is the discharge current (A), Δt and ΔV represent the discharge time (s) and potential window (V), m is the mass of the electrode material (g) and 4 is the constant multiplier to convert two electrodes into single electrode.

The coulombic efficiency can be calculated by using equation 3.2:

$$\eta = \frac{t_D}{t_C} \times 100\% \qquad (3.2)$$

where t_C and t_D represents the charge and discharge time (s), respectively.

The energy density and power density can also be calculated as follows:

$$\text{Energy density (Whkg}^{-1}) = \frac{C_S V^2}{(2\times 3.6)} \qquad (3.3)$$

$$\text{Power density(Wkg}^{-1}) = \frac{(E\times 3600)}{(\Delta t)} \qquad (3.4)$$

where C_s is the specific capacitance (Fg^{-1}), V is the potential window (V), E is the energy density (Whkg^{-1}) and Δt is the discharge time(s).

3.4.3 Electrochemical impedance spectroscopy (EIS)

Electrochemical impedance spectroscopy is an analytical technique used to measures the equivalent series resistance (ESR) and the charge-transfer resistance between the electrode and the electrolyte. This test involved the exploitation of Faraday's Law to characterise the chemical process in the electrical manner. The measurement is accomplished by measuring the impedance over a wide range of frequencies and the response of electrochemical systems is nonlinear. Typically, the complex response of the electrochemical process is revealed in Nyquist format with a semicircle in the high frequency region and a linear line in the low frequency region. The radius of the semicircle represents the charge-transfer resistance (R_{ct}) which is resulted from the Faradaic redox reaction of electrode material and the double layer capacitance on the interface between electrode and electrolyte. Meanwhile, the linear line in the low frequency region denotes the Warburg Impedance(W), which gives an insight into the kinetics of ions diffusion process. Besides, the x-intercept in the Nyquist plot is the solution resistance (R_s), which combines the ionic resistance of electrolyte, intrinsic resistance of electrode material and contact resistance at the electrode/electrolyte interface.

Chapter 4: Design and fabrication of graphene/$Ni_3V_2O_8$ as advanced electrode material for symmetric supercapacitor

4.1 Introduction

In recent years, supercapacitors have attracted tremendous attention as the next generation energy storage devices owing to its eminent power density, exceptional cycle life, high coulombic efficiency and fast charge-discharge rate[279, 280]. Supercapacitors are widely utilised in portable electronic appliances, military devices, hybrid electric vehicles and other electric networks[281]. Nevertheless, the unsatisfactory energy density has restricted its further applications as compared to lithium ion batteries (LIBs)[6]. Typically, energy density is substantially depending on the specific capacitance and potential window of the devices[7]. Hence, more researches are engrossed in the evolution of supercapacitors with not only prominent power density, exceptional cycle life but also enhanced energy density. Generally, supercapacitors are classified into two types, namely electrical double layer capacitor (EDLC) and pseudocapacitor. As for EDLC, carbonaceous materials like activated carbon, single wall carbon nanotube (SWCNT), graphene etc. are adopted as the electrode where the electrical energy is stored by assembling a double layer between the electrode and electrolyte through the electrostatic interaction[4]. Contrarily, the pseudocapacitive materials which include transition metal oxides and conducting polymer are utilised as the electrode for pseudocapacitor with the fast Faradaic redox reaction being the charge storage mechanism[11]. It is sufficiently evidenced by the fact that electrode materials are pivotal for the electrochemical performance of the supercapacitor. Typically, pseudocapacitor possesses larger specific capacitance than the EDLC owing to the multiple oxidation states of transition metal oxides, which enable the fast redox reaction and hence improve the specific capacitance[12-14, 282].

Among myriad transition metal oxides, critical advances have acclaimed mixed transition metal oxide (MTMO) as a promising and lucrative candidate for supercapacitor. The coexistence of two distinct metal species in a single crystal structure of MTMO can advocate diverse redox reactions, contributing to remarkable specific capacitance as compared to single component metal oxide[23, 24, 283, 284]. Lately, nickel vanadate ($Ni_3V_2O_8$) is one of the most sought- after electroactive materials for supercapacitor owing to its peculiar crystal structure ($A_3B_2O_8$), in which A and B are the transition metal elements with low and high oxidation states (pentavalent metal ion), respectively. This will lead to advanced electrochemical activity as compared to pure nickel oxide and vanadium oxide. According to the study of Liu et al., the pseudocapacitance is greatly influenced by the nickel element in lieu of the vanadium[6]. The vanadium with unique pentavalent properties is the only element that can serve as the B metal ion to form the $A_3B_2O_8$ type mixed transition metal oxide[6, 285]. Besides, $Ni_3V_2O_8$ with the Kagome staircase-like crystalline structure manifests excellent magnetic properties and superior catalytic performance[286-288]. In addition, nickel vanadate offers many other merits such as natural abundance, cost effective and environmental friendly. Up to date, considerable findings have been accomplished on the determination of the electrochemical performance of $Ni_3V_2O_8$ for supercapacitor and lithium ion battery applications. For instance, Liu et al. reported the synthesis of $Ni_3V_2O_8$ nanoflakes by chemical co-precipitation method and it exhibited a good specific capacitance of 1181 Fg^{-1} (three electrode system) at a current density of 0.625 Ag^{-1}[6]. Besides, Soundharrajan et al. presented the production of bitter gourds shaped like $Ni_3V_2O_8$ by metal organic framework combustion techniques (MOF-C) for lithium ion battery application and the specific capacitance obtained was 531 $mAhg^{-1}$ at a current density of 5 Ag^{-1}[30]. Other than that, Vishnukumar et al. synthesized the $Ni_3V_2O_8$@NiO nanorods by solvothermal method and the specific capacitance acquired was 653 Fg^{-1} (three electrode system) at 1 Ag^{-1}[79]. Furthermore, Zhang et al. presented the synthesis of nickel vanadate and nickel oxide nanohybrid on nickel foam by hydrothermal method and it exhibited a specific capacitance of 1540 Fg^{-1} at 8 Ag^{-1} in three electrode system[289]. However, nickel vanadate ($Ni_3V_2O_8$) also suffers from low electrical conductivity and poor cycling stability, which limits its practical applications[6, 289].

In order to conquer this conundrum, one of the most promising strategies is to hybridise the $Ni_3V_2O_8$ with carbonaceous material, which augment the electrical conductivity and accelerate the kinetic of ions and electrons migration to the electrode/electrolyte surface as well as the interior of the electrodes[25, 26]. Besides, the incorporation of carbonaceous materials provides abundant electroactive sites for effective Faradaic redox reaction and offsets the volume variation during the continuous charge-discharge process. Among the carbonaceous materials, graphene as a sheet of sp^2 bonded carbon atoms with one atom thick in a honeycomb crystal structure has gained much research enthusiasms recently[26]. This is mainly attributed to its unique physical and chemical properties such as high theoretical surface area, eminent electrical conductivity, remarkable electrochemical stability, high flexibility and good structural tenacity[18, 25]. In particular, the graphene enhances the pseudocapacitive effect by increasing the electrical conductivity and facilitating the diffusion of electrolyte ions.[42]. Nonetheless, pristine graphene suffers from low specific capacitance when employed in supercapacitor. Meanwhile, graphene tends to agglomerate or restack irreversibly, leading to the formation of graphite through the van der Waals force upon drying[18]. In order to rectify these problems, many works on the integration of mixed transition metal oxides (MTMOs) with graphene have been reported. For instance, Thiagarajan et al. reported the fabrication of $Ni_3V_2O_8$/graphene oxide nanocomposite by co-precipitation method and the specific capacitance obtained was 547 Fg^{-1} at 5 mVs^{-1}[285]. In addition, Kumar et al. revealed the hydrothermal synthesis of $Ni_3V_2O_8$ nanosheet arrays on laminated reduced graphene oxide sheet and it exhibited a specific capacitance of 170 Cg^{-1} at 0.5 Ag^{-1}[29]. The uniform distribution of MTMO on the reduced graphene oxide hinders the graphene from restacking and hence provides synergistic advantages[18]. However, according to the reported literatures, the common practice to synthesise reduced graphene oxide was through modified Hummers method followed by a chemical reduction process. This method is not eco-friendly, noxious to the researchers and also deteriorates the quality of graphene[290]. This is mainly attributed to the adoption of hazardous chemicals in the process, such as sulphuric acid, hydrazine and potassium permanganate, which normally are strong oxidising / reducing agents[291].

Motivated by the aforementioned benefits of nanostructure and graphene composite, a facile solvothermal approach was proposed to fabricate graphene/$Ni_3V_2O_8$ nanocomposite. The graphene was synthesised through a top down approach by direct liquid phase exfoliation of highly pyrolytic graphite flakes (HOPG) in an optimum ratio of ethanol and water under ultrasonication, as reported in our previous works[24, 36, 129, 277]. In particular, this method involves the use of ethanol as the exfoliating solvent, which is feasible, safe, green and cost- effective. The well-exfoliated graphene was then integrated with the $Ni_3V_2O_8$ precursors to form graphene/$Ni_3V_2O_8$ nanocomposite through solvothermal technique followed by a thermal annealing process. Additionally, graphene/$Ni_3V_2O_8$ nanocomposites with different weight ratios were synthesised to determine the synergistic effect between graphene and $Ni_3V_2O_8$. Meanwhile, the surface morphology, crystalline structure and electrochemical performance of the nanocomposites were evaluated comprehensively.

4.2 Experimental methods

4.2.1 Synthesis of graphene/$Ni_3V_2O_8$ nanocomposite

The $Ni_3V_2O_8$/graphene nanohybrid was synthesised via solvothermal approach. The as-synthesised graphene was dispersed in 40 mL deionized water and ethanol mixture with the volume ratio of 3:2 under ultrasonication for 30 minutes. Subsequently, 3.38 mmol of $Ni(NO_3)_2$ and 2.24 mmol of Na_3VO_4 were dissolved in 40 mL deionized water to form the $Ni_3V_2O_8$ precursor. After that, the well-dispersed graphene solution was added to the $Ni_3V_2O_8$ solution under mild stirring at room temperature to ensure homogeneity. Then, the solution was transferred into a 100 mL Teflon-lined stainless steel autoclave and heated at 120 ^oC for 3 hours in a furnace. The reaction involved is as follows (Equation 4.1)[32]:

$$3Ni(NO_3)_2 + 2Na_3VO_4 \leftrightarrow Ni_3V_2O_8 + 6NaNO_3 \tag{4.1}$$

Once the reaction completed, the resultant precipitate was collected and washed with absolute ethanol and deionised water thoroughly. Finally, the sample was dried in an oven at 60 ^{o}C overnight and calcined at 400 ^{o}C for 2 hours to obtain the graphene/$Ni_3V_2O_8$ nanocomposite. Pristine $Ni_3V_2O_8$ nanoparticle was synthesised in the analogous manner without the addition of graphene. The synthetic process of $Ni_3V_2O_8$/graphene nanocomposite is depicted in Figure 4.1.

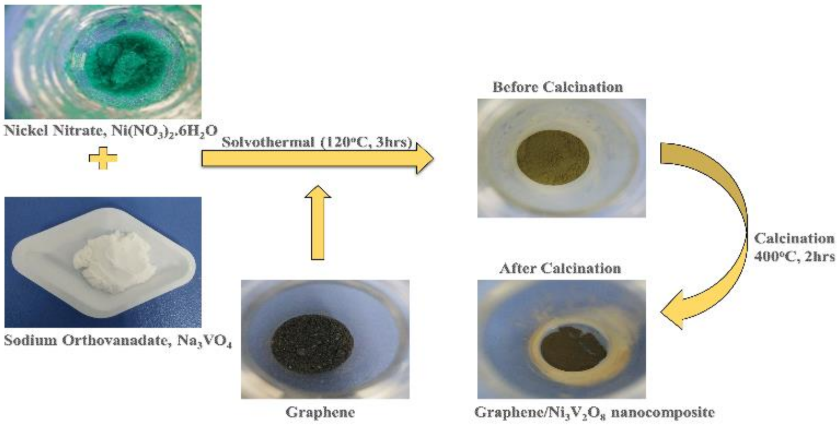

Figure 4.1: Schematic illustration on the synthetic route of graphene/$Ni_3V_2O_8$ nanocomposite.

To elucidate the effect of weight ratio of graphene to $Ni_3V_2O_8$ on the morphology and electrochemical performance of the nanocomposite, different graphene/$Ni_3V_2O_8$ nanohybrids were synthesised by varying the amount of $Ni_3V_2O_8$ precursors under the same reaction condition. The detailed formulation of $Ni_3V_2O_8$ precursor was depicted in Table 4.1.

Table 4.1: Weight Ratio of graphene to $Ni_3V_2O_8$.

Sample Code	Weight of graphene (g)	Weight of $Ni(NO_3)_2$ (g)	Weight of Na_3VO_4 (g)	Graphene:$Ni_3V_2O_8$ (Weight ratio)
G-NVO	0.2	0.492	0.206	1:1
G-2NVO	0.2	0.984	0.412	1:2
G-4NVO	0.2	1.968	0.824	1:4
G-8NVO	0.2	3.936	1.648	1:8

4.3 Results and discussion

4.3.1 Structural characterisation

The crystallographic phases of graphene/$Ni_3V_2O_8$ nanocomposites, pristine $Ni_3V_2O_8$ and exfoliated graphene were examined by XRD analysis and illustrated in Figure 4.2.

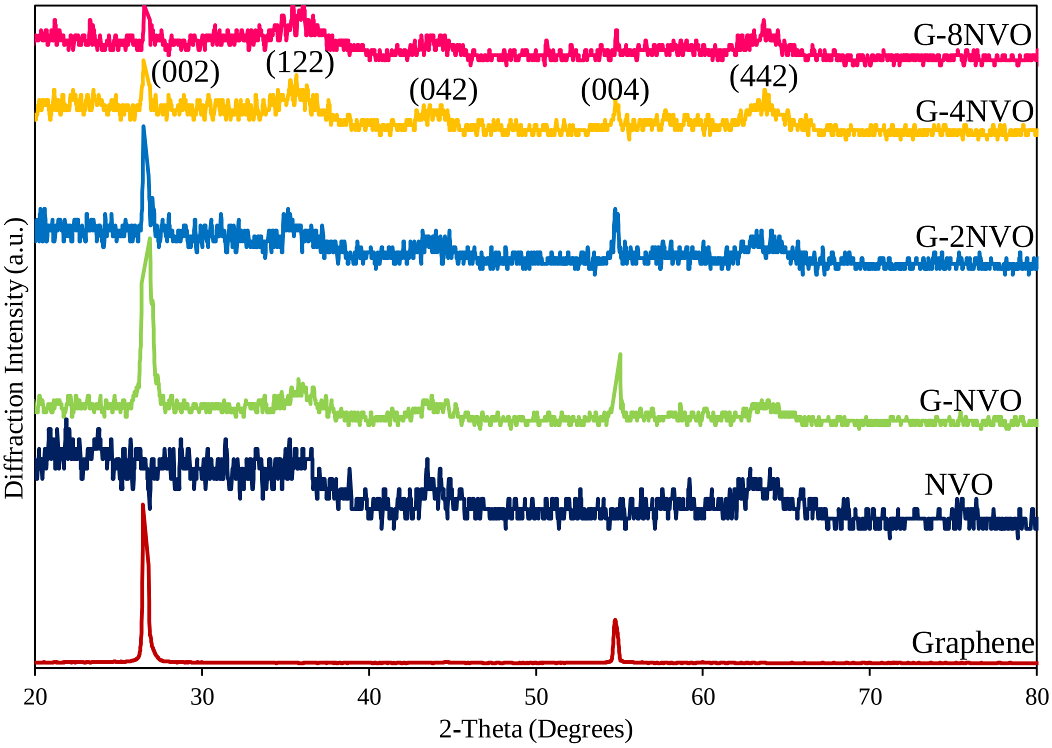

Figure 4.2: XRD patterns of pristine graphene, $Ni_3V_2O_8$ and graphene/$Ni_3V_2O_8$ nanocomposites.

As observed from Figure 4.2, the diffraction peaks of the graphene/$Ni_3V_2O_8$ nanohybrids at 2 theta values of 35.8°, 44.0° and 63.3° were well indexed to the

(122), (042) and (442) reflections of orthorhombic $Ni_3V_2O_8$ phases (JCPDS card no. 74-1484) together with the crystal lattice parameters of a=8.24 Å, b= 11.38 Å and c=5.91 Å. Besides, two diffraction peaks at 2 Theta values of 26.8 and 54.9° of graphene/$Ni_3V_2O_8$ nanocomposites are in accordance with those reported (002) and (004) of graphene phases, revealing the existence of graphene in the nanocomposites[24]. No additional peaks in the XRD patterns of graphene/$Ni_3V_2O_8$ nanocomposites indicate the high purity of the samples. In addition, it is noticeable that the intensity of the orthorhombic $Ni_3V_2O_8$ phases in the diffraction peaks of graphene/$Ni_3V_2O_8$ nanocomposites increased with the mass loading of $Ni_3V_2O_8$ reactants, which tally with the findings reported in the literatures[24, 28].

Raman spectroscopy is an effective and non-destructive analytical technique in determining the chemical composition of the carbonaceous material owing to its high vibrational intensities[37, 80, 292]. Figure 4.3 depicts the Raman spectra of pristine graphene and graphene-$Ni_3V_2O_8$ nanocomposite (G-4NVO).

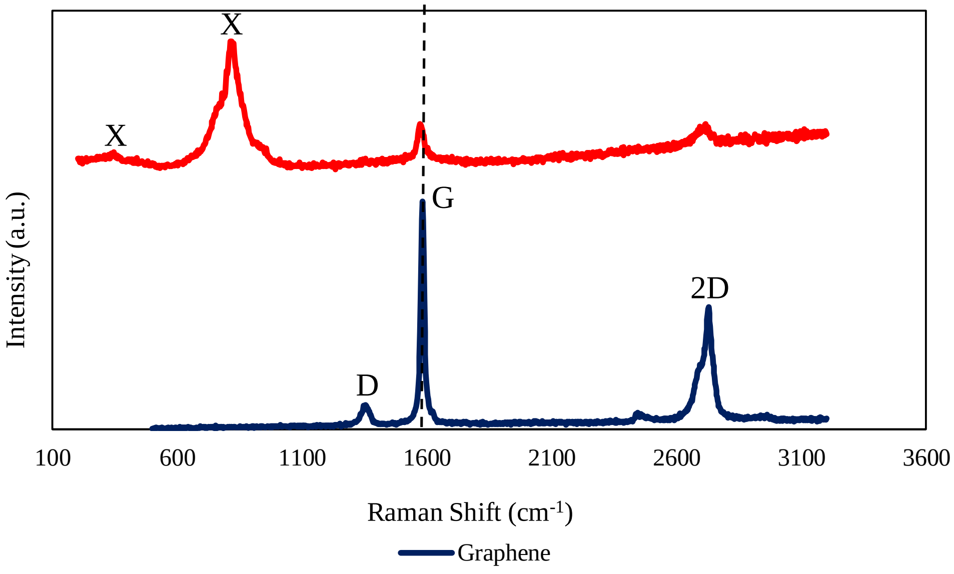

Figure 4.3: Raman spectra of pristine graphene and G-4NVO nanocomposite.

Typically, the Raman maximum at 1360, 1582 and 2726 cm^{-1} are correlated to the D, G and 2D bands of the graphene sample respectively. The appearance of G band is attributed to the first order scattering of E_{2g} phonons of the C_{sp}^2 atoms, whereas the formation of D and 2D bands are originated from the breathing mode of K-point phonons of A_{1g} symmetry (disorder)[28, 80, 129, 261, 293]. In addition, the D band also corresponds to the development of new edges (defects) during the liquid phase exfoliation of graphite to graphene sheet[24, 294, 295]. Besides, the bands at 358 cm^{-1} and 820 cm^{-1} of G-4NVO are congruent with the pristine $Ni_3V_2O_8$ while the bands at 1570 and 2726 cm^{-1} indicate the presence of graphene in the G-4NVO nanocomposite[195]. In particular, the peaks at 358 cm^{-1} and 820 cm^{-1} are assigned to the bending vibrations of V-O-V bonds and symmetric stretching mode of V-O bonds respectively[29, 195, 296]. It is worth noting that the D band of graphene vanished in the Raman spectrum of G-4NVO nanocomposite. This phenomenon can be well explicated by the fourfold increase in mass loading of $Ni_3V_2O_8$ precursors as compared to graphene in G-4NVO nanocomposite, leading to prominent $Ni_3V_2O_8$ peaks. Other than that, it is apparently observed in Figure 4.3 that the G band of G-4NVO nanocomposite down shifted slightly as compared to that of pristine graphene, suggesting the strong interaction between $Ni_3V_2O_8$ and graphene[80]. The Raman results clearly revealed the successful formation of graphene/$Ni_3V_2O_8$ nanocomposite (G-4NVO), which tally with the XRD results.

Figure 4.4 illustrated the size, surface morphology and microstructure of pristine graphene, $Ni_3V_2O_8$ nanoparticles and graphene/$Ni_3V_2O_8$ nanohybrids (G-NVO, G-2NVO, G-4NVO and G-8NVO).

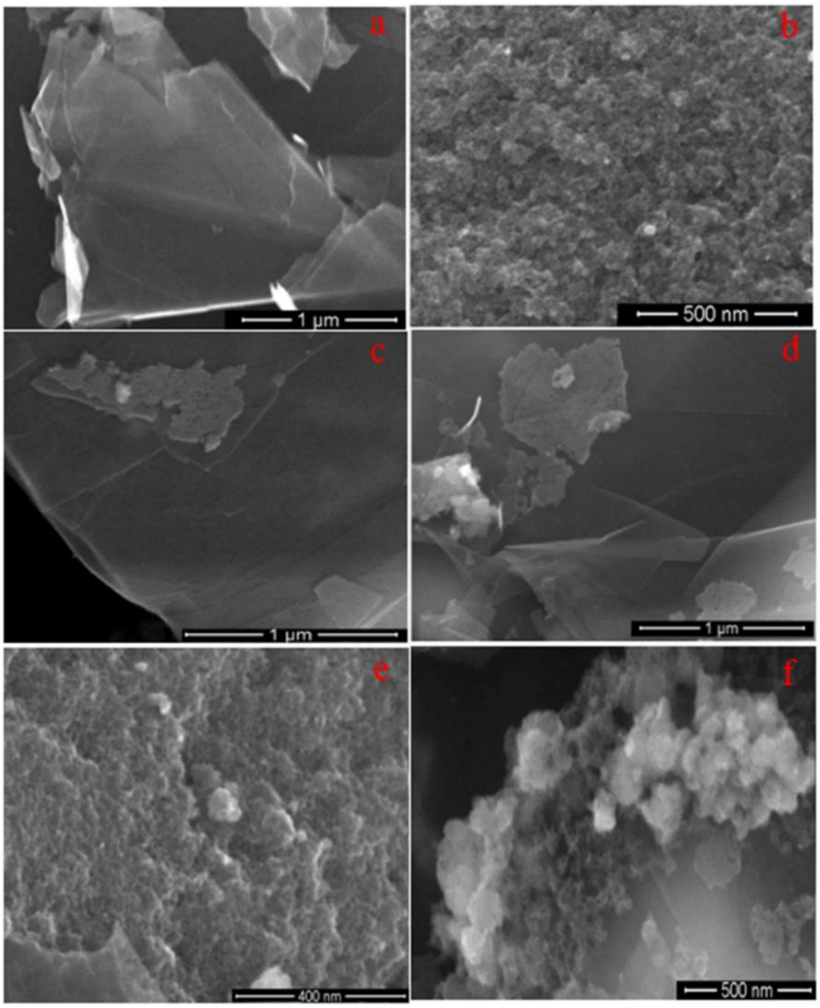

Figure 4.4: FE-SEM images of: (a) pristine graphene sheet, (b) $Ni_3V_2O_8$ nanoparticles, (c) G-NVO, (d) G-2NVO, (e) G-4NVO and (f) G-8NVO nanocomposites.

Both the graphene sheet (Figure 4.4a) and distinct $Ni_3V_2O_8$ nanoparticles (Figure 4.4b) could be observed in Figures 4.4 (c to f), suggesting that fine $Ni_3V_2O_8$ nanoparticles were successfully anchored on the surface of the graphene sheet. Here, the graphene sheet served as a substrate while the $Ni_3V_2O_8$ nanoparticles embedded on graphene sheet act as spacer which hinder the restacking of the graphene sheets[41, 189]. Besides, the presence of graphene augmented the electrical conductivity of the graphene/$Ni_3V_2O_8$ nanocomposites and shortened the electrolyte ion diffusion pathway, which led to a fast surface reversible reaction[41].

The respective sheetlike and nanoparticle structural characteristics of graphene and $Ni_3V_2O_8$ were perfectly preserved in the nanocomposite, revealing the robust structure of the graphene/$Ni_3V_2O_8$ nanocomposite[6, 189]. Other than that, it can be perceived from Figures 4.4 (c to d) that the surface decoration for samples G-NVO and G-2NVO was not uniform, whereas for G-4NVO (Figure 4.4e), the $Ni_3V_2O_8$ nanoparticles were fully embedded on the surface of the graphene sheet. The morphological disparity was due to the variation in mass loading of the $Ni_3V_2O_8$ precursors. When the weight ratio of graphene to $Ni_3V_2O_8$ precursors were 1:1 and 1:2 in samples G-NVO and G-2NVO respectively, the quantity of nanoparticles was inadequate to cover the whole graphene sheet. As the weight ratio was increased to 1:4 (G-4NVO), appreciable amounts of precursors were available and sufficient for perfect surface coverage of the whole graphene sheet. Nonetheless, agglomerations of nanoparticles could be observed in Figure 4.4f when the weight ratio was increased further to 1:8 in sample G-8NVO. All the SEM results obtained were in accordance with the findings reported in the literatures[24, 279].

Besides, the morphology of the graphene/$Ni_3V_2O_8$ nanocomposite (G-4NVO) was further examined by TEM and high resolution TEM (HRTEM) and the results are revealed in Figure 4.5.

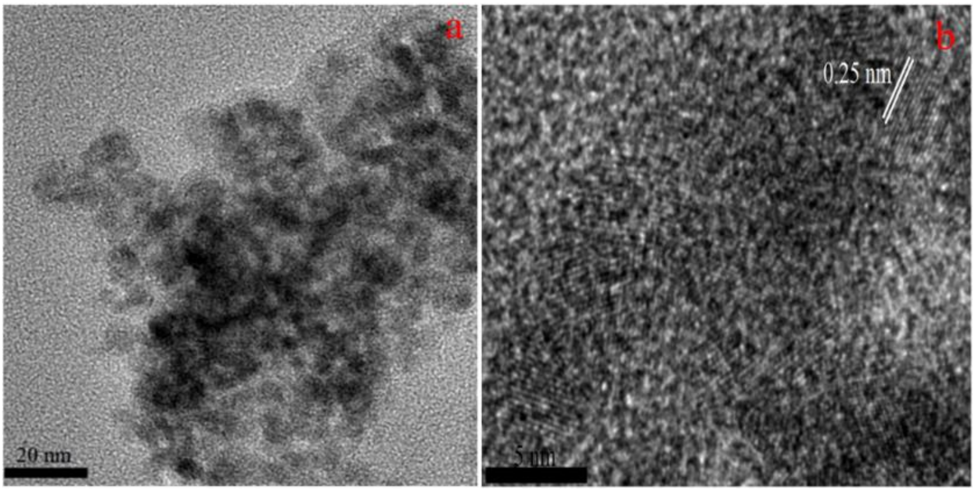

Figure 4.5: (a) TEM, (b) HRTEM images of graphene/$Ni_3V_2O_8$ nanocomposite (G-4NVO).

As delineated in Figure 4.5a, $Ni_3V_2O_8$ nanoparticles were homogeneously dispersed and well decorated on the surface of the graphene sheet. This nanostructure can shorten the electrons and ion diffusion pathway, accommodate the volume variation upon the continuous charge-discharge process and provide adequate electroactive sites between the electrode and electrolyte, leading to advanced electrochemical performance[18]. Moreover, the clear lattice fringes with interplanar spacing of 0.25 nm was noticed from Figure 4.5b, which corresponds to the (122) plane of orthorhombic nickel vanadate and this is consistent with the XRD results[32, 197]. The random orientation of lattice fringes in Figure 4.5b confirmed the poly-crystalline nature of the as-synthesised graphene/$Ni_3V_2O_8$ nanocomposite (G-4NVO).

The energy dispersive spectroscopy (EDS) spectrum of G-4NVO is demonstrated in Figure 4.6, where the microanalysis validated that merely Ni, V, O, C elements were presented in the as-prepared graphene/$Ni_3V_2O_8$ nanocomposite and this is in accordance with the XRD test.

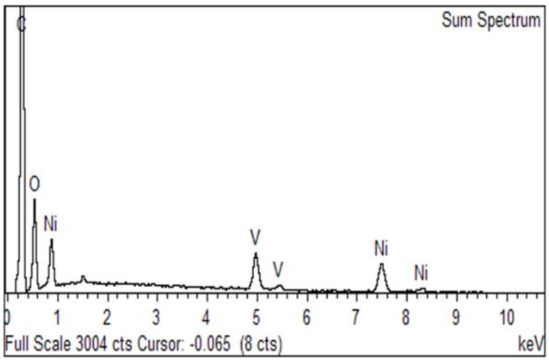

Figure 4.6: EDS spectrum of graphene/$Ni_3V_2O_8$ nanocomposite (G-4NVO).

Table 4.2: Atomic ratio of C, O, Ni, V elements in G-4NVO nanocomposite.

Element	**Weight(%)**	**Atomic(%)**
C	80.47	87.45
O	13.71	11.19
V	2.10	0.54
Ni	3.71	0.83
Totals	100	

Besides, the atomic ratio of Ni:V was approximately 1.54:1 as unveiled in Table 4.2, which corresponds to the stoichiometric ratio of $Ni_3V_2O_8$. No other peaks were observed in Figure 4.6, further confirming the formation of high purity graphene/$Ni_3V_2O_8$ nanohybrid. The element mapping analysis of Ni, V, O, C from G-4NVO nanocomposite was depicted in Figures 4.7, which proved the even distribution of $Ni_3V_2O_8$ nanoparticles on the surface of graphene sheet and this result is congruent with the SEM analysis (Figure 4.4e).

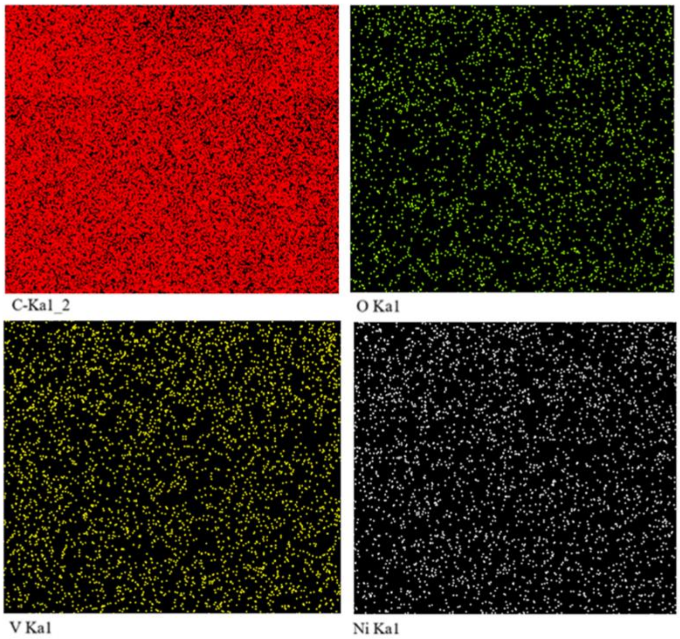

Figure 4.7: C, O, V and Ni elemental mapping analysis of G-4NVO nanocomposite.

4.3.2 Electrochemical Performance

In order to evaluate the energy storage ability of the nanocomposites, the as-fabricated electrodes were analysed using CV, galvanostatic charge-discharge and EIS measurements in 2M KOH electrolyte. Figure 4.8a delineates the cyclic voltammetry profiles of NVO, G-NVO, G-2NVO, G-4NVO and G-8NVO nanocomposite electrodes at a scan rate of 50 mVs^{-1} and potential ranging from -1 to 1 V.

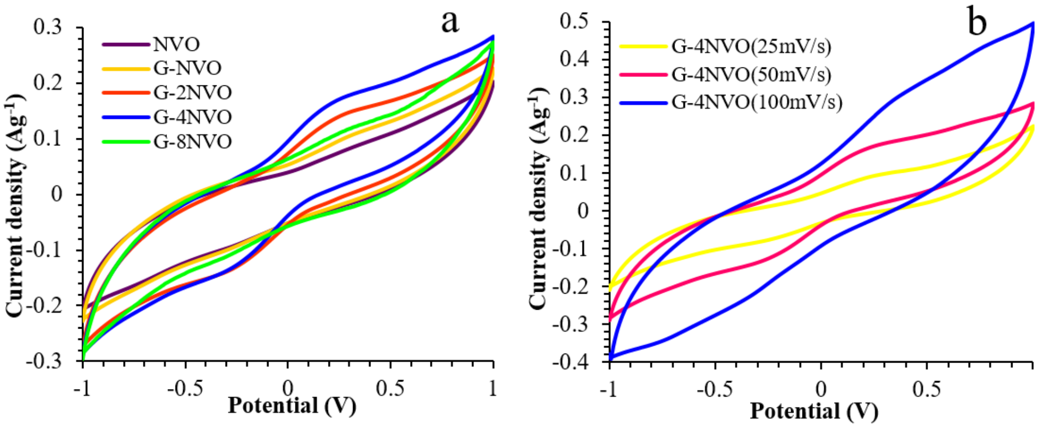

Figure 4.8: Cyclic voltammograms curves of (a) $Ni_3V_2O_8$, G-NVO, G-2NVO, G-4NVO and G-8NVO nanocomposites b) G-4NVO at different scan rates (25, 50, 100 mVs^{-1}).

Here, the principal objective of employing the positive and negative potential bias mode is to demonstrate the symmetrical nature of the electrodes in the two electrode system[197]. It is remarkable that the CV curves of the graphene/$Ni_3V_2O_8$ nanocomposites exhibited a pair of redox peaks, signifying the pseudocapacitive nature of the electrode materials, which is further substantiated by the non-ideal rectangular shape[42, 297]. The anodic and cathodic peaks were found to be located at 0.3 and -0.3 V respectively (Figure 4.8a), which could be ascribed to the reversible reaction of Ni^{2+}/Ni^{3+} and mediation of the hydroxide ion (OH^-) in the alkaline electrolyte[32, 298]. The pertinent Faradaic redox reaction is expressed as follows:

$$Ni^{2+} \leftrightarrow Ni^{3+} + \bar{e} \qquad (4.2)$$

However, the redox peaks were not prominent in the CV profile of pristine $Ni_3V_2O_8$ (NVO). Therefore, it can be speculated that the incorporation of graphene into $Ni_3V_2O_8$ will promote the fast electron diffusion and hence contribute to the strong redox feature of Ni^{2+}/Ni^{3+}[25, 299]. Besides, the as-prepared graphene/$Ni_3V_2O_8$ based electrodes revealed larger integrated area and specific current as compared to the sole $Ni_3V_2O_8$, leading to the augmented capacitive performance. This can be ascribed to the synergistic effects between the double layer capacitance and pseudocapacitance of the nanocomposites[24, 300], where graphene not only provides enormous surface area, improves the electrical conductivity and structural tenacity of the nanocomposite, but also ensures the effective redox reactions at the electrode-electrolyte interface[33]. Additionally, unambiguous difference in the integrated area between the graphene/ $Ni_3V_2O_8$ nanocomposites can be observed (G-4NVO>G-2NVO>G-8NVO>G-NVO>NVO), suggesting that the specific capacitance of the electrode was significantly influenced by the amount of $Ni_3V_2O_8$ anchored on the graphene sheet. Moreover, homogenous distribution of $Ni_3V_2O_8$ nanoparticles on the surface of graphene sheet in G-4NVO ensured fully utilisation of nickel vanadate in the redox reaction and hence ameliorated the charge storage performance[18].

Figure 4.8b manifests the cyclic voltammograms of G-4NVO at different scan rates (25, 50, 100 mVs^{-1}). The variation in the shape of CV curves was not noticeable, implying the high electrochemical reactivity of the active material[301]. Other than that, the increased in the peak current with the scan rate indicated the rapid kinetics of interfacial Faradaic redox reaction and fast electrons and ions transportation [189, 302]. Furthermore, the anodic and cathodic peaks shifted towards positive and negative manner, respectively as the scan rate increased. This is mainly attributed to the reversible reaction and the enhanced electrical polarisation, where the limited ion diffusion during the reaction leads to unsatisfactory electronic neutralisation [33, 303].

To further investigate the electrochemical performance of the electrode materials, the galvanostatic charge-discharge (GCD) measurement was performed at a constant current density of 0.5 Ag^{-1} and a potential window of 0 to 1 V. The results are depicted in Figure 4.9a.

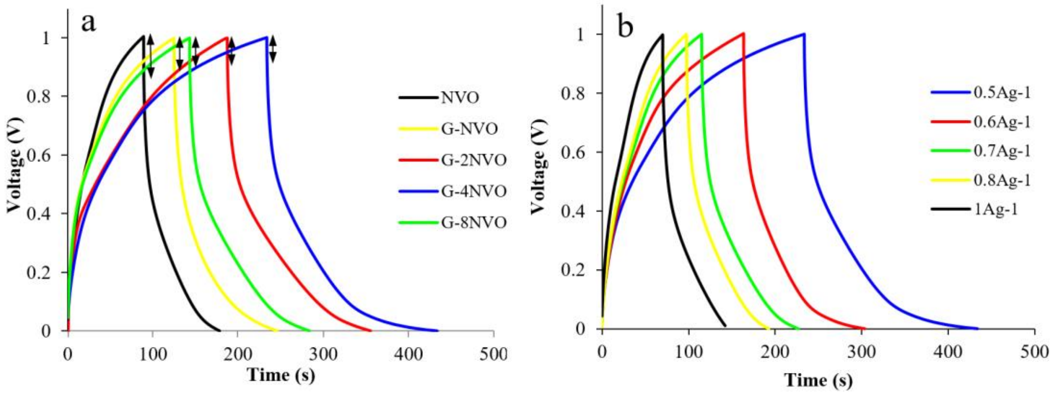

Figure 4.9: Charge-discharge curve of (a) $Ni_3V_2O_8$, G-NVO, G-2NVO, G-4NVO and G-8NVO nanocomposites. b) G-4NVO at different current densities.

Here, non-linearity of charge-discharge profiles were observed, which originated from the pseudocapacitive nature of $Ni_3V_2O_8$ with the occurrence of Faradaic redox reactions at the electrode/electrolyte interface[25, 304, 305], and this is in accordance with the CV results. Besides, the charge-discharge curves of the electrode materials were nearly symmetrical, revealing its superior electrochemical reversibility[284]. Nevertheless, the internal resistance drop (IR drop) appeared in the CD curves of all electrode materials, which could be attributed to the current of bulk electrode[18]. From Figure 4.9a, G-4NVO demonstrated the longest discharge time among all the samples, implying its eminent charge storage capability since the longer the discharge time, the higher the specific capacitance. The specific capacitances of all the electrode materials were calculated from the gradient of the CD curves by using equation 3.1[298, 306, 307].

The calculated specific capacitances of $Ni_3V_2O_8$, G-NVO, G-2NVO, G-4NVO and G-8NVO nanocomposites were 188, 236, 322, 368 and 276 Fg^{-1} respectively at a current density of 0.5 Ag^{-1}. It is interesting to note that the specific capacitance increased as the mass loading of $Ni_3V_2O_8$ precursors was increased to 1:4, whereas further increased beyond 1:4 resulted in the declined specific capacitance owing to the occurrence of agglomeration, which is substantiated by the SEM result. The capacitive performance of the electrode is comparable to those reported in literatures[29, 285].

Figure 4.9b delineates the charge-discharge curves of G-4NVO nanocomposite at current densities of 0.5, 0.6, 0.7, 0.8, 1.0 Ag^{-1} and a potential window of 0 to 1 V. Likewise, all the charge -discharge curves were nearly symmetrical at different current densities, suggesting the superior reversibility of the electrode material. Moreover, the specific capacitances of G-4NVO at different current densities were calculated from the slope of the GCD curves (Figure 4.9b) using equation 3.1 and the results are depicted in Figure 4.10.

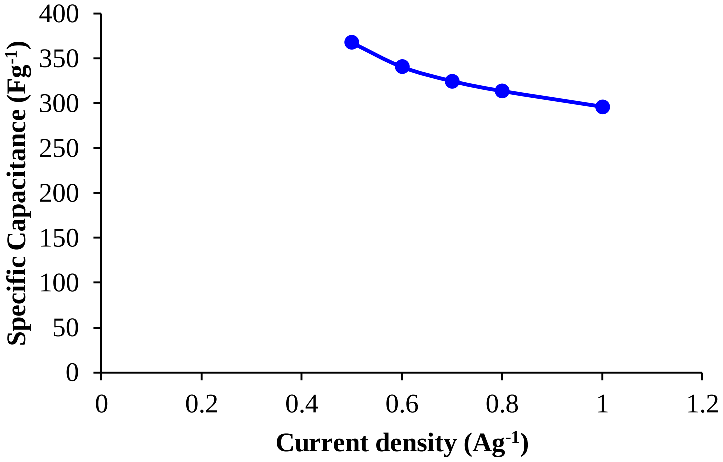

Figure 4.10: Specific capacitance (Fg^{-1}) of G-4NVO at different current densities.

Based on Figure 4.10, the specific capacitance of G-4NVO attenuated as the current density increased. This phenomenon could be ascribed to the slow diffusion of electrolyte ions (OH^-) through the electrode and insufficient time for complete electrochemical reaction at high current density. This led to limited active sites available for charge storage and thus deteriorated the specific capacitance[18, 25, 298, 308]. The calculated specific capacitances of G-4NVO were 368, 341, 325, 314 and 296 Fg^{-1} at 0.5, 0.6, 0.7, 0.8 and 1 Ag^{-1}, manifesting its good rate capability as an appealing electrode material for supercapacitor.

Furthermore, the cycling stability and coulombic efficiency (η) of the G-4NVO nanocomposite were demonstrated in Figure 4.11.

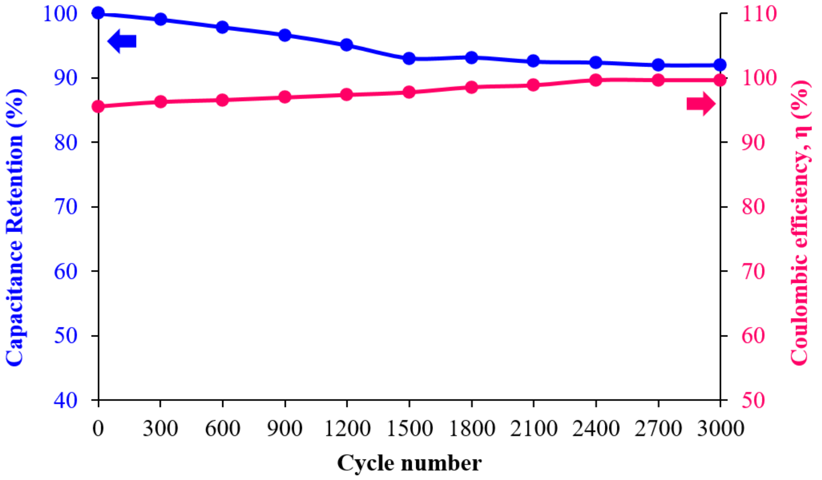

Figure 4.11: Cycling stability test and Coulombic efficiency of G-4NVO nanocomposite up to 3000 cycles.

The long term cycling test of the assembled symmetric hybrid supercapacitor was performed at a current density of 1 Ag^{-1} within a potential window of 0 to 1 V up to 3000 cycles. It can be observed that the specific capacitance decreased gradually in the first 1500 cycles and became stable up to 3000 cycles. This is due to the degradation of the active electrode material and poor interfacial contact between the electrode and the electrolyte upon the charge-discharge process[24, 234, 309, 310]. Eventually, 92 % of initial specific capacitance was retained after 3000 cycles, delineating the excellent cycling stability of G-4NVO nanocomposite. This could be assigned to its peculiar nanostructure where the incorporation of graphene not only ameliorated the conductivity of the nanocomposite, but also served as a buffering matrix to accommodate the large volume expansion during the continuous charge-discharge process[25, 59].

Furthermore, the coulombic efficiency, η of the G-4NVO electrode material after the cycling test was calculated by using equation 3.2. Based on Figure 4.11, the initial coulombic efficiency of G-4NVO nanocomposite was 95 % and it increased gradually upon cycling. Finally, the coulombic efficiency achieved nearly 100 % after the continuous charge-discharge process (3000 cycles), further signifying the high reversibility of the electrochemical reaction.

Electrochemical Impedance Spectroscopy analysis (Nyquist plot) was performed to study the interfacial behaviour of the supercapacitor and to determine the parameter influencing the performance of an active electrode material[18, 25]. The Nyquist plot of pristine $Ni_3V_2O_8$ and graphene/$Ni_3V_2O_8$ nanocomposites was illustrated in Figure 4.12.

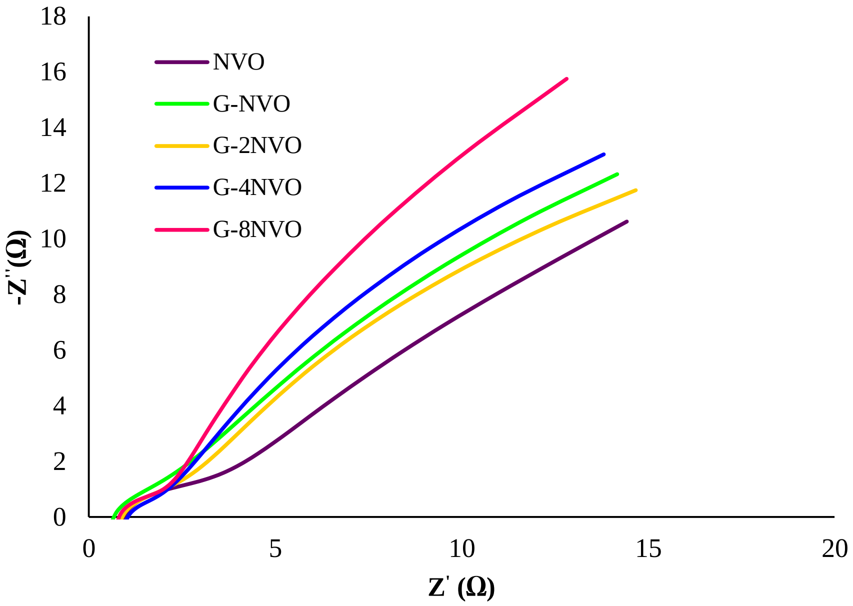

Figure 4.12: Nyquist plot of pristine $Ni_3V_2O_8$, G-NVO, G-2NVO, G-4NVO and G-8NVO nanocomposites.

The Nyquist plot can be divided into two regions: a semicircle in the high frequency region and a linear line in the low frequency region. The radius of the semicircle represents the charge-transfer resistance (R_{ct}) which is resulted from the Faradaic redox reaction of electrode material and the double layer capacitance on the interface between electrode and electrolyte. Meanwhile, the linear line in the low frequency region denotes the Warburg Impedance (W), which gives an insight into the kinetics of ion diffusion process. Besides, the x-intercept in the Nyquist plot is the solution resistance, which combines the ionic resistance of the electrolyte, intrinsic resistance of electrode material and contact resistance at the electrode/electrolyte interface[244, 311]. As unveiled in Figure 4.12, the Nyquist plot of pristine $Ni_3V_2O_8$ and graphene/$Ni_3V_2O_8$ nanocomposites based electrodes demonstrated a semicircle region and a linear line. The R_{ct} values calculated from the semicircle were found to be 3.640, 3.407, 2.801, 2.634 and 2.948 Ω for sole $Ni_3V_2O_8$, G-NVO, G-2NVO, G-4NVO and G-8NVO, respectively. It is noticeable that G-4NVO had the lowest charge transfer resistance as compared to pure $Ni_3V_2O_8$ (NVO) and other graphene/$Ni_3V_2O_8$ nanocomposites. The lower R_{ct} values were mainly attributed to the presence of graphene, which improved the electrical conductivity of the graphene/$Ni_3V_2O_8$ nanocomposites and these results are congruent with the CV and GCD analysis[18]. Moreover, the straight line of graphene/$Ni_3V_2O_8$ nanocomposites in the low frequency region were more vertical than the pure $Ni_3V_2O_8$, implying that the integration of graphene allowed the effective accessibility of the OH^- ions to the surface or in the bulk of the electrode material and shortened the ions and electrons migration pathway[18].

To further evaluate the electrochemical performance of graphene/$Ni_3V_2O_8$ nanocomposites, a Ragone plot of energy and power densities was demonstrated in Figure 4.13. The energy and power densities were calculated from the CD curves at 0.5 Ag^{-1} using equations 3.3 and 3.4[25].

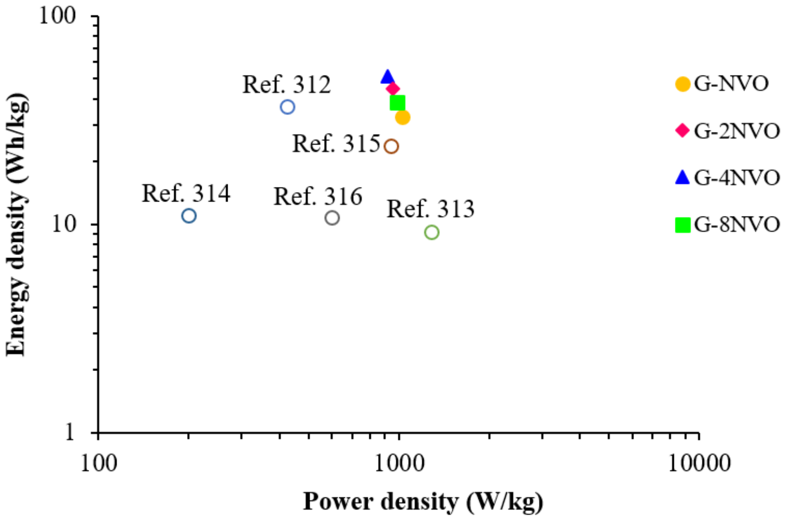

Figure 4.13: Ragone plot (Comparison of G-4NVO nanocomposite with other selected electrode materials).

Generally, a promising supercapacitor should have high energy and power densities at high charge-discharge rate[25]. Impressively, G-4NVO electrode possessed an energy density of 51 Wh/kg at a power density of 920 W/kg, which outperformed other graphene/$Ni_3V_2O_8$ electrodes and multifarious reported metal oxides[312-316].

In short, the excellent electrochemical performance of the as-prepared electrode could be ascribed to the following factors: i) The uniform distribution of $Ni_3V_2O_8$ nanoparticles on graphene could effectively impede the restacking of graphene sheet, which ensured fully utilisation of the electroactive component ($Ni_3V_2O_8$) and provided abundant electroactive sites for interaction with OH^- ions[80]. ii) The intimate contact between the graphene sheet and $Ni_3V_2O_8$ nanoparticles improved the electrical conductivity of the nanocomposites and hence resulted in rapid electron transfer and high specific capacitance[25, 38]. iii) The exfoliated structure of graphene sheet synthesised by the facile and green approach could be well preserved, which in turn contributed to the advanced electrochemical performance[24]. iv) Integration of graphene sheet with $Ni_3V_2O_8$ nanoparticles enlarged the specific surface area of the nanocomposites and curtailed the electrons and ions migration pathway[242]. v) The synergistic effect between the $Ni_3V_2O_8$ nanoparticles and graphene sheet ameliorated the stability and durability of the nanocomposites for electrochemical applications since the presence of graphene can accommodate the volume variation during the continuous charge discharge process[41].

4.4 Summary

In summary, pristine $Ni_3V_2O_8$ and graphene/$Ni_3V_2O_8$ nanocomposites have been successfully synthesised through a facile and green solvothermal technique, followed by a calcination process. The experimental results revealed that the structural and electrochemical properties varied significantly with the weight ratio of graphene to $Ni_3V_2O_8$. When the graphene to $Ni_3V_2O_8$ ratio was 1:4 (G-4NVO), $Ni_3V_2O_8$ nanoparticles were evenly decorated on the graphene sheet, contributing to barrier free contact and enhanced electrochemical performance. Besides, the G-4NVO electrode material manifested the highest specific capacitance of 368 Fg^{-1} at a current density of 0.5 Ag^{-1} among all the nanocomposites. Moreover, G-4NVO possessed excellent cycling stability with 92 % capacitance retention and coulombic efficiency of nearly 100 % after 3000 charge-discharge cycles at 1 Ag^{-1}. The eminent electrochemical performance of graphene/$Ni_3V_2O_8$ nanocomposite suggests it as a promising electrode material for supercapacitors and other energy storage devices.

Chapter 5: A facile synthesis of graphene/$Co_3V_2O_8$ nanocomposites and their enhanced charge storage performance in electrochemical capacitors

5.1 Introduction

Mixed transition metal oxides (MTMO) like metal molybdate, metal cobaltite, metal tungstate, metal vanadate and etcetera have been developed as the Faradaic electrode since their diverse oxidation states allow reversible redox reaction. Cobalt vanadate is recognised as one of the potential electroactive materials due to its low toxicity, cost-effectiveness and remarkable charge storage activity as a result of the integration of Co_2O_3 (significant contribution to specific capacitance) and multiple polymorphism of V_2O_5[252, 317]. So far, limited studies have been attempted to configure it into an active electrode material for supercapacitors. As an example, Liu and his co-workers[6] synthesised the $Co_3V_2O_8$ nanoparticles via the hydrothermal approach which delivered a value of 505 Fg^{-1} (three electrode system) specific capacitance at 0.625 Ag^{-1}. In addition, $Co_3V_2O_8$ 3D porous nanoroses were fabricated by Zhang et.al[190] through the solvothermal method. The 3D porous nanoroses displayed a specific capacitance of 371.3 Fg^{-1} when the electrode is analysed under a current density of 0.5 Ag^{-1} in three electrode configuration. However, $Co_3V_2O_8$ suffers from low specific capacitance, short shelf life and inferior rate capability due to the serious volume variation during cycling analysis, which hinders its practical application[42, 318]. As a result, integration of $Co_3V_2O_8$ with carbonaceous material appears as one of the promising solutions to rectify this conundrum in which the electrical conductivity of the nanohybrid could be significantly improved.

Particularly, graphene is a potential matrix for the deposition of MTMO owing to its inimitable properties which comprise good electrochemical stability, huge specific surface area, high structural tenacity, excellent electrical conductivity and superior mechanical properties[318-320]. Nevertheless, the restacking or aggregation of pure graphene sheet unavoidably enhances the ion diffusion resistances which contributes to the poor capacitive performance. In this context, integration of graphene with MTMO is perceived as a promising solution to this problem, for instance, the MTMO serves as a spacer which can inhibit the aggregation of the graphene sheet.

Based on the above considerations, this chapter presents the graphene/$Co_3V_2O_8$ micro-pencils nanocomposites produced by using solvothermal method and then was utilised as the main active electrode material for symmetric supercapacitor. To the extent of our knowledge, this is the first work reported the utilisation of graphene/$Co_3V_2O_8$ nanohybrid as an electrode material for advanced supercapacitor system. Furthermore, the inference of mass loading of $Co_3V_2O_8$ on the electrochemical performance of nanocomposite was investigated by preparing different mass ratios of graphene/$Co_3V_2O_8$ nanomaterials.

5.2 Experimental section

5.2.1 Fabrication of graphene/$Co_3V_2O_8$ micro-pencils nanocomposites

To fabricate the graphene/$Co_3V_2O_8$ nanocomposites, solvothermal technique was applied and the entire procedure is delineated in Figure 5.1.

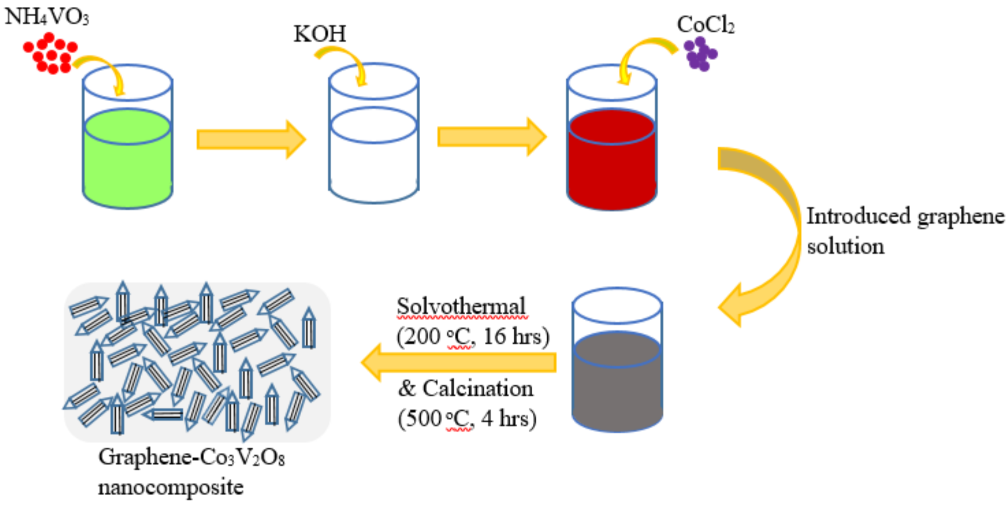

Figure 5.1: Formation process of graphene/$Co_3V_2O_8$ micro-pencils nanocomposites.

Firstly, NH_4VO_3 (0.02 mol) was dissolved into a 170 mL deionised water at 80 °C under vigorous stirring to obtain a transparent light green colour solution. Then, a reddish brown solution was obtained after mixing LiOH (0.02mol) and $CoCl_2.6H_2O$ (0.004 mol) with the solution. In the next step, the graphene suspension was slowly added to the aforementioned mixed solution and kept agitating for half an hour to reach homogeneity. The resulting mixture was then transferred into a 200 ml Teflon-lined stainless steel autoclave and heated at 200 °C for 16 hours. After that, the as-synthesised precipitates were collected, cleaned thoroughly with ethanol-water solution, dried at 80 °C in the hot air oven for 6 hours and annealed at 500 °C for 4 hours to obtain the graphene/$Co_3V_2O_8$ micro-pencils nanomaterial. Pure $Co_3V_2O_8$ was fabricated in the same experimental pathway without graphene. For comparison, variation in quantity of graphene in the nanocomposites was conducted to investigate the impact of mass ratio on the structural and energy storage capability of the nanocomposites. The detailed graphene/$Co_3V_2O_8$ nanocomposite formulation was manifested in Table 5.1.

Table 5.1: Mass ratio of graphene/$Co_3V_2O_8$ micro-pencils nanocomposites.

Sample Code	**Mass of graphene (g)**	**Mass of $Co_3V_2O_8$ (g)**	**Graphene:$Co_3V_2O_8$ (Mass ratio)**
G-CVO	0.350	0.350	1:1
G-2CVO	0.175	0.350	1:2
G-4CVO	0.090	0.350	1:4
G-6CVO	0.060	0.350	1:6

5.3 Results and discussion

5.3.1 Phase and Morphological Study

In order to provide an insight on the crystallographic data and phase composition of the as-prepared samples, XRD analysis was performed. Figure 5.2 demonstrates the XRD spectra of graphene, $Co_3V_2O_8$ micro-pencils and graphene/$Co_3V_2O_8$ nanohybrids.

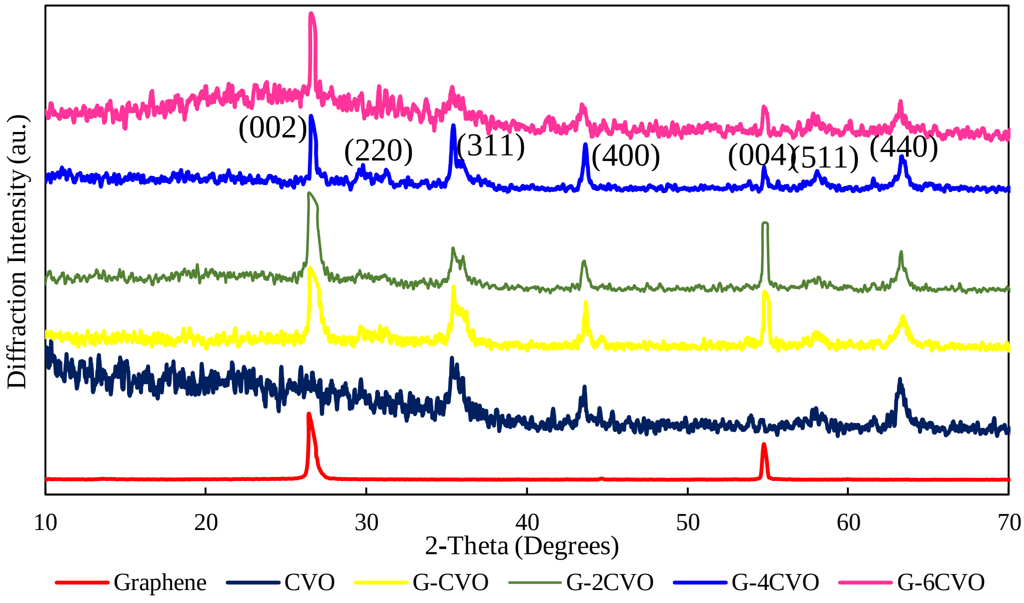

Figure 5.2: XRD patterns of graphene, $Co_3V_2O_8$ micro-pencils and graphene/$Co_3V_2O_8$ nanocomposites, (b) Raman spectra of the graphene and G-4CVO nanocomposite.

The graphene nanosheet exhibited two broad peaks at 26.8^o and 54.9^o, which correspond to the (002) and (004) crystal planes of graphene and this is in accordance with our previous reports[28, 263]. From the diffraction spectrum of graphene/$Co_3V_2O_8$ nanocomposites, the distinctive peaks (except two typical peaks originated from graphene) of the cubic crystal structure of $Co_3V_2O_8$ (JCPDS No. 16-0675) were located at 30.0^o, 35.6^o, 43.7^o, 57.8^o and 63.2^o, where these peaks could be assigned to the (220), (311), (400), (511) and (440) reflection planes, respectively[262, 321]. In addition, the samples are highly crystalline as indicated by the sharp diffraction peaks, reflecting its stable crystallographic structures. The highly stable structures might enhance the electrochemical stability by alleviating the volume variation during the continuous intercalation-deintercalation process[322]. These results reveal the graphene/$Co_3V_2O_8$ hybrid nanomaterials comprised of cubic $Co_3V_2O_8$ micro-pencils and graphene nanosheets were successfully synthesised.

Raman spectroscopy has also been applied to determine the degree of graphitisation and bonding modalities between the elements of pristine graphene and G-4CVO nanomaterial (Figure 5.3).

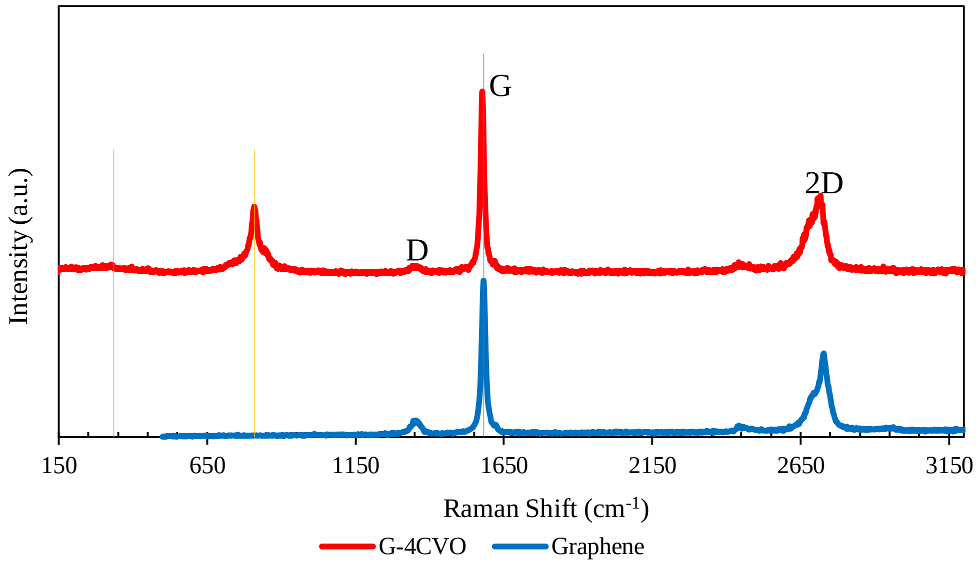

Figure 5.3: Raman spectra of the graphene and G-4CVO nanocomposite.

From the Raman analysis of G-4CVO, the prominent bands of graphene, namely D, G and 2D bands are located at 1360, 1582 and 2726 cm^{-1}, respectively. The G band corresponds to the in-plane bond stretching motion of C sp^2 atoms, while D and 2D bands represent the disorder or defective graphitic structure[250, 322]. Besides, two peaks at around 335 and 810 cm^{-1} are observed, which can be correlated to the Raman spectra of $Co_3V_2O_8$[323]. The bands at 335 cm^{-1} and 810 cm^{-1} are correlated with the asymmetric stretching vibration of V-O-Co bonds and symmetric vibration of V-O bonds, respectively[262, 263, 322]. These results further affirm the successful synthesis of graphene/$Co_3V_2O_8$ nanocomposites. In addition, a redshift of G band can be noticed in the Raman spectra of G-4CVO, implying the intimate interaction between graphene and $Co_3V_2O_8$[80].

In order to determine the surface morphological structure of graphene, sole $Co_3V_2O_8$ and graphene/$Co_3V_2O_8$ nanocomposites, FESEM was conducted and the outcomes are portrayed in Figure 5.4.

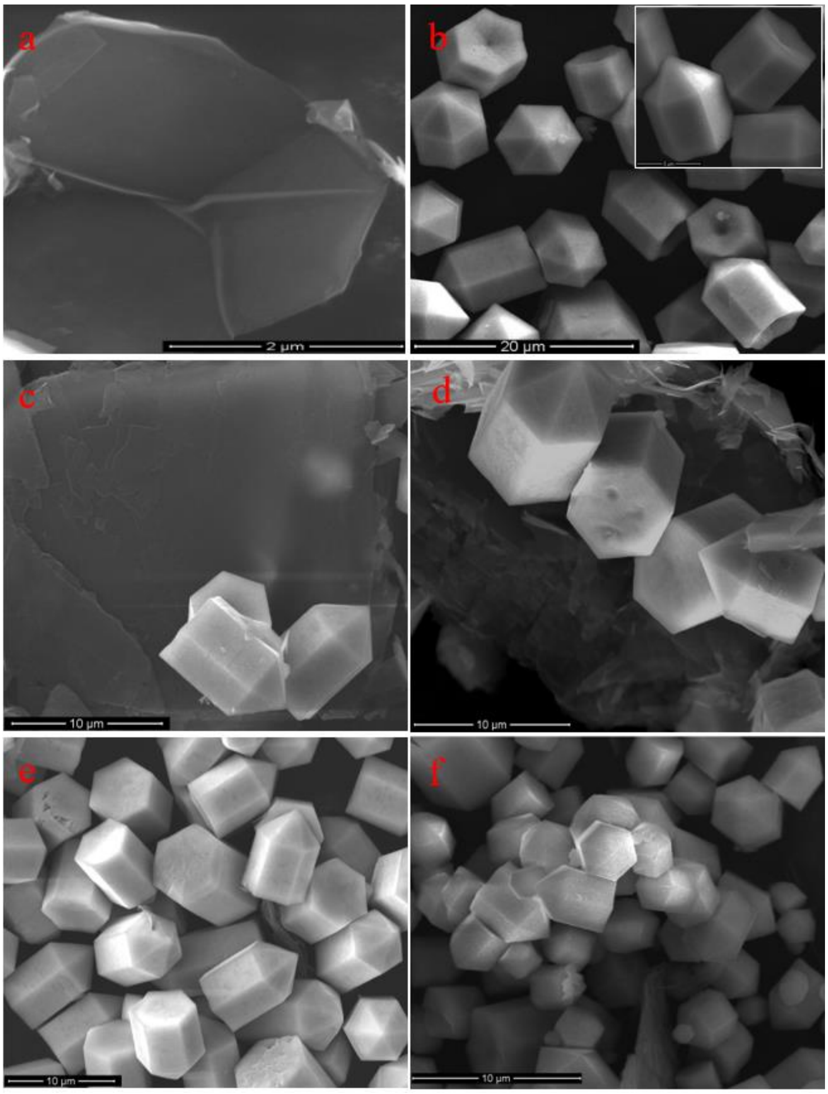

Figure 5.4: FESEM micrographs of (a) graphene, (b) pure $Co_3V_2O_8$ micro-pencils, (c) G-CVO, (d) G-2CVO, (e) G-4CVO and (f) G-6CVO.

From Figure 5.4b, it can be noticed that $Co_3V_2O_8$ possess an exterior geometry of short pencil-like structure with hexagonal prism and these $Co_3V_2O_8$ micro-pencils have a consistent microscale size distribution of approximately 3 µm in length and 5 µm in height[262, 321]. Besides, both the graphene sheet (Figure 5.4a) and 3D skeletal configuration of $Co_3V_2O_8$ micro-pencils (Figure 5.4b) are discernible in Figure 5.4(c to f), implying the successful decoration of $Co_3V_2O_8$ micro-pencils onto the surface of graphene to form hybrid nanocomposites. Such novel nanoarchitectures could effectively sustain the volume variation within the lattice of active materials during the inter/de-intercalation cycles due to their improved structural strength and tenacity[324]. In addition to enlarging the effective surface area of the nanostructure, the graphene nanomaterial also serves as a conductive scaffold to facilitate the ions and charges migration [27, 325]. The morphological disparities of the graphene/$Co_3V_2O_8$ nanocomposites with a variation of mass loadings are indicated in Figure 5.4 (c to f). In contrast to G-CVO and G-2CVO, G-4CVO manifested an evenly distribution of $Co_3V_2O_8$ micro-pencils on the surface of graphene as a result of sufficient quantity of $Co_3V_2O_8$ micro-pencils available to perfectly cover the whole surface of graphene and this configuration is believed to contribute significantly towards the enhancement of electrochemical activity. However, excessive mass loading of precursors in G-6CVO (Figure 5.4f) resulted in structural agglomeration, which inevitably reduce the homogeneity and active sites of the nanocomposite, leading to inferior capacitive performance.

Furthermore, TEM was conducted to further determine the morphology of the G-4CVO (Figure 5.5).

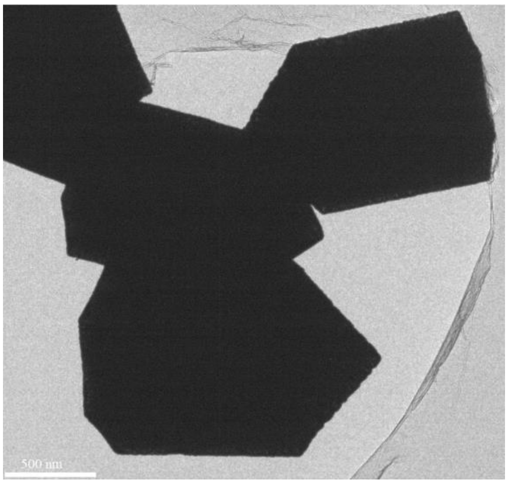

Figure 5.5: TEM image of G-4CVO nanocomposite.

It is noteworthy that graphene sheets do not stack together and high density of $Co_3V_2O_8$ micro-pencils can be observed on the graphene surface, which is congruent with the SEM results (Figure 5.4e). In addition, the EDS analysis of the as-prepared G-4CVO nanocomposite has been conducted and the results are depicted in Figure 5.6a.

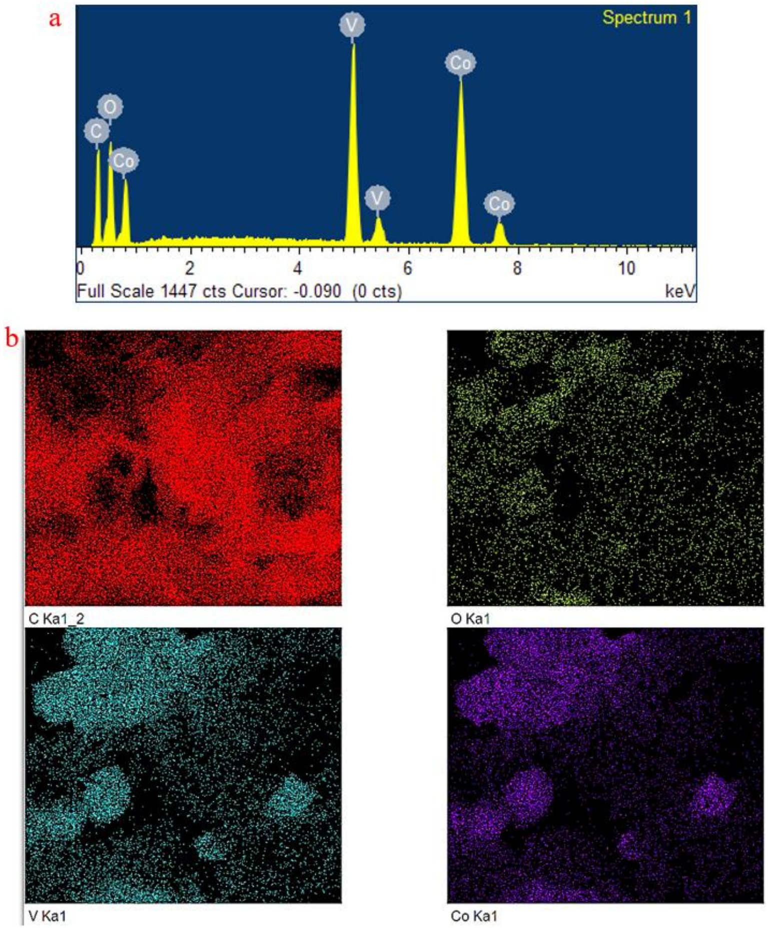

Figure 5.6: (a) EDS of G-4CVO nanocomposite, (b) Elemental mapping analysis of V, Co, O, and C in G-4CVO nanocomposite.

The peaks in the EDS spectrum can be ascribed to the C, Co, V and O elements, validating their contribution in the as-synthesised nanocomposite (G-4CVO). No other peaks were observed in the EDS analysis, further verifying the purity of the nanomaterial. Meanwhile, the EDS mapping analysis of G-4CVO (Figure 5.6b) shows the even scattering of the Co, V, O and C elements, which further advocates the homogenous dispersion of $Co_3V_2O_8$ on the graphene surface.

Table 5.2: Atomic ratios of C, O, V and Co elements in G-4CVO nanocomposite.

Element	**Weight (%)**	**Atomic (%)**
C	24.64	47.64
O	20.27	29.43
V	19.83	9.04
Co	35.25	13.89
Total	100	

The atomic ratio of Co:V in Table 5.2 was approximately 1.54:1, which coincides with the stoichiometric ratio of $Co_3V_2O_8$.

The XPS spectrum of G-4CVO is delineated in Figure 5.7 to give an insight on the chemical composition and the oxidation states of graphene/$Co_3V_2O_8$ sample.

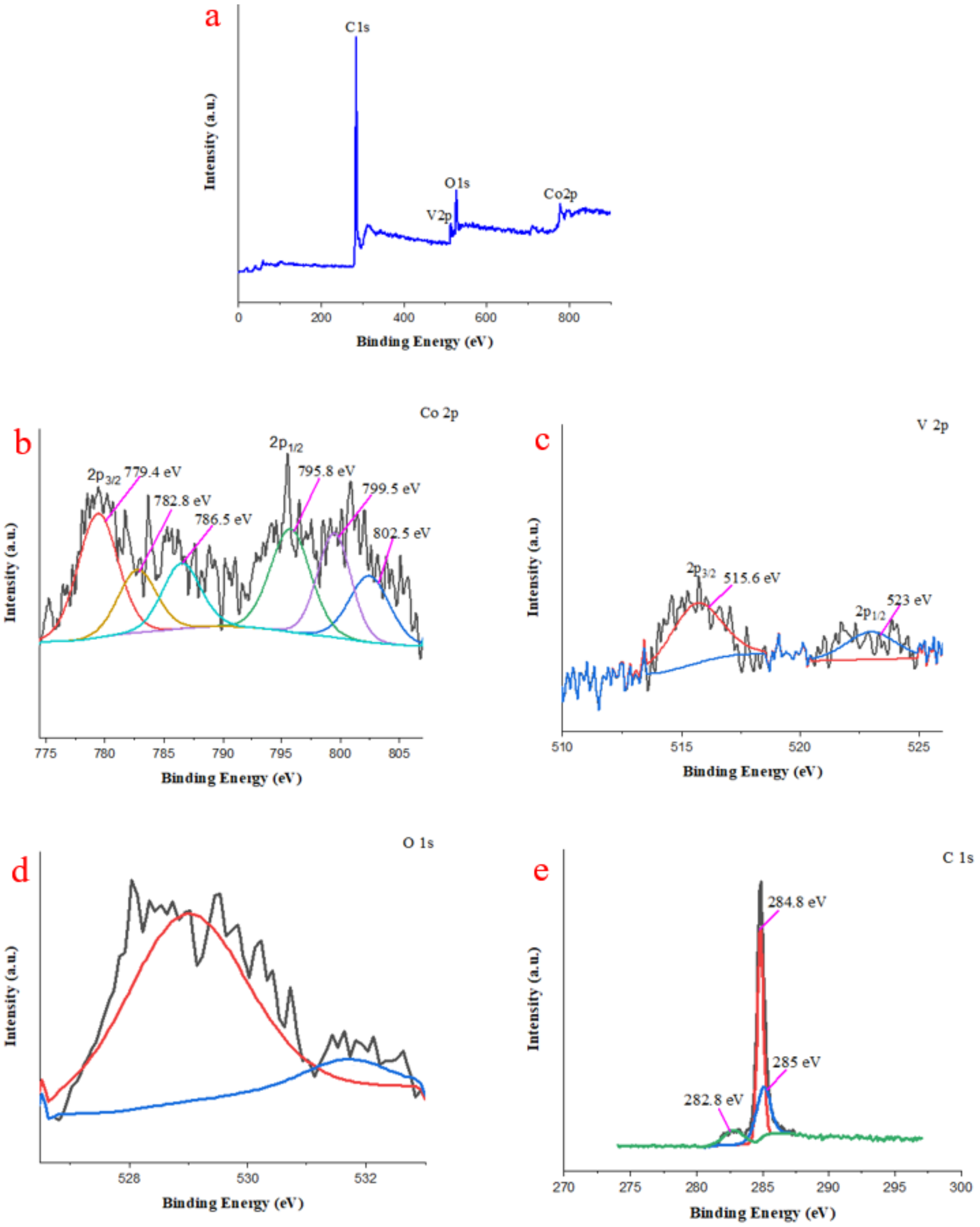

Figure 5.7: XPS spectra of G-4CVO: (a) Full survey spectra, (b) Co 2p, (c) V 2p, (d) O 1s and (e) C 1s.

Four distinctive peaks assigning to the C 1s, O 1s, Co 2p and V 2p are evident from the wide-scan XPS survey spectrum of G-4CVO (Figure 5.7a), testifying the presence of these elements in G-4CVO nanocomposites. From Figure 5.7b, a doublet centred at 780 and 795 eV can be assigned to the spin orbit coupling levels of Co $2p_{3/2}$ and Co $2p_{1/2}$, respectively and accompanied by two prominent satellite peaks at 786.5 and 802.5 eV. Figure 5.7b further confirms the presence of 2 oxidation states of cobalt element: Co^{2+}(779.4 and 795.8 eV) and Co^{3+}(782.8 and 799.5 eV)[25, 192, 262, 326]. As for V element (Figure 5.7c), the peaks at *ca.* 515.6 and 523 eV can be assigned to the V 2p$_{3/2}$ and V 2p$_{1/2}$ of V^{5+} states[190, 262]. Figure 5.7d depicts the O1s orbital spectrum, where the 2 resolved peaks at 529 and 531.7 eV can be described by the metal-oxygen bonds (Co-O and V-O bonding) and the adsorbed oxygen, respectively[25, 185, 186, 265]. In addition, the high resolution C 1s spectrum (Figure 5.7e) can be de-convoluted into 3 fittings peaks: 284.8, 285 eV (C=C/C-C carbon species) and 282.8 eV (carbidic Co-C bonds) [25, 327, 328].

5.3.2 Electrochemical measurement

The charge storage performances of the nanocomposites were assessed by performing the cyclic voltammetry analysis (CV), galvanostatic charge-discharge (GCD) and electrochemical impedance spectroscopy (EIS) tests. The CV curves of the pristine $Co_3V_2O_8$ and graphene/$Co_3V_2O_8$ nanocomposites in the potential ranging from -1 to 1V with the scanning rate of 5 mVs^{-1} are delineated in Figure 5.8a.

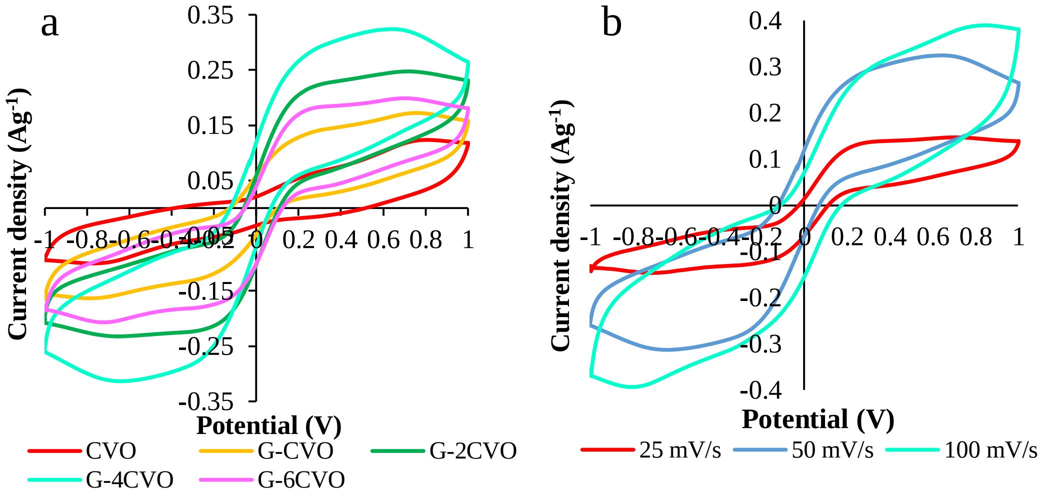

Figure 5.8: CV analysis of (a) pure $Co_3V_2O_8$, G-CVO, G-2CVO, G-4CVO and G-6CVO nanocomposites at scan rate of 50 mVs^{-1}. (b) G-4CVO at scan rates of 25, 50 and 100 mVs^{-1}.

It is worth noting that two pairs of didymous anodic and cathodic peaks are visible in each voltammogram, implying the electrode materials are strongly pseudocapacitive in nature[34, 190]. Notably, the redox reactions of Co^{2+}/Co^{3+} with the OH^- ions is reversible and hence contributed to these didymous redox peaks and its corresponding Faradaic electrochemical reactions are described in Equations (5.1) to (5.4)[34, 329]:

$$Co^{2+} \leftrightarrow Co^{3+} + e^- \tag{5.1}$$

$$Co^{2+} + 2OH^- \rightarrow Co(OH)_2 \tag{5.2}$$

$$Co(OH)_2 + OH^- \leftrightarrow CoOOH + H_2O + e^- \tag{5.3}$$

$$CoOOH + OH^- \leftrightarrow CoO_2 + H_2O + e^- \tag{5.4}$$

Besides, the curves of the anode and cathode are almost symmetrical, reflecting its superior reversibility and close-to-ideal capacitive behaviour. The enhanced charge storage ability of the graphene/$Co_3V_2O_8$ nanocomposites is reflected by their larger integrated area of the CV loop as compared to that of the pure $Co_3V_2O_8$ electrode. This can be elucidated by the positive interaction between graphene and $Co_3V_2O_8$ micro-pencils which resulted in rapid ions and electrons transportation[326]. Moreover, the presence of graphene provides an abundant exposed surface area for ions adsorption, leading to effective Faradaic redox reaction[330, 331]. From Figure 5.8a, the integrated area under of the CV curves of nanocomposites was ranked in the following order: G-4CVO>G-2CVO>G-6CVO>G-CVO, suggesting that the amount of $Co_3V_2O_8$ anchoring on the surface of graphene nanomaterial has a substantial effect on the capacitive performance of the electrode material [265].

Figure 5.8b manifests the CV curves of G-4CVO obtained at various scan rates (25, 50 and 100 mVs^{-1}). The outstanding rate capability and rapid electrochemical response of G-4CVO was indicated by the unaltered CV curves at a wide range of potential sweep rates[332, 333]. Additionally, the increased peak current at higher scan rate indicates a steerable ion transportation process with rapid interfacial kinetics[34, 326]. It is noticeable from Figure 5.8b that the increment in the scan rate resulted in the shifting of redox peaks. For instance, the anodic peak is shifted to a more positive direction while the cathodic peak moved to more negative potential. This phenomenon can be ascribed to the limited ions diffusion to attain electronic neutralisation during the reversible reaction at high scan rate[334].

In addition, the charge storage abilities of the as-prepared electrode materials were accessed by conducting galvanostatic charge-discharge analysis (GCD). Figure 5.9a illustrates the galvanostatic charge-discharge profiles of the nanocomposites obtained at the following conditions: working potential is ranging from 0 to 1 V at 0.8 Ag^{-1}.

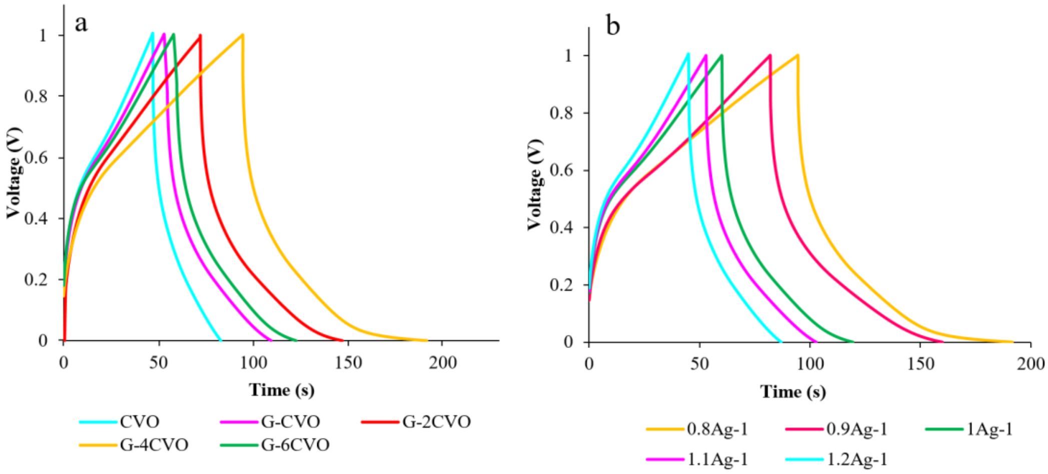

Figure 5.9: GCD profiles of (a) pristine $Co_3V_2O_8$, G-CVO, G-2CVO, G-4CVO and G-6CVO nanocomposites at 0.8 Ag^{-1}, (b) G-4CVO at 0.8, 0.9, 1, 1.1 and 1.2 Ag^{-1}.

From Figure 5.9a, the good capacitive activity and excellent reversibility of the electrode materials can be advocated by the nearly symmetrical charge-discharge curves[326]. The non-linearity of these curves could be attributed to the pseudocapacitive nature of $Co_3V_2O_8$ micro-pencils and the occurrence of Faradaic redox reactions, which tally with the CV profiles[263]. It is noteworthy that G-4CVO possessed the longest discharge time as compared to pure $Co_3V_2O_8$ and other nanocomposites, revealing its excellent charge storage performance. As for all the electrode materials, their specific capacitances were computed by equation 3.1. The specific capacitance of G-4CVO was about 275.2 Fg^{-1} at 0.8 Ag^{-1}, which outperformed the pure $Co_3V_2O_8$ (128 Fg^{-1}), G-CVO (179.2 Fg^{-1}), G-2CVO (230.4 Fg^{-1}) and G-6CVO (204.8 Fg^{-1}). This can be attributed to the inimitable nanoarchitecture of the nanocomposite and the effective hybridisation of ample $Co_3V_2O_8$ micro-pencils onto the surface of graphene sheets. Nonetheless, overloading of $Co_3V_2O_8$ micro-pencils in G-6CVO results in the deterioration on the specific capacitance. This can be ascribed to the agglomeration of the nanocomposite, leading to the loss of exposure active sites[265, 331].

Figure 5.9b demonstrates the charge-discharge profiles of G-4CVO at different current densities of 0.8, 0.9, 1, 1.1 and 1.2 Ag^{-1}. From Figure 5.9b, the shortened discharge time at higher current density can be elucidated based on the ions transfer resistance and diffusion time. At high current density, the larger ions transfer resistance and limited diffusion time hinder the diffusion process of electrolyte ions from the surface of electrode material to its interior[334]. Besides, the specific capacitances of G-4CVO were calculated at different current densities and the outcomes are shown in Figure 5.10.

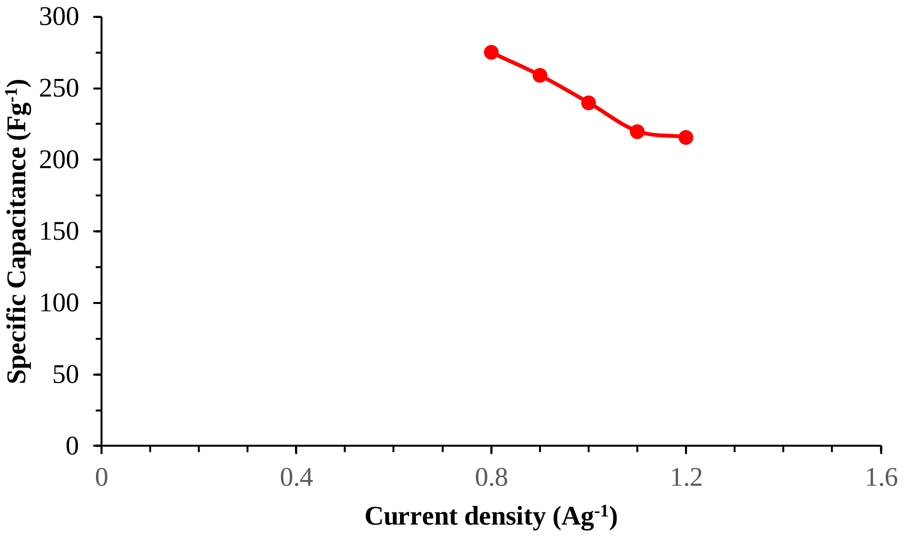

Figure 5.10: Specific capacitances of G-4CVO at current densities of 0.8, 0.9, 1, 1.1 and 1.2 Ag^{-1}.

The calculated specific capacitances of G-4CVO at various current densities were as follows: 275.2 Fg^{-1} (0.8 Ag^{-1}), 259.2 Fg^{-1} (0.9 Ag^{-1}), 240 Fg^{-1} (1 Ag^{-1}), 220 Fg^{-1} (1.1 Ag^{-1}) and 216 Fg^{-1} (1.2 Ag^{-1}). In addition, a capacitance retention of 78 % was achieved even when a high current density of 1.2 Ag^{-1} is used, indicating its good rate capability. This is owing to the positive interaction between graphene and $Co_3V_2O_8$ micro-pencils, large specific surface area and well preserved nanostructures[326, 332]. Furthermore, the cycling stability of the G-4CVO electrode was determined over 3000 cycles at 1 Ag^{-1} and the result is portrayed in Figure 5.11.

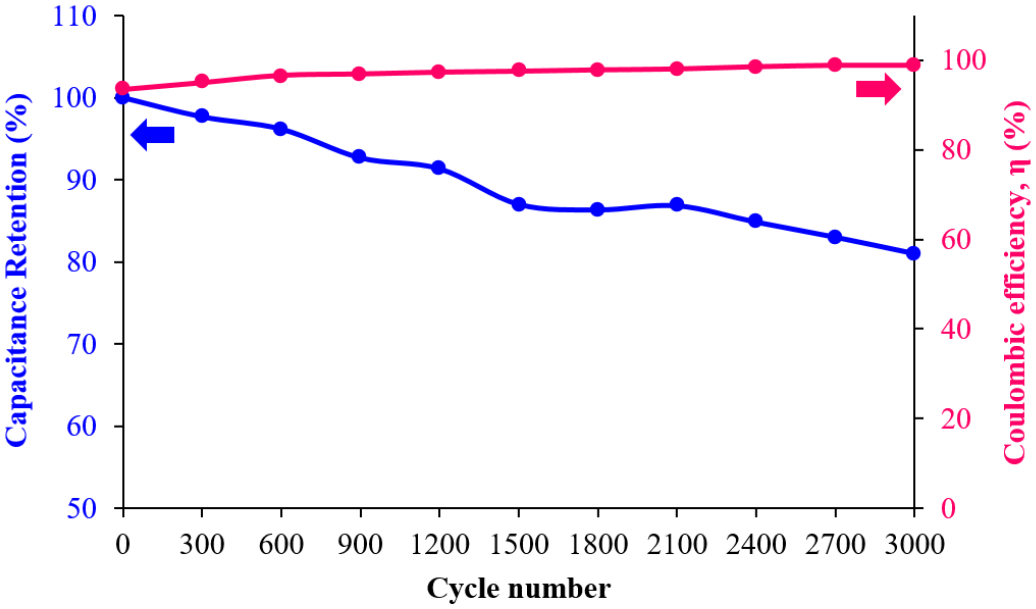

Figure 5.11: Cycling analysis (Blue) and Faraday efficiency (Pink) of G-4CVO electrode obtained after 3000 charge-discharge cycles.

After 3000 cycles of continuous GCD process, the specific capacitance of G-4CVO nanocomposite declined from 240 to 194.4 Fg^{-1} (81% retention of its initial capacitance), implying its eminent electrochemical cycling stability. This exceptional cycle-ability is believed due to the strong interaction between the graphene sheet and $Co_3V_2O_8$ micro-pencils and the presence of $Co_3V_2O_8$ micro-pencils impede the graphene from restacking during the cycling analysis[332]. In addition, the graphene nanosheets (buffering scaffold) in G-4CVO nanocomposite alleviated the volume changes of the active material (expansion and contraction) during the continuous cyclic analysis, leading to eminent cycling stability [333]. Besides, the coulombic efficiency (η) of the optimised electrode material (G-4CVO) over the charge discharge cycles was computed by equation 3.2 and the corresponding results are delineated in Figure 5.11. A coulombic efficiency of 98 %

was obtained after 3000 cycles, further confirming its good electrochemical reversibility[333].

EIS test was conducted to further evaluate the electrochemical properties of the as-prepared electrode materials and the corresponding Nyquist plots of pure $Co_3V_2O_8$ and graphene/$Co_3V_2O_8$ nanocomposites are plotted in Figure 5.12.

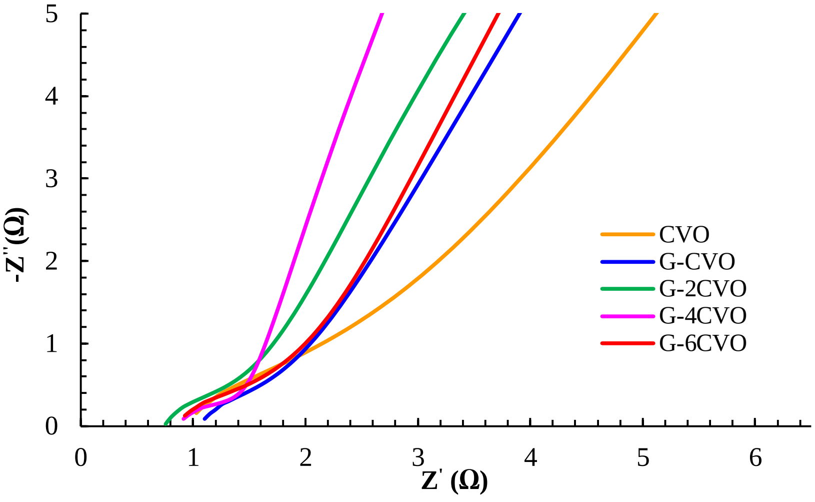

Figure 5.12: Nyquist plots of pristine $Co_3V_2O_8$ and graphene/$Co_3V_2O_8$ nanocomposites in the symmetrical two-electrode system.

As seen from Figure 5.12, all the plots present a quasi-semicircle (denoted as charge transfer resistance, R_{ct}) and oblique line (Warburg impedance) at high and low frequency regions, respectively. At high frequency region, the interception with the real x-axis is regarded as the solution resistance (R_s), which is a combination of internal resistances of the electrode material, namely the electrolyte resistance as well as the contact resistance at the interfaces of electrode/electrolyte [311, 326]. Here, the R_s values ranging from 0.8 to 1.1 Ω were delivered by all the electrode materials, suggesting their low internal resistances and high conductivity of the electrolyte[42, 130]. Besides, the R_{ct} values of pure $Co_3V_2O_8$ and graphene/$Co_3V_2O_8$ nanocomposites were obtained in the following order: G-4CVO (1.25 Ω) < G-2CVO (1.73 Ω) < G-6CVO (2.11 Ω) < G-CVO (2.38 Ω) < CVO (4.22 Ω). As compared to the pure $Co_3V_2O_8$ and other samples, the steeper the line of G-4CVO in the low frequency region is closer to the ideal behaviour of the supercapacitor, indicating its rapid kinetics of diffusion. Other than improving the electrical conductivity of the electrode material, the integration of graphene with $Co_3V_2O_8$ also shortens the charge transfer pathway, which in turn contributed to the lowest R_{ct} value and enhanced electrochemical performance of G-4CVO[18].

The feasibility of the electrode materials for practical supercapacitor application can be evaluated based on two important criteria, namely the associated energy and power densities. A Ragone plot illustrating these two important characteristics of pure $Co_3V_2O_8$ and graphene/$Co_3V_2O_8$ nanocomposites is depicted in Figure 5.13.

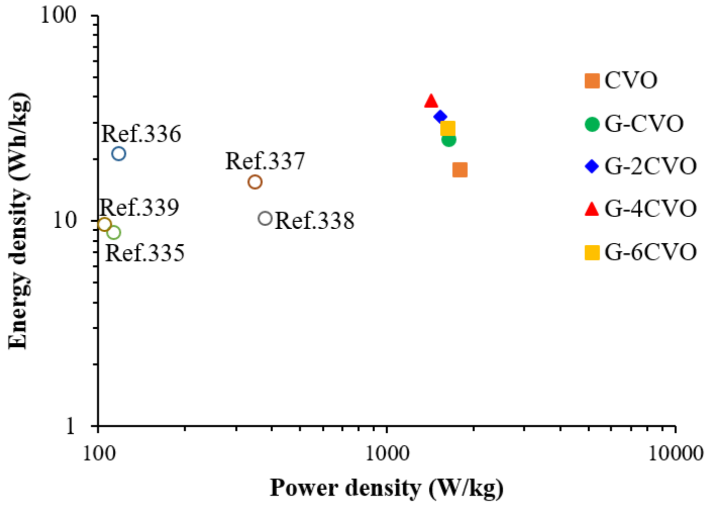

Figure 5.13: Ragone plot of pristine $Co_3V_2O_8$ and graphene/$Co_3V_2O_8$ nanocomposites.

It can be observed from Figure 5.13 that G-4CVO electrode outperformed pure $Co_3V_2O_8$, other combinations of graphene/$Co_3V_2O_8$ nanocomposites and symmetric/asymmetric based supercapacitor reported in other studies[335-339], as indicated by its relatively high energy and power densities of 38.2 Wh/kg and 1420 W/kg, respectively. This suggests the capability of graphene/$Co_3V_2O_8$ nanocomposite based supercapacitor as a credible energy storage device.

There are several factors contributing to the superior energy storage ability of graphene/$Co_3V_2O_8$ nanomaterials: (i) The intimate contact between the graphene sheet and $Co_3V_2O_8$ micro-pencils guarantees an excellent electrical conductivity and shorten the ion diffusion pathway substantially, which beneficial for ions and charges transfer and acceleration of Faradaic redox reaction[340, 341]. (ii) The role of graphene sheet as a buffering matrix in alleviating the volume variation during the intercalation-deintercalation process[340]. (iii) The structure of the liquid phase exfoliated graphene nanosheets can be well preserved, leading to advanced supercapacitive performance[24]. (iv) Homogenous dispersion of $Co_3V_2O_8$ micro-pencils on the surface of graphene sheets offers large accessible specific surface area for electrolyte ions, assuring the effective utilisation of the active materials[342].

5.4 Summary

In summary, $Co_3V_2O_8$ micro-pencils were successfully decorated on the graphene nanosheets via solvothermal technique followed by annealing process. The FESEM and TEM analysis confirm the exfoliation of graphene sheet and it is uniformly coated with $Co_3V_2O_8$ micro-pencils. Benefiting from the unique microstructure of $Co_3V_2O_8$ and strong interactive effect between $Co_3V_2O_8$ and graphene, the optimised graphene/$Co_3V_2O_8$ nanocomposite (G-4CVO) is holding a great potential as an effective electrode material for advanced supercapacitor system, as affirmed by its remarkable specific capacitance of 275.2 Fg^{-1} at a current density of 0.8 Ag^{-1}. Furthermore, the electrode material maintained 81 % of its charge storage capability after 3000 cycles, signifying its outstanding cycling stability. Additionally, G-4CVO delivered impressive energy and power densities (38.2 Wh/kg at 1420 W/kg). These eminent electrochemical properties suggested that graphene/$Co_3V_2O_8$ nanocomposite (electrode material) is promising for future supercapacitor applications.

Chapter 6: Facile synthesis of graphene-$Zn_3V_2O_8$ nanocomposites as a high performance electrode material for symmetric supercapacitor

6.1 Introduction

Zinc vanadate has been extensively investigated for their optical, photocatalytic and energy storage applications in lithium ion batteries. Nevertheless, only a few attempts have been made to utilise zinc vanadate for supercapacitor applications. For instance, $Zn_3V_2O_8$ nanoplatelets were successfully synthesised by Vijayakumar and his co-workers[23] via hydrothermal methods, which exhibited a maximum specific capacitance of 302 Fg^{-1} (three electrode system) at a scan rate of $5mVs^{-1}$. Besides, Li et al.[185] fabricated the nanostructured $Zn_2V_2O_7$ through microwave-assisted approach and it delivered a specific capacitance of $427.7Fg^{-1}$ at 1 $mAcm^{-2}$ in three electrode configuration. Similar to other MTMOs, zinc vanadate also suffers from rapid capacitance fading at high current densities and inferior cycling stability. This can be explicated by the existence of large volume expansion originated from the deficient conversion $(ZnO + 2Li^+ + 2e^- \leftrightarrow Zn + Li_2O)$, alloying-dealloying reaction $(Zn + xLi + xe^- \leftrightarrow Li_xZn)$, sluggish ions diffusion as well as poor electrical conductivity of the electrode materials[343]. Hence, integration of zinc vanadate with carbonaceous material like graphene has emerged as a promising strategy to conquer the obstacles and develop an advanced performance supercapacitor electrode which couples the advantages of both EDLC and pseudocapacitors to attain excellent cycling stability, high energy and power densities. Graphene as a 2D allotrope of carbon with superior electrical conductivity, huge specific surface area, broad working voltage window, good chemical and thermal stabilities is recognised as an excellent conductive scaffold in the nanocomposite[28, 344, 345]. Nonetheless, the capacitances are substantially restrained by the agglomeration of graphene nanosheets. Thus, loading of MTMO onto the surface of graphene will impede the aggregation of graphene sheets, leading to enhanced electrochemical performance[52, 346].

Despite the capacitive activity of $Zn_3V_2O_8$ has been investigated, the hybridisation of $Zn_3V_2O_8$ with graphene as the active electrode material for supercapacitor applications has not been studied and published previously. Thus, we made an effort to develop the graphene/$Zn_3V_2O_8$ nanocomposites and determine their appropriateness for supercapacitor application based on their electrochemical properties. In this chapter, a facile solvothermal synthesis of graphene/$Zn_3V_2O_8$ nanocomposites were reported. To further evaluate the synergistic effect between graphene sheet and $Zn_3V_2O_8$, different weight ratios of graphene/$Zn_3V_2O_8$ nanomaterials were prepared and analysed comprehensively to optimise their electrochemical properties.

6.2 Experimental methods

6.2.1 Synthesis of 2D $Zn_3V_2O_8$ hexagonal nanosheets on graphene

The assembly of 2D $Zn_3V_2O_8$ hexagonal nanosheets on graphene was demonstrated in Figure 6.1.

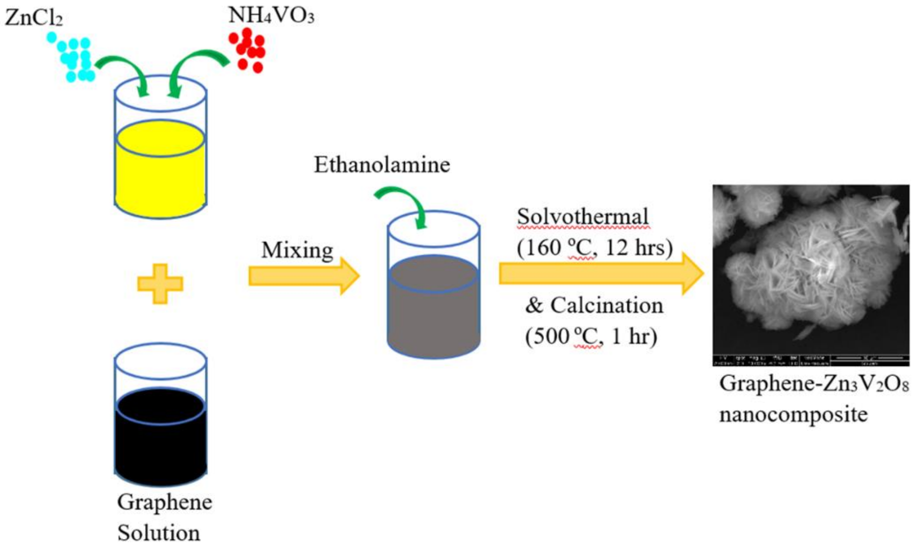

Figure 6.1: Schematic illustration of the assembly of graphene-2D $Zn_3V_2O_8$ hexagonal nanosheets via solvothermal approach.

Here, a high reaction temperature of 160^{o}C was adopted in the process to ensure complete formation of $Zn_3V_2O_8$ hexagonal nanosheets since it is an endothermic process. Contrarily, reaction under low temperature will result in fragmented nanosheets[188].

The direct anchoring of $Zn_3V_2O_8$ hexagonal nanosheets on the graphene sheet was assembled through one-pot solvothermal method followed by a calcination treatment. Firstly, 0.2 g of the as-produced graphene was dispersed in a 40 mL solution of ethanol and water with the volume ratio of 2:3 for 30 min. The yellow precursor solution was acquired by mixing 6 mmol of $ZnCl_2$ and 4 mmol of NH_4VO_3 into 40 mL of deionised water. After that, the well-dispersed graphene solution was mixed with the precursor solution under vigorous stirring to ensure homogeneity. Then, ethanolamine was added to adjust the pH of the entire solution to about 10. The final solution was transferred into a 100 mL Teflon-lined stainless steel autoclave to enable a solvothermal process at 160 ^{o}C for 12 hours. The autoclave was allowed to cool to room temperature and the resulted precipitate was then collected and washed thoroughly with ethanol and water by centrifugation. Finally, the sample was dried in an oven at 80 ^{o}C overnight and calcined at 500 ^{o}C in air for 1 hour to obtain the graphene-$Zn_3V_2O_8$ nanocomposite. The bare $Zn_3V_2O_8$ hexagonal nanosheets were synthesised in the similar manner as above without the integration of graphene.

For comparison purpose, different weight ratios of graphene to $Zn_3V_2O_8$ precursor were synthesised to determine the effects of weight ratio on the structural and electrochemical properties of the nanocomposite. The products were denoted as G-ZVO, G-1.5ZVO, G-3ZVO and G-6ZVO and the details of the $Zn_3V_2O_8$ precursor solution were manifested in Table 6.1.

Table 6.1: Different weight ratios of graphene to $Zn_3V_2O_8$.

Name of composite	**Weight of graphene (g)**	**Weight of $ZnCl_2$ (g)**	**Weight of NH_4VO_3 (g)**	**Graphene-$Zn_3V_2O_8$ (Weight ratio)**
G-ZVO	0.2	0.409	0.234	1:1
G-1.5ZVO	0.2	0.613	0.351	1:1.5
G-3ZVO	0.2	1.227	0.702	1:3
G-6ZVO	0.2	2.453	1.404	1:6

6.3 Results and Discussions

6.3.1 Structural Analysis

Powder X-ray diffraction (XRD) analysis was performed to give an insight into the crystallinity and phase purity of the pristine $Zn_3V_2O_8$, graphene sheet and graphene-$Zn_3V_2O_8$ nanocomposites with different weight ratios. The results are shown in Figure 6.2.

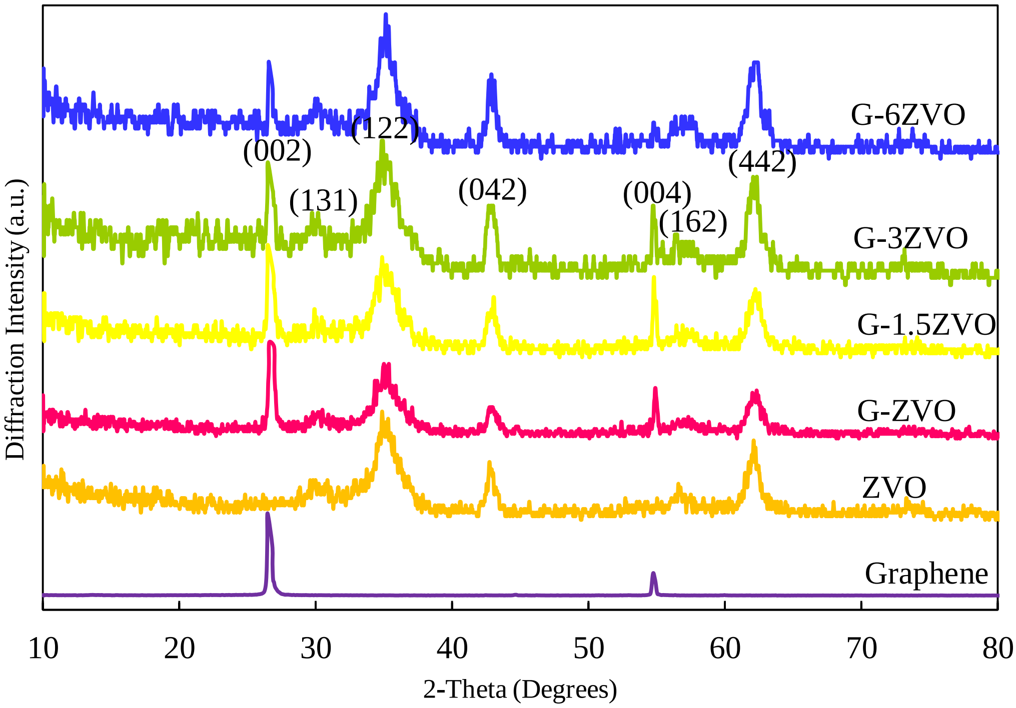

Figure 6.2: XRD patterns of pristine $Zn_3V_2O_8$, graphene and graphene-$Zn_3V_2O_8$ with different weight ratios.

As depicted in Figure 6.2, the XRD patterns of graphene-$Zn_3V_2O_8$ nanocomposites were appointed to the standard orthorhombic crystal structure of $Zn_3V_2O_8$ (JCPDS No. 034-0378)[23, 343]. Five characteristic peaks were observed at around 30°, 34.9°, 44.3°, 56.7° and 62.3°, which could be assigned to the (131), (122), (042), (162) and (442) planes of orthorhombic $Zn_3V_2O_8$, respectively, with (122) plane as the mother peak[187]. Furthermore, two diffraction peaks at 2 theta values of 26.8° and 54.9° of graphene-$Zn_3V_2O_8$ nanocomposites were coinciding with those reported (002) and (004) of graphene phases, revealing the successful hybridisation of graphene sheet with $Zn_3V_2O_8$[263]. In addition, the well-resolved diffraction lines together with the sharp diffraction peaks implied that the graphene-$Zn_3V_2O_8$ nanocomposites were highly crystalline in nature. The absence of other peaks confirmed the high purity of the products.

The structural analysis of graphene-$Zn_3V_2O_8$ nanocomposite (G-3ZVO) and sole graphene was further conducted by Raman spectroscopy as demonstrated in Figure 6.3.

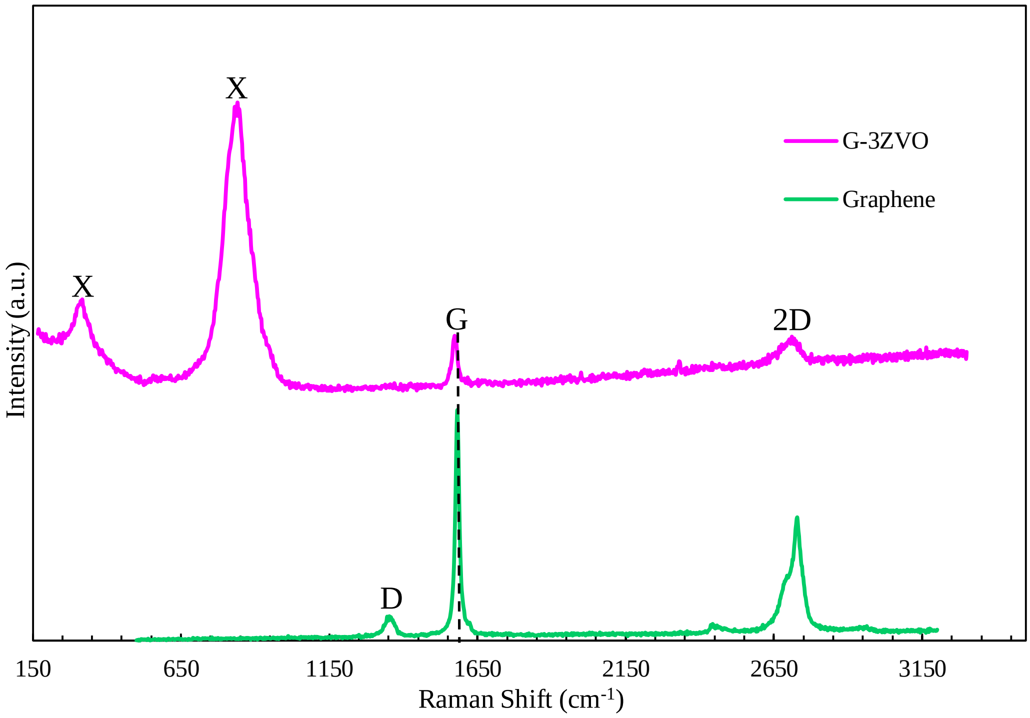

Figure 6.3: Raman spectra of graphene and graphene-$Zn_3V_2O_8$ nanocomposite (G-3ZVO).

In general, graphene exhibited three vibrational peaks at 1360, 1582 and 2726 cm^{-1}, which can be ascribed to the G (vibration of sp2-bonded carbon atoms in a 2D hexagonal lattice), D and 2D (disorder and defects in the hexagonal lattice) bands, respectively[38, 242]. Besides, four prominent peaks are discernible in the Raman spectrum of G-3ZVO nanocomposite, where the peaks at 318 and 845 cm^{-1} are corresponded to the $Zn_3V_2O_8$ bands while the peaks at 1575 and 2726 cm^{-1} are attributed to the presence of graphene, further confirming the co-existence of graphene and $Zn_3V_2O_8$. In particular, the peak at 318 cm^{-1} is assigned to the bending vibrations of V-O-V bonds, whereas the peaks at 845 cm^{-1} is corresponded to the symmetric stretching mode of V-O bonds[29, 263]. The disappearance of D band in the G-3ZVO nanocomposite is due to the higher mass loading of $Zn_3V_2O_8$ which supressed the characteristic peaks of graphene[263]. In addition, the intensive interaction between graphene and $Zn_3V_2O_8$ led to the Raman shift of the G band in the spectrum of G-3ZVO[80].

The morphology, size and microstructure of the as-synthesised graphene sheet, pure $Zn_3V_2O_8$ and graphene-$Zn_3V_2O_8$ nanocomposites were examined by FESEM and the outcomes are delineated in Figure 6.4.

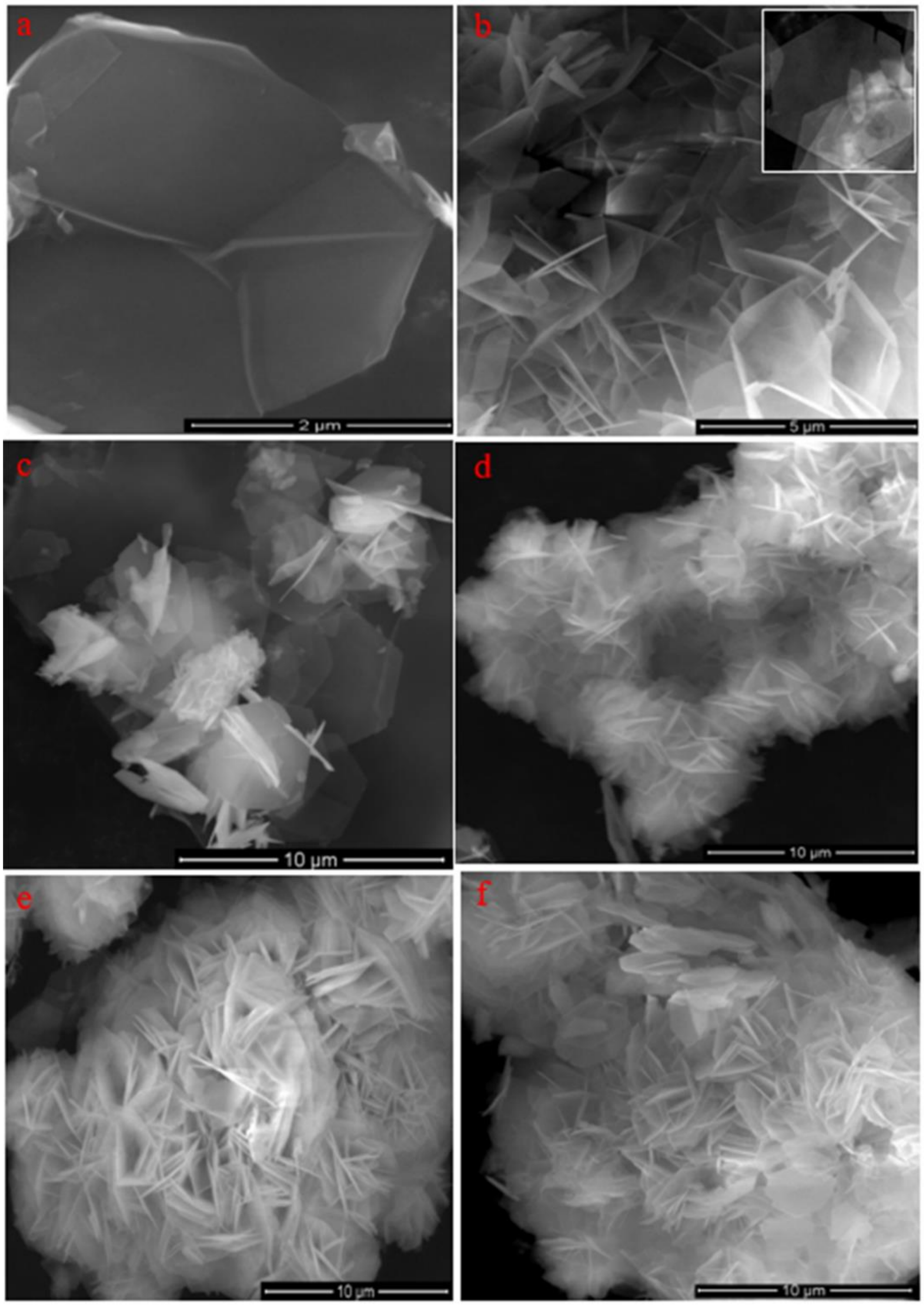

Figure 6.4: FE-SEM images of: (a) graphene sheet, (b) pure $Zn_3V_2O_8$ hexagonal nanosheets, (c) G-ZVO, (d) G-1.5ZVO, (e) G-3ZVO and (f) G-6ZVO nanocomposites.

Both the graphene sheet (Figure 6.4a) and pristine $Zn_3V_2O_8$ hexagonal nanosheets(Figure 6.4b) could be observed in Figures 6.4 (c to f), suggesting that the $Zn_3V_2O_8$ hexagonal nanosheets were successfully deposited on the surface of graphene sheet with good interface compatibility. This novel graphene-$Zn_3V_2O_8$

nanoarchitecture is expected to possess high flexibility and strong structural tenacity, which can efficiently accommodate the volume variation during the continuous charge-discharge process[276]. In contrast to other samples (G-ZVO, G-1.5ZVO and G-6ZVO), Figure 6.4e (G-3ZVO) demonstrates that the $Zn_3V_2O_8$ hexagonal nanosheets were evenly distributed on the surface of graphene sheets. This can be elucidated by the adequate amount of precursors available to completely cover the entire surface of graphene sheets. Here, the role of $Zn_3V_2O_8$ nanosheets as spacers can hamper the graphene sheets from restacking. Meanwhile, graphene with a large specific surface area can also prohibit the agglomeration of $Zn_3V_2O_8$ nanosheets. These “sheet on sheet” nanostructures were intertwined with each other to form a loose structure as well as a three dimensional network architecture. These structures offer more electroactive sites for Faradaic redox reaction and shorten the ions migration path, and hence resulted in advanced electrochemical performance[41, 243]. Contrarily, excess amount of precursors decorated on the graphene sheet as shown in Figure 6.4f (G-6ZVO) will inevitably reduce the homogeneity and distribution density of the $Zn_3V_2O_8$ hexagonal nanosheets on graphene, leading to poor supercapacitive performance.

To better understand the microstructure of the graphene-$Zn_3V_2O_8$ nanocomposite (G-3ZVO), TEM and high resolution TEM (HRTEM) were conducted and the results are portrayed in Figure 6.5.

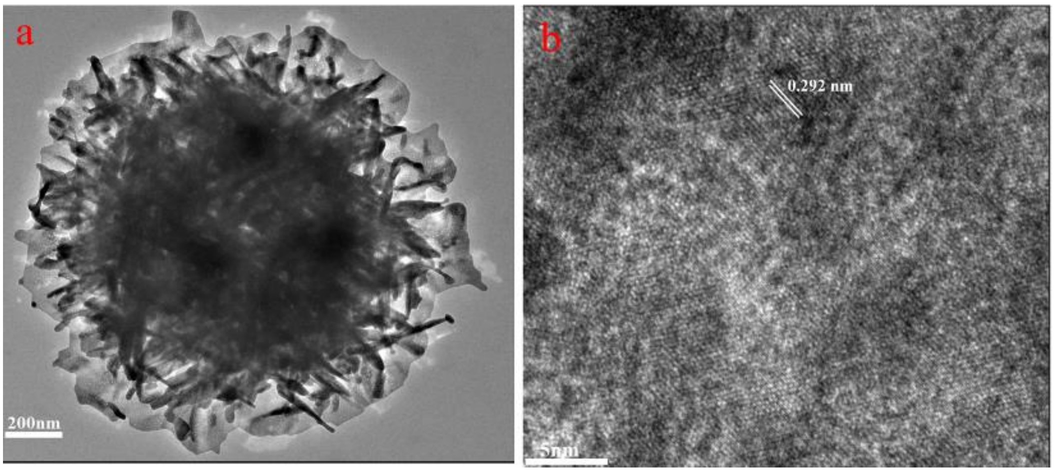

Figure 6.5: (a) TEM and (b) HRTEM images of G-3ZVO nanocomposite.

It is noticeable in Figure 6.5a that the $Zn_3V_2O_8$ hexagonal nanosheets were fully anchored on the basal planes and edges of the graphene sheets, which is tallied with the SEM analysis (Figure 6.4e). In addition, the low contrast between the graphene sheet and the carbon of the carbon-copper grids implies that an ultrathin layer of the graphene sheet was acquired through the decoration of $Zn_3V_2O_8$ nanosheets. The HRTEM image in Figure 6.5b reveals the high crystallinity of G-3ZVO nanocomposite together with the lattice spacing of 0.292 nm, which corresponds to the (040) plane of the $Zn_3V_2O_8$ crystal[188].

The energy-dispersive X-ray spectroscopy (EDX) analysis was performed to identify the elemental compositions of the graphene-$Zn_3V_2O_8$ nanocomposites, and the results are revealed in Figure 6.6a.

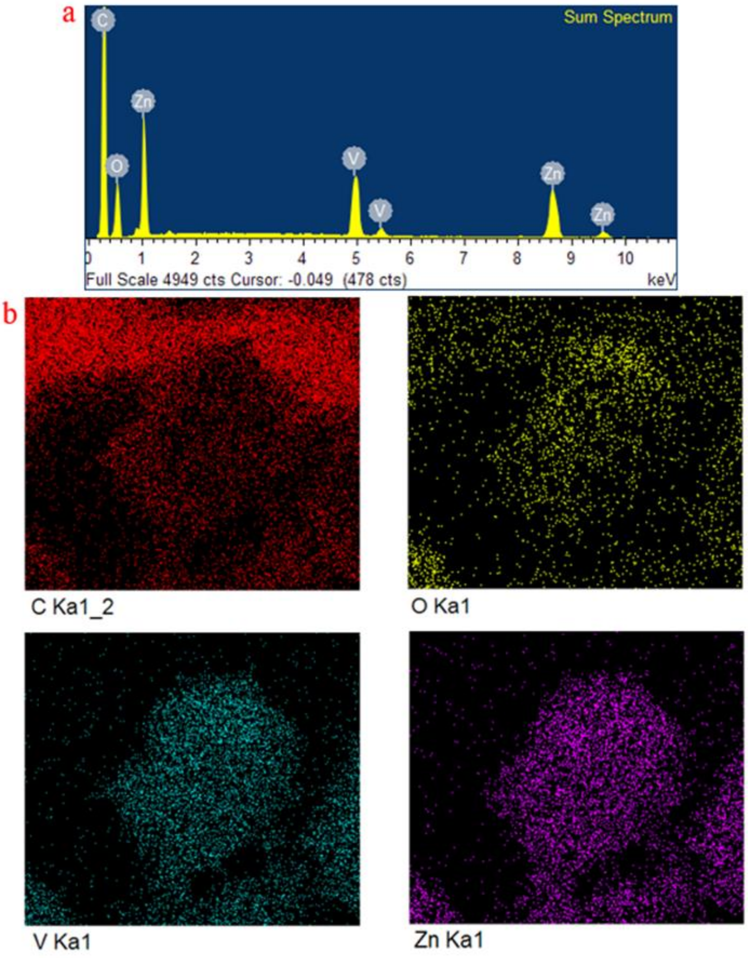

Figure 6.6: (a) EDX pattern of graphene-$Zn_3V_2O_8$ nanocomposite (G-3ZVO), (b) Elemental mapping analysis of C, Zn, V, and O in G-3ZVO nanocomposite.

The EDX result proved that the G-3ZVO is composed of merely C, O, Zn and V elements, which is congruent with the XRD and XPS results. As no other peaks were detectable in Figure 6.6a, the formation of high purity graphene/$Zn_3V_2O_8$ nanomaterial is further verified. At the same time, the EDX mapping analysis in Figure 6.6b validates the distributions and intensities of Zn, V, O, C elements within the nanocomposite. The negligible elemental isolation of four elements also confirms the homogenous distribution of these elements throughout the whole nanocomposite.

Furthermore, the informative results such as elemental composition and valence states of the graphene/$Zn_3V_2O_8$ nanocomposite (G-3ZVO) were characterised by XPS (Figure 6.7).

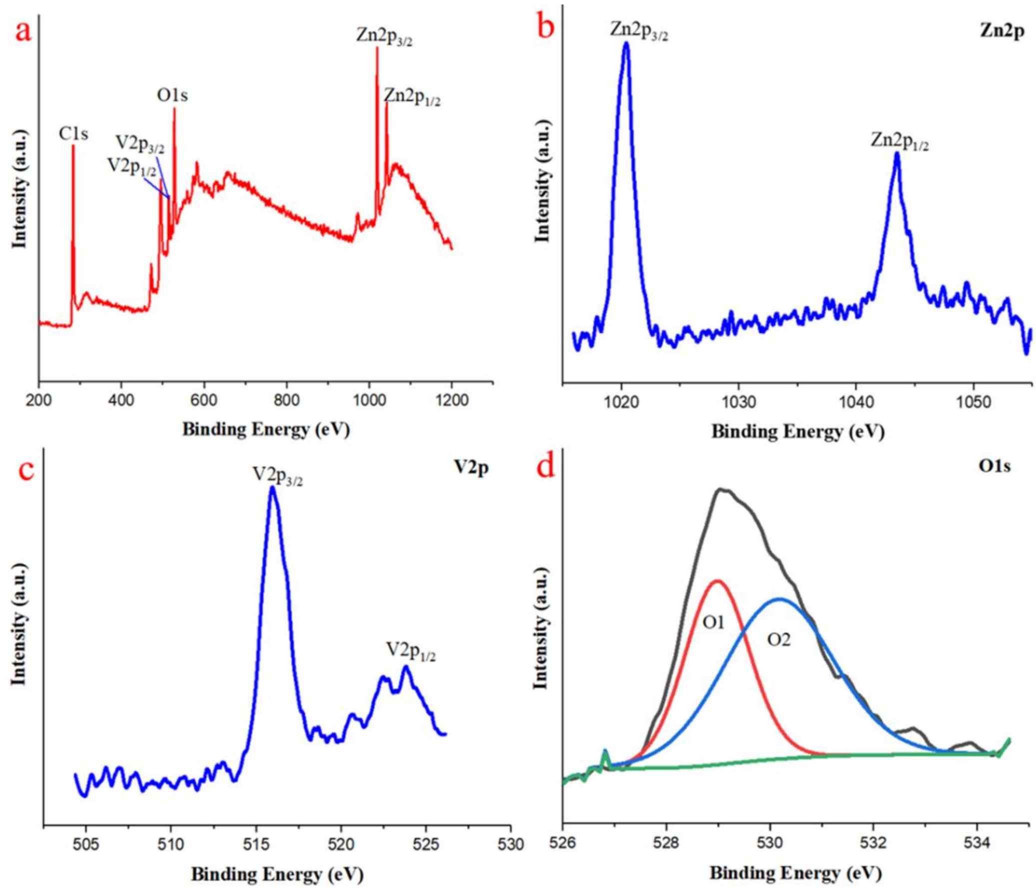

Figure 6.7: XPS spectra of: (a) Full survey spectrum, (b) Zn 2p, (c) V 2p and (d) O 1s.

The full survey spectrum in Figure 6.7a further affirms that the as-synthesised G-3ZVO comprises Zn, V, O and C elements with the presence of Zn 2p, V 2p, O 1s and C 1s states, respectively, which are in agreement with the EDX result. Figure 6.7b depicts the high resolution Zn 2p spectrum, where the peaks at binding energies of 1020.3 and 1043.2 eV can be assigned to Zn $2p_{3/2}$ and Zn $2p_{1/2}$, respectively[23, 186]. The high resolution V2p XPS spectrum in Figure 6.7c shows two apparent signals at *ca*. 516.1 eV and 523.4 eV, which correspond to the V $2p_{3/2}$

and V $2p_{1/2}$ of V^{5+} state[343]. Figure 6.7d manifests the high resolution O1s XPS spectrum and the spectrum was deconvoluted into two components, namely O1 and O2 with the binding energies of 529 and 530.2 eV, respectively. O1 is attributed to the metal-oxygen bond, such as V-O bonding in the G-3ZVO whereas O2 is related to the adsorbed-oxygen[23, 186].

6.3.2 Electrochemical Characterisation

In order to evaluate the energy storage competency of the nanohybrids, the as-fabricated electrodes were investigated by CV, GCD and EIS measurements in a 2M aqueous KOH electrolyte. Figure 6.8a shows the cyclic voltammograms of pure $Zn_3V_2O_8$ and graphene-$Zn_3V_2O_8$ nanocomposite electrodes at a scan rate of 50 mVs^{-1} and voltage ranging from -1 to 1 V.

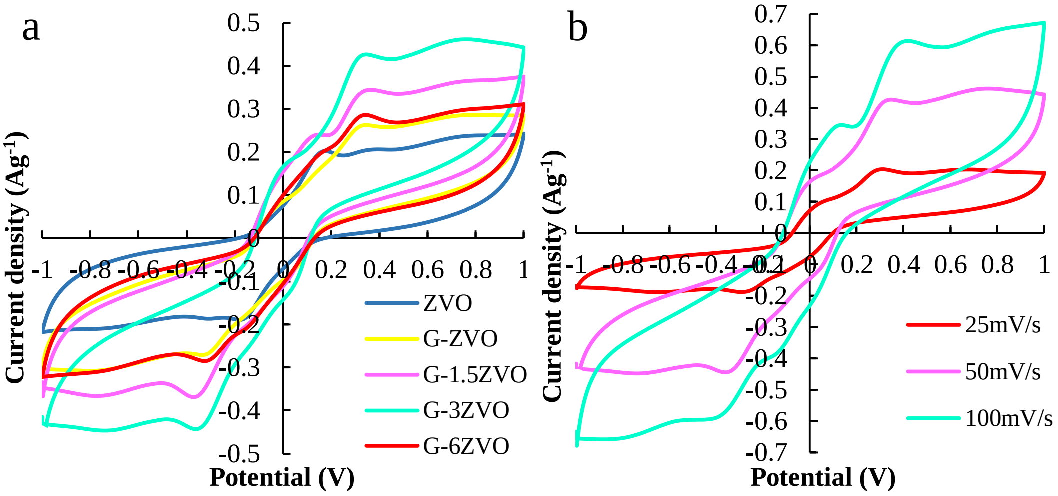

Figure 6.8: Cyclic voltammograms of (a) $Zn_3V_2O_8$, G-ZVO, G-1.5ZVO, G-3ZVO and G-6ZVO nanocomposites at a scan rate of 50 mVs^{-1}. (b) G-3ZVO at the scan rates of 25, 50 and 100 mVs^{-1}.

It is noteworthy in all the CV curves that well-defined redox peaks were visible during the positive and negative sweep, suggesting the strong pseudocapacitive nature of the electrode materials[23]. The two pairs of redox peaks observed for all the electrodes could be ascribed to the reversible electron transfer process of Zn / Zn^{2+} and V^{3+} / V^{5+} redox couples as well as the intercalation and de-intercalation of K^+ ion from the electrolyte into zinc oxide[23, 188]. In addition, the reversibility of the redox reactions was advocated by the symmetrical anodic and cathodic peaks[347]. As anticipated, the integrated area of the CV loop was enlarged by the incorporation of $Zn_3V_2O_8$ with graphene as compared to bare $Zn_3V_2O_8$ electrode, reflecting that the charge storage capability of graphene-$Zn_3V_2O_8$ nanocomposite was enhanced[275]. This phenomenon is likely attributed to the synergistic effect of the hybrid nanocomposite (EDLC coupled with pseudocapacitance) where the presence of graphene increases the specific surface area of the nanocomposites and thus promotes the diffusion of electrolyte ions and exposes more active sites to the electrolyte[348]. It is noticeable that the integrated area of the CV curve for each nanocomposite was substantially different, indicating that the quantity of $Zn_3V_2O_8$ embedded on the graphene sheet has a significant influence on the electrochemical properties of the respective electrode material[24, 263].

Figure 6.8b manifests the cyclic voltammetry profiles of G-3ZVO at different scan rates of 25, 50 and 100 mVs^{-1}. The shapes of the CV curves were not deformed even at high scan rates, suggesting the advanced ionic and electronic diffusion, excellent reversibility and good rate capability of the graphene-$Zn_3V_2O_8$ nanohybrid (G-3ZVO)[28, 349]. Besides, the enhancement in the peak current as the scan rate increases indicates that the kinetics of the interfacial Faradaic redox reactions and the rate of charge transfer were rapid enough even at high scan rate[29, 41, 242]. As the scan rate increases, the internal resistance of the electrode material caused the potential of oxidation and reduction peaks shifted towards more positive and negative directions, respectively[41, 231].

The specific capacitances of $Zn_3V_2O_8$ and graphene-$Zn_3V_2O_8$ nanocomposites were evaluated by chronopotentiometry with the potential window varied from 0 to 1.0 V and at a constant current density of 0.8 Ag^{-1} in 2M KOH aqueous electrolyte. The results are delineated in Figure 6.9.

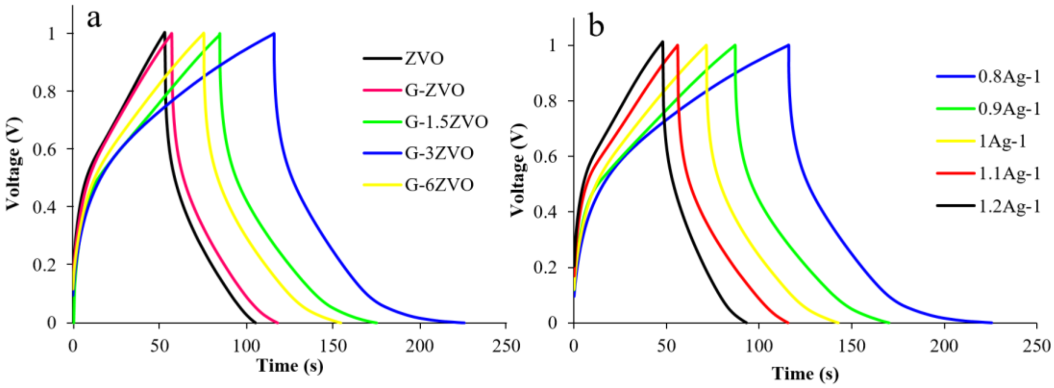

Figure 6.9: Galvanostatic charge-discharge profiles of (a) G-ZVO, G-1.5ZVO, G-3ZVO and G-6ZVO nanohybrids and pristine ZVO at a current density of 0.8 Ag^{-1}. (b) G-3ZVO nanocomposite at various current densities.

The non-linearity of the charge-discharge curves was attributed to the Faradaic redox reactions of Zn / Zn^{2+} and V^{3+} / V^{5+} redox couples collated with the OH^- ions and this coincides with the CV results. Besides, the nearly symmetrical charging and discharging curves signify the excellent reversibility of the electrode materials[24, 263]. It can be inferred from Figure 6.9a that G-3ZVO possessed the longest discharge time, suggesting its eminent capacitive performance.

The specific capacitances of all the samples were computed using equation 3.1. A superior specific capacitance of 313.6 Fg^{-1} at 0.8 Ag^{-1} was delivered by G-3ZVO electrode, which is much higher than those of the pristine $Zn_3V_2O_8$ (179.2 Fg^{-1}), G-

ZVO (211.2 Fg^{-1}), G-1.5ZVO (275.2 Fg^{-1}) and G-6ZVO (256 Fg^{-1}) nanocomposites. These findings highlight the significant contribution of graphene and optimum weight ratio between graphene and $Zn_3V_2O_8$ nanomaterials to the capacitive performance, where the presence of graphene and the homogenous distribution of $Zn_3V_2O_8$ hexagonal sheets on the surface of graphene render more electroactive sites for effective redox reactions, leading to enhanced charge storage capability[41, 231].

In order to determine the rate capability of G-3ZVO electrode material, the charge-discharge curves at various current densities were conducted and the results are shown in Figure 6.9b. Here, it can be noticed that the discharge time declined with the current density by virtue of insufficient access time for the electrolyte ions to penetrate into the bulk electrode at high current density[41, 318]. The specific capacitances of G-3ZVO at different current densities are demonstrated in Figure 6.10.

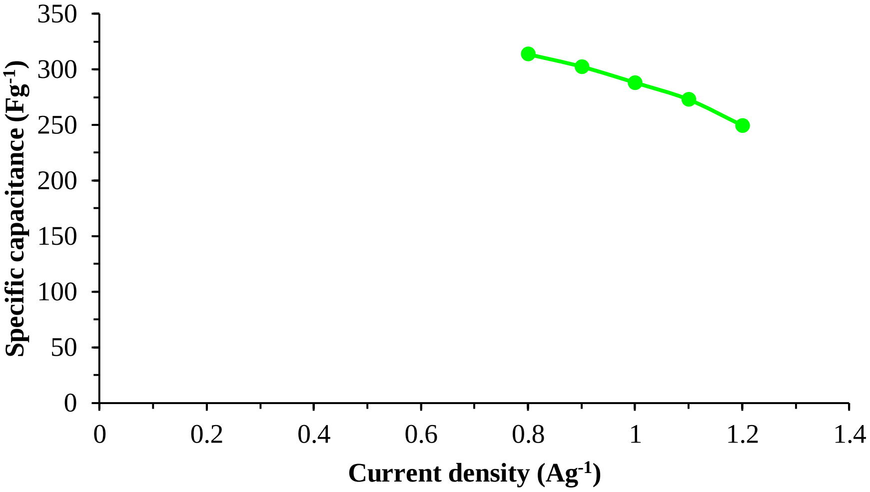

Figure 6.10: Specific capacitances (Fg^{-1}) of G-3ZVO at the current densities of 0.8, 0.9, 1, 1.1, 1.2 Ag^{-1}.

The specific capacitance of G-3ZVO declined as the current density increased, with the values of 313.6 Fg^{-1}, 302.4 Fg^{-1}, 288 Fg^{-1}, 272.8 Fg^{-1} and 249.6 Fg^{-1} at the current densities of 0.8, 0.9, 1, 1.1 and 1.2 Ag^{-1}, respectively. The G-3ZVO electrode was able to retain nearly 80% of its specific capacitance even at high current density, revealing its outstanding rate capability. The deterioration of specific capacitance at high current density can be attributed to: (i) incremental potential difference (ii) sluggish migration of electrolyte ions into the interior of active material[238, 249].

Long term cycling stability is another critical evaluation criterion in practical application of supercapacitors. The cycling test for G-3ZVO nanocomposite was conducted for 3000 cycles at a constant current density of 1 Ag^{-1} and the results are depicted in Figure 6.11.

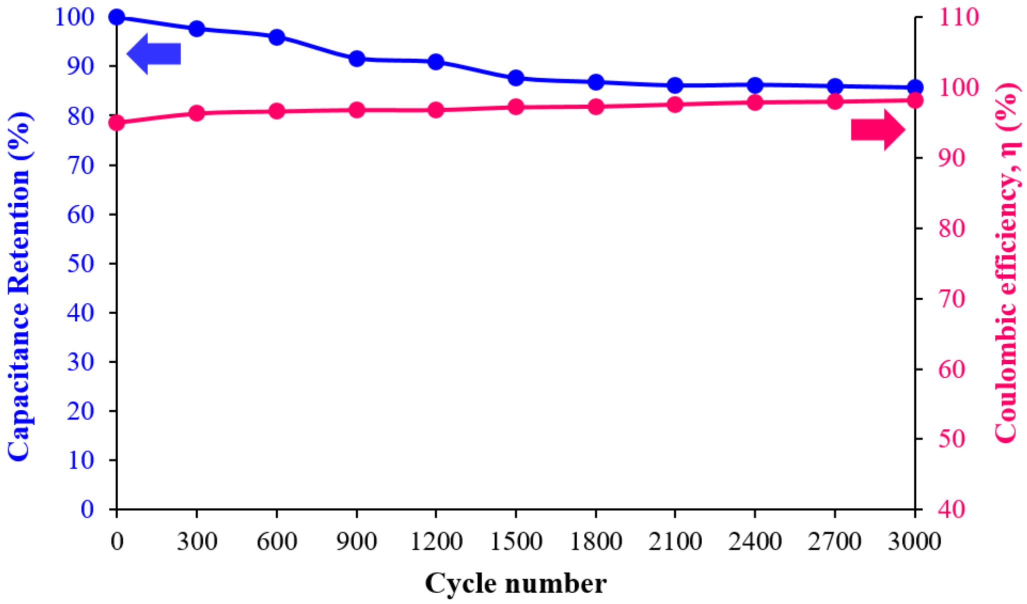

Figure 6.11: Cycling performance and Coulombic efficiency (%) of G-3ZVO electrode material over 3000 cycles.

As delineated in Figure 6.11, a gradual deterioration on the specific capacitance was observed for the first 1800 cycles and became steadily until it reached 3000 cycles. The specific capacitance of the G-3ZVO nanohybrid electrode was about 246.8 Fg^{-1} after 3000 successive charge-discharge process (86 % capacitance retention), revealing its prominent long term stability. The decay in specific capacitance could be due to the poor interfacial contact between the electrode and electrolyte during the cycling process[309, 310]. Additionally, the gradual degradation of the G-3ZVO nanocomposite electrode and the inevitable pulverisation of the active electrode under continuous volume distortion during the intercalation-deintercalation process can also lead to the capacitance fading[41, 231].

Besides, the coulombic efficiency (η) of G-3ZVO electrode material over the cycle analysis was calculated from the galvanostatic charge-discharge profiles by using equation 3.2 and the results are presented in Figure 6.11. The initial coulombic efficiency of the electrode material was about 95 % and it increased gradually up to 98 % after 3000 cycles. This result further signifies the excellent reversibility of the G-3ZVO electrode material.

Figure 6.12 illustrates the outcomes of the EIS analysis of pristine $Zn_3V_2O_8$ and graphene-$Zn_3V_2O_8$ nanocomposites, which were carried out in 2M KOH aqueous electrolyte.

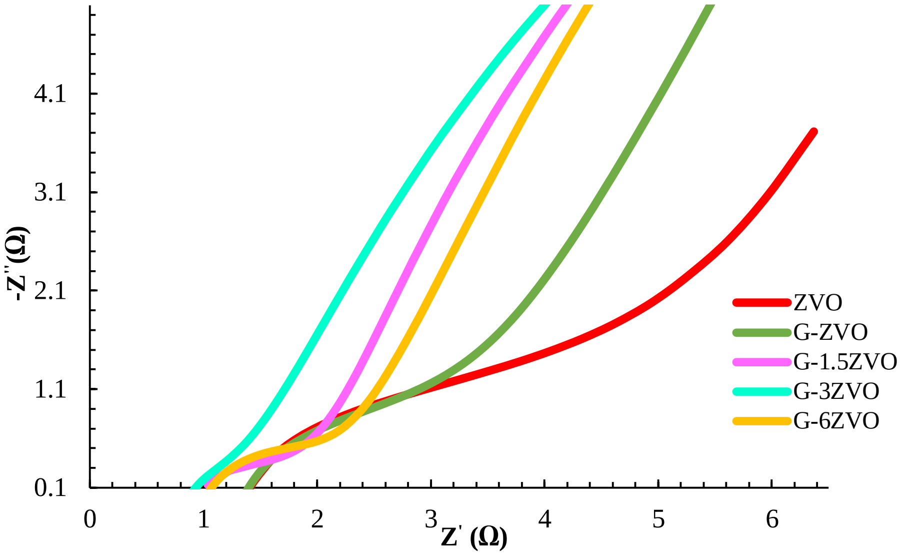

Figure 6.12: EIS curves of pristine $Zn_3V_2O_8$ and graphene-$Zn_3V_2O_8$ nanocomposites using a symmetric two-electrodes system.

Here, the Nyquist plots of all the electrode materials reveal a semicircle in the high frequency region representing the charge transfer resistance (R_{ct}) and an inclined line in the low frequency region denoting the Warburg impedance[26, 275]. The R_{ct} is originated from the Faradaic redox reactions within the electrode material and the double layer capacitance on the surface of the electrode material. The interception of the Nyquist plot with the real x-axis gives the solution resistance (R_s) which encompasses the intrinsic resistance of active material, electrolyte resistance and the contact resistance of the active material/current collector interface[41, 231]. The solution resistances (R_s) of all the electrode materials were obtained in the range of 1 to 1.5 Ω, implying the low internal resistance of the electrode materials and good conductivity of the electrolyte[42, 130]. In addition, the G-3ZVO (1.93 Ω) has the lowest charge transfer resistance, which outperformed other samples such as pure $Zn_3V_2O_8$ (5.15 Ω), G-ZVO (3.94 Ω), G-1.5ZVO (2.15 Ω) and G-6ZVO (2.44 Ω) nanocomposites. These results further advocate that the integration of graphene could substantially ameliorate the electrical conductivity of the nanocomposite and hence enhanced electrochemical performance[25, 263]. In the low frequency region, G-3ZVO demonstrated a steeper line as compared to the pure $Zn_3V_2O_8$ and other graphene/$Zn_3V_2O_8$ nanocomposites, suggesting its excellent diffusion kinetics. This can be attributed to the hybridisation of graphene with $Zn_3V_2O_8$ where the presence of graphene sheets allows rapid diffusion of electrolyte ions by shortening the ion transportation pathway[25].

Moreover, energy and power densities are two crucial factors to be considered in the practical applications of a supercapacitor, where an advanced supercapacitor should possess high energy and power densities contemporaneously. Thus, a Ragone plot demonstrating the relation between the energy and power densities is illuminated in Figure 6.13 to compare the overall performance of graphene-$Zn_3V_2O_8$ nanocomposites with the previously reported literature values. The energy and power densities were computed from the charge-discharge profiles using equations (3.3) and (3.4).

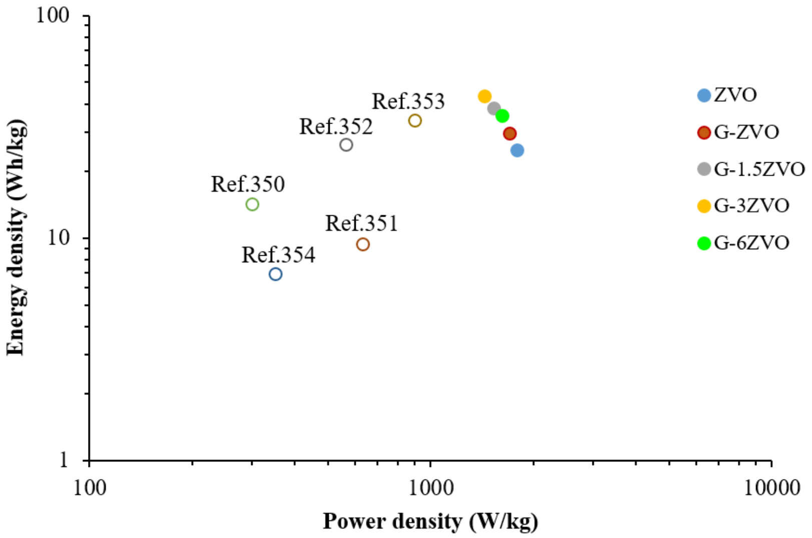

Figure 6.13: Ragone plot of sole $Zn_3V_2O_8$ and graphene-$Zn_3V_2O_8$ nanocomposites.

It was found that G-3ZVO delivered a remarkable energy density of 43.55 Wh/kg at a power density of 1438.5 W/kg, which surpassed the rest of the graphene-$Zn_3V_2O_8$ nanocomposites, $Zn_3V_2O_8$ virgin material and other previously reported symmetric or asymmetric supercapacitor[350-354]. This could be easily explicated by the superior specific capacitance and lower charge transfer resistance of G-3ZVO nanocomposite.

The above analyses unveiled the successful anchoring of $Zn_3V_2O_8$ 2D hexagonal nanosheets on graphene sheet to form a “sheet on sheet” like nanoarchitecture, which offers better electrochemical performance than the pristine $Zn_3V_2O_8$. The improved electrochemical performance can be ascribed to several factors: (i) the synergistic effect between $Zn_3V_2O_8$ nanosheets and highly conductive graphene sheets results in the formation of 3D network architecture which offers larger specific surface area and shortens the ion diffusion pathway for effective reversible redox reactions[41, 243, 248, 261]. (ii) Graphene not only enhances the electrical conductivity and structural integrity, but also serves as a buffer matrix for effective strain accommodation during the continuous charge-discharge process[41, 261]. (iii) The exfoliated structure of graphene sheet synthesised by this facile and green approach could be well preserved, which in turn contributed to the advanced electrochemical performance[24, 263]. (iv) The uniform dispersion of $Zn_3V_2O_8$ nanosheets retains the 3D structure of the nanocomposite by impeding the graphene sheets from restacking, leading to excellent electrochemical activities[228, 263].

6.4 Summary

In this work, $Zn_3V_2O_8$ hexagonal nanosheets embedded in the graphene networks were successfully synthesised through a facile and green solvothermal approach, followed by a thermal treatment. Benefiting from the interconnected “sheet on sheet” like nanostructure and the synergistic effect between $Zn_3V_2O_8$ and graphene, the optimised electrode material (G-3ZVO) exhibited an outstanding specific capacitance of 313.6 Fg^{-1} at 0.8 Ag^{-1} and preserved 86% of the initial capacitance after 3000 continuous charge-discharge cycles. Besides, an impressive energy density of 43.55 Wh/kg at a power density of 1438.5 W/kg was obtained by G-3ZVO. Its excellent electrochemical performance will undoubtedly induce the graphene-$Zn_3V_2O_8$ nanocomposite as an appealing candidate for advanced future energy storage applications.

Chapter 7: One dimensional MnV_2O_6 nanobelts on graphene as outstanding electrode material for high energy density symmetric supercapacitor

7.1 Introduction

Manganese vanadate (MnV_2O_6) with nanobelt shaped (1D) and unique brannerite structure could be considered as a potential electrode material in supercapacitor since it has good capacitive performance, peculiar electron properties and narrow band gap. In addition, manganese is a cost-effective, naturally abundant and environmentally friendly metal. However, a severe volume variation might happen during the continuous inter/deintercalation process, resulting in inferior cycling stability[355, 356].

For hybrid supercapacitor application, incorporation of manganese vanadate with carbonaceous material like activated carbon, carbon nanotubes, graphite flakes and graphene is necessary to alleviate the conundrum, as aforementioned effectively[357, 358]. Compared to other carbonaceous material, graphene is outperformed as it has large specific surface area, good flexibility, good conductivity and ready for functionalisation. The pros of graphene/manganese vanadate nanoarchitecture include: (i) Intimate contact of these two phases allow the synergistic effects between them, and hence enhance the overall capacitive performance. (ii) Graphene acts as a buffering matrix to accommodate the volume expansion during the continuous charge-discharge process. (iii) The electrical connectivity of single electroactive species can be improved effectively, and hence shorten the ions and electrons diffusion path[359, 360].

Many attempts have been made to study the electrochemical performance of graphene/metal vanadates in supercapacitor application. For instance, Patil and his group synthesised the fern-like rGO/$BiVO_4$ hybrid nanostructure for symmetric supercapacitor and it demonstrated a specific capacitance of 151 Fg^{-1} at 0.15 mA/cm^2[42]. Besides, $Ni_3V_2O_8$ nanoparticles deposited on graphene oxide was successfully developed by K. Thiagarajan and it was found to possess a specific capacitance of 547 Fg^{-1} (three electrode system) at a scan rate of 5mVs^{-1}[285]. However, the incorporation of the MnV2O6 nanobelt with graphene as potential electrode material for supercapacitor is still not being studied till date, which probably attributed to the rare synthesis process. This inspired the author to develop a simple fabrication method to synthesise these MnV_2O_6/graphene nanocomposites and evaluate its potential application in symmetric supercapacitor.

Herein, we report a hybrid electrode comprised of MnV_2O_6 nanobelt and graphene nanosheets, which derived from the facile solvothermal approach. To the best of our knowledge, this is the first paper reporting the application of MnV_2O_6/graphene nanocomposites as the active electrode material for supercapacitor. Moreover, different weight ratios of MnV_2O_6/graphene nanocomposites were fabricated to further optimise their energy storage properties.

7.2 Experimental

7.2.1 Synthesis of graphene/MnV_2O_6 nanocomposites

As for graphene/MnV_2O_6 nanocomposites, solvothermal approach was applied where 0.75 mmol of $Mn(NO_3)_2$ and 1.5 mmol of NH_4VO_3 were dissolved separately into two beakers (each with 20 mL of deionised water). Notably, the deionised water was heated to 80 ^{o}C before the dissolution of NH_4VO_3. Then, the NH_4VO_3 solution was added dropwise into the $Mn(NO_3)_2$ solution and allow for mixing. After that, the as-prepared graphene dispersion (20 mL) was added into the mixture and mixed for 30 minutes to achieve homogeneity. The resulting mixture was then transferred into the Teflon lined stainless steel hydrothermal reactor and heated at 200 ^{o}C for 6 hours. After cooled to room temperature, the resulting precipitate was collected via centrifugation and washed with ethanol and deionised water to the neutral condition. The products were then dried at 80 ^{o}C overnight and allowed for analysis. A pure MnV_2O_6 sample was synthesised by the method as aforementioned without the presence of graphene nanomaterial.

A variation of samples with different of proportions (mass ratio), which are denoted as G-MVO, G-4MVO, G-8MVO and G-12MVO, were prepared respectively and the details are stated in Table 7.1. Here, the mass of graphene was set to 0.2 g.

Table 7.1: Details of graphene/MnV_2O_6 nanocomposites with different proportions.

Nanocomposites	**$Mn(NO_3)_2$ (mmol)**	**NH_4VO_3 (mmol)**
G-MVO	0.75	1.50
G-4MVO	3.00	6.00
G-8MVO	6.00	12.00
G-12MVO	9.00	18.00

7.3 Results and Discussions

7.3.1 Characterisation of MnV_2O_6 and graphene/MnV_2O_6 nanohybrids

The formation mechanism of graphene-MnV_2O_6 nanobelts nanocomposite is depicted in Figure 7.1 and the related chemical reaction can be described as follow[361]:

$$2VO_3^- + Mn^{2+} \rightarrow MnV_2O_6 \qquad (7.1)$$

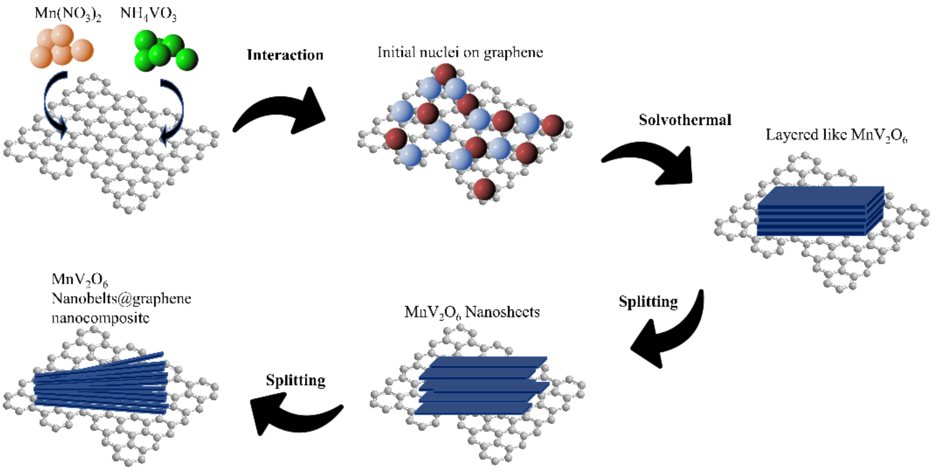

Figure 7.1: Schematic illustration on the growth mechanism of MnV_2O_6 nanobelts on graphene.

The replacement reaction process is conducted hydrothermally without any surfactants. Firstly, the positive metal ions (V^{5+} and Mn^{2+}) were adsorbed onto the surface of graphene sheet due to the electrostatic interactions[362]. Meanwhile, dimeric polyvanadate ions (V_2O_5) were formed after heating the NH_4VO_3 in the hydrothermal process. The V_2O_5 precursor was reacted with H_2O to form the HVO_3, which subsequently interacted with $Mn(NO_3)_2$ to form the layered like MnV_2O_6 nanostructures. The MnV_2O_6 nanostructures were gradually exfoliated to form the sheet-like MnV_2O_6 under hydrothermal condition. Lastly, the sheet-like MnV_2O_6 encountered the “splitting” process to relieve strong stress and depress the energy, which hence resulted in graphene-MnV_2O_6 nanobelts nanocomposite[363-365].

The phase and crystal structure of graphene, pure MnV_2O_6 and graphene/MnV_2O_6 nanocomposites were analysed by XRD, as delineated in Figure 7.2.

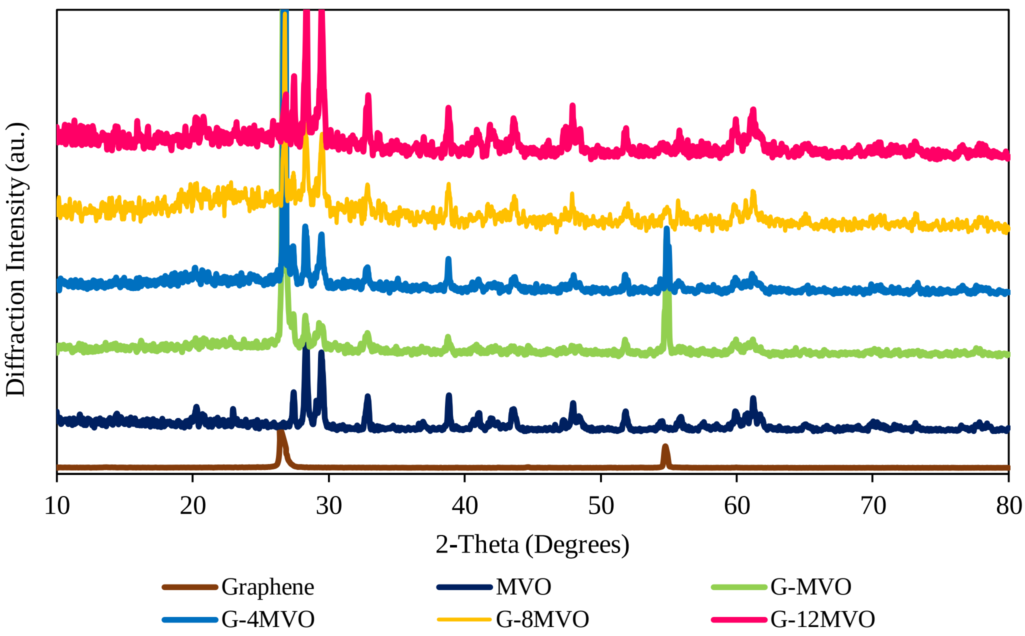

Figure 7.2: XRD patterns of pristine graphene, MnV_2O_6 and graphene/MnV_2O_6 nanocomposites.

The XRD spectra of nanocomposites show two high intensity peaks at $2\Theta=26.8^o$ and 54.9^o, which correspond to (002) and (004) planes of graphene. This confirms the presence of graphene in the nanocomposites[265]. Besides, the typical reflection peaks of MnV_2O_6 was presented in the XRD patterns of all graphene/MnV_2O_6 nanocomposites, which can be well indexed to monoclinic structure of MnV_2O_6 (JCPDS Card No: 35-0139)[355, 365]. No other characteristic peaks can be observed from the XRD curves of nanocomposites, confirming the purity of the samples. The sharp diffraction peaks of the nanocomposites indicated that the products are highly crystalline in nature, which might improve the electrochemical stability during the continuous charge-discharge process[322].

The insight on the morphologies of the graphene/MnV_2O_6 nanocomposites were examined by the FESEM, as shown in Figure 7.3.

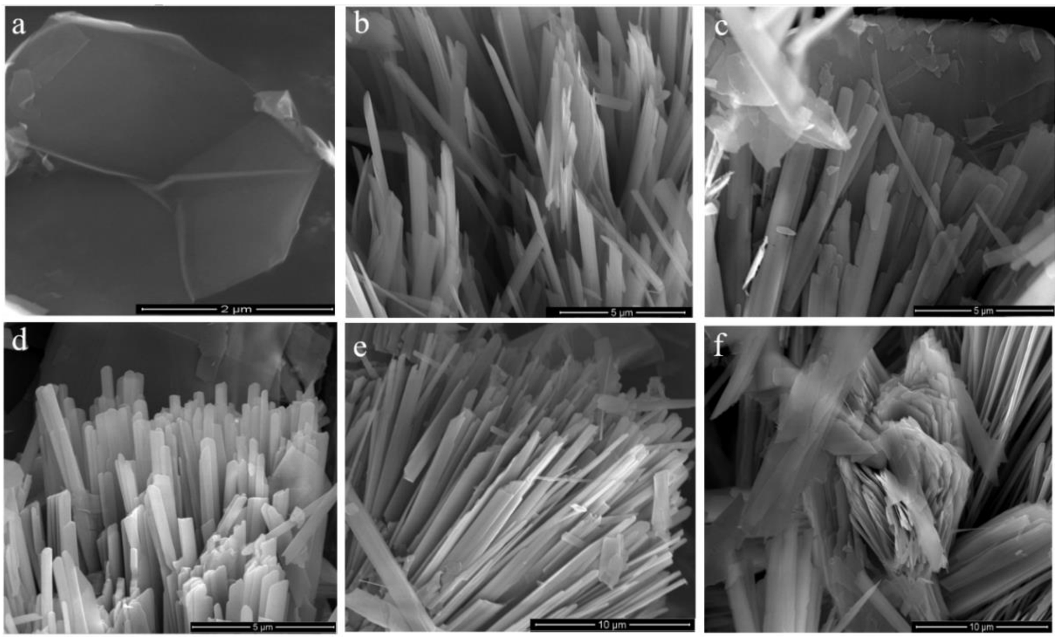

Figure 7.3: FESEM images of (a) Pristine graphene, (b) Pristine MnV_2O_6, (c) G-MVO, (d) G-4MVO, (e) G-8MVO and (f) G-12MVO.

Figure 7.3b depicts a micrograph of the pure MnV2O6 sample, where a large quantity of nanobelts with the thickness of 30-40 nm and a length of 300-400 nm could be observed. Figures 7.3c-f reveal the microstructures of G-MVO, G-4MVO, G-8MVO and G-12MVO nanocomposites, respectively, where MnV_2O_6 nanobelts were successfully loaded on the graphene sheet. The deposition process is believed owed to the strong electrostatic interaction between the MnV_2O_6 and the graphene sheet[247]. As the composite proportion increased, the aspect ratio of MnV_2O_6 decorated on graphene change accordingly[366]. In figure 7.3e, the MnV_2O_6 nanobelts were distributed homogeneously on the surface of graphene with intimate interfacial contact. This improves the synergistic effect between electrode and electrolyte[267]. Besides, depositing the transition metal oxide nanomaterials with graphene can prevent the graphene sheets from restacking, resulting in the enhancement of active surface area which beneficial for energy storage. Additionally, this nanoarchitecture can shorten the ion transportation pathway and allowed more electrolyte ions access into the inner realm of the electrode, and hence favouring the electrochemical performance[367, 368].

The TEM image as presented in figure 7.4a further reveal that the nanobelts were well deposited on the surface of graphene, and this is in agreement with the SEM results.

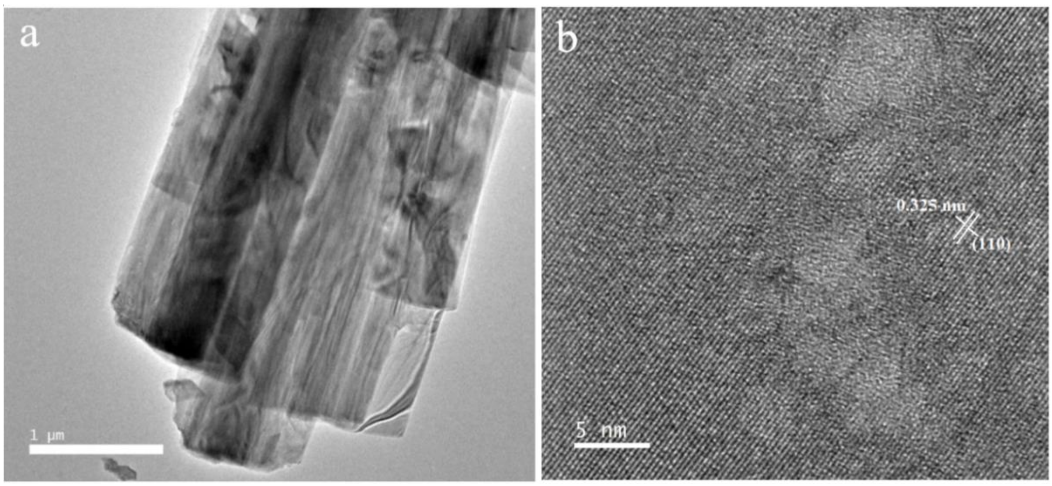

Figure 7.4: (a) TEM and (b) HRTEM images of G-8MVO.

To determine the crystallinity of the aligned nanobelts and provide more information on the atomic structure of the nanocomposite, HRTEM analysis was conducted and the result is shown in Figure 7.4b. The clear atomic lattice fringe of the G-8MVO nanocomposite can be observed, suggesting the highly crystalline nature of the nanomaterial[369]. The lattice spacing of 0.325 nm can be measured from the lattice fringe, which correspond well to the (110) planes of the monoclinic

MnV2O6 nanobelts and this is consistent with the tropism of (110) planes in XRD spectra (Figure 7.2)[356, 369].

EDS measurement was also employed to determine the purity and the chemical composition of the G-8MVO nanocomposite (Figure 7.5a).

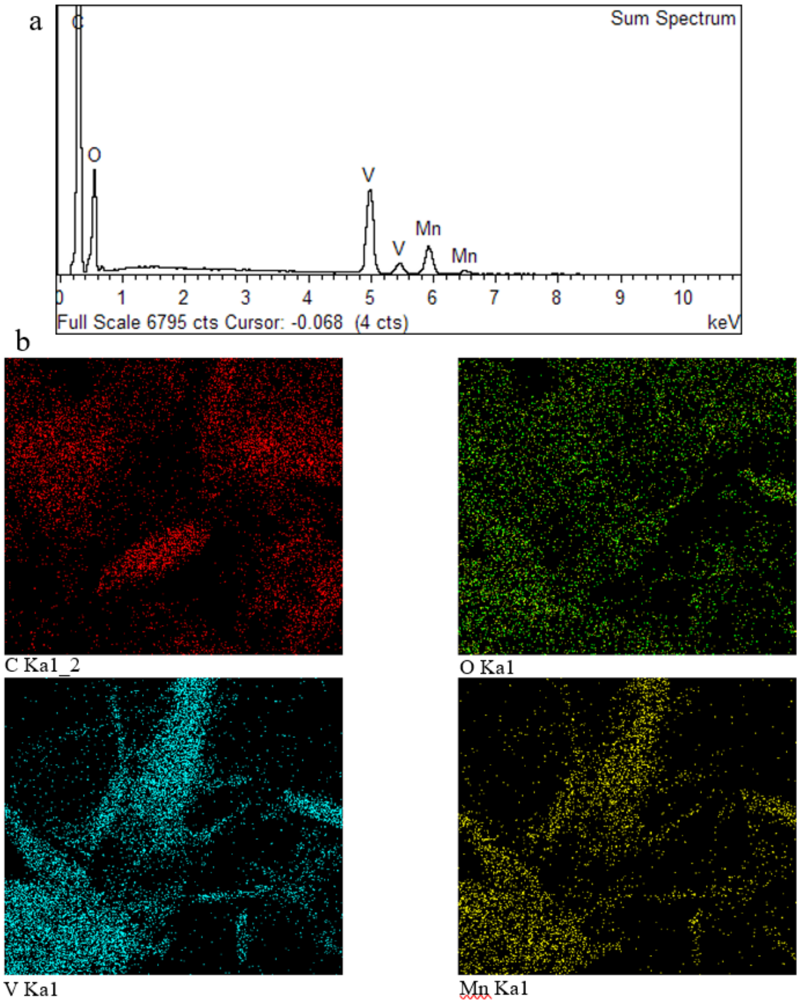

Figure 7.5: (a) EDS scanning of G-8MVO and (b) its corresponding elemental mapping analysis.

It is noteworthy that only Mn, V, O and C elements can be observed from the EDS spectrum with no addition peak, confirm the purity of the nanocomposite. Furthermore, the EDS mapping result (Figure 7.5b) reveals a uniform dispersion of MnV_2O_6 nanobelts in the graphene-MnV_2O_6 nanocomposite.

The G-8MVO nanocomposite was further analysed by X-ray photoemission spectroscopy to identify the elemental species of the nanocomposite.

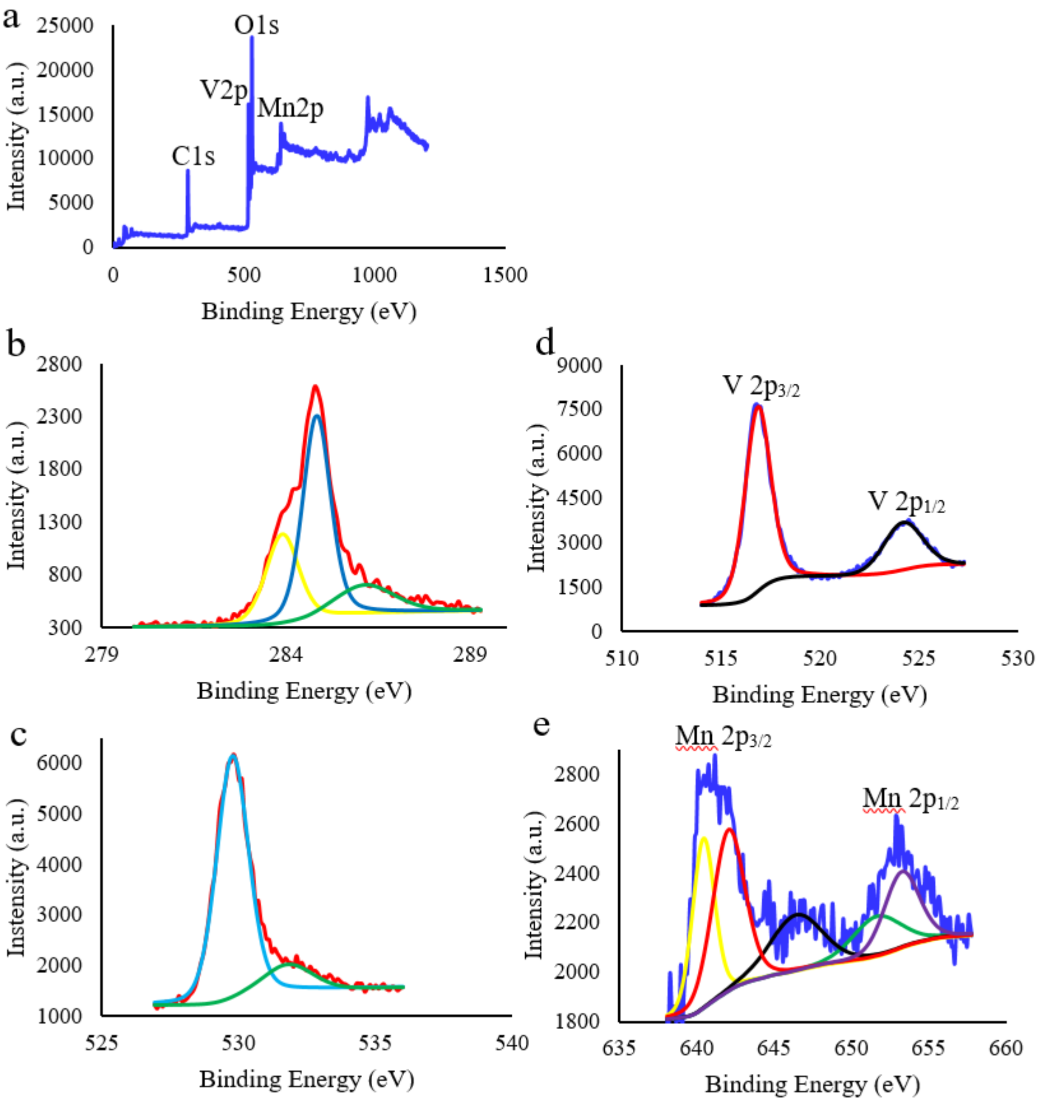

Figure 7.6: (a) Full survey spectra of graphene/MnV_2O_6 nanocomposites and (b-e) high resolution XPS spectra of C1s, O1s, V2p and Mn2p respectively.

The full survey spectrum (Figure 7.6a) shows the photoemission signature of Mn, V, O and C without any impurities. The deconvoluted spectral region of C1s, Mn2p, V2p and O1s of G-8MVO nanocomposite were portrayed in Figures 7.6b-e and each binding energy spectrum was standardised to the C1s core level by using the Gaussian fitting technique. In Figure 7.6b, the pronounced peaks at 284.8 and 286.1

eV are corresponding to the C=C/C-C while the peak at 283.9 eV can be due to the carbon-metal interaction[264, 282, 370]. The O1s spectra (Figure 7.6c) reveals two components at 531.9 eV and 529.8 eV, which are attributed to the adsorption of water on the surface or in the graphene-MnV_2O_6 nanocomposite and the oxygen bonded to Mn and V (Mn-O-V), respectively[364, 370]. In Figure 7.6d, the V2p spectrum of the G-8MVO nanocomposite reveals two peaks at 516.8 eV and 524.2 eV, which is the characteristics of V^{5+} in V $2p_{3/2}$ and V $2p_{1/2}$, respectively. In the deconvoluted spectra of Mn2p (Figure 7.6e), two asymmetrical peaks separated by nearly 11.1 eV can be assigned to Mn $2p_{3/2}$ and Mn $2p_{1/2}$ orbitals. The Mn $2p_{3/2}$ orbital was deconvoluted into two components located at 640.4 and 642.2 eV, which attributed to Mn^{2+}. Similarly, two deconvoluted peaks were observed at 651.6 and 653.3 eV for Mn $2p_{1/2}$ orbital. Meanwhile, a shake-up satellite peak can be observed at 646.4 eV, which are also ascribed to manganese (II)[364, 371]. The XPS results further confirm the successful synthesis of graphene/MnV_2O_6 nanocomposite.

Raman spectroscopy was further applied to explore the molecular structure of the as-prepared nanocomposites. The Raman spectra of pure graphene and G-8MVO nanocomposite are depicted in Figure 7.7, which clearly identifies the Raman scattering of graphene and the vibration modes metal-oxide bonds.

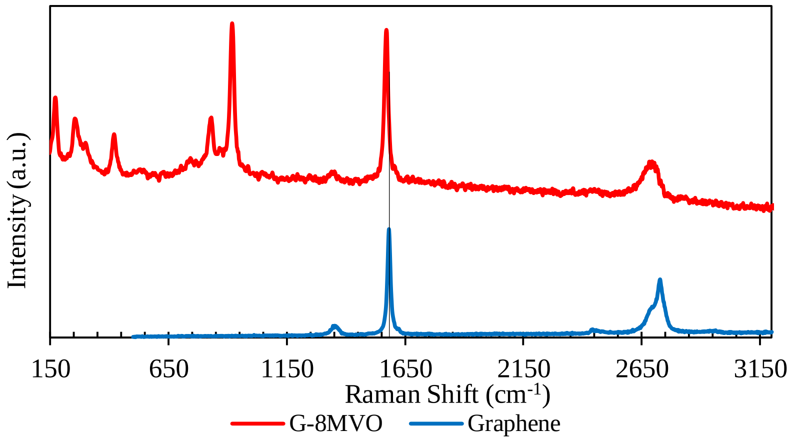

Figure 7.7: Raman spectra of pristine graphene and graphene/MnV_2O_6 nanocomposite (G-8MVO).

The peaks at around 150-450 cm^{-1} could be assigned to the bending mode of V-O and the asymmetric stretching mode of V-O-Mn, while the peaks at 800-950 cm^{-1} could be due to the symmetric stretching vibration of V-O bonds[264, 372, 373]. The characteristic D (disorder band or a ring breathing mode from sp^2 carbon), G (in-plane vibration mode of sp^2 hybridised carbon atom) and 2D (second order of D band) bands at 1360, 1573 and 2700 cm^{-1} implied the presence of graphene in the as-prepared nanocomposites[245, 374]. A slightly shifted G bands observed in the Raman spectrum of G-8MVO represents the charge transfer between graphene and MnV_2O_6, suggesting the intimate contact and interaction between them[80].

7.3.2 Electrochemical properties of MnV_2O_6 and graphene/MnV_2O_6 nanohybrids

The electrochemical behaviour of MnV_2O_6 and graphene/MnV_2O_6 nanocomposites was determined by performing cyclic voltammetry (CV), galvanostatic charge-discharge (GCD) and electrochemical impedance spectroscopy (EIS) in a symmetrical two electrode configuration. Figure 7.8a shows the CV profiles of

MnV_2O_6 and graphene/MnV_2O_6 nanocomposites within a voltage ranging from -1 to 1 at a scan rate of 50 mVs^{-1}.

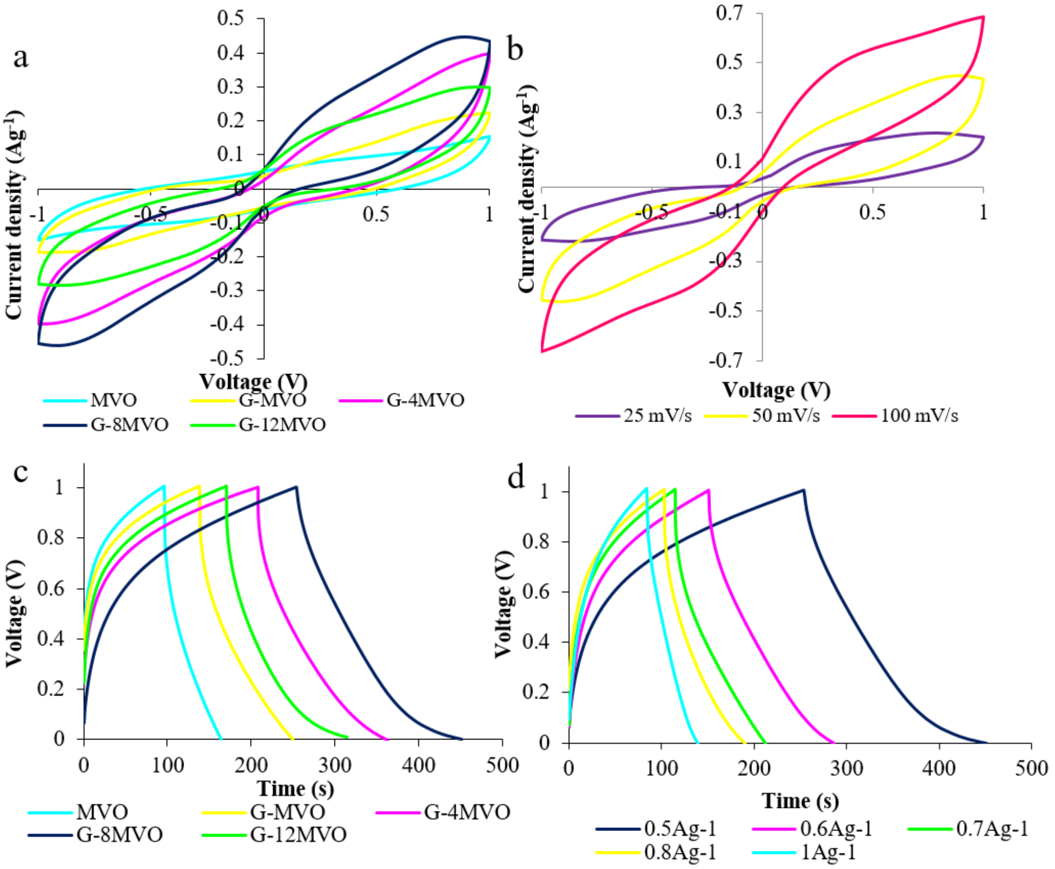

Figure 7.8: Cyclic voltammetry profiles of (a) pure MnV_2O_6 and graphene/MnV_2O_6 nanocomposites, (b) G-8MVO at different scan rates and galvanostatic charge discharge of (c) pure MnV_2O_6 and graphene/MnV_2O_6 nanocomposites, (d) G-8MVO at different current densities.

These MnV_2O_6 and graphene/MnV_2O_6 electrodes present a classical pseudocapacitive nature, which is evidenced from the non-rectangular shapes. Two pairs of redox peaks (0.25 V, 0.85 V, -0.25 V, -0.85 V) can be noticed for graphene/MnV_2O_6 nanocomposites, corresponding to the charge transfer kinetics of Mn/Mn(II) and V(IV)/V(V)[355, 364]. Besides, the CV curvature of G-8MVO shows the largest integrated area, revealing prompt redox kinetics processes and higher specific capacitance of this electrode compared to MnV_2O_6 and other graphene/MnV_2O_6 nanocomposites. The enhanced energy storage capacity of G-

8MVO could be originated from the synergistic effect of the graphene network and MnV_2O_6 as the embodiment of graphene nanosheets increase the specific surface area and provide abundant electroactive sites, which eventually promotes the electrolyte access and exposure of electroactive sites to the electrolyte. Moreover, graphene as a conducting matrix shorten the ions and electrons diffusion path and reduces the internal resistance[265, 375]. Furthermore, the shape of CV curves (G-8MVO) was maintained even at high scan rates (Figure 7.8b), further confirming its excellent rate capability and electrochemical reversibility. The anodic and cathodic peaks are found shifted towards positive and negative direction with increasing scan rate, which resulted from internal resistance. Extensive reports have been published regarding the observance of this shifting phenomena. In addition, the increase in peak current density can be observed when elevating the scan rate from 25 to 100 mVs^{-1}, which might be owing to the effect of scan rate on the migration of electrolyte ions and their diffusion to the interior of electrode[14, 42]. At low scan rate, a thick diffusion layer forms at the electrode surface and it inhibited the flux of electrolyte ions into the electrode, resulted in low peak current. In contrast, no diffusion layer is allowed to grow on the electrode surface at high scan rate, which ameliorated the flux of electrolyte ions into the electrode and hence leading to increase peak current[376].

To determine the potential of MnV_2O_6 and graphene/MnV_2O_6 nanocomposites electrodes for supercapacitor, these nanomaterials were further analysed through the GCD method. By referring to the GCD profile of the as-prepared nanomaterials, the specific capacitance of the electrode can be calculated by using equation 3.1[264]:

Ultimately, the superior specific capacitance of the nanohybrid can be evaluated based on the GCD analysis of each nanohybrid electrode (Figure 7.8c). The non-linear curves were observed for all the nanohybrids, further revealing that specific capacitance derives from the Faradaic redox reaction (pseudocapacitive in nature) and these results are in line with the CV analysis (Figure 7.8a).

Table 7.2: Specific capacitance of the nanocomposites at 0.5Ag^{-1}.

Electrode	Specific Capacitance (Fg^{-1})
MVO	164
G-MVO	236
G-4MVO	308
G-8MVO	348
G-12MVO	282

G-8MVO with an optimised weight ratio of 1:8 exhibited the highest specific capacitance than the virgin MnV_2O_6 and other graphene/MnV_2O_6 combinations (Table 7.2). A significant increment of specific capacitance was perceived for G-8MVO after incorporation of graphene, as described by the longest discharge curve density of the GCD profile of G-8MVO compared to other as-prepared nanocomposites. It is well known that the weight ratio of graphene to mixed transition metal oxide plays a critical role in determining the charge storage properties. The better specific capacitance of G-8MVO could be due to the adequate deposition of MnV_2O_6 on the graphene surface, which allows the effective utilisation of the electrode material and enhanced the electrochemical features. Besides, the conductive network of graphene intensifies the electrical conductivity and shortens the ion's diffusion path throughout the hybrid electrode material and hence promotes the penetration of electrolytic ions into the inner cavity of the electrode. Nevertheless, beyond the optimum weight ratio of graphene to MnV_2O_6, the MnV_2O_6 will agglomerate on the surface of graphene rather than distributed evenly. This will obstruct the ions migration route and increase the ions diffusion resistance, which hinder the penetration of electrolyte ions to the cavity of the electrode[377]. Thus, the specific capacitance was increased initially as the weight ratio is increased from 1 to 8, but decreased drastically with an abrupt increase in the weight ratio. Furthermore, the G-8MVO exhibited specific capacitance as high as 348 Fg^{-1}, 331.2 Fg^{-1}, 313.6 Fg^{-1}, 294.4 Fg^{-1} and 272 Fg^{-1} at 0.5, 0.6, 0.7, 0.8 and 1 Ag^{-1}, respectively (Figure 7.8d). For G-8MVO electrode, 78.2 % of the primary capacitance was retained at 1 Ag^{-1}, revealing its excellent rate capability. This can be attributed to the outstanding electrical conductivity and the synergistic effects between graphene and MnV_2O_6. Moreover, the sluggish rate of diffusion of OH^- ions into the bulk of electrode with increasing current density might be the reason that lead to the decrement of specific capacitance[376, 378].

Electrochemical impedance spectroscopy (EIS) is also conducted to determine the peculiar electrochemical mechanism and resistive properties of the as-synthesised nanocomposites in the frequency ranging from 0.01 Hz to 100 kHz.

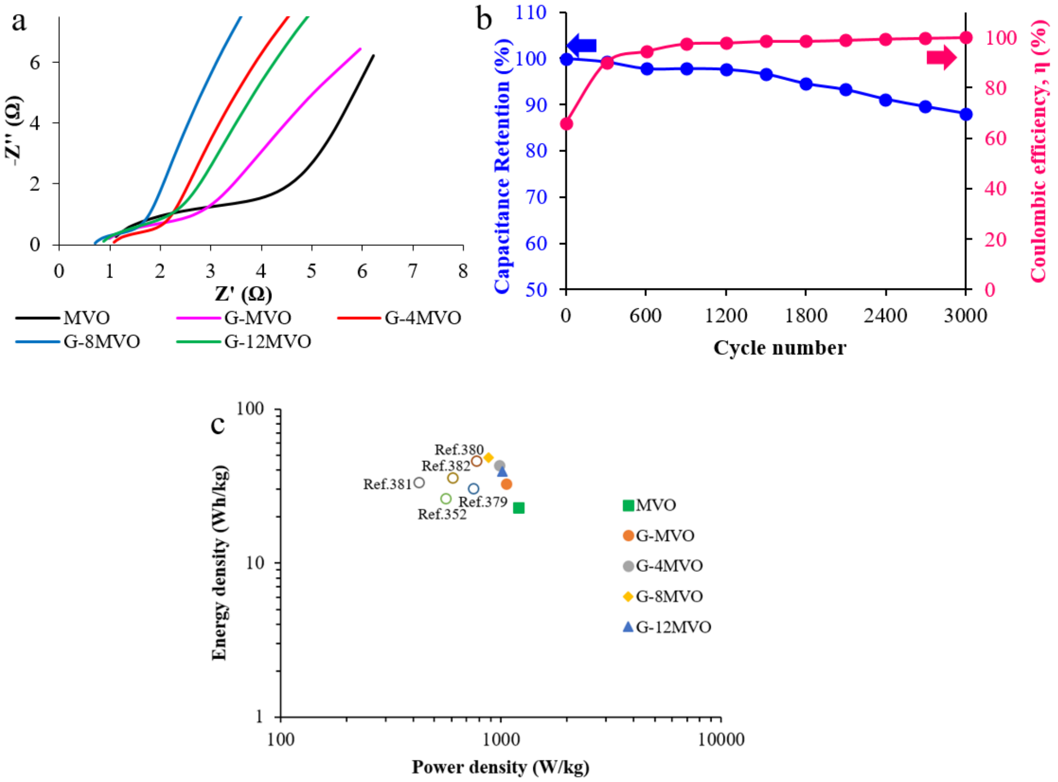

Figure 7.9: (a) Nyquist plots of pure MnV_2O_6 and graphene/MnV_2O_6 nanocomposites, (b) Cycling stability and coulombic efficiency of G-8MVO and (c) Ragone plot of the as-synthesised nanocomposites.

In the Nyquist plot (Figure 7.9a), the interception of the semicircle end with the real impedance axis is referred as the solution resistance (R_s), which is associated to: (i) ionic resistance of the electrolyte, (ii) inherent resistance of the electrode and (iii) contact resistance between the current collector and the active material. The radius of the semicircle is denoted as the charge transfer resistance (R_{ct}) of the electrode and the electrolyte interface. The slope of the line at low frequency region is recognised as the Warburg Impedance (W)[376, 377]. It is noteworthy that the gradient of the Warburg impedance line of G-8MVO nanocomposite was higher than the other samples, which can be elucidated by its fast ions and electrons diffusion process. The R_{ct} values were observed to be 1.73 Ω, 2.17 Ω, 2.71 Ω, 3.55 Ω and 6.59 Ω for G-8MVO, G-4MVO, G-12MVO, G-MVO and MVO, respectively. G-8MVO is found to possess the lowest R_{ct} values among these samples, suggesting its best potential for electrochemical reactions. This can be attributed to the graphene network and the MnV_2O_6, which intensifies the electrochemical performance with exclusive redox reaction kinetics. Moreover, the R_s values of the nanocomposites were found to be ranging from 0.75 to 1 Ω, further confirming the excellent electrical conductivity of the electrodes with the presence of graphene.

Cycling lifespan is another beneficial feature to study the electrochemical behaviour of the graphene/MnV_2O_6 nanocomposite. The cycling stability test was carried out at the constant current density of 1 Ag^{-1} for 3000 cycles. As presented in Figure 7.9b, G-8MVO nanocomposite delivered enhanced durability. Particularly, 88 % of the capacitance was still retained even after 3000 cycles. The exceptional robustness of G-8MVO nanocomposite can be explicated by the integration of graphene scaffold, which inhibits the aggregation of nanostructures effectively and prevent the structural deterioration during the repeating charge-discharge process[378]. Notably, a remarkable columbic efficiency of nearly 100 % was achieved for G-8MVO nanomaterial after 3000 cycles, revealing the excellent reversibility of the electrode material. This result is calculated from equation (3.2)[264].

Since the practical performance of a supercapacitor can be evaluated by determining the sustainability of its high energy density at high power density, Ragone plots was generated (Figure 7.9c) and the related energy density and power density were calculated through equations (3.3) and (3.4)[264]. Evidently, the maximum energy density of 48.3 Wh/kg at a power density of 880.6 W/kg was achieved for G-8MVO electrode in the optimum potential window of 1 V, which was much higher than the other combination of graphene/MnV_2O_6 nanocomposites and some reported literature values[352, 379-382].

The excellent specific capacitance with satisfactory cycling stability and rate capability of G-8MVO nanocomposite can be ascribed to the following factors: (i) The hierarchical structure of MnV_2O_6 nanobelts favours the electron transport, which is crucial for high power energy storage. (ii) The presence of graphene increases the specific surface area between the active material and the electrolyte as compared to virgin MnV_2O_6, resulting in effective redox reaction. (iii) Integration of graphene increases the electrical conductivity and boosts the electron mobility of the nanocomposite. (iv) During the hydrothermal reaction, the decoration of MnV_2O_6 nanobelts on the graphene surface weakens the π-π interaction between the graphene sheet and this will inhibit the agglomeration between the graphene and increase the interplanar spacing, resulted in the advance accessibility of the graphene sheet to the electrolyte. (v) The inter-component synergistic effect and appropriate Mn/V ratio can reduce the electron diffusion resistance and allow more participation of active atoms in the electrochemical reactions at high current density, and hence ameliorating the rate capability.

7.4 Summary

In summary, manganese vanadate nanobelts on graphene were synthesised via a solvothermal process. The MnV_2O_6 nanobelts were homogenously dispersed on the surface of graphene without any severe agglomeration at appropriate graphene/MnV_2O_6 ratio (1:8). Benefiting from the hierarchical nano-architecture of the graphene/MnV_2O_6 nanocomposite, the synthesised G-8MVO nanocomposite delivered promising capacitive and cycling performance as the electrode material for supercapacitor. A maximum specific capacitance of 348 Fg^{-1} was achieved for G-8MVO electrode at the current density of 0.5 Ag^{-1}. A capacitance retention of 88 % was achieved after 3000 cycles at 1 Ag^{-1}, suggesting its excellent specific capacitance and cycling stability. To the best of our knowledge, this is the first paper reporting on the synthesis technique and the supercapacitive property of graphene/MnV_2O_6 nanohybrid. The promising cycling stability along with excellent energy density and power density make the G-8MVO nanocomposite as a promising candidate for supercapacitor application.

Chapter 8: Three-dimensional lion's mane like AlV_3O_9 deposited on graphene surface for supercapacitors with a promising electrochemical performance

8.1 Introduction

Recently, metal vanadate has evoked a broad interest in the field of energy storage. This is because vanadium is a multivalent metallic element which comprises multiple oxidation states, such as +5, +4 and +3, and hence enhances the charge storage ability [3]. Various metallic vanadates, such as $Ni_3V_2O_8$ [263, 285], $BiVO_4$ [318, 348] and $Co_3V_2O_8$ [190] were extensively exploited for supercapacitor application. However, only a few studies have been reported on the application of AlV_3O_9, which could have desirable electrochemical properties as an active electrode for the energy storage application. For example, a comparison between Al-inserted vanadium pentoxide (V_2O_5) and pristine V_2O_5 as the cathode material for lithium ion batteries was reported by Cheah *et al.* [383]. Their findings suggested that the charge storage ability could be improved with the presence of Al.

As inspired by the aforementioned findings, it can be hypothesised that the integration of graphene with AlV_3O_9 may deliver outstanding electrochemical activities in a supercapacitor. Herein, one-pot solvothermal technique was applied in the fabrication of graphene/AlV_3O_9 microsphere nanocomposites. To the best of our knowledge, the author believed that this is the first study reported on the synthesis of graphene/AlV_3O_9 nanocomposites and their corresponding electrochemical performances as novel active electrode materials for the symmetric supercapacitor application. The objectives of this study are summarised as follows: (i) characterising the as-prepared graphene/AlV_3O_9 nanocomposites through multiple characterisation techniques; (ii) analysing the electrochemical performance of the as-synthesised graphene/AlV_3O_9 nanocomposites; (iii) examining the synergistic effect of electrochemical storage between graphene and AlV_3O_9 by varying their weight ratios.

8.2 Experimental methods

8.2.1 Graphene/AlV_3O_9 microspheres nanocomposites

In brief, 1.8 mmol of NH_4VO_3 was dissolved into 80 mL DI water at 80 ^{o}C. A 40 mL graphene dispersion was then added into the solution and mixed for 10 minutes. Subsequently, HCl (1M) was added slowly into the mixture to adjust the pH to about 3. 3.6 mmol of $AlCl_3$ was added into the mixture under continuous magnetic stirring. The resulting mixture was then poured into the 150 mL of a Teflon-lined stainless steel hydrothermal reactor and kept at 160 ^{o}C for 6 hours. After that, the precipitate was collected, washed through centrifugation and dried at 80 ^{o}C for 6 hours. Finally, the dried product was annealed in air at 450 ^{o}C for 2 hours to obtained the crystalline graphene/AlV_3O_9 nanocomposites. Pure AlV_3O_9 was prepared with the same method without addition of graphene.

Additionally, nanocomposites with different weight ratios of graphene/AlV_3O_9 were also prepared to study the synergistic effect between graphene and AlV_3O_9 as mentioned in Table 8.1.

Table 8.1: List of graphene/AlV_3O_9 nanocomposites with different weight ratio.

Nanocomposites	**Graphene (g)**	**$AlCl_3.6H_2O$ (g)**	**NH_4VO_3 (g)**
G-AlV	0.200	0.211	0.869
G-3AlV	0.200	0.632	2.607
G-5AlV	0.200	1.053	4.346
G-7AlV	0.200	1.474	6.084

8.3 Results and discussions

8.3.1 Material Characterisation

Figure 8.1 demonstrates the detailed morphological structures of the as-prepared graphene/AlV_3O_9 nanocomposites.

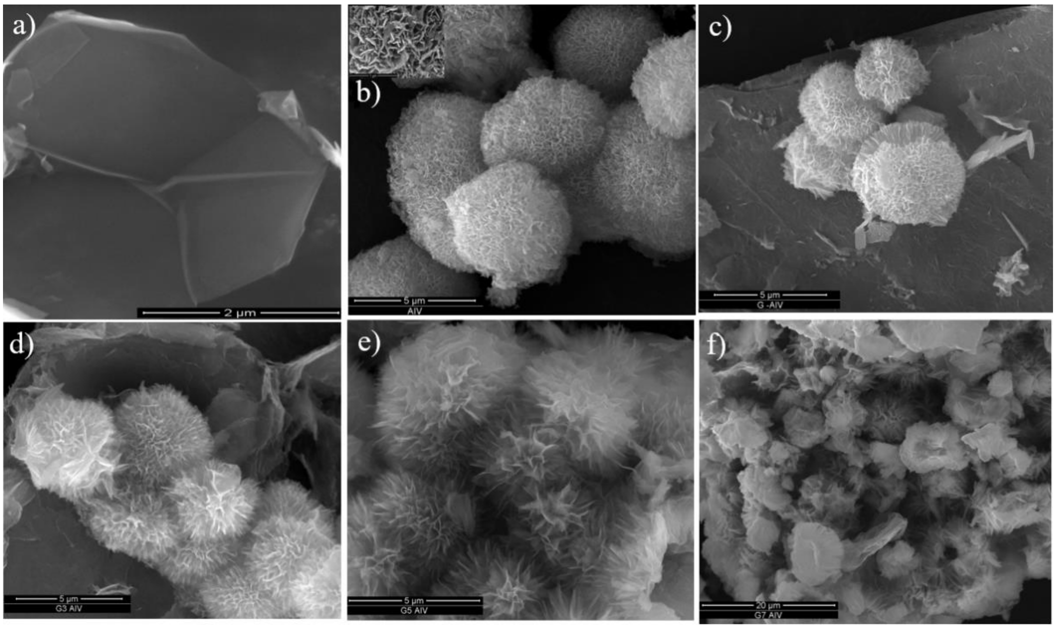

Figure 8.1: FESEM of: a) graphene, b) sole AlV_3O_9 and (c to f) graphene/AlV_3O_9 nanocomposites at different weight ratios (G-AlV, G-3AlV, G-5AlV and G-7AlV).

As shown in Figure 8.1a, the pristine graphene sheets are well exfoliated. The wrinkles observed over the graphene surface are attributed to the pleated graphene sheets. It is worth mentioning that the sole AlV_3O_9 presents 3D hierarchical microspheres with the lion’s mane like structure. The diameters of these microspheres are within the range of 3 to 7 μm, where the building blocks for these microspheres are nanoflakes. Both the graphene and AlV_3O_9 are observed in the morphological structure of the graphene-AlV_3O_9 nanocomposites (Figures 8.1c to f), indicating that the AlV_3O_9 microspheres were successfully decorated on the graphene surface. These unique nanoarchitectures were expected to improve the electrical conductivity and the charge storage ability of the sole AlV_3O_9 by enhancing the electrolyte and the ion transmission process [384, 385].

The weight ratios between graphene and AlV_3O_9 and their influences on the morphological structure were also investigated in this study and the results are illustrated in Figures 8.1c to f. Notably, the lion’s mane like AlV_3O_9 microspheres are evenly decorated on the graphene surface in G-5AlV (Figure 8.1e) as the amount of AlV_3O_9 was just appropriate for covering the graphene sheet. This is beneficial for the effective Faradaic redox reaction as the surface ratio of Faradaic AlV_3O_9 was fully utilised and hence resulted in an exceptional capacitive performance [265, 386]. Nonetheless, the AlV_3O_9 microspheres tended to agglomerate with each other as the weight ratio of graphene and AlV_3O_9 was increased to 1:7. This highly dense structure may impede the electrical conductivity and the active sites of the nanocomposites, and hence resulting in sluggish ion and electron penetration process which limited their capacitive performance [231].

The morphological structure of G-5AlV was further characterised by TEM (Figure 8.2a) and HRTEM (Figure 8.2b).

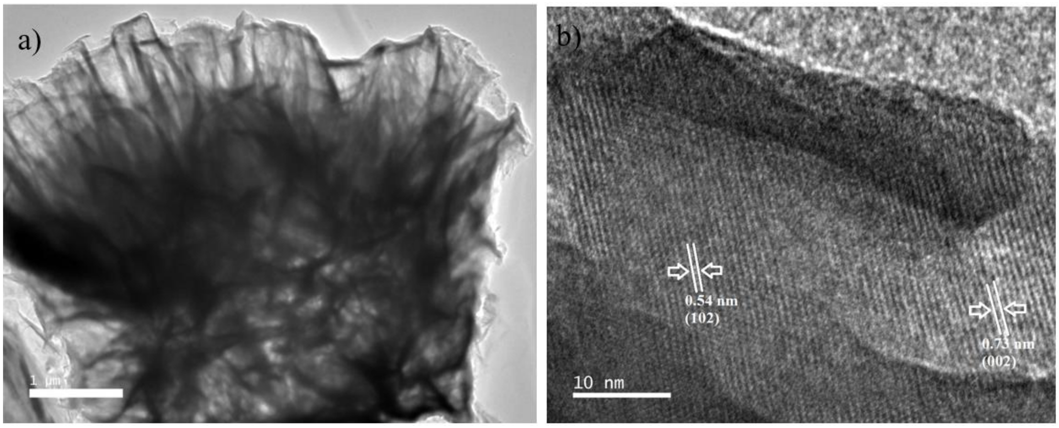

Figure 8.2: a) TEM image of G-5AlV, b) HRTEM image of G-5AlV nanocomposite.

From the TEM micrograph, it is evident that the AlV_3O_9 microspheres with a lion’s mane like structure were deposited on the graphene sheet and these micropsheres were assembled by the nanoflakes. The lattice spacing in the G-5AlV nanocomposites from Figure 8.2b was found to be 0.54 nm and 0.73 nm, which could be ascribed to the (102) and (002) planes of AlV_3O_9, respectively.

The presence of cobalt (Co), vanadium (V), oxygen (O) and carbon (C) in the EDX spectrum of G-5AlV (Figure 8.3a) confirms the high compositional purity of the nanocomposite and the successful deposition of lion’s mane like AlV_3O_9 microspheres on graphene sheets.

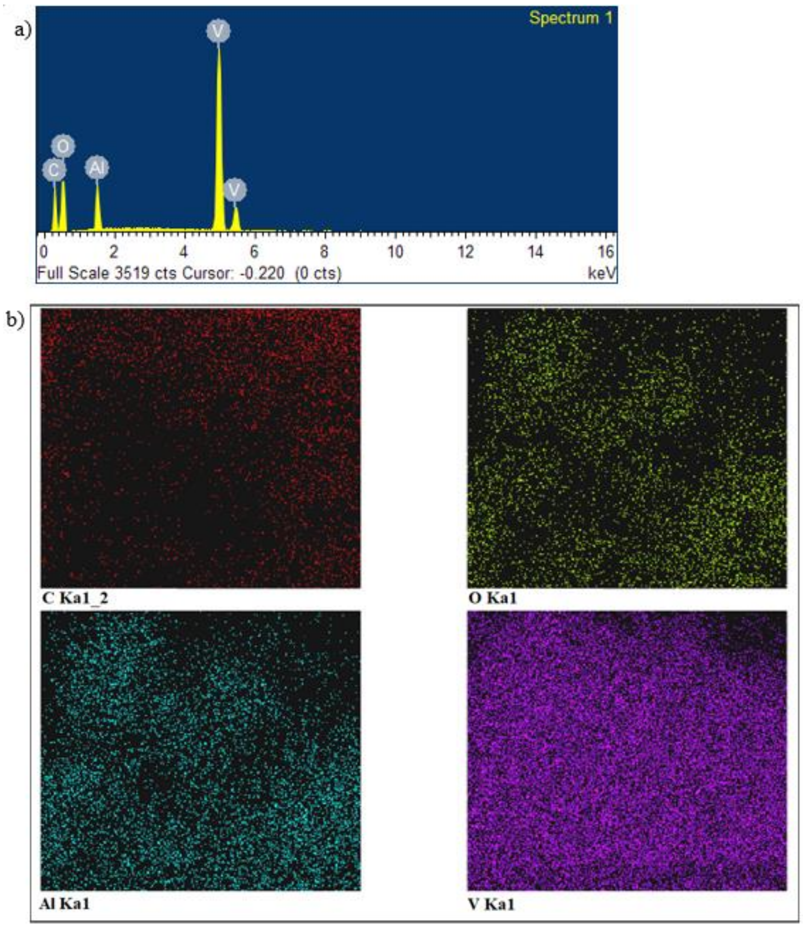

Figure 8.3: a) EDX scanning of G-5AlV nanocomposite from SEM images and b) elemental mapping analysis of C, O, Al, V elements.

Their corresponding elemental mappings in Figure 8.3b further indicate the homogenous distribution of AlV_3O_9 microspheres on the graphene surface, which is in agreement with the SEM result in Figure 8.1e.

To study the valence oxidation states of the elements in G-5AlV nanocomposite, XPS analysis was conducted and the corresponding results are presented in Figure 8.4.

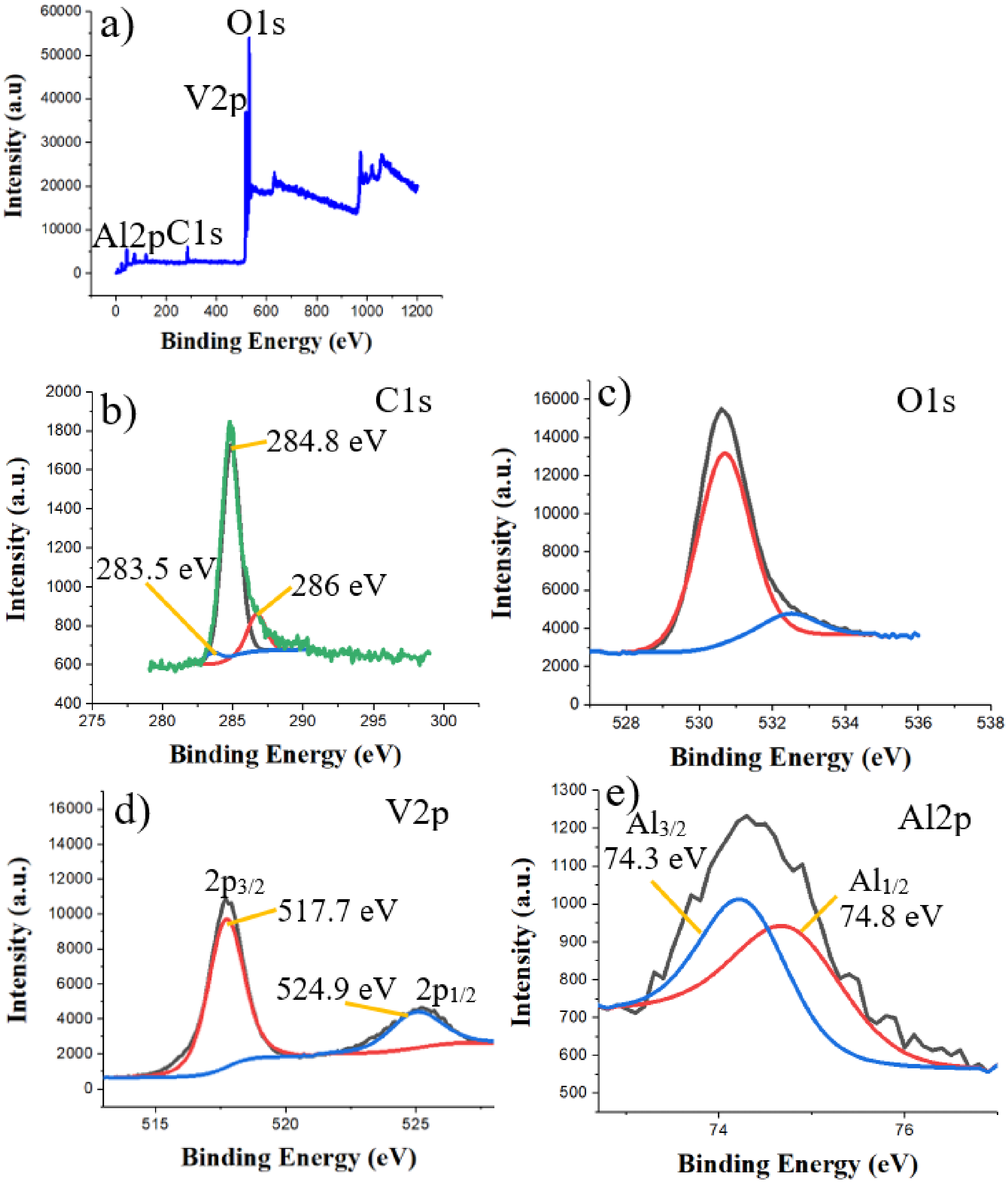

Figure 8.4: a) XPS full analysis spectrum of G-5AlV nanocomposite, b) Core-level survey spectra of C1s, O1s, V2p and Al2p orbits.

Figure 8.4a delineates the full XPS survey spectrum of G-5AlV, where the existence of carbon, aluminium, vanadium and oxygen elements are again validated. The C1s spectrum in Figure 8.4b demonstrates 3 peaks, whereas the predominant peaks at 284.8 and 286 eV denote the C=C and C-C bondings, respectively, and the relatively low intensity peak at 283.5 eV represents the C-Al interaction [265]. Two peaks could be resolved from the O1s spectrum in which the peak located at 532.5 eV could be attributed to the adsorbed oxygen species, while the peak at 530.6 eV associates to the lattice metal-oxygen interaction such as the Al-O and V-O bonds [231]. The Al 2p spectrum in Figure 8.4c encompasses two resolved peaks at 74.3 and 74.8 eV. The first peak could be assigned to the Al $2p_{3/2}$ while the latter one could be attributed to Al $2p_{1/2}$. The V2p spectrum reveals two de-convoluted peaks at 517.7 and 524.9 eV, which could be attributed to the V $2p_{3/2}$ and V $2p_{1/2}$ of vanadium with the oxidation state of +5, respectively [194].

Figure 8.5 illustrates the Raman spectra of the pure graphene and the graphene-AlV_3O_9 nanocomposite.

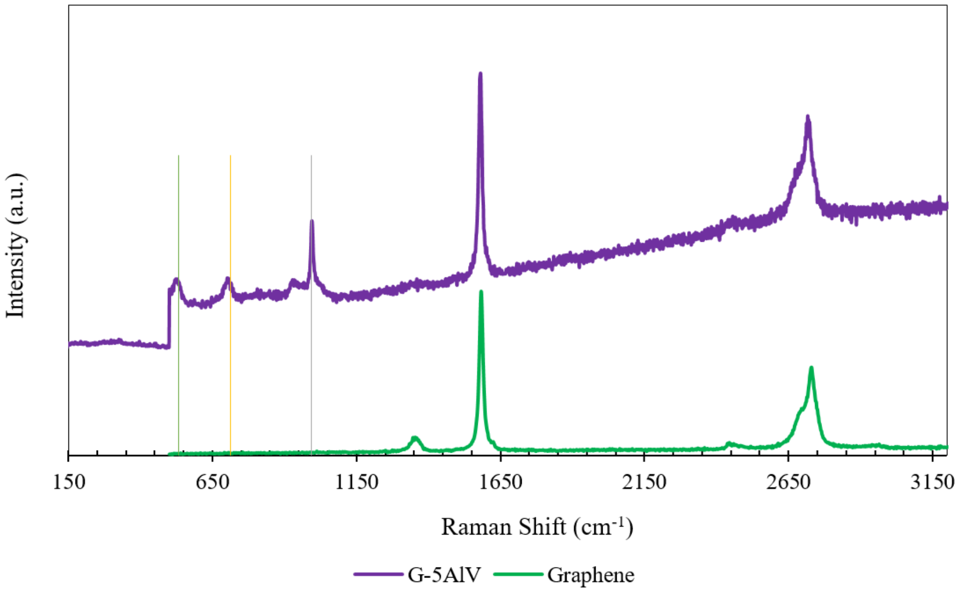

Figure 8.5: Raman survey spectra of graphene and G-5AlV.

The graphene sheet could be classified into 3 bands, namely G, D and 2D along with their respective protruding peaks at the Raman shifts of 1582, 1360 and 2726 cm^{-1}. The D and 2D bands relate to the disorganised vibration of C-C in the sp^3

lattice structure while the G band is attributed to the first order scattering of sp^2 carbon atoms (E_{2g} phonons) [387-390]. The other three distinct peaks could be observed in the regions of 500-550 cm^{-1}, 700-750 cm^{-1} and 950-1000 cm^{-1}. The peak in the region of 500-550 cm^{-1} could be assigned to the (Al-O-V) asymmetric stretching vibration. Furthermore, the peak at 600-750 cm^{-1} is related to the anti-stretching vibration of the V-O bonds while the peak at 950-1000 cm^{-1} is correlated to the stretching of terminal V=O in the vanadate species with the tetrahedral coordination [391, 392].

Figure 8.6 depicts the XRD patterns of graphene, AlV_3O_9 and graphene-AlV_3O_9 nanocomposites.

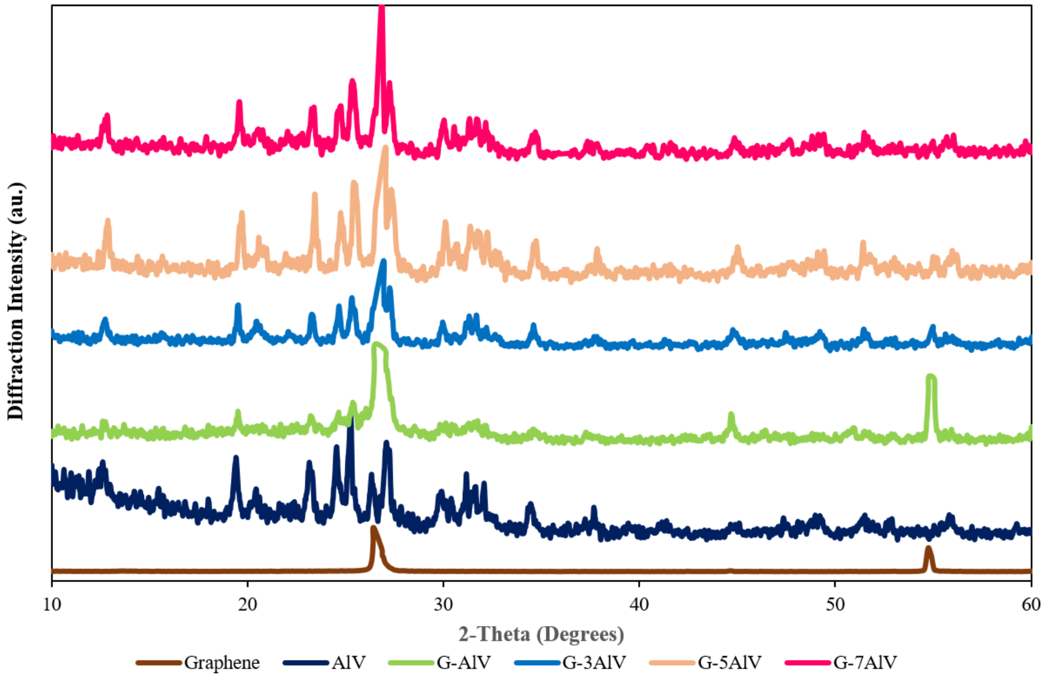

Figure 8.6: XRD of graphene, pure AlV_3O_9 and graphene/AlV_3O_9 nanocomposites (G-AlV, G-3AlV, G-5AlV and G-7AlV).

Two strong maxima at 26.8° and 54.9° could be observed from the XRD spectra of graphene, which are attributed to the (002) and (004) graphene planes, respectively

[263, 265]. Besides, the sharp diffraction peaks of AlV_3O_9 could be observed after calcining the nanocomposites at 450ºC for 2 hours, implying the high crystallinity of the product and this result reveals the monoclinic phase of the crystalline AlV_3O_9 (JCPDS-49-0694)[193, 194]. Notably, all the diffraction peaks of graphene and AlV_3O_9 are present in the reflection patterns of the graphene-AlV_3O_9 nanocomposites without indications of other impurity phases. This suggests the high purity of the as-synthesised nanocomposites and that the incorporation of graphene did not interfere with the monoclinic lattices of AlV_3O_9.

8.3.2 Electrochemical characterisation

To evaluate the electrochemical potential of the nanocomposites, CV analysis was conducted at the constant scan rate of 50 mVs^{-1} and the corresponding profile is shown in Figure 8.7a.

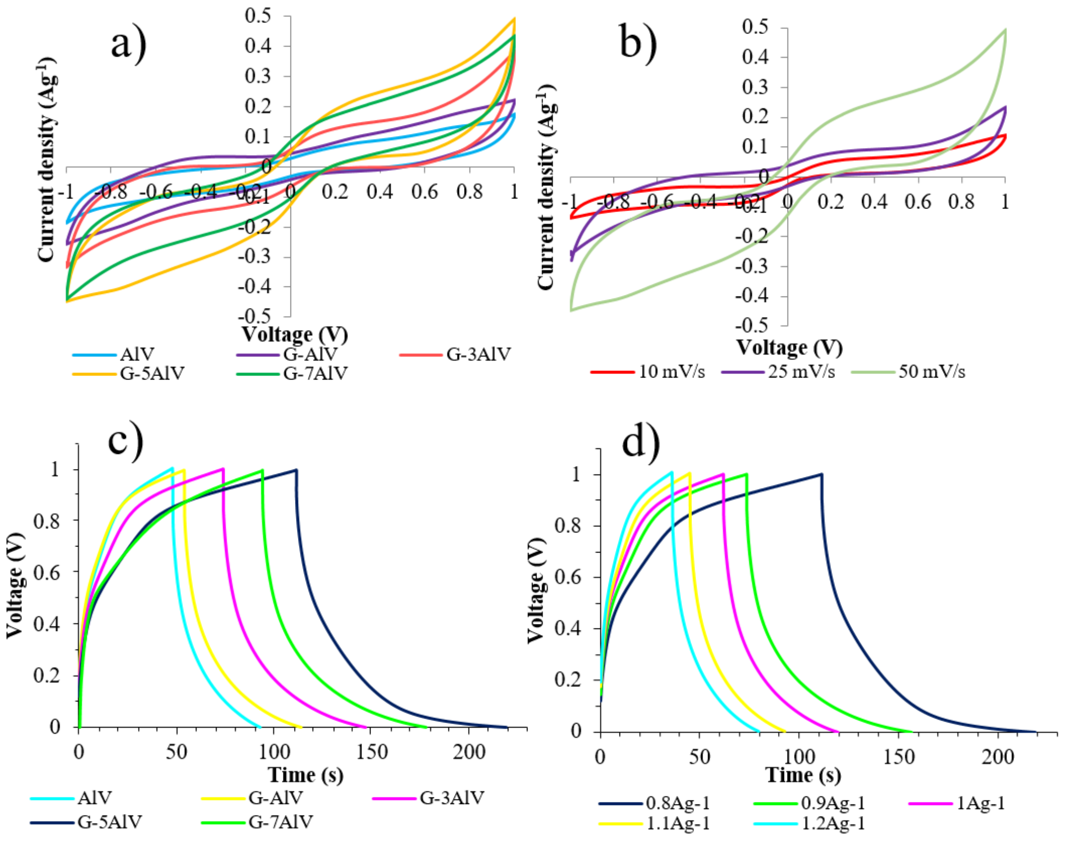

Figure 8.7: CV profiles of a) sole AlV_3O_9 and graphene/AlV_3O_9 nanocomposites at the scan rate of 50 mV/s, b) G-5AlV at different scan rates and GCD profiles of c) pure AlV_3O_9 and graphene/AlV_3O_9 nanocomposites at 0.8 Ag^{-1}, d) G-5AlV at different current densities.

Apparently, G-5AlV nanocomposite possessed the largest enclosed area with the highest current density, suggesting its superior energy storage capacity [393]. This could be attributed to the favourable framework formed by the intimate connection between the graphene sheet and the well-distributed AlV_3O_9 microspheres [342]. At the potentials ranging from -0.3 to 0.3 V, a pair of oxidation and reduction peaks correlated to the X-O/X-O-OH redox reactions (X=Al, V) suggests the contribution of a pseudocapacitance [394]. The CV curves of the G-5AlV nanomaterial at different scan rates are delineated in Figure 8.7b, in which a slight shift of the redox peaks could be noticed. This phenomenon could be explicated by the polarisation of the electrode material [381]. Despite the scan rate was increased, the almost invariable shape and symmetrical redox peaks of the CV curves reveal its low resistivity, relatively fast redox reactions and good reversibility [381, 394].

Figure 8.7c illustrates the voltage as a function of time for all the electrodes at the current density of 0.8 Ag^{-1} within the voltage range from 0 to 1 V. It is worth noting that the charge discharge profiles are nearly symmetrical, indicating the high reversibility nature of the electrode materials [231, 385]. Besides, the non-linear shape of the GCD curves is resulted from the charge transfer process and the adsorption/desorption at the interface between the electrode and the electrolyte. This confirms the hybridisation of the electrical double layer capacitance with the pseudocapacitance properties, and this finding is congruent with the redox peaks in the CV profiles [388]. As shown in Figure 8.7c, G-5AlV delivered the longest discharge time and the smallest IR drop, demonstrating its superior specific capacitance and smaller internal resistance. The equation 3.1 was used to calculate the specific capacitance of the electrode materials. The as-prepared nanocomposites possessed different values of specific capacitance at the constant current density of 0.8 Ag^{-1}, with the values of 140.8 Fg^{-1}, 185.6 Fg^{-1}, 208 Fg^{-1}, 268.8 $F{\cdot}g^{-1}$ and 236.8 Fg^{-1} for AlV, G-AlV, G-3AlV, G-5AlV and G-7AlV nanocomposites, respectively. Notably, G-5AlV exhibited the highest specific capacitance. This exceptional charge storage ability emphasises the prominent contribution of graphene which provides a larger number of redox sites for the efficacious redox reactions and thus improves the electrical conductivity at the optimal mass ratio of graphene-AlV_3O_9 [265].

To further examine the rate capability of the nanocomposite, the GCD analysis of G-5AlV at different current densities was performed and the results are presented in Figure 8.7d. Gradual reduction of the discharge time could be observed as the current density increased, suggesting the lack of the diffusion time for the electrolyte ions to access to the bulk at a high current density condition [265]. The specific capacitances of G-5AlV at different current densities were further analysed and the corresponding result is illustrated in Figure 8.8a.

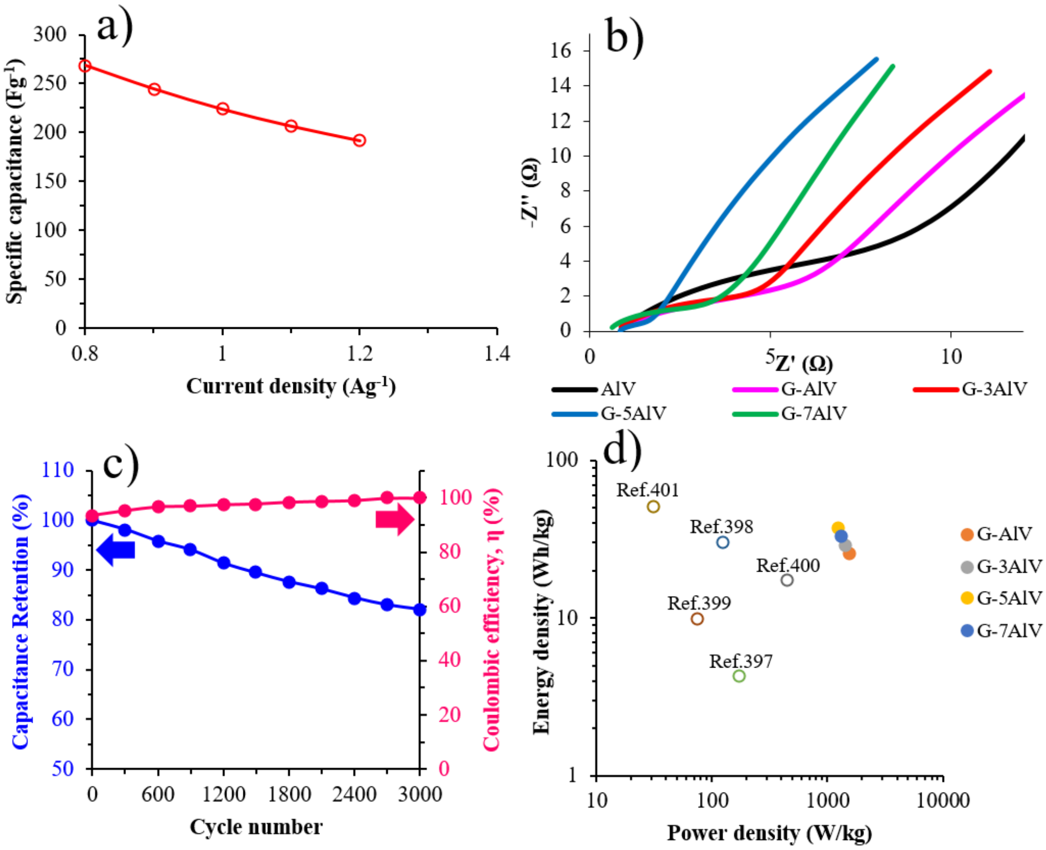

Figure 8.8: a) Specific capacitance of G-5AlV at different current densities, b) EIS plots of pure AlV$_3$O$_9$ and graphene/AlV$_3$O$_9$ nanocomposites, c) Cycling stability and coulombic efficiency of G-5AlV and d) Ragone plot of the as-synthesised nanocomposites.

A descending trend of specific capacitance is noticeable as the current density increased, with the specific capacitance of 268.8, 244.8, 224, 206.6 and 192 Fg^{-1} at 0.8, 0.9, 1, 1.1 and 1.2 Ag^{-1}, respectively. A capacitance retention of 72 % was achieved in the high current density situation, revealing the relatively good rate capability of the G-5AlV nanocomposite. It is believed that the reduction of specific capacitance was originated from the ineffective interaction between the electrode and the electrolyte ions [385]. EIS analysis was carried out in the range of 0.01 Hz to 100 kHz to determine the charge transportation process and the ions diffusion behaviour of the nanocomposites, and the corresponding spectra are shown in Figure 8.8b. Typically, a semicircle at the mid-high frequency region denotes the resistance of charge transfer between the electrodes whereas the low frequency straight line represents the diffusion of electrolyte to the bulk electrode. From Figure 8.8b, it can be seen that G-5AlV demonstrates the lowest R_{ct} followed by G-7AlV, G-3AlV, G-AlV and the pure AlV_3O_9. This could be ascribed to the intimate interfacial connection between the graphene sheet and the AlV_3O_9 microspheres in the G-5AlV sample. These results can also be corroborated with the complete utilisation of the active electrode material as a result of evenly distribution of AlV_3O_9 on the graphene [265, 333, 395]. In addition, the horizontal intercept point of the EIS curves represents the equivalent series resistance (R_{esr}) which is the combination of the resistances of the internal contact, the electrode, the electrolyte and the collector. The obtained R_{esr} of G-5AlV is approximately 0.85 Ω, implying its good ionic and electrical conductivity, and rapid kinetics of charge transfer during the Faradaic reaction at the electrode/electrolyte interface. Moreover, the rapid ions and electrons diffusion kinetics was evidenced by the steeper linear line of G-5AlV in the low frequency region [42, 388].

Cycling stability is another significant parameter assessing the applicability of the supercapacitor electrode. The charge storage ability as a function of the cycle number at a constant current density of 1 Ag^{-1} was determined and illustrated in

Figure 8.8c. Astonishingly, the specific capacitance of G-5AlV was decayed from 224 Fg^{-1} to 184 Fg^{-1} after 3000 cycles (this means a capacitance retention of 82 % of the initial), where this minor decline could be ascribed to the gradual deactivation of the G-5AlV electrode material.

Besides, an exceptional coulombic efficiency (η) of nearly 100 % was obtained for G-5AlV after 3000 cycles, which could be determined by adopting equation 3.2. In overall, the superior coulombic efficiency and cyclic stability of the G-5AlV nanocomposite could be attributed to: (i) the synergistic effect between the graphene and the hierarchical AlV_3O_9 microsphere, in which the graphene serves as a buffering scaffold to remit the volume change during the repeating inter/de-intercalation process of OH^- ions in the electrochemical reactions [388, 396]. (ii) The role of graphene as a skeleton of the nanocomposite which can effectively retain the structural stability upon the long term cycling analysis [333].

The specific energy (E) and the specific power (P) are two significant parameters determining the practicability of the supercapacitor. A Ragone plot of E as a function of P of the graphene-AlV_3O_9 nanocomposites is depicted in Figure 8.8d. Here, the G-5AlV electrode material achieved the maximum energy density of 37.33 Wh/kg at the power density of 1249.07 W/kg, which are higher than those of several reported electrode materials[397-401].

The excellent charge storage ability of G-5AlV could be explicated based on its special features: (i) the homogenous distribution of 3D lion's mane like AlV_3O_9 microspheres on the graphene contributed to the full utilisation of the electrode material and hence resulted in an effective Faradaic reaction [388]; (ii) graphene as the backbone of the nanocomposite could improve the electrolyte ion transmission during the reversible redox reaction as a result of its good chemical stability and superior electrical conductivity [331].

8.4 Summary

A proper amount of AlV_3O_9 anchored on the graphene material is a crucial parameter for determining the charge storage properties of the electrode. With this consideration, G-5AlV is a promising electrode material due to its evenly distributed nanoarchitecture, good electrical conductivity, large specific surface area and advanced charge storage ability. G-5AlV delivered a superior specific capacitance of 268.80 Fg^{-1} at 0.8 Ag^{-1} and maintained 72 % of the initial capacitance (192 Fg^{-1}) as the current density increased, implying its relatively good rate capability. Besides, a capacitance retention of 82 % was achieved together with a coulombic efficiency of nearly 100 % after 3000 repeated charge-discharge cycles, confirming its excellent cycling stability and good reversibility. In addition, the remarkable energy and power densities of G-5AlV suggest that it has a great potential for practical utilisation in supercapacitor.

Chapter 9: Conclusion and future prospective

9.1 Conclusions

A series of mixed transition metal oxide/graphene nanocomposites, with its peculiar architectures like nanoparticles, micro-pencils, nano flakes, nanobelts and microspheres embedded in graphene sheet have been successfully synthesised, characterised and assessed as electrode material for the symmetric supercapacitor application.

Based on the results obtained, the enhancement of the physical, chemical and electrochemical properties of nanocomposites with the integration graphene is clearly evidenced. Furthermore, a summary of the electrochemical performance of the optimal ratio of graphene/MTMO nanocomposites is delineated in Table 9.1.

Table 9.1: A comparison of the electrochemical performance of the optimal electrode materials.

	G-4NVO	**G-4CVO**	**G-3ZVO**	**G-8MVO**	**G-5AlV**
Specific capacitance (Fg^{-1})	368.0	275.2	313.6	348.0	268.8
Capacitance retention (after 3000 cycles)	92 %	81 %	86 %	88 %	82 %
Coulombic efficiency	99 %	98 %	98 %	99 %	99 %
Energy density (Wh/kg)	51.00	38.20	43.55	48.33	37.33

By comparing the electrochemical performance between the five optimised electrode materials (G-4NVO, G-4CVO, G-3ZVO, G-8MVO and G-5AlV), it is noteworthy that graphene/$Ni_3V_2O_8$ with the weight ratio 1:4 (G-4NVO) provides the largest specific capacitance of 368 Fg^{-1}. Additionally, a capacitance retention of 92 % and coulombic efficiency of 99 % were also achieved after 3000 continuous intercalation/deintercalation process. This is because the smaller particle size of the $Ni_3V_2O_8$ nanoparticles on graphene provides more electroactive sites available for faradaic redox reaction. Besides, it also facilitated the ions and electrons diffusion process by shortening the diffusion pathway, and hence led to the superior electrochemical performance. The excellent cycling stability can be attributed to the synergistic effect between graphene and $Ni_3V_2O_8$ where graphene can act as a buffering matrix to resist the volume expansion effectively during the cycling process. Moreover, G-4NVO demonstrated high coulombic efficiency, suggesting the superior reversibility of the electrode material.

Based on the works in this thesis, all the research objectives have been achieved and the following conclusions can be drawn:

- Mixed transition metal oxide (MTMO) and graphene/mixed transition metal oxide nanocomposites with controllable morphological structures were successfully prepared by facile solvothermal technique.
- The incorporation of graphene onto mixed transition metal oxide with an optimum weight ratio provide best synergistic effect, which greatly enhanced the physical (specific surface area, electrical conductivity, structural tenacity and etc.) and electrochemical properties (specific capacitance, cycling stability and etc.) of the nanocomposites.
- The enhancement of electrochemical performances can be ascribed to the synergistic effect between graphene and MTMO where the deposition of MTMO on graphene effectively inhibits the agglomeration of graphene sheets, facilitating the ions and electrons diffusion and hence improve the specific capacitance. Besides, the hybridisation of graphene into MTMO

enhances the electrical conductivity of the nanocomposites, which allow rapid ion diffusion and low charge transfer resistance. Graphene can also act as a buffering matrix to accommodate the volume variation during the cycling test, resulting in excellent cycling stability of the nanocomposites. Moreover, homogenous distribution of MTMO on the graphene surface allows the effective utilisation of the electrode material and enhanced the electrochemical features.

- Among the optimised electrodes, G-4NVO possessed the excellent supercapacitive performance since it has the highest energy density, specific capacitance, cycling stability and coulombic efficiency. G-4NVO also delivered a comparable energy density and power density as compared to other research findings, which undoubtedly induce it as an appealing candidate for advanced future energy storage applications.

9.2 Recommendations

As for supercapacitor, electrode materials play a pivotal role in determining its physical and electrochemical performance. Novel mixed transition metal oxide/graphene nanocomposites with appealing structures and excellent energy storage ability will still attract the research attentions in the couple of years owing to its high flexibility, good structural strength and impressive electrochemical performances. In this section, some recommendations on future research activities and perspectives on the development of supercapacitor are deliberated.

Motivated by the aforementioned results, a simplified prototype device of high performance electrode materials based on the graphene/$Ni_3V_2O_8$ developed by a facile solvothermal process can be assembled and evaluated in future study. Other mixed transition metal oxide such as tungsten, ruthenium, silver and etc. and its integration with graphene are also expected to be designed and evaluated in the future. Other than transition metal oxide, the hybridisation of graphene with another element series such as lanthanide, alkaline metal and metalloids can be recognised as one of the new research directions in exploring the novel and effective electrode material. Besides, discovering a new approach to incorporate graphene with transition metal oxide and other elements to form a robust nanostructure is still the frontier of the research.

Other than electrode materials, selection on electrolyte (aqueous, organic, ionic liquid) also serves as a factor determining the supercapacitor performance, including specific capacitance, cycling stability, power density and most importantly safety. Designing an efficient electrolyte is still one of the challenges in this field. Thus, more research works should be carried out in future regarding the development of efficient electrolyte and the understanding of the electrode-electrolyte interactions.

References:

[1] S. Zheng, H. Xue, H. Pang, Supercapacitors based on metal coordination materials, Coordination Chemistry Reviews, (2017).

[2] L. Feng, Y. Zhu, H. Ding, C. Ni, Recent progress in nickel based materials for high performance pseudocapacitor electrodes, Journal of Power Sources, 267 (2014) 430-444.

[3] Y. Yan, B. Li, W. Guo, H. Pang, H. Xue, Vanadium based materials as electrode materials for high performance supercapacitors, Journal of Power Sources, 329 (2016) 148-169.

[4] Y. Zhang, L. Li, H. Su, W. Huang, X. Dong, Binary metal oxide: advanced energy storage materials in supercapacitors, J. Mater. Chem. A, 3 (2015) 43-59.

[5] R.S. Kate, S.A. Khalate, R.J. Deokate, Overview of nanostructured metal oxides and pure nickel oxide (NiO) electrodes for supercapacitors: A review, Journal of Alloys and Compounds, 734 (2018) 89-111.

[6] M.-C. Liu, L.-B. Kong, L. Kang, X. Li, F.C. Walsh, M. Xing, C. Lu, X.-J. Ma, Y.-C. Luo, Synthesis and characterization of M3V2O8 (M = Ni or Co) based nanostructures: a new family of high performance pseudocapacitive materials, Journal of Materials Chemistry A, 2 (2014) 4919-4919.

[7] R. Sahoo, A. Roy, S. Dutta, C. Ray, T. Aditya, A. Pal, T. Pal, Liquor ammonia mediated V insertion in thin Co_3O_4 sheets for improved pseudocapacitors with high energy density and high specific capacitance value, Chem. Commun., 51 (2015) 15986-15989.

[8] D.R. Rolison, L.F. Nazar, Electrochemical energy storage to power the 21st century, MRS Bulletin, 36 (2011) 486-493.

[9] A. González, E. Goikolea, J.A. Barrena, R. Mysyk, Review on supercapacitors: Technologies and materials, Renewable and Sustainable Energy Reviews, 58 (2016) 1189-1206.

[10] P. Sharma, T.S. Bhatti, A review on electrochemical double-layer capacitors, Energy Conversion and Management, 51 (2010) 2901-2912.

[11] D. Chen, Q. Wang, R. Wang, G. Shen, Ternary oxide nanostructured materials for supercapacitors: a review, J. Mater. Chem. A, 3 (2015) 10158-10173.

[12] G. Lota, K. Fic, E. Frackowiak, Carbon nanotubes and their composites in electrochemical applications, Energy & Environmental Science, 4 (2011) 1592-1592.

[13] S.W. Lee, B.M. Gallant, Y. Lee, N. Yoshida, D.Y. Kim, Y. Yamada, S. Noda, A. Yamada, Y. Shao-Horn, Self-standing positive electrodes of oxidized few-walled carbon nanotubes for light-weight and high-power lithium batteries, Energy Environ. Sci., 5 (2012) 5437-5444.

[14] X. Xu, J. Shen, N. Li, M. Ye, Facile synthesis of reduced graphene oxide/CoWO4nanocomposites with enhanced electrochemical performances for supercapacitors, Electrochimica Acta, 150 (2014) 23-34.

[15] C. Wu, J. Cai, Q. Zhang, X. Zhou, Y. Zhu, L. Li, P. Shen, K. Zhang, Direct growth of urchin-like $ZnCo_2O_4$ microspheres assembled from nanowires on nickel foam as high-performance electrodes for supercapacitors, Electrochimica Acta, 169 (2015) 202-209.

[16] H.W. Jang, D.A. Felker, C.W. Bark, Y. Wang, M.K. Niranjan, C.T. Nelson, Y. Zhang, D. Su, C.M. Folkman, S.H. Baek, S. Lee, K. Janicka, Y. Zhu, X.Q. Pan, D.D. Fong, E.Y. Tsymbal, M.S. Rzchowski, C.B. Eom, Metallic and Insulating Oxide Interfaces Controlled by Electronic Correlations, Science, 331 (2011) 886.

[17] Y.-Z. Zhang, Y. Wang, T. Cheng, W.-Y. Lai, H. Pang, W. Huang, Flexible supercapacitors based on paper substrates: a new paradigm for low-cost energy storage, Chem. Soc. Rev., 44 (2015) 5181-5199.

[18] Y. Xu, J. Wei, L. Tan, J. Yu, Y. Chen, A Facile approach to $NiCoO_2$ intimately standing on nitrogen doped graphene sheets by one-step hydrothermal synthesis for supercapacitors, J. Mater. Chem. A, 3 (2015) 7121-7131.

[19] P.L. Taberna, S. Mitra, P. Poizot, P. Simon, J.M. Tarascon, High rate capabilities Fe3O4-based Cu nano-architectured electrodes for lithium-ion battery applications, Nature Materials, 5 (2006) 567-573.

[20] T.S. Kasırga, J.M. Coy, J.H. Park, D.H. Cobden, Visualization of one-dimensional diffusion and spontaneous segregation of hydrogen in single crystals of VO 2, Nanotechnology, 27 (2016) 345708-345708.

[21] Y. Wang, J. Guo, T. Wang, J. Shao, D. Wang, Y.-W. Yang, Mesoporous Transition Metal Oxides for Supercapacitors, Nanomaterials, 5 (2015) 1667-1689.

[22] H. Wang, H. Dai, Strongly coupled inorganic-nano-carbon hybrid materials for energy storage, Chem. Soc. Rev., 42 (2013) 3088-3113.

[23] S. Vijayakumar, S.-H. Lee, K.-S. Ryu, Synthesis of $Zn_3V_2O_8$ nanoplatelets for lithium-ion battery and supercapacitor applications, RSC Advances, 5 (2015) 91822-91828.

[24] E.R. Ezeigwe, P.S. Khiew, C.W. Siong, M.T.T. Tan, Solvothermal synthesis of NiCo2O4nanocomposites on liquid-phase exfoliated graphene as an electrode material for electrochemical capacitors, Journal of Alloys and Compounds, 693 (2017) 1133-1142.

[25] S. Al-Rubaye, R. Rajagopalan, S.X. Dou, Z. Cheng, Facile synthesis of a reduced graphene oxide wrapped porous NiCo2O4 composite with superior performance as an electrode material for supercapacitors, Journal of Materials Chemistry A, 5 (2017) 18989-18997.

[26] L. Ma, X. Shen, H. Zhou, Z. Ji, K. Chen, G. Zhu, High performance supercapacitor electrode materials based on porous NiCo 2 O 4 hexagonal nanoplates / reduced graphene oxide composites, CHEMICAL ENGINEERING JOURNAL, 262 (2015) 980-988.

[27] Y. Li, L.-b. Kong, M.-c. Liu, W.-b. Zhang, L. Kang, crossmark, Materials Letters, 186 (2017) 289-292.

[28] E.R. Ezeigwe, P.S. Khiew, C.W. Siong, I. Kong, M.T.T. Tan, Synthesis of NiMoO4nanorods on graphene and superior electrochemical performance of the resulting ternary based composites, Ceramics International, 43 (2017) 13772-13780.

[29] R. Kumar, P.K. Gupta, P. Rai, A. Sharma, Free-standing $Ni_3(VO_4)_2$ nanosheet arrays on aminated r-GO sheets for supercapacitor applications, New Journal of Chemistry, 42 (2018) 1243-1249.

[30] V. Soundharrajan, B. Sambandam, J. Song, S. Kim, J. Jo, D.T. Pham, S. Kim, V. Mathew, J. Kim, Bitter gourd-shaped Ni3V2O8anode developed by a one-pot metal-organic framework-combustion technique for advanced Li-ion batteries, Ceramics International, 43 (2017) 13224-13232.

[31] Y. Wei, S. Chen, D. Su, B. Sun, J. Zhu, G. Wang, 3D mesoporous hybrid $NiCo_2O_4$@graphene nanoarchitectures as electrode materials for supercapacitors with enhanced performances, J. Mater. Chem. A, 2 (2014) 8103-8109.

[32] R. Kumar, P. Rai, A. Sharma, 3D urchin-shaped $Ni_3(VO_4)_2$ hollow nanospheres for high-performance asymmetric supercapacitor applications, J. Mater. Chem. A, 4 (2016) 9822-9831.

[33] E. Umeshbabu, G. Rajeshkhanna, P. Justin, G.R. Rao, Synthesis of mesoporous NiCo2O4-rGO by a solvothermal method for charge storage applications, RSC Adv., 5 (2015) 66657-66666.

[34] H. Fan, L. Quan, M. Yuan, S. Zhu, K. Wang, Y. Zhong, L. Chang, H. Shao, J. Wang, J. Zhang, C.-n. Cao, Thin Co3O4 nanosheet array on 3D porous graphene/nickel foam as a binder-free electrode for high-performance supercapacitors, Electrochimica Acta, 188 (2016) 222-229.

[35] J. Yan, T. Wei, W. Qiao, B. Shao, Q. Zhao, L. Zhang, Z. Fan, Rapid microwave-assisted synthesis of graphene nanosheet/Co 3O4 composite for supercapacitors, Electrochimica Acta, 55 (2010) 6973-6978.

[36] E.R. Ezeigwe, M.T.T. Tan, P.S. Khiew, C.W. Siong, Solvothermal synthesis of graphene–MnO2 nanocomposites and their electrochemical behavior, Ceramics International, 41 (2015) 11418-11427.

[37] T.H. Ko, S. Radhakrishnan, M.K. Seo, M.S. Khil, H.Y. Kim, B.S. Kim, A green and scalable dry synthesis of NiCo2O4/graphene nanohybrids for high-performance supercapacitor and enzymeless glucose biosensor applications, Journal of Alloys and Compounds, 696 (2017) 193-200.

[38] J. Xu, L. Li, P. Gao, L. Yu, Y. Chen, P. Yang, S. Gai, P. Yang, Facile preparation of NiCo2O4 nanobelt/graphene composite for electrochemical capacitor application, Electrochimica Acta, 166 (2015) 206-214.

[39] M. Shahid, J. Liu, Z. Ali, I. Shakir, M.F. Warsi, Structural and electrochemical properties of single crystalline MoV 2O8 nanowires for energy storage devices, Journal of Power Sources, 230 (2013) 277-281.

[40] J.P. Wang, S.L. Wang, Z.C. Huang, Y.M. Yu, J.L. Liu, Synthesis of long chain-like nickel cobalt oxide nanoneedles-reduced graphene oxide composite material for high-performance supercapacitors, Ceramics International, 40 (2014) 12751-12758.

[41] X. Xu, L. Pei, Y. Yang, J. Shen, M. Ye, Facile synthesis of $NiWO_4$/reduced graphene oxide nanocomposite with excellent capacitive performance for supercapacitors, Journal of Alloys and Compounds, 654 (2016) 23-31.

[42] S.S. Patil, D.P. Dubal, V.G. Deonikar, M.S. Tamboli, J.D. Ambekar, P. Gomez-Romero, S.S. Kolekar, B.B. Kale, D.R. Patil, Fern-like rGO/BiVO4 Hybrid Nanostructures for High-Energy Symmetric Supercapacitor, ACS Applied Materials & Interfaces, 8 (2016) 31602-31610.

[43] L. Zhang, S. Zheng, L. Wang, H. Tang, H. Xue, G. Wang, H. Pang, Fabrication of Metal Molybdate Micro/Nanomaterials for Electrochemical Energy Storage, Small, 13 (2017) 1-19.

[44] W. Alexander Frank, Structural Inroganic Chemistry, 2012.

[45] D. Rehder, The future of/for vanadium, Dalton Transactions, 42 (2013) 11749-11749.

[46] M. Valizadeh Kiamahalleh, S. Hussein Sharifzein, G. Najafpour, S. Abdsata, Suranibuniran, Multiwalled carbon nanotubes based nanocomposites for supercapacitors: a review of electrode materials, Nano, 07 (2012).

[47] J. Mandapati, K. Balasubramanian, Simple Capacitors to Supercapacitors-An Overview, Int. J. Electrochem. Sci, 3 (2008) 1196-1217.

[48] P. Xiong, J. Zhu, L. Zhang, X. Wang, Recent advances in graphene-based hybrid nanostructures for electrochemical energy storage, Nanoscale Horizons, 1 (2016) 340-374.

[49] L.L. Zhang, X.S. Zhao, Carbon-based materials as supercapacitor electrodes, Chemical Society Reviews, 38 (2009) 2520-2520.

[50] M. Endo, T. Takeda, Y.J. Kim, K. Koshiba, K. Ishii, High Power Electric Double Layer Capacitor (EDLC ' s); from Operating Principle to Pore Size Control in Advanced Activated Carbons, Carbon Science, 1 (2001) 117-128.

[51] J.P. Valleau, G.M. Torrie, The electrical double layer. III. Modified Gouy–Chapman theory with unequal ion sizes, The Journal of Chemical Physics, 76 (1982) 4623-4630.

[52] M.D. Stoller, S. Park, Y. Zhu, J. An, R.S. Ruoff, Graphene-Based Ultracapacitors, Nano Letters, 8 (2008) 3498-3502.

[53] J. Phiri, P. Gane, T.C. Maloney, General overview of graphene: Production, properties and application in polymer composites, Materials Science and Engineering: B, 215 (2017) 9-28.

[54] W.A. Christinelli, R. Gonçalves, E.C. Pereira, A new generation of electrochemical supercapacitors based on layer-by-layer polymer films, Journal of Power Sources, 303 (2016) 73-80.

[55] R. Kötz, M. Carlen, Principles and applications of electrochemical capacitors, Electrochimica Acta, 45 (2000) 2483-2498.

[56] P. Simon, Y. Gogotsi, Materials for electrochemical capacitors, Nature Materials, 7 (2008) 845-845.

[57] C.-M. Chuang, C.-W. Huang, H. Teng, J.-M. Ting, Effects of Carbon Nanotube Grafting on the Performance of Electric Double Layer Capacitors, Energy & Fuels, 24 (2010) 6476-6482.

[58] Z. Wu, Y. Zhu, X. Ji, $NiCo_2O_4$ -based materials for electrochemical supercapacitors, J. Mater. Chem. A, 2 (2014) 14759-14772.

[59] Y. Wang, Y. Song, Y. Xia, Electrochemical capacitors: mechanism, materials, systems, characterization and applications, Chem. Soc. Rev., 45 (2016) 5925-5950.

[60] F.-X. Ma, L. Yu, C.-Y. Xu, X.W. Lou, Self-supported formation of hierarchical NiCo2O4 tetragonal microtubes with enhanced electrochemical properties, Energy Environ. Sci., 9 (2016) 862-866.

[61] L. Yu, B. Guan, W. Xiao, X.W. Lou, Formation of Yolk-Shelled Ni–Co Mixed Oxide Nanoprisms with Enhanced Electrochemical Performance for Hybrid Supercapacitors and Lithium Ion Batteries, Advanced Energy Materials, 5 (2015) 1500981-1500981.

[62] X. Li, L. Zhi, Graphene hybridization for energy storage applications, Chemical Society Reviews, (2018) 42-46.

[63] K. Chen, S. Song, F. Liu, D. Xue, Structural design of graphene for use in electrochemical energy storage devices, Chem. Soc. Rev., 44 (2015) 6230-6257.

[64] R. Raccichini, A. Varzi, S. Passerini, B. Scrosati, The role of graphene for electrochemical energy storage, Nature Materials, 14 (2014) 271-271.

[65] Z.-S. Wu, W. Ren, D.-W. Wang, F. Li, B. Liu, H.-M. Cheng, High-Energy MnO2 Nanowire/Graphene and Graphene Asymmetric Electrochemical Capacitors, ACS Nano, 4 (2010) 5835-5842.

[66] H. Xia, C. Hong, B. Li, B. Zhao, Z. Lin, M. Zheng, S.V. Savilov, S.M. Aldoshin, Facile Synthesis of Hematite Quantum-Dot/Functionalized Graphene-Sheet Composites as Advanced Anode Materials for Asymmetric Supercapacitors, Advanced Functional Materials, 25 (2015) 627-635.

[67] J. Chang, H. Xu, J. Sun, L. Gao, High pseudocapacitance material prepared via in situ growth of Ni(OH)2 nanoflakes on reduced graphene oxide, J. Mater. Chem., 22 (2012) 11146-11150.

[68] H. Wang, H.S. Casalongue, Y. Liang, H. Dai, Ni(OH)2 Nanoplates Grown on Graphene as Advanced Electrochemical Pseudocapacitor Materials, Journal of the American Chemical Society, 132 (2010) 7472-7477.

[69] S. Chen, J. Zhu, X. Wu, Q. Han, X. Wang, Graphene Oxide−MnO2 Nanocomposites for Supercapacitors, ACS Nano, 4 (2010) 2822-2830.

[70] Z.S. Wu, D.W. Wang, W. Ren, J. Zhao, G. Zhou, F. Li, H.M. Cheng, Anchoring Hydrous RuO2 on Graphene Sheets for High-Performance Electrochemical Capacitors, Advanced Functional Materials, 20 (2010) 3595-3602.

[71] Y. Cui, C. Wang, S. Wu, G. Liu, F. Zhang, T. Wang, Lotus-root-like NiO nanosheets and flower-like NiO microspheres: synthesis and magnetic properties, CrystEngComm, 13 (2011) 4930-4934.

[72] M. Liu, J. Chang, J. Sun, L. Gao, A facile preparation of NiO/Ni composites as high-performance pseudocapacitor materials, RSC Adv., 3 (2013) 8003-8008.

[73] X. Xia, Y. Zhang, D. Chao, C. Guan, Y. Zhang, L. Li, X. Ge, I.M. Bacho, J. Tu, H.J. Fan, Solution synthesis of metal oxides for electrochemical energy storage applications, Nanoscale, 6 (2014) 5008-5048.

[74] F. Jiao, A.H. Hill, A. Harrison, A. Berko, A.V. Chadwick, P.G. Bruce, Synthesis of Ordered Mesoporous NiO with Crystalline Walls and a Bimodal Pore Size Distribution, Journal of the American Chemical Society, 130 (2008) 5262-5266.

[75] L. Jun, X. Dongfeng, Thermal Oxidation Strategy towards Porous Metal Oxide Hollow Architectures, Advanced Materials, 20 (2008) 2622-2627.

[76] S. Feng, R. Xu, New Materials in Hydrothermal Synthesis, Accounts of Chemical Research, 34 (2001) 239-247.

[77] M.M. Sk, C.Y. Yue, K. Ghosh, R.K. Jena, Review on advances in porous nanostructured nickel oxides and their composite electrodes for high-performance supercapacitors, Journal of Power Sources, 308 (2016) 121-140.

[78] K. Byrappa, M. Yoshimura, 1 - Hydrothermal Technology—Principles and Applications, in: K. Byrappa, M. Yoshimura (Eds.), William Andrew Publishing, Norwich, NY, 2001, pp. 1-52.

[79] P. Vishnukumar, B. Saravanakumar, G. Ravi, V. Ganesh, R.K. Guduru, R. Yuvakkumar, Synthesis and characterization of NiO/Ni3V2O8nanocomposite for supercapacitor applications, Materials Letters, 219 (2018) 114-118.

[80] X. Xia, W. Lei, Q. Hao, W. Wang, X. Wang, One-step synthesis of CoMoO4/graphene composites with enhanced electrochemical properties for supercapacitors, Electrochimica Acta, 99 (2013) 253-261.

[81] D. Guo, Y. Luo, X. Yu, Q. Li, T. Wang, High performance NiMoO4 nanowires supported on carbon cloth as advanced electrodes for symmetric supercapacitors, Nano Energy, 8 (2014) 174-182.

[82] R. Jiang, C. Cui, H. Ma, Using graphene nanosheets as a conductive additive to enhance the capacitive performance of α-MnO2, Electrochimica Acta, 104 (2013) 198-207.

[83] I. Bilecka, M. Niederberger, Microwave chemistry for inorganic nanomaterials synthesis, Nanoscale, 2 (2010) 1358-1374.

[84] X. Gu, W. Zhu, C. Jia, R. Zhao, W. Schmidt, Y. Wang, Synthesis and microwave absorbing properties of highly ordered mesoporous crystalline NiFe2O4, Chem. Commun., 47 (2011) 5337-5339.

[85] K.-H. Chang, Y.-F. Lee, C.-C. Hu, C.-I. Chang, C.-L. Liu, Y.-L. Yang, A unique strategy for preparing single-phase unitary/binary oxides-graphene composites, Chem. Commun., 46 (2010) 7957-7959.

[86] A.K. Rai, L.T. Anh, C.-J. Park, J. Kim, Electrochemical study of NiO nanoparticles electrode for application in rechargeable lithium-ion batteries, Ceramics International, 39 (2013) 6611-6618.

[87] S. Vijayakumar, S. Nagamuthu, G. Muralidharan, Supercapacitor Studies on NiO Nanoflakes Synthesized Through a Microwave Route, ACS Applied Materials & Interfaces, 5 (2013) 2188-2196.

[88] N. Behm, D. Brokaw, C. Overson, D. Peloquin, J.C. Poler, High-throughput microwave synthesis and characterization of NiO nanoplates for supercapacitor devices, Journal of Materials Science, 48 (2013) 1711-1716.

[89] M. Saraf, K. Natarajan, Shaikh M. Mobin, Microwave assisted fabrication of a nanostructured reduced graphene oxide (rGO)/Fe2O3 composite as a promising next generation energy storage material, RSC Advances, 7 (2017) 309-317.

[90] L. Xiao, D. Wu, S. Han, Y. Huang, S. Li, M. He, F. Zhang, X. Feng, Self-Assembled Fe2O3/Graphene Aerogel with High Lithium Storage Performance, ACS Applied Materials & Interfaces, 5 (2013) 3764-3769.

[91] C. Liu, Z. Yu, D. Neff, A. Zhamu, B.Z. Jang, Graphene-Based Supercapacitor with an Ultrahigh Energy Density, Nano Letters, 10 (2010) 4863-4868.

[92] R. Singh, C.C. Tripathi, Electrochemical Exfoliation of Graphite into Graphene for Flexible Supercapacitor Application, Materials Today: Proceedings, 5 (2018) 1125-1130.

[93] M. Devi, U.V. Varadaraju, Lithium insertion in lithium iron molybdate, Electrochemistry Communications, 18 (2012) 112-115.

[94] X.H. Huang, J.P. Tu, C.Q. Zhang, F. Zhou, Hollow microspheres of NiO as anode materials for lithium-ion batteries, Electrochimica Acta, 55 (2010) 8981-8985.

[95] W. Te-Yu, C. Chun-Hung, C. Hsing-Chi, L. Shih-Yuan, H. Chi-Chang, A Cost-Effective Supercapacitor Material of Ultrahigh Specific Capacitances: Spinel Nickel Cobaltite Aerogels from an Epoxide-Driven Sol–Gel Process, Advanced Materials, 22 (2010) 347-351.

[96] C. Yuan, J. Li, L. Hou, J. Lin, X. Zhang, S. Xiong, Polymer-assisted synthesis of a 3D hierarchical porous network-like spinel NiCo2O4 framework towards high-performance electrochemical capacitors, J. Mater. Chem. A, 1 (2013) 11145-11151.

[97] M.-C. Liu, L.-B. Kong, C. Lu, X.-M. Li, Y.-C. Luo, L. Kang, A Sol–Gel Process for Fabrication of NiO/NiCo2O4/Co3O4 Composite with Improved Electrochemical Behavior for Electrochemical Capacitors, ACS Applied Materials & Interfaces, 4 (2012) 4631-4636.

[98] G.H. Jeong, S. Baek, S. Lee, S.W. Kim, Metal Oxide/Graphene Composites for Supercapacitive Electrode Materials, Chem Asian J, 11 (2016) 949-964.

[99] R.N. Singh, M. Hamdani, J.F. Koenig, G. Poillerat, J.L. Gautier, P. Chartier, Thin films of Co3O4 and NiCo2O4 obtained by the method of chemical spray pyrolysis for electrocatalysis III. The electrocatalysis of oxygen evolution, Journal of Applied Electrochemistry, 20 (1990) 442-446.

[100] K. Liang, X. Tang, W. Hu, High-performance three-dimensional nanoporous NiO film as a supercapacitor electrode, J. Mater. Chem., 22 (2012) 11062-11067.

[101] J. Du, G. Zhou, H. Zhang, C. Cheng, J. Ma, W. Wei, L. Chen, T. Wang, Ultrathin Porous NiCo2O4 Nanosheet Arrays on Flexible Carbon Fabric for High-Performance Supercapacitors, ACS Applied Materials & Interfaces, 5 (2013) 7405-7409.

[102] Y. Zhang, B. Wang, F. Liu, J. Cheng, X.-w. Zhang, L. Zhang, Full synergistic contribution of electrodeposited three-dimensional NiCo2O4@MnO2 nanosheet networks electrode for asymmetric supercapacitors, Nano Energy, 27 (2016) 627-637.

[103] N. Wang, B. Sun, P. Zhao, M. Yao, W. Hu, S. Komarneni, Electrodeposition preparation of NiCo2O4 mesoporous film on ultrafine nickel wire for flexible asymmetric supercapacitors, Chemical Engineering Journal, 345 (2018) 31-38.

[104] L. Huang, D. Chen, Y. Ding, Z.L. Wang, Z. Zeng, M. Liu, Hybrid Composite Ni(OH)2@NiCo2O4 Grown on Carbon Fiber Paper for High-Performance Supercapacitors, ACS Applied Materials & Interfaces, 5 (2013) 11159-11162.

[105] G. Zhang, T. Wang, X. Yu, H. Zhang, H. Duan, B. Lu, Nanoforest of hierarchical Co3O4@NiCo2O4 nanowire arrays for high-performance supercapacitors, Nano Energy, 2 (2013) 586-594.

[106] Y. Changzhou, L. Jiaoyang, H. Linrui, Z. Xiaogang, S. Laifa, L.X. Wen, Ultrathin Mesoporous NiCo2O4 Nanosheets Supported on Ni Foam as Advanced Electrodes for Supercapacitors, Advanced Functional Materials, 22 4592-4597.

[107] W. Wei, L. Mi, S. Cui, B. Wang, W. Chen, Carambola-like Ni@Ni1.5Co1.5S2 for Use in High-Performance Supercapacitor Devices Design, ACS Sustainable Chemistry & Engineering, 3 (2015) 2777-2785.

[108] A. Ramadoss, K.-N. Kang, H.-J. Ahn, S.-I. Kim, S.-T. Ryu, J.-H. Jang, Realization of high performance flexible wire supercapacitors based on 3-dimensional NiCo2O4/Ni fibers, J. Mater. Chem. A, 4 (2016) 4718-4727.

[109] M. Tebyetekerwa, X. Wang, Y. Wu, S. Yang, M. Zhu, S. Ramakrishna, Controlled synergistic strategy to fabricate 3D-skeletal hetero-nanosponges with high performance for flexible energy storage applications, J. Mater. Chem. A, 5 (2017) 21114-21121.

[110] I. Shakir, M. Sarfraz, U.A. Rana, M. Nadeem, M.A. Al-Shaikh, Synthesis of hierarchical porous spinel nickel cobaltite nanoflakes for high performance electrochemical energy storage supercapacitors, RSC Adv., 3 (2013) 21386-21389.

[111] G.Q. Zhang, H.B. Wu, H.E. Hoster, M.B. Chan-Park, X.W. Lou, Single-crystalline NiCo2O4 nanoneedle arrays grown on conductive substrates as binder-

free electrodes for high-performance supercapacitors, Energy Environ. Sci., 5 (2012) 9453-9456.

[112] H.B. Wu, H. Pang, X.W. Lou, Facile synthesis of mesoporous Ni0.3Co2.7O4 hierarchical structures for high-performance supercapacitors, Energy Environ. Sci., 6 (2013) 3619-3626.

[113] M.J. Barmi, M.M. Sundaram, Role of polymeric surfactant in the synthesis of cobalt molybdate nanospheres for hybrid capacitor applications, RSC Adv., 6 (2016) 36152-36162.

[114] H. Xu, J.-X. Zhuang, J.-L. Li, J.-L. Zhang, H.-L. Lu, Liquid precipitation synthesis of Co3O4 for high-performance electrochemical capacitors, Ionics, 20 (2014) 489-494.

[115] R.R. Salunkhe, Y.V. Kaneti, Y. Yamauchi, Metal–Organic Framework-Derived Nanoporous Metal Oxides toward Supercapacitor Applications: Progress and Prospects, ACS Nano, 11 (2017) 5293-5308.

[116] G. Xu, P. Nie, H. Dou, B. Ding, L. Li, X. Zhang, Exploring metal organic frameworks for energy storage in batteries and supercapacitors, Materials Today, 20 (2017) 191-209.

[117] H.-C. Zhou, J.R. Long, O.M. Yaghi, Introduction to Metal–Organic Frameworks, Chemical Reviews, 112 (2012) 673-674.

[118] B.M. Wiers, M.-L. Foo, N.P. Balsara, J.R. Long, A Solid Lithium Electrolyte via Addition of Lithium Isopropoxide to a Metal–Organic Framework with Open Metal Sites, Journal of the American Chemical Society, 133 (2011) 14522-14525.

[119] K.Y. Valentino, T. Jing, S.R. R, J. Xuchuan, Y. Aibing, W.K. C.-W, Y. Yusuke, Nanoarchitectured Design of Porous Materials and Nanocomposites from Metal-Organic Frameworks, Advanced Materials, 29 1604898-1604898.

[120] W. Xia, A. Mahmood, R. Zou, Q. Xu, Metal-organic frameworks and their derived nanostructures for electrochemical energy storage and conversion, Energy Environ. Sci., 8 (2015) 1837-1866.

[121] S. Kong, R. Dai, H. Li, W. Sun, Y. Wang, Microwave Hydrothermal Synthesis of Ni-based Metal–Organic Frameworks and Their Derived Yolk–Shell NiO for Li-Ion Storage and Supported Ammonia Borane for Hydrogen Desorption, ACS Sustainable Chemistry & Engineering, 3 (2015) 1830-1838.

[122] Y. Kimitsuka, E. Hosono, S. Ueno, H. Zhou, S. Fujihara, Fabrication of Porous Cubic Architecture of ZnO Using Zn-terephthalate MOFs with Characteristic Microstructures, Inorganic Chemistry, 52 (2013) 14028-14033.

[123] Z. Xiu, M.H. Alfaruqi, J. Gim, J. Song, S. Kim, T.V. Thi, P.T. Duong, J.P. Baboo, V. Mathew, J. Kim, Hierarchical porous anatase TiO2 derived from a titanium metal-organic framework as a superior anode material for lithium ion batteries, Chem. Commun., 51 (2015) 12274-12277.

[124] J. Wang, S. Dong, Y. Zhang, Z. Chen, S. Jiang, L. Wu, X. Zhang, Metal–organic framework derived titanium-based anode materials for lithium ion batteries, Nano-Structures & Nano-Objects, 15 (2018) 48-53.

[125] J. Yang, H. Ye, Z. Zhang, F. Zhao, B. Zeng, Metal–organic framework derived hollow polyhedron CuCo2O4 functionalized porous graphene for sensitive glucose sensing, Sensors and Actuators B: Chemical, 242 (2017) 728-735.

[126] G. Cao, L. Ximeng, R. Weina, L. Xin, C. Chuanwei, W. John, Rational Design of Metal-Organic Framework Derived Hollow NiCo2O4 Arrays for Flexible Supercapacitor and Electrocatalysis, Advanced Energy Materials, 7 (2017) 1602391-1602391.

[127] R. Ramachandran, S.M. Chen, G. Gnana kumar, An overview of electrochemical energy storage devices of various electrodes and morphological studies of supercapacitors, International Journal of Electrochemical Science, 10 (2015) 10355-10388.

[128] Z. Yin, Y. Xiao, X. Wang, W. Wang, D. Zhao, M. Cao, MoV2O8 nanostructures: controlled synthesis and lithium storage mechanism, Nanoscale, 8 (2016) 508-516.

[129] E.R. Ezeigwe, M.T.T. Tan, P.S. Khiew, C.W. Siong, One-step green synthesis of graphene/ZnO nanocomposites for electrochemical capacitors, Ceramics International, 41 (2014) 715-724.

[130] C. Lee, S.K. Kim, J.H. Choi, H. Chang, H.D. Jang, Electrochemical performances of iron-cobalt oxides nanoparticles loaded crumpled graphene for supercapacitor, Journal of Alloys and Compounds, 735 (2018) 2030-2037.

[131] L. Qi, C.J. G, X.J. Q, Nanostructured Electrodes for High-Performance Pseudocapacitors, Angewandte Chemie International Edition, 52 (2013) 1882-1889.

[132] G. Chen, H. Guan, C. Dong, X. Xiao, Y. Wang, Effect of calcination temperatures on the electrochemical performances of nickel oxide/reduction graphene oxide (NiO/RGO) composites synthesized by hydrothermal method, Journal of Physics and Chemistry of Solids, 98 (2016) 209-219.

[133] R.B. Rakhi, W. Chen, D. Cha, H.N. Alshareef, Influence of calcination temperature on the morphology and energy storage properties of cobalt oxide nanostructures directly grown over carbon cloth substrates, Materials for Renewable and Sustainable Energy, 2 (2013) 17-17.

[134] M.V. Reddy, G.V. Subba Rao, B.V.R. Chowdari, Metal Oxides and Oxysalts as Anode Materials for Li Ion Batteries, Chemical Reviews, 113 (2013) 5364-5457.

[135] J.G. Kim, D.L. Pugmire, D. Battaglia, M.A. Langell, Analysis of the NiCo2O4 spinel surface with Auger and X-ray photoelectron spectroscopy, Applied Surface Science, 165 (2000) 70-84.

[136] Y. Bitla, Y.-Y. Chin, J.-C. Lin, C.N. Van, R. Liu, Y. Zhu, H.-J. Liu, Q. Zhan, H.-J. Lin, C.-T. Chen, Y.-H. Chu, Q. He, Origin of metallic behavior in NiCo2O4 ferrimagnet, Scientific Reports, 5 (2015) 15201-15201.

[137] D. Yan, W. Wang, X. Luo, C. Chen, Y. Zeng, Z. Zhu, NiCo2O4 with oxygen vacancies as better performance electrode material for supercapacitor, Chemical Engineering Journal, 334 (2018) 864-872.

[138] Y. Li, X. Hou, Z. Zhang, Z. Hai, H. Xu, D. Cui, S. Zhuiykov, C. Xue, NiCo2O4 particles with diamond-shaped hexahedron structure for high-performance supercapacitors, Applied Surface Science, 436 (2018) 242-251.

[139] M. Saraf, K. Natarajan, S.M. Mobin, Multifunctional porous NiCo2O4 nanorods: sensitive enzymeless glucose detection and supercapacitor properties with impedance spectroscopic investigations, New J. Chem., 41 (2017) 9299-9313.

[140] T. Huang, B. Liu, P. Yang, Z. Qiu, Z. Hu, Facilely Synthesized NiCo 2 O 4 Nanoparticles as Electrode Material for Supercapacitors, Int. J. Electrochem. Sci, 13 (2018) 6144-6154.

[141] G. Zhang, X.W. Lou, Controlled Growth of NiCo2O4 Nanorods and Ultrathin Nanosheets on Carbon Nanofibers for High-performance Supercapacitors, Scientific Reports, 3 (2013) 1470-1470.

[142] H. Chen, G. Jiang, W. Yu, D. Liu, Y. Liu, L. Li, Q. Huang, Electrospun carbon nanofiberic coated with ambutan-like NiCo2O4 microspheres as electrode materials, MRS Communications, 7 (2017) 90-96.

[143] J. Zhicheng, M. Guangyao, Z. Yulong, X. Zheng, Q. Yinghuai, Q. Yitai, A Facile Method for Synthesis of Porous NiCo2O4 Nanorods as a High-Performance Anode Material for Li-Ion Batteries, Particle & Particle Systems Characterization, 32 (2015) 1012-1019.

[144] S. Sahoo, S. Ratha, C. Rout, Spinel NiCo2O4 Nanorods for Supercapacitor Applications, American Journal of Engineering and Applied Sciences, 8 (2015) 371-379.

[145] S. Jiang, Y. Sun, H. Dai, P. Ni, W. Lu, Y. Wang, Z. Li, Z. Li, A facile enhancement in battery-type of capacitive performance of spinel NiCo2O4 nanostructure via directly tuning thermal decomposition temperature, Electrochimica Acta, 191 (2016) 364-374.

[146] A.K. Yedluri, H.-J. Kim, Enhanced electrochemical performance of nanoplate nickel cobaltite (NiCo2O4) supercapacitor applications, RSC Advances, 9 (2019) 1115-1122.

[147] A.J.C. Mary, A.C. Bose, Hydrothermal synthesis of Mn-doped ZnCo2O4 electrode material for high-performance supercapacitor, Applied Surface Science, 425 (2017) 201-211.

[148] H.S. Jadhav, A. Roy, W.-J. Chung, J.G. Seo, Growth of urchin-like ZnCo2O4 microspheres on nickel foam as a binder-free electrode for high-performance supercapacitor and methanol electro-oxidation, Electrochimica Acta, 246 (2017) 941-950.

[149] J. Zhu, D. Song, T. Pu, J. Li, B. Huang, W. Wang, C. Zhao, L. Xie, L. Chen, Two-dimensional porous ZnCo2O4 thin sheets assembled by 3D nanoflake array with enhanced performance for aqueous asymmetric supercapacitor, Chemical Engineering Journal, 336 (2018) 679-689.

[150] Y. Pan, H. Gao, M. Zhang, L. Li, Z. Wang, Facile synthesis of ZnCo2O4 micro-flowers and micro-sheets on Ni foam for pseudocapacitor electrodes, Journal of Alloys and Compounds, 702 (2017) 381-387.

[151] Y. Pan, H. Gao, M. Zhang, L. Li, G. Wang, X. Shan, Three-dimensional porous ZnCo2O4 sheet array coated with Ni(OH)2 for high-performance asymmetric supercapacitor, Journal of Colloid and Interface Science, 497 (2017) 50-56.

[152] Y. Shang, T. Xie, Y. Gai, L. Su, L. Gong, H. Lv, F. Dong, Self-assembled hierarchical peony-like ZnCo2O4 for high-performance asymmetric supercapacitors, Electrochimica Acta, 253 (2017) 281-290.

[153] X. Xiao, G. Wang, M. Zhang, Z. Wang, R. Zhao, Y. Wang, Electrochemical performance of mesoporous ZnCo2O4 nanosheets as an electrode material for supercapacitor, Ionics, 24 (2017) 2435-2443.

[154] Y. Gai, Y. Shang, L. Gong, L. Su, L. Hao, F. Dong, J. Li, A self-template synthesis of porous ZnCo2O4 microspheres for high-performance quasi-solid-state asymmetric supercapacitors, RSC Adv., 7 (2017) 1038-1044.

[155] A. Pendashteh, S.E. Moosavifard, M.S. Rahmanifar, Y. Wang, M.F. El-Kady, R.B. Kaner, M.F. Mousavi, Highly Ordered Mesoporous CuCo2O4 Nanowires, a Promising Solution for High-Performance Supercapacitors, Chemistry of Materials, 27 (2015) 3919-3926.

[156] A. Pendashteh, M.S. Rahmanifar, R.B. Kaner, M.F. Mousavi, Facile synthesis of nanostructured CuCo2O4 as a novel electrode material for high-rate supercapacitors, Chem. Commun., 50 (2014) 1972-1975.

[157] H.S. Jadhav, S.M. Pawar, A.H. Jadhav, G.M. Thorat, J.G. Seo, Hierarchical Mesoporous 3D Flower-like CuCo2O4/NF for High-Performance Electrochemical Energy Storage, Scientific Reports, 6 (2016) 31120-31120.

[158] S. Vijayakumar, S.-H. Lee, K.-S. Ryu, Hierarchical CuCo2O4 nanobelts as a supercapacitor electrode with high areal and specific capacitance, Electrochimica Acta, 182 (2015) 979-986.

[159] J. Cheng, H. Yan, Y. Lu, K. Qiu, X. Hou, J. Xu, L. Han, X. Liu, J.-K. Kim, Y. Luo, Mesoporous CuCo2O4 nanograsses as multi-functional electrodes for supercapacitors and electro-catalysts, J. Mater. Chem. A, 3 (2015) 9769-9776.

[160] K. Qiu, M. Lu, Y. Luo, X. Du, Engineering hierarchical nanotrees with CuCo2O4 trunks and NiO branches for high-performance supercapacitors, J. Mater. Chem. A, 5 (2017) 5820-5828.

[161] Y. Zhang, J. Xu, Y. Zheng, Y. Zhang, X. Hu, T. Xu, Construction of CuCo2O4@CuCo2O4 hierarchical nanowire arrays grown on Ni foam for high-performance supercapacitors, RSC Adv., 7 (2017) 3983-3991.

[162] R. BoopathiRaja, M. Parthibavarman, A. Nishara Begum, Hydrothermal induced novel CuCo2O4 electrode for high performance supercapacitor applications, Vacuum, 165 (2019) 96-104.

[163] A.A. Ensafi, S.E. Moosavifard, B. Rezaei, S.K. Kaverlavani, Engineering onion-like nanoporous CuCo2O4 hollow spheres derived from bimetal–organic frameworks for high-performance asymmetric supercapacitors, Journal of Materials Chemistry A, 6 (2018) 10497-10506.

[164] Y. Huang, F. Cui, Y. Zhao, J. Lian, J. Bao, H. Li, Controlled growth of ultrathin NiMoO4 nanosheets on carbon nanofiber membrane as advanced electrodes for asymmetric supercapacitors, Journal of Alloys and Compounds, 753 (2018) 176-185.

[165] K. Seevakan, A. Manikandan, P. Devendran, A. Shameem, T. Alagesan, Microwave combustion synthesis, magneto-optical and electrochemical properties of NiMoO4 nanoparticles for supercapacitor application, Ceramics International, 44 (2018) 13879-13887.

[166] X. Tian, X. Li, T. Yang, K. Wang, H. Wang, Y. Song, Z. Liu, Q. Guo, Porous worm-like NiMoO4 coaxially decorated electrospun carbon nanofiber as binder-free electrodes for high performance supercapacitors and lithium-ion batteries, Applied Surface Science, 434 (2018) 49-56.

[167] M. Chandra Adhikary, M. H. Priyadarsini, S. Kumar Rath, C. Kumar Das, 3D porous NiMoO4 nanoflakes arrays for advanced supercapacitor electrodes, Journal of Nanoparticle Research, 19 (2017) 314.

[168] B. Saravanakumar, S.P. Ramachandran, G. Ravi, V. Ganesh, A. Sakunthala, R. Yuvakkumar, Morphology dependent electrochemical capacitor performance of NiMoO4 nanoparticles, Materials Letters, 209 (2017) 1-4.

[169] L. Lin, T. Liu, J. Liu, R. Sun, J. Hao, K. Ji, Z. Wang, Facile synthesis of groove-like NiMoO4 hollow nanorods for high-performance supercapacitors, Applied Surface Science, 360 (2016) 234-239.

[170] M. Pang, S. Jiang, Y. Ji, J. Zhao, B. Xing, Q. Pan, H. Yang, W. Qu, L. Gu, H. Wang, Comparison of α-NiMoO4 nanorods and hierarchical α-NiMoO4@δ-MnO2 core-shell hybrid nanorod/nanosheet aligned on Ni foam for supercapacitors, Journal of Alloys and Compounds, 708 (2017) 14-22.

[171] Y. Zhang, J. Xu, Y. Zheng, Y. Zhang, X. hu, T. Xu, NiCo2S4@NiMoO4 Core-Shell Heterostructure Nanotube Arrays Grown on Ni Foam as a Binder-Free Electrode Displayed High Electrochemical Performance with High Capacity, Nanoscale Research Letters, 12 (2017).

[172] M. Wang, J. Zhang, X. Yi, B. Liu, X. Zhao, X. Liu, High-performance asymmetric supercapacitor made of NiMoO4 nanorods@Co3O4 on a cellulose-based carbon aerogel, Beilstein Journal of Nanotechnology, 11 (2020) 240-251.

[173] J. Yesuraj, O. Padmaraj, S.A. Suthanthiraraj, Synthesis, Characterization, and Improvement of Supercapacitor Properties of NiMoO4 Nanocrystals with Polyaniline, Journal of Inorganic and Organometallic Polymers and Materials, 30 (2020) 310-321.

[174] M. Li, Y. Wang, H. Yang, P.K. Chu, Hierarchical CoMoO4@Co3O4 nanocomposites on an ordered macro-porous electrode plate as a multi-dimensional

electrode in high-performance supercapacitors, J. Mater. Chem. A, 5 (2017) 17312-17324.

[175] L. Jinlong, G. Wenli, L. Tongxiang, Synthesis of Co3O4@CoMoO4 core–shell architectures nanocomposites as high-performance supercapacitor electrode, Journal of Electroanalytical Chemistry, 783 (2016) 250-257.

[176] J. Ge, J. Wu, L. Fan, Q. Bao, J. Dong, J. Jia, Y. Guo, J. Lin, Hydrothermal synthesis of CoMoO4/Co1-xS hybrid on Ni foam for high-performance supercapacitors, Journal of Energy Chemistry, 27 (2018) 478-485.

[177] L. Fang, F. Wang, T. Zhai, Y. Qiu, M. Lan, K. Huang, Q. Jing, Hierarchical CoMoO4 nanoneedle electrodes for advanced supercapacitors and electrocatalytic oxygen evolution, Electrochimica Acta, 259 (2018) 552-558.

[178] C. Wang, Z. Guan, Y. Shen, S. Yu, X.-Z. Fu, R. Sun, C.-P. Wong, Shape-controlled synthesis of CoMoO4@Co1.5Ni1.5S4 hybrids with rambutan-like structure for high-performance all-solid-state supercapacitors, Chemical Engineering Journal, 346 (2018) 193-202.

[179] J. Xie, Z. Zhan, S. Zhang, G. Li, H. Xia, Y. Yang, J. Xiong, CoMoO4 nanoplates decorated CuCo2O4 nanowires as advanced electrodes for high-performance hybrid supercapacitors, Materials Letters, 226 (2018) 30-33.

[180] Y. Feng, W. Liu, L. Sun, Y. Zhu, Y. Chen, M. Meng, J. Li, J. Yang, Y. Zhang, K. Liu, Hierarchical MnCo2O4@CoMoO4 core-shell nanowire arrays supported on Ni foam for supercapacitor, Journal of Alloys and Compounds, 753 (2018) 761-770.

[181] Y.-P. Gao, K.-J. Huang, C.-X. Zhang, S.-S. Song, X. Wu, High-performance symmetric supercapacitor based on flower-like zinc molybdate, Journal of Alloys and Compounds, 731 (2018) 1151-1158.

[182] Z. Fan, X. Zhang, Deposition of fan-shaped ZnMoO4 on ZnCo2O4 nanowire arrays for high electrochemical performance, Applied Physics A, 123 (2017) 290.

[183] C. Lv, J. Sun, G. Chen, C. Yan, D. Chen, Achieving Ni3V2O8amorphous wire encapsulated in crystalline tube nanostructure as anode materials for lithium ion batteries, Nano Energy, 33 (2017) 138-145.

[184] B. Sambandam, V. Soundharrajan, J. Song, S. Kim, J. Jo, D.T. Pham, S. Kim, V. Mathew, K.H. Kim, Y.-K. Sun, J. Kim, Ni 3 V 2 O 8 nanoparticles as an excellent anode material for high-energy lithium-ion batteries, Journal of Electroanalytical Chemistry, 810 (2018) 34-40.

[185] Y. Li, Y. Teng, Z. Zhang, Y. Feng, P. Xue, W. Tong, X. Liu, Microwave-assisted synthesis of novel nanostructured Zn3(OH)2V2O7 ·2H2O and Zn2V2O7 as electrode materials for supercapacitors, New Journal of Chemistry, 41 (2017) 15298-15304.

[186] Z. Yin, J. Qin, W. Wang, M. Cao, Rationally designed hollow precursor-derived Zn3V2O8nanocages as a high-performance anode material for lithium-ion batteries, Nano Energy, 31 (2017) 367-376.

[187] B. Sambandam, V. Soundharrajan, J. Song, S. Kim, J. Jo, D.T. Pham, S. Kim, V. Mathew, J. Kim, Zn3V2O8porous morphology derived through a facile and green approach as an excellent anode for high-energy lithium ion batteries, Chemical Engineering Journal, 328 (2017) 454-463.

[188] L.-H. Gan, D. Deng, Y. Zhang, G. Li, X. Wang, L. Jiang, C.-R. Wang, Zn3V2O8 hexagon nanosheets: a high-performance anode material for lithium-ion batteries, Journal of Materials Chemistry A, 2 (2014) 2461-2461.

[189] Y.M. Hu, M.C. Liu, Y.X. Hu, Q.Q. Yang, L.B. Kong, W. Han, J.J. Li, L. Kang, Design and synthesis of Ni2P/Co3V2O8nanocomposite with enhanced electrochemical capacitive properties, Electrochimica Acta, 190 (2016) 1041-1049.

[190] J. Zhang, B. Yuan, S. Cui, N. Zhang, J. Wei, X. Wang, D. Zhang, R. Zhang, Q. Huo, Facile synthesis of 3D porous Co3V2O8 nanoroses and 2D NiCo2V2O8 nanoplates for high performance supercapacitors and their electrocatalytic oxygen evolution reaction properties, Dalton Trans., 46 (2017) 3295-3302.

[191] Y. Zhang, Y. Liu, J. Chen, Q. Guo, T. Wang, H. Pang, Cobalt vanadium oxide thin nanoplates: Primary electrochemical capacitor application, Scientific Reports, 4 (2014) 2-6.

[192] V. Soundharrajan, B. Sambandam, J. Song, S. Kim, J. Jo, P.T. Duong, S. Kim, V. Mathew, J. Kim, Facile green synthesis of a Co3V2O8nanoparticle electrode for high energy lithium-ion battery applications, Journal of Colloid and Interface Science, 501 (2017) 133-141.

[193] G. Yang, H. Song, G. Yang, M. Wu, C. Wang, 3D hierarchical AlV_3O_9 microspheres: First synthesis, excellent lithium ion cathode properties, and investigation of electrochemical mechanism, Nano Energy, 15 (2015) 281-292.

[194] L. Liu, G. Fang, B. Huang, J. Zhou, K. Cai, S. Liang, Electrochemical performance of AlV3O9nanoflowers for lithium ion batteries application, Journal of Alloys and Compounds, 723 (2017) 92-99.

[195] L. Niu, Y. Wang, F. Ruan, C. Shen, S. Shan, M. Xu, Z. Sun, C. Li, X. Liu, Y. Gong, In situ growth of $NiCoS_4@Ni_3V_2O_8$ on Ni foam as a binder-free electrode for asymmetric supercapacitors, J. Mater. Chem. A, 4 (2016) 5669-5677.

[196] X.-x. Wang, Y. Li, M.-c. Liu, L.-b. Kong, Fabrication and electrochemical investigation of MWO 4 (M = Co , Ni) nanoparticles as high-performance anode materials for lithium-ion batteries, Ionics, 24 (2018) 363-372.

[197] Z. Dai, C. Peng, J.H. Chae, K.C. Ng, G.Z. Chen, Cell voltage versus electrode potential range in aqueous supercapacitors, Scientific Reports, 5 (2015).

[198] S. Chen, G. Yang, Y. Jia, H. Zheng, Three-dimensional NiCo2O4@NiWO4 core-shell nanowire arrays for high performance supercapacitors, J. Mater. Chem. A, 5 (2017) 1028-1034.

[199] C. Sanming, Y. Guang, J. Yi, Z. Huajun, Facile Synthesis of CoWO4 Nanosheet Arrays Grown on Nickel Foam Substrates for Asymmetric Supercapacitors, ChemElectroChem, 3 (2016) 1490-1496.

[200] V. Lokhande, T. Ji, Hydrothermal Synthesis of CoWO4 as Active Material for Supercapacitor Electrode, in, 2016, pp. 409-413`.

[201] L. Niu, Z. Li, Y. Xu, J. Sun, W. Hong, X. Liu, J. Wang, S. Yang, Simple Synthesis of Amorphous NiWO4 Nanostructure and Its Application as a Novel Cathode Material for Asymmetric Supercapacitors, ACS Applied Materials & Interfaces, 5 (2013) 8044-8052.

[202] S.R. Ede, A. Ramadoss, U. Nithiyanantham, S. Anantharaj, S. Kundu, Bio-molecule Assisted Aggregation of ZnWO4 Nanoparticles (NPs) into Chain-like Assemblies: Material for High Performance Supercapacitor and as Catalyst for Benzyl Alcohol Oxidation, Inorganic Chemistry, 54 (2015) 3851-3863.

[203] S. Nianxiang, X. Shenglin, W. Fangfang, B. Jing, C. Yanting, M. Hongzhi, F. Jinkui, X. Baojuan, Hydrothermal Synthesis of ZnWO4 Hierarchical Hexangular Microstars for Enhanced Lithium-Storage Properties, European Journal of Inorganic Chemistry, 2017 (2017) 734-740.

[204] M. Feng, D. An, H. Zhang, G. Ma, C. Zhang, Z. Ma, Facile synthesis of cobalt / nickel tungstate and its application in hybrid supercapacitor, 5 (2017) 1954-1960.

[205] L. Lin, L. Li, S. Hussain, S. Zhao, L. Wu, X. Peng, N. Hu, Hierarchical 3D NiCo2O4@ZnWO4 core-shell structures as binder-free electrodes for all-solid-state supercapacitors, Applied Surface Science, 452 (2018) 113-122.

[206] S. Han, L. Lin, K. Zhang, L. Luo, X. Peng, N. Hu, ZnWO4 nanoflakes decorated NiCo2O4 nanoneedle arrays grown on carbon cloth as supercapacitor electrodes, Materials Letters, 193 (2017) 89-92.

[207] S. Jha, S. Mehta, Y. Chen, P. Renner, S.S. Sankar, D. Parkinson, S. Kundu, H. Liang, NiWO4 nanoparticle decorated lignin as electrodes for asymmetric flexible supercapacitors, Journal of Materials Chemistry C, 8 (2020) 3418-3430.

[208] Y. Yang, J. Zhu, W. Shi, J. Zhou, D. Gong, S. Gu, L. Wang, Z. Xu, B. Lu, 3D nanoporous ZnWO4 nanoparticles with excellent electrochemical performances for supercapacitors, Materials Letters, 177 (2016) 34-38.

[209] V.V. Deshmukh, Nagpure, P. A., Burghate, D. K. and Chaudhari G. N., Synthesis and electrochemical study of manganese ferrite (MnFe2O4) Nanoparticles, International Journal of Current Research, 8 (2016) 35988-35991.

[210] N. Arsalani, A.G. Tabrizi, L.S. Ghadimi, Novel PANI/MnFe2O4 nanocomposite for low-cost supercapacitors with high rate capability, Journal of Materials Science: Materials in Electronics, 29 (2018) 6077-6085.

[211] H. Kennaz, A. Harat, O. Guellati, N. Manyala, M. Guerioune, Synthesis of Cobalt Ferrite Nanoparticles By Hydrothermal Method for Supercapacitors Application, (2016) 267-271.

[212] V.S. Kumbhar, A.D. Jagadale, N.M. Shinde, C.D. Lokhande, Chemical synthesis of spinel cobalt ferrite (CoFe2O4) nano-flakes for supercapacitor application, Applied Surface Science, 259 (2012) 39-43.

[213] B. Wang, P. Guo, H. Bi, Q. Li, G. Zhang, R. Wang, Electrocapacitive Properties of MnFe2O4 Electrodes in Aqueous LiNO3 Electrolyte with Surfactants, International Journal of Electrochemical Science, 8 (2013) 8966-8977.

[214] A. Shanmugavani, D. Kalpana, R.K. Selvan, Electrochemical properties of CoFe2O4 nanoparticles as negative and Co(OH)2 and Co2Fe(CN)6 as positive electrodes for supercapacitors, Materials Research Bulletin, 71 (2015) 133-141.

[215] J.S. Sagu, K.G.U. Wijayantha, A.A. Tahir, The Pseudocapacitive Nature of CoFe2O4 Thin Films, Electrochimica Acta, 246 (2017) 870-878.

[216] S. Giri, D. Ghosh, M. Mandal, C. Kumar Das, Flexible Supercapacitor Based on Freestanding NiMn2O4 Flower Grown on Carbon Fiber, in: International Conference on Functional Materials Kharagpur, 2014.

[217] Y. Ouyang, Y. Feng, H. Zhang, L. Liu, Y. Wang, Designing Sandwiched and Crystallized NiMn2O4/C Arrays for Enhanced Sustainable Electrochemical Energy Storage, ACS Sustainable Chemistry & Engineering, 5 (2017) 196-205.

[218] K.M. Ri, N.R. Mohan, K. Seok, K. Mi-Ra, K. Il, NiMn2O4 Nanosheet-Decorated Hierarchically Porous Polyaromatic Carbon Spheres for High-Performance Supercapacitors, ChemElectroChem, 4 (2017) 1214-1221.

[219] M. Zhang, S. Guo, L. Zheng, G. Zhang, Z. Hao, L. Kang, Z.-H. Liu, Preparation of NiMn2O4 with large specific surface area from an epoxide-driven sol−gel process and its capacitance, Electrochimica Acta, 87 (2013) 546-553.

[220] H. Wei, J. Wang, L. Yu, Y. Zhang, D. Hou, T. Li, Facile synthesis of NiMn2O4 nanosheet arrays grown on nickel foam as novel electrode materials for high-performance supercapacitors, Ceramics International, 42 (2016) 14963-14969.

[221] J. Bhagwan, S. Rani, V. Sivasankaran, K.L. Yadav, Y. Sharma, Improved energy storage, magnetic and electrical properties of aligned, mesoporous and high aspect ratio nanofibers of spinel-NiMn2O4, Applied Surface Science, 426 (2017) 913-923.

[222] R. Sahoo, A. Pal, T. Pal, 2D materials for renewable energy storage devices: Outlook and challenges, Chem. Commun., 52 (2016) 13528-13542.

[223] S.K. Tiwari, R.K. Mishra, S.K. Ha, A. Huczko, Evolution of Graphene Oxide and Graphene: From Imagination to Industrialization, ChemNanoMat, 4 (2018) 598-620.

[224] S.K. Tiwari, S. Sahoo, N. Wang, A. Huczko, Graphene research and their outputs: Status and prospect, Journal of Science: Advanced Materials and Devices, 5 (2020) 10-29.

[225] S.T. Bulbula, Y. Lu, Y. Dong, X.-Y. Yang, Hierarchically porous graphene for batteries and supercapacitors, New Journal of Chemistry, 42 (2018) 5634-5655.

[226] Y. Wei, B. Sun, D. Su, J. Zhu, G. Wang, 3D Free-Standing NiCo 2 O 4 @ graphene Foam for High- Performance Supercapacitors, Energy Technology, 4 (2016) 737-743.

[227] S. Sun, S. Wang, S. Li, Y. Li, Y. Zhang, J. Chen, Z. Zhang, S. Fang, P. Wang, Asymmetric supercapacitors based on a $NiCo_2O_4$ three dimensional graphene composite and three dimensional graphene with high energy density, J. Mater. Chem. A, 4 (2016) 18646-18653.

[228] S.K. Kaverlavani, S.E. Moosavifard, A. Bakouei, Designing graphene-wrapped nanoporous $CuCo_2O_4$ hollow spheres electrodes for high-performance asymmetric supercapacitors, J. Mater. Chem. A, 5 (2017) 14301-14309.

[229] Z. Wang, X. Zhang, Z. Zhang, N. Qiao, Y. Li, Z. Hao, Hybrids of NiCo2O4nanorods and nanobundles with graphene as promising electrode materials for supercapacitors, Journal of Colloid and Interface Science, 460 (2015) 303-309.

[230] L. Ma, X. Shen, Z. Ji, X. Cai, G. Zhu, K. Chen, Porous NiCo2O4nanosheets/reduced graphene oxide composite: Facile synthesis and excellent capacitive performance for supercapacitors, Journal of Colloid and Interface Science, 440 (2015) 211-218.

[231] Z. Gao, L. Zhang, J. Chang, Z. Wang, D. Wu, F. Xu, Y. Guo, K. Jiang, ZnCo2O4-reduced graphene oxide composite with balanced capacitive performance in asymmetric supercapacitors, Applied Surface Science, 442 (2018) 138-147.

[232] I.K.a. Moon, K.Y.b. Chun, Ultra-high pseudocapacitance of mesoporous ZnCo2O4 nanosheets on reduced graphene oxide utilizing a neutral aqueous electrolyte, RSC Advances, 5 (2015) 807-811.

[233] I.K. Moon, S. Yoon, J. Oh, Three-Dimensional Hierarchically Mesoporous ZnCo2O4Nanowires Grown on Graphene/Sponge Foam for High-Performance,

Flexible, All-Solid-State Supercapacitors, Chemistry - A European Journal, 23 (2017) 597-604.

[234] S. Sahoo, J.J. Shim, Nanostructured 3D zinc cobaltite/nitrogen-doped reduced graphene oxide composite electrode for supercapacitor applications, Journal of Industrial and Engineering Chemistry, 54 (2017) 205-217.

[235] H. Tong, S. Yue, F. Jin, L. Lu, Q. Meng, X. Zhang, Honeycomb-like NiCo2O4@Ni(OH)2 supported on 3D N−doped graphene/carbon nanotubes sponge as an high performance electrode for Supercapacitor, Ceramics International, 44 (2018) 3113-3121.

[236] A.K. Samantara, S. Kamila, A. Ghosh, B.K. Jena, Highly ordered 1D NiCo2O4 nanorods on graphene: An efficient dual-functional hybrid materials for electrochemical energy conversion and storage applications, Electrochimica Acta, 263 (2018) 147-157.

[237] C. Zhang, C. Lei, C. Cen, S. Tang, M. Deng, Y. Li, Y. Du, Interface polarization matters: Enhancing supercapacitor performance of spinel NiCo2O4 nanowires by reduced graphene oxide coating, Electrochimica Acta, 260 (2018) 814-822.

[238] L. Jinlong, H. Miura, Y. Meng, A novel mesoporous NiMoO4@rGO nanostructure for supercapacitor applications, Materials Letters, 194 (2017) 94-97.

[239] L. Jinlong, Y. Meng, L. Tongxiang, Enhanced performance of NiMoO4nanoparticles and quantum dots and reduced nanohole graphene oxide hybrid for supercapacitor applications, Applied Surface Science, 419 (2017) 624-630.

[240] D. Zhou, P. Cheng, J. Luo, W. Xu, J. Li, D. Yuan, Facile synthesis of graphene@NiMoO4 nanosheet arrays on Ni foam for a high-performance asymmetric supercapacitor, Journal of Materials Science, 52 (2017) 13909-13919.

[241] H. Qian, L. Jinlong, L. Tongxiang, W. Chen, In Situ Synthesis of Mesoporous NiMoO4 on Ball Milled Graphene for High Performance Supercapacitors, Journal of The Electrochemical Society, 164 (2017) E173-E179.

[242] T. Liu, H. Chai, D. Jia, Y. Su, T. Wang, W. Zhou, Rapid microwave-assisted synthesis of mesoporous NiMoO4 nanorod/reduced graphene oxide composites for high-performance supercapacitors, Electrochimica Acta, 180 (2015) 998-1006.

[243] Y. Li, J. Jian, L. Xiao, H. Wang, L. Yu, G. Cheng, J. Zhou, M. Sun, Synthesis of NiMoO4nanosheets on graphene sheets as advanced supercapacitor electrode materials, Materials Letters, 184 (2016) 21-24.

[244] D. Ghosh, S. Giri, C.K. Das, Synthesis, characterization and electrochemical performance of graphene decorated with 1D NiMoO4 ·nH2O nanorods, Nanoscale, 5 (2013) 10428-10428.

[245] J. Yuan, D. Yao, L. Jiang, Y. Tao, J. Che, G. He, H. Chen, Mn-Doped NiMoO4 Mesoporous Nanorods/Reduced Graphene Oxide Composite for High-Performance All-Solid-State Supercapacitor, ACS Applied Energy Materials, 3 (2020) 1794-1803.

[246] M. Jiang, X. Zhang, Carbon fiber/Ni-Co layered double hydroxide@NiMoO4/graphene oxide sandwich structure flexible electrode materials: Facile synthesis and high supercapacitor performance, Journal of Alloys and Compounds, 794 (2019) 13-20.

[247] S. Arshadi R, R. Mamoory, F. Dabir, N. Blomquist, M. Phadatare, H. Olin, Synthesis of NiMoO4/3D-rGO Nanocomposite in Alkaline Environments for Supercapacitor Electrodes, Crystals, 9 (2019) 31.

[248] L. Jinlong, Y. Meng, K. Suzuki, H. Miura, Synthesis of CoMoO4@RGO nanocomposites as high-performance supercapacitor electrodes, Microporous and Mesoporous Materials, 242 (2017) 264-270.

[249] Y. Jiang, X. Zheng, X. Yan, Y. Li, X. Zhao, Y. Zhang, 3D architecture of a graphene/CoMoO4composite for asymmetric supercapacitors usable at various temperatures, Journal of Colloid and Interface Science, 493 (2017) 42-50.

[250] K. Xu, J. Chao, W. Li, Q. Liu, Z. Wang, X. Liu, R. Zou, J. Hu, CoMoO4·0.9H2O nanorods grown on reduced graphene oxide as advanced electrochemical pseudocapacitor materials, RSC Advances, 4 (2014) 34307-34314.

[251] X. Yu, B. Lu, Z. Xu, Super long-life supercapacitors based on the construction of nanohoneycomb-like strongly coupled CoMoO4-3D graphene hybrid electrodes, Advanced Materials, 26 (2014) 1044-1051.

[252] Y. Fu, X. Yue, L. Pan, S. Xu, Y. Zhu, D. Xiong, L. Wang, P.K. Chu, Three-dimensional CoMoO4nanorods/nanographene composites on a Ni coated macroporous electrically conductive network with excellent electrochemical performance, Materials Science and Engineering B: Solid-State Materials for Advanced Technology, 226 (2017) 177-187.

[253] J. Ahmed, M. Ubaidullah, T. Ahmad, N. Alhokbany, S.M. Alshehri, Synthesis of Graphite Oxide/Cobalt Molybdenum Oxide Hybrid Nanosheets for Enhanced Electrochemical Performance in Supercapacitors and the Oxygen Evolution Reaction, ChemElectroChem, 6 (2019) 2524-2530.

[254] L. Wan, J. Shen, Y. Zhang, X. Li, Novel ZnMoO4/reduced graphene oxide hybrid as a high-performance anode material for lithium ion batteries, Journal of Alloys and Compounds, 708 (2017) 713-721.

[255] R. Xue, W. Hong, Z. Pan, W. Jin, H. Zhao, Y. Song, J. Zhou, Y. Liu, Enhanced electrochemical performance of ZnMoO4/reduced graphene oxide composites as anode materials for lithium-ion batteries, Electrochimica Acta, 222 (2016) 838-844.

[256] B.J. Reddy, P.V.A. Simon, Investigation of novel zinc molybdate – graphene nanocomposite for supercapacitor applications, Applied Physics A, (2018).

[257] Y. Wang, P. He, W. Lei, F. Dong, T. Zhang, Novel FeMoO4/graphene composites based electrode materials for supercapacitors, Composites Science and Technology, 103 (2014) 16-21.

[258] X. Mu, J. Du, Y. Zhang, Z. Liang, H. Wang, B. Huang, J. Zhou, X. Pan, Z. Zhang, E. Xie, Construction of Hierarchical CNT/rGO-Supported MnMoO4 Nanosheets on Ni Foam for High-Performance Aqueous Hybrid Supercapacitors, ACS Applied Materials & Interfaces, 9 (2017) 35775-35784.

[259] D. Ghosh, S. Giri, M. Moniruzzaman, T. Basu, M. Mandal, C.K. Das, α $MnMoO_4$ /graphene hybrid composite: high energy density supercapacitor electrode material, Dalton Trans., 43 (2014) 11067-11076.

[260] S. Dutta, S. Pal, S. De, Hydrothermally synthesized BiVO4-reduced graphene oxide nanocomposite as a high performance supercapacitor electrode with excellent cycle stability, New Journal of Chemistry, 42 (2018) 10161-10166.

[261] Y. Yu, C. Niu, C. Han, K. Zhao, J. Meng, X. Xu, P. Zhang, L. Wang, Y. Wu, L. Mai, Zinc Pyrovanadate Nanoplates Embedded in Graphene Networks with

Enhanced Electrochemical Performance, Industrial & Engineering Chemistry Research, (2016).

[262] M. Wu, J. Yang, T. Feng, W. Jiang, D. Xia, F. Gong, J. Liao, Graphene coated $Co_3V_2O_8$ micro-pencils for enhanced-performance in lithium ion batteries, New Journal of Chemistry, 41 (2017) 10634-10639.

[263] W.H. Low, P.S. Khiew, S.S. Lim, C.W. Siong, E.R. Ezeigwe, Facile solvothermal designing of graphene/Ni3V2O8 nanocomposite as electrode for high performance symmetric supercapacitor, Journal of Alloys and Compounds, 768 (2018) 995-1005.

[264] W.H. Low, C.W. Siong, C.H. Chia, S.S. Lim, P.S. Khiew, A facile synthesis of graphene/Co3V2O8 nanocomposites and their enhanced charge storage performance in electrochemical capacitors, Journal of Science: Advanced Materials and Devices, 4 (2019) 515-523.

[265] W.H. Low, P.S. Khiew, S.S. Lim, C.W. Siong, C.H. Chia, E.R. Ezeigwe, Facile synthesis of graphene-Zn3V2O8 nanocomposite as a high performance electrode material for symmetric supercapacitor, Journal of Alloys and Compounds, 784 (2019) 847-858.

[266] H.R. Naderi, A. Sobhani-Nasab, M. Rahimi-Nasrabadi, M.R. Ganjali, Decoration of nitrogen-doped reduced graphene oxide with cobalt tungstate nanoparticles for use in high-performance supercapacitors, Applied Surface Science, 423 (2017) 1025-1034.

[267] X.-h. Guan, Z.-w. Zhang, L. Yang, G.-s. Wang, One-Pot Hydrothermal Synthesis of Hexagonal WO3 Nanorods/Graphene Composites as High-

Performance Electrodes for Supercapacitors, ChemPlusChem, 82 (2017) 1174-1181.

[268] P. He, K. Yang, W. Wang, F. Dong, L. Du, Y. Deng, Reduced graphene oxide-CoFe2O4 composites for supercapacitor electrode, Russian Journal of Electrochemistry, 49 (2013) 359-364.

[269] A.D. Adhikari, R. Oraon, S.K. Tiwari, P. Saren, J.H. Lee, N.H. Kim, G.C. Nayak, CdS-CoFe2O4@Reduced Graphene Oxide Nanohybrid: An Excellent Electrode Material for Supercapacitor Applications, Industrial & Engineering Chemistry Research, 57 (2018) 1350-1360.

[270] B. Dong, M. Li, C. Xiao, D. Ding, G. Gao, S. Ding, Tunable growth of perpendicular cobalt ferrite nanosheets on reduced graphene oxide for energy storage, Nanotechnology, 28 (2017).

[271] L. Li, H. Bi, S. Gai, F. He, P. Gao, Y. Dai, X. Zhang, D. Yang, M. Zhang, P. Yang, Uniformly Dispersed ZnFe 2 O 4 Nanoparticles on Nitrogen-Modified Graphene for High-Performance Supercapacitor as Electrode, Scientific Reports, 7 (2017) 1-12.

[272] W. Zhang, B. Quan, C. Lee, S.-K. Park, X. Li, E. Choi, G. Diao, Y. Piao, One-Step Facile Solvothermal Synthesis of Copper Ferrite–Graphene Composite as a High-Performance Supercapacitor Material, ACS Applied Materials & Interfaces, 7 (2015) 2404-2414.

[273] P. Kakvand, M.S. Rahmanifar, M.F. El-Kady, A. Pendashteh, M.A. Kiani, M. Hashami, M. Najafi, A. Abbasi, M.F. Mousavi, R.B. Kaner, Synthesis of NiMnO3/C nano-composite electrode materials for electrochemical capacitors, Nanotechnology, 27 (2016).

[274] S. Giri, D. Ghosh, C.K. Das, One pot synthesis of ilmenite-type NiMnO3-"nitrogen-doped" graphene nanocomposite as next generation supercapacitors, Dalton transactions (Cambridge, England : 2003), 42 (2013) 14361-14364.

[275] L. Wang, G. Duan, J. Zhu, S.M. Chen, X. Liu, High capacity supercapacitor material based on reduced graphene oxide loading mesoporpus murdochite-type Ni6MnO8nanospheres, Electrochimica Acta, 219 (2016) 284-294.

[276] G. Gao, S. Lu, Y. Xiang, B. Dong, W. Yan, S. Ding, Free-standing ultrathin $CoMn_2O_4$ nanosheets anchored on reduced graphene oxide for high-performance supercapacitors, Dalton Trans., 44 (2015) 18737-18742.

[277] J.S.Y. Chia, M.T.T. Tan, P.S. Khiew, J.K. Chin, H. Lee, D.C.S. Bien, C.W. Siong, A novel one step synthesis of graphene via sonochemical-assisted solvent exfoliation approach for electrochemical sensing application, Chemical Engineering Journal, 249 (2014) 270-278.

[278] J. Zhang, Transition-Metal-Oxide-Based Nanostructures As Supercapacitor Electrodes, in: Deaprtment of Chemical & Biomolecular Engineering, National University of Singapore, 2012.

[279] R. Sahoo, A. Pal, T. Pal, Proportion of composition in a composite does matter for advanced supercapacitor behavior, J. Mater. Chem. A, 4 (2016) 17440-17454.

[280] X. He, Q. Liu, J. Liu, R. Li, H. Zhang, R. Chen, J. Wang, High-performance all-solid-state asymmetrical supercapacitors based on petal-like NiCo2S4/Polyaniline nanosheets, Chemical Engineering Journal, 325 (2017) 134-143.

[281] Y. Zhao, X. He, R. Chen, Q. Liu, J. Liu, D. Song, H. Zhang, H. Dong, R. Li, M. Zhang, J. Wang, Hierarchical NiCo2S4@CoMoO4 core-shell heterostructures nanowire arrays as advanced electrodes for flexible all-solid-state asymmetric supercapacitors, Applied Surface Science, 453 (2018) 73-82.

[282] Y. Li, M. Zhang, D. Pan, Y. Wang, J. Xie, Z. Yan, J. Jing, Ultrathin hollow-structured NiCo2O4nanorod supported on improved N-doped graphene for superior supercapacitor applications, Journal of Alloys and Compounds, 722 (2017) 903-912.

[283] S.G. Mohamed, C.-J. Chen, C.K. Chen, S.-F. Hu, R.-S. Liu, High-Performance Lithium-Ion Battery and Symmetric Supercapacitors Based on FeCo2O4 Nanoflakes Electrodes, ACS Applied Materials & Interfaces, 6 (2014) 22701-22708.

[284] H. Wang, C.M.B. Holt, Z. Li, X. Tan, B.S. Amirkhiz, Z. Xu, B.C. Olsen, T. Stephenson, D. Mitlin, Graphene-nickel cobaltite nanocomposite asymmetrical supercapacitor with commercial level mass loading, Nano Research, 5 (2012) 605-617.

[285] K. Thiagarajan, J. Theerthagiri, R.A. Senthil, P. Arunachalam, J. Madhavan, M.A. Ghanem, Synthesis of Ni3V2O8@graphene oxide nanocomposite as an efficient electrode material for supercapacitor applications, Journal of Solid State Electrochemistry, 22 (2018) 527-536.

[286] N. Rogado, G. Lawes, D.A. Huse, A.P. Ramirez, R.J. Cava, The Kagomé-staircase lattice : Magnetic ordering in Ni 3 V 2 O 8 and Co 3 V 2 O 8.

[287] G. Lawes, A.B. Harris, T. Kimura, N. Rogado, R.J. Cava, A. Aharony, T. Yildirim, M. Kenzelmann, C. Broholm, A.P. Ramirez, Magnetically Driven Ferroelectric Order in Ni 3 V 2 O 8, 087205 (2005) 1-4.

[288] D. Wang, J. Tang, Z. Zou, J. Ye, Photophysical and Photocatalytic Properties of a New Series of Visible-Light-Driven Photocatalysts M3V2O8 (M = Mg, Ni, Zn), Chemistry of Materials, 17 (2005) 5177-5182.

[289] W.-B. Zhang, L.-B. Kong, X.-J. Ma, Y.-C. Luo, L. Kang, Nickel vanadate and nickel oxide nanohybrid on nickel foam as pseudocapacitive electrodes for electrochemical capacitors, RSC Adv., 4 (2014) 41772-41777.

[290] W. Du, X. Jiang, L. Zhu, From graphite to graphene: direct liquid-phase exfoliation of graphite to produce single- and few-layered pristine graphene, J. Mater. Chem. A, 1 (2013) 10592-10606.

[291] S. Park, R.S. Ruoff, Chemical methods for the production of graphenes, Nature Nanotechnology, 4 (2009) 217-224.

[292] S. Abureden, Advanced Nanostructure Materials for Hybrid Supercapacitors, in, 2017.

[293] H. Wang, R. Li, M. Li, Z. Li, Flower-like Fe2O3@multiple graphene aerogel for high-performance supercapacitors, Journal of Alloys and Compounds, 742 (2018) 759-768.

[294] A.C. Ferrari, Raman spectroscopy of graphene and graphite: Disorder, electron–phonon coupling, doping and nonadiabatic effects, Solid State Communications, 143 (2007) 47-57.

[295] A.C. Ferrari, D.M. Basko, Raman spectroscopy as a versatile tool for studying the properties of graphene, Nature Nanotechnology, 8 (2013) 235-246.

[296] H. Fu, Z. Duan, G. Henkelman, Computational Study of Structure and Reactivity of Oligomeric Vanadia Clusters Supported on Anatase and Rutile TiO 2 Surfaces, The Journal of Physical Chemistry C, 119 (2015) 150605113708003-150605113708003.

[297] K. Liang, W. He, X. Deng, H. Ma, X. Xu, Controlled synthesis of NiCo2S4 hollow spheres as high-performance electrode materials for supercapacitors, Journal of Alloys and Compounds, 735 (2018) 1395-1401.

[298] W. Du, Z. Wang, Z. Zhu, S. Hu, X. Zhu, Y. Shi, H. Pang, X. Qian, Facile synthesis and superior electrochemical performances of $CoNi_2S_4$ /graphene nanocomposite suitable for supercapacitor electrodes, J. Mater. Chem. A, 2 (2014) 9613-9619.

[299] B. Zhao, H. Zhuang, T. Fang, Z. Jiao, R. Liu, X. Ling, B. Lu, Y. Jiang, Self-assembly of NiO/graphene with three-dimension hierarchical structure as high performance electrode material for supercapacitors, Journal of Alloys and Compounds, 597 (2014) 291-298.

[300] H.Y. Tan, B.Z. Yu, L.L. Cao, T. Cheng, X.L. Zheng, X.H. Li, W.L. Li, Z.Y. Ren, Layer-dependent growth of two-dimensional Co3O4 nanostructure arrays on graphene for high performance supercapacitors, Journal of Alloys and Compounds, 696 (2017) 1180-1188.

[301] L. Liu, H. Zhang, J. Yang, Y. Mu, Y. Wang, Self-assembled novel dandelion-like NiCo2O4 microspheres@nanomeshes with superior electrochemical performance for supercapacitors and lithium-ion batteries, J. Mater. Chem. A, 3 (2015) 22393-22403.

[302] W. Li, F. Yang, Z. Hu, Y. Liu, Template synthesis of C@NiCo2O4 hollow microsphere as electrode material for supercapacitor, Journal of Alloys and Compounds, 749 (2018) 305-312.

[303] X. He, R. Li, J. Liu, Q. Liu, R. chen, D. Song, J. Wang, Hierarchical FeCo2O4@NiCo layered double hydroxide core/shell nanowires for high performance flexible all-solid-state asymmetric supercapacitors, Chemical Engineering Journal, 334 (2018) 1573-1583.

[304] E. Umeshbabu, G. Rajeshkhanna, G. Ranga Rao, Effect of solvents on the morphology of NiCo2O4/graphene nanostructures for electrochemical pseudocapacitor application, Journal of Solid State Electrochemistry, 20 (2016) 1837-1844.

[305] J. Zhou, Y. Huang, X. Cao, B. Ouyang, W. Sun, C. Tan, Y. Zhang, Q. Ma, S. Liang, Q. Yan, H. Zhang, Two-dimensional $NiCo_2O_4$ nanosheet-coated three-dimensional graphene networks for high-rate, long-cycle-life supercapacitors, Nanoscale, 7 (2015) 7035-7039.

[306] M.D. Stoller, R.S. Ruoff, Best practice methods for determining an electrode materials performance for ultracapacitors, Energy Environ. Sci., 3 (2010) 1294-1301.

[307] X. He, Q. Liu, J. Liu, R. Li, H. Zhang, R. Chen, J. Wang, Hierarchical NiCo2O4@NiCoAl-layered double hydroxide core/shell nanoforest arrays as advanced electrodes for high-performance asymmetric supercapacitors, Journal of Alloys and Compounds, 724 (2017) 130-138.

[308] H. Chen, J. Jiang, L. Zhang, H. Wan, T. Qi, D. Xia, Highly conductive NiCo2S4 urchin-like nanostructures for high-rate pseudocapacitors, Nanoscale, 5 (2013) 8879-8883.

[309] D. Kong, W. Ren, C. Cheng, Y. Wang, Z. Huang, H.Y. Yang, Three-Dimensional NiCo2O4@Polypyrrole Coaxial Nanowire Arrays on Carbon Textiles for High-Performance Flexible Asymmetric Solid-State Supercapacitor, ACS Applied Materials & Interfaces, 7 (2015) 21334-21346.

[310] J.M. Xu, K.Y. Ma, J.P. Cheng, Controllable in situ synthesis of Ni(OH)2 and NiO films on nickel foam as additive-free electrodes for electrochemical capacitors, Journal of Alloys and Compounds, 653 (2015) 88-94.

[311] L. Li, J. Xu, J. Lei, J. Zhang, F. McLarnon, Z. Wei, N. Li, F. Pan, A one-step{,} cost-effective green method to in situ fabricate Ni(OH)2 hexagonal platelets on Ni foam as binder-free supercapacitor electrode materials, J. Mater. Chem. A, 3 (2015) 1953-1960.

[312] Q. Sun, T. He, Y. Li, A novel all solid-state asymmetric supercapacitor with superior electrochemical performance in a wide temperature range using a hydroquinone modified graphene xerogel as the cathode and N-doped Ti3C2Tx as the anode, Journal of Materials Chemistry A, 8 (2020) 1687-1696.

[313] M. Li, J. Yu, X. Wang, Z. Yang, 3D porous MnO2@carbon nanosheet synthesized from rambutan peel for high-performing supercapacitor electrodes materials, Applied Surface Science, 530 (2020) 147230.

[314] V. Shrivastav, S. Sundriyal, A. Kaur, U.K. Tiwari, S. Mishra, A. Deep, Conductive and porous ZIF-67/PEDOT hybrid composite as superior electrode for

all-solid-state symmetrical supercapacitors, Journal of Alloys and Compounds, 843 (2020) 155992.

[315] S.S. Karade, S. Lalwani, J.-H. Eum, H. Kim, Coin cell fabricated symmetric supercapacitor device of two-steps synthesized V2O5 Nanorods, Journal of Electroanalytical Chemistry, 864 (2020) 114080.

[316] Z. Pan, X. Ji, Facile synthesis of nitrogen and oxygen co-doped C@Ti3C2 MXene for high performance symmetric supercapacitors, Journal of Power Sources, 439 (2019) 227068.

[317] K. Chi, Z. Zhang, Q. Lv, C. Xie, J. Xiao, F. Xiao, S. Wang, Well-Ordered Oxygen-Deficient CoMoO4 and Fe2O3 Nanoplate Arrays on 3D Graphene Foam: Toward Flexible Asymmetric Supercapacitors with Enhanced Capacitive Properties, ACS Applied Materials & Interfaces, 9 (2017) 6044-6053.

[318] L. Deng, J. Liu, Z. Ma, G. Fan, Z.-h. Liu, Free-standing graphene/bismuth vanadate monolith composite as a binder-free electrode for symmetrical supercapacitors, RSC Advances, 8 (2018) 24796-24804.

[319] Y. Cheng, L. Huang, X. Xiao, B. Yao, L. Yuan, T. Li, Z. Hu, B. Wang, J. Wan, J. Zhou, Flexible and cross-linked N-doped carbon nanofiber network for high performance freestanding supercapacitor electrode, Nano Energy, 15 (2015) 66-74.

[320] A.K. Geim, Graphene: Status and Prospects, Science, 324 (2009) 1530.

[321] F. Gong, D. Xia, C. Bi, J. Yang, W. Zeng, C. Chen, Y. Ding, Z. Xu, J. Liao, M. Wu, Systematic comparison of hollow and solid Co3V2O8 micro-pencils as advanced anode materials for lithium ion batteries, Electrochimica Acta, 264 (2018) 358-366.

[322] G. Gao, S. Lu, B. Dong, Y. Xiang, K. Xi, S. Ding, Mesoporous Co3V2O8 nanoparticles grown on reduced graphene oxide as a high-rate and long-life anode material for lithium-ion batteries, Journal of Materials Chemistry A, 4 (2016) 6264-6270.

[323] Y.-S. Seo, S.-H. Kim, J.S. Ahn, I.-K. Jeong, Determination of the local symmetry and the multiferroic-ferromagnetic crossover in Ni3−xCoxV2O8 by using Raman scattering spectroscopy, Journal of the Korean Physical Society, 62 (2013) 116-120.

[324] Y. Sun, X. Hu, W. Luo, J. Shu, Y. Huang, Self-assembly of hybrid Fe2Mo3O8–reduced graphene oxide nanosheets with enhanced lithium storage properties, Journal of Materials Chemistry A, 1 (2013) 4468-4474.

[325] S.E. Moosavifard, J. Shamsi, M.K. Altafi, Z.S. Moosavifard, All-solid state, flexible, high-energy integrated hybrid micro-supercapacitors based on 3D LSG/CoNi2S4 nanosheets, Chemical Communications, 52 (2016) 13140-13143.

[326] L. Xie, Y. Liu, H. Bai, C. Li, B. Mao, L. Sun, W. Shi, Core-shell structured ZnCo2O4@ZnWO4 nanowire arrays on nickel foam for advanced asymmetric supercapacitors, Journal of Colloid and Interface Science, 531 (2018) 64-73.

[327] M. Ahmed, M. Khawaja, M. Notarianni, B. Wang, D. Goding, B. Gupta, J.J. Boeckl, A. Takshi, N. Motta, S.E. Saddow, F. Iacopi, A thin film approach for SiC-derived graphene as an on-chip electrode for supercapacitors, Nanotechnology, 26 (2015) 434005.

[328] F. Hadish, S. Jou, B.-R. Huang, H.-A. Kuo, C.-W. Tu, Functionalization of CVD Grown Graphene with Downstream Oxygen Plasma Treatment for Glucose Sensors, Journal of The Electrochemical Society, 164 (2017) B336-B341.

[329] J. Shao, H. Zhou, M. Zhu, J. Feng, A. Yuan, Facile synthesis of metal-organic framework-derived Co3O4 with different morphologies coated graphene foam as integrated anodes for lithium-ion batteries, Journal of Alloys and Compounds, 768 (2018) 1049-1057.

[330] Z. Yang, H. Zhang, B. Ma, L. Xie, Y. Chen, Z. Yuan, K. Zhang, J. Wei, Facile synthesis of reduced graphene oxide/tungsten disulfide/tungsten oxide nanohybrids for high performance supercapacitor with excellent rate capability, Applied Surface Science, 463 (2019) 150-158.

[331] W. Chen, X. Yu, Z. Zhao, S. Ji, L. Feng, Hierarchical architecture of coupling graphene and 2D WS2 for high-performance supercapacitor, Electrochimica Acta, 298 (2019) 313-320.

[332] B.S. Singu, K.R. Yoon, Exfoliated graphene-manganese oxide nanocomposite electrode materials for supercapacitor, Journal of Alloys and Compounds, 770 (2019) 1189-1199.

[333] K.H. Oh, G.S. Gund, H.S. Park, Stabilizing NiCo2O4 hybrid architectures by reduced graphene oxide interlayers for improved cycling stability of hybrid supercapacitors, Journal of Materials Chemistry A, 6 (2018) 22106-22114.

[334] D. Guo, L. Zhang, X. Song, L. Tan, H. Ma, J. Jiao, D. Zhu, F. Li, NiCo2O4 nanosheets grown on interconnected honeycomb-like porous biomass carbon for high performance asymmetric supercapacitors, New Journal of Chemistry, 42 (2018) 8478-8484.

[335] R. Ramachandran, Q. Hu, K. Rajavel, P. Zhu, C. Zhao, F. Wang, Z.-X. Xu, Non-peripheral octamethyl-substituted copper (II) phthalocyanine nanorods with MXene sheets: An excellent electrode material for symmetric supercapacitor with

enhanced electrochemical performance, Journal of Power Sources, 471 (2020) 228472.

[336] E. Cevik, A. Bozkurt, Redox active polymer metal chelates for use in flexible symmetrical supercapacitors: Cobalt-containing poly(acrylic acid) polymer electrolytes, Journal of Energy Chemistry, 55 (2021) 145-153.

[337] C. Zhou, Q. Wang, X.H. Yan, J.J. Wang, D.F. Wang, X.X. Yuan, H. Jiang, Y.H. Zhu, X.N. Cheng, A facile route to synthesize Ag decorated MoO3 nanocomposite for symmetric supercapacitor, Ceramics International, 46 (2020) 15385-15391.

[338] X. Yuan, X. Yan, C. Zhou, D. Wang, Y. Zhu, J. Wang, X. Tao, X. Cheng, Promising carbon nanosheets decorated by self-assembled MoO2 nanoparticles: Controllable synthesis, boosting performance and application in symmetric coin cell supercapacitors, Ceramics International, 46 (2020) 19981-19989.

[339] Y. Wang, R. Liu, Y. Tian, Z. Sun, Z. Huang, X. Wu, B. Li, Heteroatoms-doped hierarchical porous carbon derived from chitin for flexible all-solid-state symmetric supercapacitors, Chemical Engineering Journal, 384 (2020) 123263.

[340] D. Yang, Q. Zhao, L. Huang, B. Xu, N.A. Kumar, X.S. Zhao, Encapsulation of NiCo2O4 in nitrogen-doped reduced graphene oxide for sodium ion capacitors, Journal of Materials Chemistry A, 6 (2018) 14146-14154.

[341] E.R. Ezeigwe, C.J. Sin, P.S. Khiew, C.W. Siong, M.T.T. Tan, Cobalt oxide nanoparticles grown on exfoliated graphene for enhanced electrochemical performance, Materials Chemistry and Physics, 183 (2016) 56-64.

[342] Y. Zhou, L. Wen, K. Zhan, Y. Yan, B. Zhao, Three-dimensional porous graphene/nickel cobalt mixed oxide composites for high-performance hybrid supercapacitor, Ceramics International, 44 (2018) 21848-21854.

[343] C. Bie, J. Pei, J. Wang, K. Hua, D. Chen, G. Chen, Graphite Nanoplates Firmly Anchored with Well-dispersed Porous Zn3V2O8 Nanospheres: Rational Fabrication and Enhanced Lithium Storage Capability, Electrochimica Acta, 248 (2017) 140-149.

[344] H.-J. Choi, S.-M. Jung, J.-M. Seo, D.W. Chang, L. Dai, J.-B. Baek, Graphene for energy conversion and storage in fuel cells and supercapacitors, Nano Energy, 1 (2012) 534-551.

[345] Z.-S. Wu, G. Zhou, L.-C. Yin, W. Ren, F. Li, H.-M. Cheng, Graphene/metal oxide composite electrode materials for energy storage, Nano Energy, 1 (2012) 107-131.

[346] K. Zhang, L.L. Zhang, X.S. Zhao, J. Wu, Graphene/Polyaniline Nanofiber Composites as Supercapacitor Electrodes, Chemistry of Materials, 22 (2010) 1392-1401.

[347] R. Kumar, P. Rai, A. Sharma, Free-standing NiV_2S_4 nanosheet arrays on a 3D Ni framework via an anion exchange reaction as a novel electrode for asymmetric supercapacitor applications, J. Mater. Chem. A, 4 (2016) 17512-17520.

[348] S. Dutta, S. Pal, S. De, Hydrothermally synthesized BiVO4–reduced graphene oxide nanocomposite as a high performance supercapacitor electrode with excellent cycle stability, New Journal of Chemistry, 42 (2018) 10161-10166.

[349] M.-C. Liu, L.-B. Kong, C. Lu, X.-J. Ma, X.-M. Li, Y.-C. Luo, L. Kang, Design and synthesis of CoMoO4–NiMoO4 ·xH2O bundles with improved

electrochemical properties for supercapacitors, Journal of Materials Chemistry A, 1 (2013) 1380-1387.

[350] D. Johnsirani, A. Pandurangan, Chromium, fluorine and nitrogen tri-doped graphene sheets as an active electrode material for symmetric supercapacitors, Diamond and Related Materials, 105 (2020) 107800.

[351] C. Mevada, P.S. Chandran, M. Mukhopadhyay, Room-temperature synthesis of tin oxide nanoparticles using gallic acid monohydrate for symmetrical supercapacitor application, Journal of Energy Storage, 28 (2020) 101197.

[352] T. Zhang, H. Yue, X. Gao, F. Yao, H. Chen, X. Lu, Y. Wang, X. Guo, Polyaniline nanowire arrays on three-dimensional hollow graphene balls for high-performance symmetric supercapacitor, Journal of Electroanalytical Chemistry, 855 (2019) 113574.

[353] Y. Zhang, J. Ding, W. Xu, M. Wang, R. Shao, Y. Sun, B. Lin, Mesoporous LaFeO3 perovskite derived from MOF gel for all-solid-state symmetric supercapacitors, Chemical Engineering Journal, 386 (2020) 124030.

[354] Y.-H. Chiu, L.-Y. Lin, Effect of activating agents for producing activated carbon using a facile one-step synthesis with waste coffee grounds for symmetric supercapacitors, Journal of the Taiwan Institute of Chemical Engineers, 101 (2019) 177-185.

[355] D. Deng, Y. Zhang, G. Li, X. Wang, L.-H. Gan, L. Jiang, C.-R. Wang, 2 D Manganese Vanadate Nanoflakes as High-Performance Anode for Lithium-Ion Batteries, Chemistry – An Asian Journal, 9 (2014) 1265-1269.

[356] H. Peng, J. Ding, N. Wang, G. Li, Facile synthesis of MnV2O6 nanostructures with controlled morphologies, Materials Letters, 63 (2009) 1404-1406.

[357] R. Ramachandran, Q. Hu, F. Wang, Z.-X. Xu, Synthesis of N-CuMe2Pc nanorods/graphene oxide nanocomposite for symmetric supercapacitor electrode with excellent cyclic stability, Electrochimica Acta, 298 (2019) 770-777.

[358] D. Qiu, X. Ma, J. Zhang, B. Zhao, Z. Lin, In situ synthesis of mesoporous Co3O4 nanorods anchored on reduced graphene oxide nanosheets as supercapacitor electrodes, Chemical Physics Letters, 710 (2018) 188-192.

[359] C. Qu, L. Zhang, W. Meng, Z. Liang, B. Zhu, D. Dang, S. Dai, B. Zhao, H. Tabassum, S. Gao, H. Zhang, W. Guo, R. Zhao, X. Huang, M. Liu, R. Zou, MOF-derived α-NiS nanorods on graphene as an electrode for high-energy-density supercapacitors, Journal of Materials Chemistry A, 6 (2018) 4003-4012.

[360] B. Zhao, D. Chen, X. Xiong, B. Song, R. Hu, Q. Zhang, B.H. Rainwater, G.H. Waller, D. Zhen, Y. Ding, Y. Chen, C. Qu, D. Dang, C.-P. Wong, M. Liu, A high-energy, long cycle-life hybrid supercapacitor based on graphene composite electrodes, Energy Storage Materials, 7 (2017) 32-39.

[361] Y. Liu, Y. Zhang, J. Du, W. Yu, Y. Qian, Synthesis and characterization of single-crystal MnV2O6 nanobelts, Journal of Crystal Growth, 291 (2006) 320-324.

[362] S. Sun, S. Wang, S. Li, Y. Li, Y. Zhang, J. Chen, Z. Zhang, S. Fang, P. Wang, Asymmetric supercapacitors based on a NiCo2O4/three dimensional graphene composite and three dimensional graphene with high energy density, Journal of Materials Chemistry A, 4 (2016) 18646-18653.

[363] W. Huang, S. Gao, X. Ding, L. Jiang, M. Wei, Crystalline MnV2O6 nanobelts: Synthesis and electrochemical properties, Journal of Alloys and Compounds, 495 (2010) 185-188.

[364] X. Zhang, X. Li, F. Jiang, W. Du, C. Hou, Z. Xu, L. Zhu, Z. Wang, H. Liu, W. Zhou, H. Yuan, Improved electrochemical performance of 2D accordion-like MnV2O6 nanosheets as anode materials for Li-ion batteries, Dalton Transactions, (2020).

[365] S. Zhang, R. Hu, L. Liu, D. Wang, Hydrothermal synthesis of MnV2O6 nanobelts and its application in lithium-ion battery, Materials Letters, 124 (2014) 57-60.

[366] S. Deng, D. Sun, C. Wu, H. Wang, J. Liu, Y. Sun, H. Yan, Synthesis and electrochemical properties of MnO2 nanorods/graphene composites for supercapacitor applications, Electrochimica Acta, 111 (2013) 707-712.

[367] A.K. Das, S. Sahoo, P. Arunachalam, S. Zhang, J.-J. Shim, Facile synthesis of Fe3O4 nanorod decorated reduced graphene oxide (RGO) for supercapacitor application, RSC Advances, 6 (2016) 107057-107064.

[368] J. Mao, C. He, J. Qi, A. Zhang, Y. Sui, Y. He, Q. Meng, F. Wei, An Asymmetric Supercapacitor with Mesoporous NiCo2O4 Nanorod/Graphene Composite and N-Doped Graphene Electrodes, Journal of Electronic Materials, (2017).

[369] S. Lei, K. Tang, Y. Jin, C. Chen, Preparation of aligned MnV2O6 nanorods and their anodic performance for lithium secondary battery use, Nanotechnology, 18 (2007) 175605.

[370] E. Umeshbabu, G. Rajeshkhanna, P. Justin, G.R. Rao, Synthesis of mesoporous NiCo2O4–rGO by a solvothermal method for charge storage applications, RSC Advances, 5 (2015) 66657-66666.

[371] M. Simões, Y. Surace, S. Yoon, C. Battaglia, S. Pokrant, A. Weidenkaff, Hydrothermal vanadium manganese oxides: Anode and cathode materials for lithium-ion batteries, Journal of Power Sources, 291 (2015).

[372] J.I. Viegas, R.L. Moreira, A. Dias, Polymorphism and Optical–Vibration Properties of MnV2O6·nH2O (n = 0, 2, 4) Prepared by Microwave Irradiation, Crystal Growth & Design, 19 (2019) 3233-3243.

[373] A.G. Souza Filho, O.P. Ferreira, E.J.G. Santos, J. Mendes Filho, O.L. Alves, Raman Spectra in Vanadate Nanotubes Revisited, Nano Letters, 4 (2004) 2099-2104.

[374] M. Wall, The Raman Spectroscopy of Graphene and the Determination of Layer Thickness, in, Thermo Fisher Scientific, Madison, 2011.

[375] S.H. Kazemi, F. Bahmani, H. Kazemi, M.A. Kiani, Binder-free electrodes of NiMoO4/graphene oxide nanosheets: synthesis, characterization and supercapacitive behavior, RSC Advances, 6 (2016) 111170-111181.

[376] D. Moitra, C. Anand, B.K. Ghosh, M. Chandel, N.N. Ghosh, One-Dimensional BiFeO3 Nanowire-Reduced Graphene Oxide Nanocomposite as Excellent Supercapacitor Electrode Material, ACS Applied Energy Materials, 1 (2018) 464-474.

[377] L. Halder, A. Kumar Das, A. Maitra, A. Bera, S. Paria, S.K. Karan, S.K. Si, S. Ojha, A. De, B.B. Khatua, A polypyrrole-adorned, self-supported, pseudocapacitive zinc vanadium oxide nanoflower and nitrogen-doped reduced graphene oxide-based asymmetric supercapacitor device for power density applications, New Journal of Chemistry, 44 (2020) 1063-1075.

[378] A. Mohammadi Zardkhoshoui, S.S. Hosseiny Davarani, Formation of graphene-wrapped multi-shelled NiGa2O4 hollow spheres and graphene-wrapped yolk–shell NiFe2O4 hollow spheres derived from metal–organic frameworks for high-performance hybrid supercapacitors, Nanoscale, 12 (2020) 1643-1656.

[379] Z. Cao, C. Liu, Y. Huang, Y. Gao, Y. Wang, Z. Li, Y. Yan, M. Zhang, Oxygen-vacancy-rich NiCo2O4 nanoneedles electrode with poor crystallinity for high energy density all-solid-state symmetric supercapacitors, Journal of Power Sources, 449 (2020) 227571.

[380] N. Joseph, C.B. A, Construction of few layered metallic MoS2 microspheres using glucose induced carbon spheres and its application in symmetric supercapacitor device, Journal of Electroanalytical Chemistry, 874 (2020) 114461.

[381] H. Liu, W. Zhu, D. Long, J. Zhu, G. Pezzotti, Porous V2O5 nanorods/reduced graphene oxide composites for high performance symmetric supercapacitors, Applied Surface Science, 478 (2019) 383-392.

[382] X. Xu, W. Zhong, X. Zhang, J. Dou, Z. Xiong, Y. Sun, T. Wang, Y. Du, Flexible symmetric supercapacitor with ultrahigh energy density based on NiS/MoS2@N-rGO hybrids electrode, Journal of Colloid and Interface Science, 543 (2019) 147-155.

[383] Y.L. Cheah, V. Aravindan, S. Madhavi, Improved Elevated Temperature Performance of Al-Intercalated V2O5 Electrospun Nanofibers for Lithium-Ion Batteries, ACS Applied Materials & Interfaces, 4 (2012) 3270-3277.

[384] L. Liu, Y. Wang, Q. Meng, B. Cao, A novel hierarchical graphene/polyaniline hollow microsphere as electrode material for supercapacitor applications, Journal of Materials Science, 52 (2017) 7969-7983.

[385] S. Jadhav, R.S. Kalubarme, C. Terashima, B.B. Kale, V. Godbole, A. Fujishima, S.W. Gosavi, Manganese dioxide/ reduced graphene oxide composite an electrode material for high-performance solid state supercapacitor, Electrochimica Acta, 299 (2019) 34-44.

[386] S. Kumari, S. Maity, A.A. Vannathan, D. Shee, P.P. Das, S.S. Mal, Improved electrochemical performance of graphene oxide supported vanadomanganate (IV) nanohybrid electrode material for supercapacitors, Ceramics International, (2019).

[387] J. Zhang, Z. Zhang, Y. Jiao, H. Yang, Y. Li, J. Zhang, P. Gao, The graphene/lanthanum oxide nanocomposites as electrode materials of supercapacitors, Journal of Power Sources, 419 (2019) 99-105.

[388] H. Wang, C. Shen, J. Liu, W. Zhang, S. Yao, Three-dimensional MnCo2O4/graphene composites for supercapacitor with promising electrochemical properties, Journal of Alloys and Compounds, 792 (2019) 122-129.

[389] C. Gómez-Navarro, R.T. Weitz, A.M. Bittner, M. Scolari, A. Mews, M. Burghard, K. Kern, Electronic Transport Properties of Individual Chemically Reduced Graphene Oxide Sheets, Nano Letters, 7 (2007) 3499-3503.

[390] S. Ramesh, K. Karuppasamy, S. Msolli, H.-S. Kim, H.S. Kim, J.-H. Kim, A nanocrystalline structured NiO/MnO2@nitrogen-doped graphene oxide hybrid nanocomposite for high performance supercapacitors, New Journal of Chemistry, 41 (2017) 15517-15527.

[391] B.L. Hurley, S. Qiu, R.G. Buchheit, Raman Spectroscopy Characterization of Aqueous Vanadate Species Interaction with Aluminum Alloy 2024-T3 Surfaces, Journal of The Electrochemical Society, 158 (2011) C125-C131.

[392] R.L. Frost, S.J. Palmer, J. Čejka, J. Sejkora, J. Plášil, S. Bahfenne, E.C. Keeffe, A Raman spectroscopic study of the different vanadate groups in solid-state compounds—model case: mineral phases vésigniéite [BaCu3(VO4)2(OH)2] and volborthite [Cu3V2O7(OH)2 ·2H2O], Journal of Raman Spectroscopy, 42 (2011) 1701-1710.

[393] B. Bashir, A. Rahman, H. Sabeeh, M.A. Khan, M.F. Aly Aboud, M.F. Warsi, I. Shakir, P.O. Agboola, M. Shahid, Copper substituted nickel ferrite nanoparticles anchored onto the graphene sheets as electrode materials for supercapacitors fabrication, Ceramics International, 45 (2019) 6759-6766.

[394] Q. Gao, J. Wang, J. Wang, Morphology-controllable synthesis of CuCo2O4 arrays on Ni foam as advanced electrodes for supercapacitors, Journal of Alloys and Compounds, 789 (2019) 193-200.

[395] S. Li, K. Yang, P. Ye, H. Jiang, Z. Zhang, Q. Huang, L. Wang, Hierarchical interpenetrating rHGO-decorated NiCo2O4 nanowires architectures for high-performance supercapacitors, Applied Surface Science, 473 (2019) 326-333.

[396] Y. Gao, Y. Xia, H. Wan, X. Xu, S. Jiang, Enhanced cycle performance of hierarchical porous sphere MnCo2O4 for asymmetric supercapacitors, Electrochimica Acta, 301 (2019) 294-303.

[397] S. Sundriyal, S. Mishra, A. Deep, Study of Manganese-1,4-Benzenedicarboxylate Metal Organic Framework Electrodes Based Solid State Symmetrical Supercapacitor, Energy Procedia, 158 (2019) 5817-5824.

[398] N. Cai, J. Fu, V. Chan, M. Liu, W. Chen, J. Wang, H. Zeng, F. Yu, MnCo2O4@nitrogen-doped carbon nanofiber composites with meso-microporous

structure for high-performance symmetric supercapacitors, Journal of Alloys and Compounds, 782 (2019) 251-262.

[399] Y. Zhang, G. Wen, S. Fan, Y. Chu, S. Li, B. Xu, J. Zhang, Phenolic hydroxyl functionalized partially reduced graphene oxides for symmetric supercapacitors with significantly enhanced electrochemical performance, Journal of Power Sources, 435 (2019) 226799.

[400] Y. Ma, M. Chen, X. Zheng, D. Yu, X. Dong, Synergetic effect of swelling and chemical blowing to develop peach gum derived nitrogen-doped porous carbon nanosheets for symmetric supercapacitors, Journal of the Taiwan Institute of Chemical Engineers, 101 (2019) 24-30.

[401] X. Wang, Y. Zhang, J. Zheng, X. Liu, C. Meng, Hydrothermal synthesis of VS4/CNTs composite with petal-shape structures performing a high specific capacity in a large potential range for high-performance symmetric supercapacitors, Journal of Colloid and Interface Science, 554 (2019) 191-201.